

AD \_\_\_\_\_

Award Number: W81XWH-07-1-0306

TITLE: PROSPECT: PROFILING OF RESISTANCE PATTERNS & ONCOGENIC  
SIGNALING PATHWAYS IN EVALUATION OF CANCERS OF THE THORAX AND  
THERAPEUTIC TARGET IDENTIFICATION

PRINCIPAL INVESTIGATOR: WAUN KI HONG, MD

CONTRACTING ORGANIZATION: University of Texas M.D. Anderson Cancer Center  
Houston, TX 77030

REPORT DATE: June 2011

TYPE OF REPORT: Annual

PREPARED FOR: U.S. Army Medical Research and Materiel Command  
Fort Detrick, Maryland 21702-5012

DISTRIBUTION STATEMENT: Approved for public release; distribution unlimited

The views, opinions and/or findings contained in this report are those of the author(s) and should not be construed as an official Department of the Army position, policy or decision unless so designated by other documentation.

<b>REPORT DOCUMENTATION PAGE</b>				<i>Form Approved</i> <b>OMB No. 0704-0188</b>	
Public reporting burden for this collection of information is estimated to average 1 hour per response, including the time for reviewing instructions, searching existing data sources, gathering and maintaining the data needed, and completing and reviewing this collection of information. Send comments regarding this burden estimate or any other aspect of this collection of information, including suggestions for reducing this burden to Department of Defense, Washington Headquarters Services, Directorate for Information Operations and Reports (0704-0188), 1215 Jefferson Davis Highway, Suite 1204, Arlington, VA 22202-4302. Respondents should be aware that notwithstanding any other provision of law, no person shall be subject to any penalty for failing to comply with a collection of information if it does not display a currently valid OMB control number. <b>PLEASE DO NOT RETURN YOUR FORM TO THE ABOVE ADDRESS.</b>					
<b>1. REPORT DATE</b> 01-06-2011		<b>2. REPORT TYPE</b> Annual		<b>3. DATES COVERED</b> 1 JUN 2007 - 31 MAY 2011	
<b>4. TITLE AND SUBTITLE</b> n PROSPECT: PROFILING OF RESISTANCE PATTERNS & ONCOGENIC SIGNALING PATHWAYS IN EVALUATION OF CANCERS OF THE THORAX AND THERAPEUTIC TARGET IDENTIFICATION				<b>5a. CONTRACT NUMBER</b>	
				<b>5b. GRANT NUMBER</b> W81XWH-07-1-0306	
				<b>5c. PROGRAM ELEMENT NUMBER</b>	
<b>6. AUTHOR(S)</b>  WAUN KI HONG, MD  <b>E-Mail:</b> whong@mdanderson.org				<b>5d. PROJECT NUMBER</b>	
				<b>5e. TASK NUMBER</b>	
				<b>5f. WORK UNIT NUMBER</b>	
<b>7. PERFORMING ORGANIZATION NAME(S) AND ADDRESS(ES)</b>  University of Texas M.D. Anderson Cancer Center Houston, TX 77030				<b>8. PERFORMING ORGANIZATION REPORT NUMBER</b>	
<b>9. SPONSORING / MONITORING AGENCY NAME(S) AND ADDRESS(ES)</b> U.S. Army Medical Research and Materiel Command Fort Detrick, Maryland 21702-5012				<b>10. SPONSOR/MONITOR'S ACRONYM(S)</b>	
				<b>11. SPONSOR/MONITOR'S REPORT NUMBER(S)</b>	
<b>12. DISTRIBUTION / AVAILABILITY STATEMENT</b> Approved for Public Release; Distribution Unlimited					
<b>13. SUPPLEMENTARY NOTES</b>					
<b>14. ABSTRACT</b>  We will develop a high throughput therapeutic-target focused (TTF) profiling platform and will combine this with tumor genome wide mRNA profiling and with serum or plasma profiling of phosphopeptides and DNA. We will use these molecular profiles to help define how various molecular factors alone and in combination relate to resistance to therapy, to prognosis, and to metastatic patterns at relapse. Using tumor and blood samples from non-small cell lung cancer (NSCLC) patients as well as NSCLC cell lines with defined chemotherapy resistance patterns, we will examine how molecular profiles may confer resistance and will identify new, potential therapeutic targets. The PROSPECT approach will be novel in that we will assess tumors from NSCLC patients undergoing surgical resection after having received neoadjuvant therapy as a model of resistance. Tumor surviving neoadjuvant therapy would be expected to be enriched for resistant cells. We will define what combinations of targeted therapies are most effective against resistant cell lines with similar molecular profiles, and this will drive later clinical trials (beyond the scope of this Program).					
<b>15. SUBJECT TERMS</b> Lung cancer, mesothelioma, target-focused profiling, resistance					
<b>16. SECURITY CLASSIFICATION OF:</b>			<b>17. LIMITATION OF ABSTRACT</b>  UU	<b>18. NUMBER OF PAGES</b>  151	<b>19a. NAME OF RESPONSIBLE PERSON</b> USAMRMC
<b>a. REPORT</b> U	<b>b. ABSTRACT</b> U	<b>c. THIS PAGE</b> U			<b>19b. TELEPHONE NUMBER</b> (include area code)

## TABLE OF CONTENTS

<b>INTRODUCTION .....</b>	<b>4</b>
<b>PROGRESS REPORT (BODY) .....</b>	<b>4</b>
<i>Project 1 .....</i>	<i>4</i>
<i>Project 2 .....</i>	<i>9</i>
<i>Project 3.....</i>	<i>13</i>
<i>Project 4.....</i>	<i>28</i>
<i>Project 5.....</i>	<i>32</i>
<i>Pathology Core .....</i>	<i>37</i>
<i>Biostatistics Core .....</i>	<i>41</i>
<b>KEY RESEARCH ACCOMPLISHMENTS .....</b>	<b>44</b>
<b>REPORTABLE OUTCOMES.....</b>	<b>47</b>
<b>CONCLUSIONS .....</b>	<b>50</b>
<b>APPENDICES.....</b>	<b>52</b>
<b>Appendix A - Abstracts and Publications</b>	
<b>Appendix B - Biostatistics Database Screenshots</b>	

## **INTRODUCTION**

Lung cancer is the leading cause of cancer death in the world. Non-small cell lung cancer (NSCLC) accounts for 85% of all lung cancer cases. Only 15% of patients diagnosed with lung cancer survive five years from diagnosis. Therapy for advanced disease increases average life expectancy by only a few months, and slightly improves quality of life. Similarly, adjuvant chemotherapy for resected disease has only a modest impact on survival rates. More effective therapy is needed. We believe that applying state-of-the-art molecular tools to carefully conducted clinical trials will lead to the identification of molecular mechanisms that contribute to lung cancer therapeutic resistance and that drive prognosis, and that this in turn will lead to the development of drugs with novel biological and therapeutic functions. Therefore, we have undertaken a translational research program named **PROSPECT: Profiling of Resistance Patterns & Oncogenic Signaling Pathways in Evaluation of Cancers of the Thorax and Therapeutic Target Identification**. The goal of PROSPECT is to use therapeutic target-focused (TTF) profiling along with genome-wide mRNA and serum phosphopeptide profiling to identify and evaluate molecular targets and pathways that contribute to therapeutic sensitivity or resistance, prognosis, and recurrence patterns, and to use this information to guide formulation of new rational therapeutic strategies for NSCLC and mesotheliomas. In the Program, we have 5 research projects and 3 Cores to address 3 central issues: therapeutic resistance, prognosis and new therapeutic targets and strategies.

## **PROGRESS REPORT (BODY):**

**Project 1: Therapeutic target-focused (TTF) profiling for the identification of molecular targets and pathways that contribute to drug sensitivity or resistance *in vitro* and the development of rational treatment strategies for NSCLC.**

(Leader: Dr. John Heymach; Co-Leader: Dr. John Minna)

### **Hypotheses:**

We hypothesize that a broad, systematic molecular profiling of NSCLC cell lines, using both TTF and global approaches, will lead to the following results:

1. The identification of new potential therapeutic targets for NSCLC
2. The development of predictive markers for *in vitro* sensitivity to targeted agents, which will form the starting point for the development of a predictive model of *in vivo* sensitivity using clinical specimens as described in Aim 3.
3. Insights into the molecular mechanism underlying therapeutic resistance and into the relationship of resistance mechanisms to factors innately affecting tumor growth rate and prognosis
4. Identification of readily translatable therapeutic strategies to combat these resistance mechanisms.

### **Specific Aims:**

In this project, we will develop and validate a novel therapeutic target-focused (TTF) profiling platform at M.D. Anderson Cancer Center. The platform will provide a high throughput, quantitative, scalable, and highly sensitive set of assays to assess activation of key signaling pathways (e.g., PI3K/AKT, STAT, RAS-RAF-ERK) as well as other potential therapeutic targets such as receptor tyrosine kinases (RTKs). It will be coupled with global profiling of gene expression using Affymetrix 2.0 array. These molecular profiles will then be coupled with information from a broad drug and therapeutic target siRNA (DATS) screen to develop markers for predicting drug sensitivity *in vitro* based on molecular profiles, elucidate the molecular determinants of sensitivity or resistance to a given therapeutic agent, and identify potential

therapeutic targets for tumor cells resistant to a given agent. This project lays the foundation for Project 3, where the same TTF and global profiling approaches will be used to characterize clinical tumor specimens and investigate molecular markers identified in this project, for Project 4, in which the profiles and therapeutic targets for mesothelioma will be explored, and for Project 2, in which the profiles will be correlated with patient prognosis and metastatic patterns. The specific aims of this project are as follows:

**Specific Aim 1: To develop a TTF profile for assessing critical signaling pathways and potential therapeutic targets, and to apply TTF and gene expression profiling to NSCLC and mesothelioma cell lines.**

- 1.1. Development and technical validation of a TTF profile using reverse phase lysate arrays (RPPA) and multiplexed bead array technology.
- 1.2. Application of TTF profiling to a cell line panel representing malignant (NSCLC and mesothelioma) and non-malignant (endothelial and stromal cells, normal bronchial epithelium) cell types.
- 1.3. Gene expression profiling of the cell line panel using Affymetrix microarrays.
- 1.4. Correlation of TTF and gene expression profiles from the cell line panel to determine gene expression signatures that correlate with activation of individual proteins (e.g., EGFR activation) and critical signaling pathways (e.g., RAS pathway activation).

**Specific Aim 2: To determine the sensitivity of the cell line panel to the selected drug and therapeutic target siRNA (DATS) screen.**

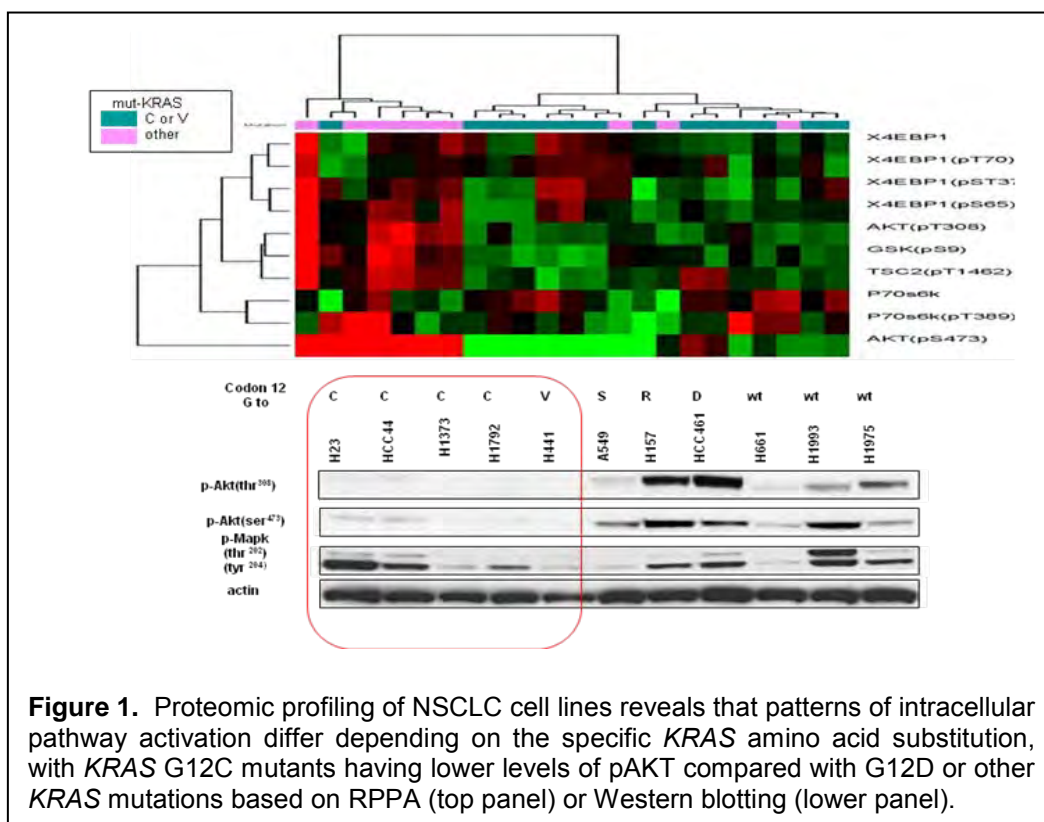
- 2.1. Screening of the cell line panel for sensitivity to a panel of 20-25 targeted agents and standard chemotherapy agents.
- 2.2. Screening of the cell line panel using siRNA representing potential therapeutic targets, including molecules targeted by specific agents in Aim 2.1 (e.g., EGFR, IGFR-1, etc.) and potential therapeutic targets for which drugs are not currently available (e.g., RTKs for which drugs are currently in development).
- 2.3. Comparison of *in vitro* and *in vivo* profiles (TTF and global) and drug sensitivity in selected NSCLC cell lines and xenografts grown from the same lines.

**Specific Aim 3: Development of markers for predicting drug and targeted siRNA sensitivity *in vitro* based on TTF and molecular profiles, and identification of candidate therapeutic targets in chemotherapy-resistant lines.**

**Summary of Research Findings**

The overall goals of this project are to systematically investigate signaling pathways and potential therapeutic targets using NSCLC cell lines and tumors; and, by correlating these molecular profiles with drug sensitivity phenotypes, to develop markers for predicting response and resistance and to develop strategies for overcoming resistance. We have made substantial progress towards these goals in the past year, with several discoveries of potentially high impact, reflected in part by several publications in journals such as the *Journal of Clinical Investigations*, *Journal of Thoracic Oncology* and *Cancer Research*.

Major advances this year included: 1) the identification of *KDR* amplification as a marker and mechanism of chemoresistance, and the signaling mechanisms by which *KDR* amplification drives a malignant phenotype, done in conjunction with Project 3 (I. Wistuba); 2) Identification of differences in the downstream signaling promoted by specific *KRAS* mutants; 3) Identification of fundamental differences in signaling underlying NSCLC and SCLC, revealing PARP1 and Chk1

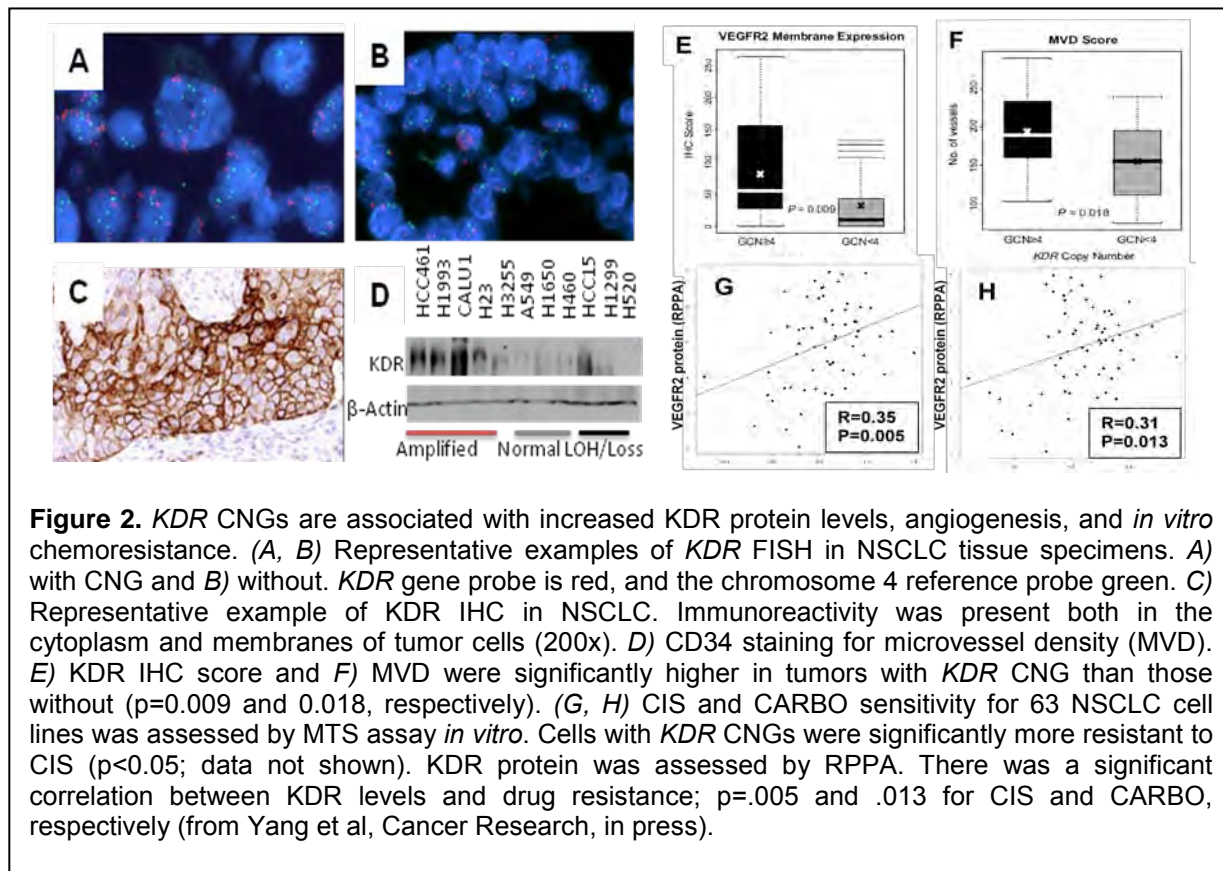


as therapeutic targets in SCLC; 4) Identification of an EMT signature that predicts resistance to erlotinib as well as to PI3K and MEK inhibitors, and application of this signature to the DoD-sponsored BATTLE trial; 5) Identification of a 5-gene signature, including the lipocalin-2 gene (*LCN2*) that predicts response to EGFR TKIs in patients with wild-type EGFR. These accomplishments are described in more detail in below.

We extended our previous studies of proteomic profiling of NSCLC to include both clinical samples (as described in our recent BATTLE annual report) and cell lines (supported under this PROSPECT grant). We also expanded the number of NSCLC cell lines for profiling from 70 to approximately 100. In our initial profiling on NSCLC tumors using reverse phase proteomic profiling (RPPA), we identified several signaling pathways, particularly the AMPK/LKB1 pathway, associated with disease recurrence. One of the findings that emerged from this profiling is that different amino acid substitutions in the *RAS* oncogene result in distinct patterns of downstream pathway activation. In collaboration with Dr. Garth Powis and as reported in the BATTLE grant, we identified that *KRAS* mutants bearing the G12C mutation have lower levels of PI3K and MEK pathway activation, as demonstrated in Figure 1, and have improved progression-free survival, compared to patients with G12D or other substitutions treated with tyrosine kinase inhibitors in the BATTLE clinical trial. Furthermore, we observed that G12D mutants had greater radiation resistance, and confirmed this finding in NSCLC patients. We are currently investigating different approaches to targeting these particular mutants in cell lines; for example, it appears that G12D mutants may have greater sensitivity to PI3K pathway inhibition, but G12C mutants may be more sensitive to inhibitors downstream of PLCgamma. We have markedly increased the drugs and targets that have been screened over the past year, with a particular focus on therapeutic targets being investigated in clinical testing such as MEK (AZD6244) and PI3K/AKT (MK2206), which are currently being tested in the recently activated BATTLE-2 clinical trial. We have also added two inhibitors of the receptor tyrosine kinase Axl, which emerged from our profiling as a target associated with EMT, and inhibitors of the

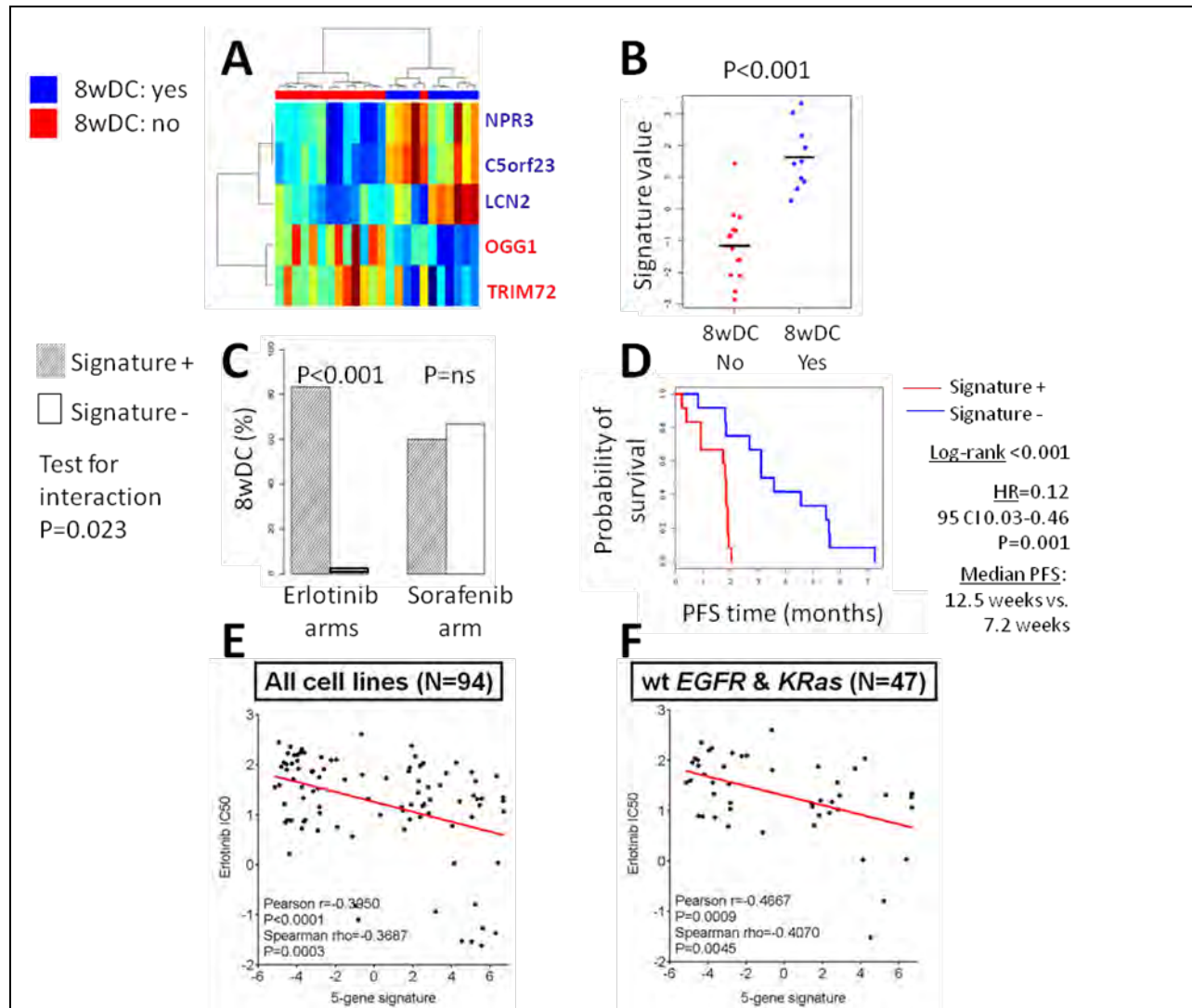
fibroblast growth factor receptors (FGFR) based on our observation that upregulation may be associated with resistance to VEGF inhibitors (Cascone et al., JCI, 2011). We have also added pemetrexed-based combinations to our cell line screening based on our earlier identification of proteomic markers of pemetrexed response, particularly the P16/Rb/E2F pathway. These combinations are being tested in our recently opened BATTLE-Front-line (-FL) trial, which will enable the validation of markers discovered in our preclinical studies from this grant.

Over the past year, a number of new candidate markers have emerged at least in part from our cell line screens. One example is tumor cell KDR, which is being further investigated in collaboration with Dr. Wistuba's laboratory outside the scope of this grant. We found that tumor cell *KDR* copy number gains (CNGs) were associated with relapse after adjuvant chemotherapy and increased tumor angiogenesis; through our cell line studies, we identified that tumor *KDR* CNGs were associated with resistance to platinum chemotherapy agents (Figure 2). Further investigation revealed that *KDR* CNGs were associated with increased levels of HIF-1 $\alpha$  under normoxic conditions, and that *KDR* knockdown overcame resistance to chemotherapy in these cell lines. Based on these studies, we are currently investigating whether *KDR* CNGs may be useful markers for predicting benefit from VEGF inhibitors in combination with chemotherapy.



A second biomarker effort involved the development of a signature for predicting response in patients treated with erlotinib. *EGFR* mutation is already established as a marker for a subset (approximately 12%) of patients with NSCLC; however, for the vast majority with wild-type *EGFR*, there are currently no validated markers for predicting response. We developed a five-gene signature that included LCN2 (lipocalin-2) for predicting disease control in patients treated with erlotinib in the BATTLE study (Figure 3). We then examined a panel of cell lines and found that both the five-gene signature and LCN2 alone were associated with sensitivity to erlotinib in

either the overall set of cell lines or those with wild-type EGFR (Heymach et al., Proc AACR, 2011; Saintigny et al., Proc AACR, 2011). We are currently investigating whether LCN2 is mechanistically involved in EGFR response and linking EGFR/PI3K signaling with the apoptosis pathways. Preliminary data suggests that LCN2 knockdown reduces erlotinib sensitivity, although this effect appears to be context-dependent. We are also attempting to validate the signature through other independent trials of erlotinib for NSCLC.





### **Key Research Accomplishments**

- Identified KDR amplification as a marker and mechanism of chemoresistance.
- Identified differences in the downstream signaling promoted by specific KRAS mutants.
- Demonstrated fundamental differences in signaling underlying NSCLC and SCLC, revealing PARP1 and Chk1 as therapeutic targets in SCLC.
- Discovered an EMT signature that predicts resistance to erlotinib as well as PI3K and MEK inhibitors.
- Identified a 5-gene signature, including lipocalin-2 (LCN2) that predicts response to EGFR TKIs in patients with wild-type EGFR.

### **Conclusions**

We have made substantial progress towards the overall goals of this project to systematically investigate signaling pathways and potential therapeutic targets using NSCLC cell lines and tumors; and, by correlating these molecular profiles with drug sensitivity phenotypes, to develop markers for predicting response and resistance and to develop strategies for overcoming resistance. We will continue to investigate these findings during the unfunded extension, and we will have a complete report on the identification of candidate therapeutic targets in chemotherapy-resistant cell lines at that time.

### **Project 2: Tumor molecular profiles in patients with operable non-small cell lung cancer (NSCLC): impact on stage, prognosis, and relapse pattern.**

(Leaders: Drs. David Stewart, Jack Roth; Co-Leaders: Drs. Roy Herbst, Edward Kim, Katherine Pisters, Stephen Swisher)

#### **Hypotheses:**

We hypothesize that:

1. In tumors from patients with NSCLC, patterns of co-expression of molecules that modulate cell proliferation, survival, angiogenesis, invasion, metastasis and apoptosis will substantially influence tumor stage and size at the time of diagnosis, and will largely define patient prognosis.
2. Impact of adjuvant and neoadjuvant therapies on disease-free, progression-free, and overall survival will vary across prognostically distinct groups.
3. Specific molecular signatures in primary tumors will predict both metastatic patterns at relapse and molecular profiles of recurrent tumors, and this could help guide adjuvant strategies and therapeutic strategies at relapse.

#### **Specific Aims:**

**Aim 1: To define characteristic TTF/gene expression profiles of prognostically distinct subpopulations of patients with resectable NSCLC, and to assess the extent to which these molecular profiles correlate with tumor stage and/or size.**

The main goal of this aim is to use 150 archival NSCLC tumor samples from our tissue bank (with corresponding clinical data) and to prospectively collect tumor samples, blood samples, and clinical data from 300 additional patients undergoing surgical resection of NSCLC. The tissue and blood samples will be used by Project 3 and the Pathology Core to generate comprehensive TTF/gene expression molecular profiles using methods developed in Project 1. We will construct Kaplan-Meier estimated survival curves for disease-free survival, progression-

free-survival, and overall survival, and will use Cox proportional hazards models and recursive partitioning methods to identify important biomarkers and prognostically distinct subpopulations. We will also correlate TTF/gene expression molecular profiles with initial tumor size and stage. In addition, we will explore the feasibility of using nonlinear regression analyses of semilog plots of % disease-free survival, % progression-free survival, and % overall survival vs time to facilitate identification of prognostically distinct subpopulations with characteristic TTF/gene expression molecular profiles.

**Aim 2: To assess the impact of adjuvant and neoadjuvant chemotherapy on disease-free survival, progression-free survival, and overall survival in prognostically distinct subgroups, and to provide tumor, blood and clinical data to Project 3 for an assessment of factors contributing to resistance to chemotherapy and to Project 5 for assessment of profiling of EGFR and related molecules by new quantum dot technologies.**

Of the 450 patients included in the project, we will assess 100 new prospectively recruited patients who will receive neoadjuvant therapy, 100 patients who will receive postoperative adjuvant therapy (including approximately 20 tumor bank patients and 80 new patients), and 250 patients who did not receive adjuvant or neoadjuvant therapy (including approximately 130 tumor bank patients and 120 new patients). We will collect patient clinical data on all 450 patients and will collect blood samples on the 300 new, prospectively recruited patients. Tumor and blood samples and clinical data will be provided to Project 3 for studies of therapeutic resistance and to Project 5 for assessment of profiling of epidermal growth factor receptor (EGFR) and related molecules by new quantum dot technologies, while in Project 2 we will assess impact of adjuvant and neoadjuvant therapy on outcome in each prognostic group.

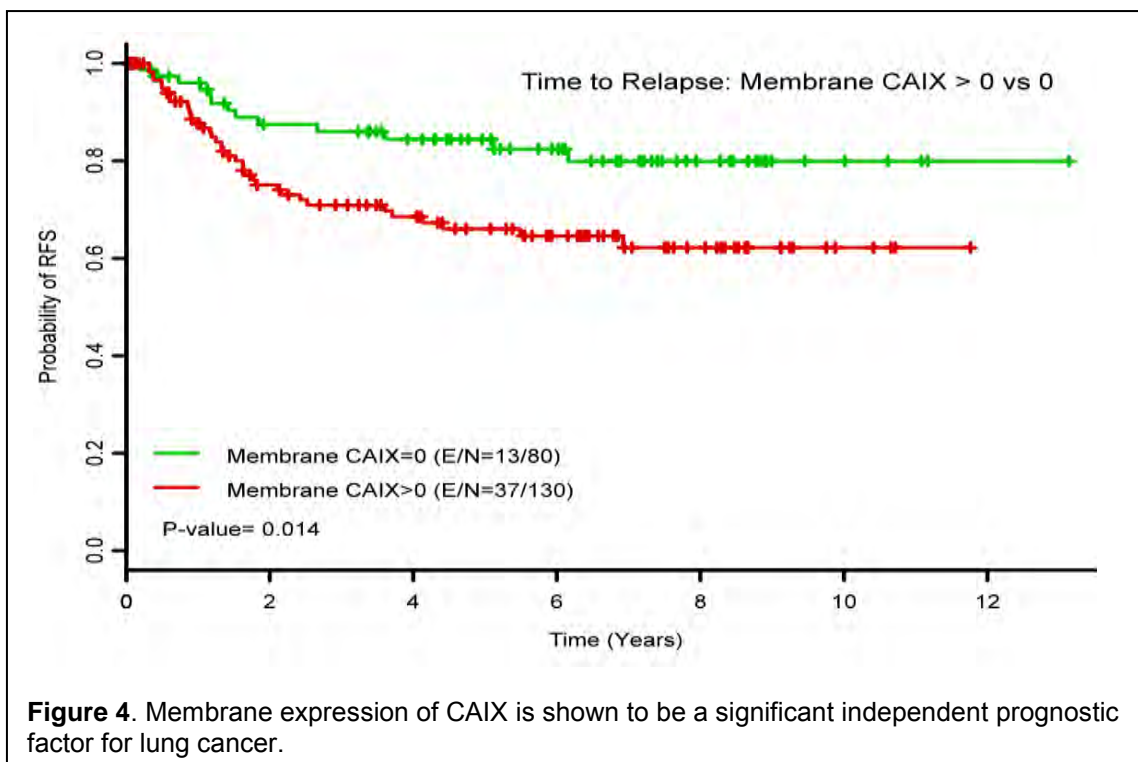
**Aim 3: To correlate TTF/gene expression molecular profiles in the primary tumor with metastatic patterns and with tumor molecular profiles at relapse.**

For patients who relapse, we will define metastatic sites at relapse, obtain tumor tissues from selected patients who undergo biopsies to confirm relapse, and define TTF/gene expression molecular profiles in the patients' original primary tumor specimens that predict sites of later relapse (and in particular that predict relapse in brain). We will also assess whether tumor at relapse is enriched for particular molecular characteristics that may promote metastasis when compared to the primary tumor, and will assess the extent to which TTF/gene expression molecular profile at diagnosis may help guide choice of therapies at relapse.

### **Summary of Research Findings**

During the fourth year of research, we continued to collect extensive clinical follow-up data on 272 NSCLC patients who had previously undergone tumor resection and for whom we have high quality fresh-frozen and formaldehyde-fixed paraffin-embedded (FFPE) tumor samples in our lung cancer tissue bank. Clinical data collected include follow-up duration, survival status at last follow-up, contribution of lung cancer to patient's death (for those who have died), follow-up duration for detection of relapse, date of first detection of relapse for each individual organ system (e.g., lung, brain, liver, bone, etc), and date of first detection of a new primary lung cancer. During the initial analyses on immunohistochemistry (IHC) data from FFPE specimens, we identified membrane expression of carbonic anhydrase IX (CAIX) and expression of Nerf2 and Keap1 as being significant independent prognostic factors (Figure 4). We also performed extensive molecular analyses of these 272 tumor specimens (gene expression profiles, microRNA profiling, mutation analyses, etc.) in collaboration with Project 3, and results are outlined in more detail in the reports from Project 3 and the Pathology Core. Detailed proteomic analyses are also underway for both tumor and blood samples, and we are now in the process

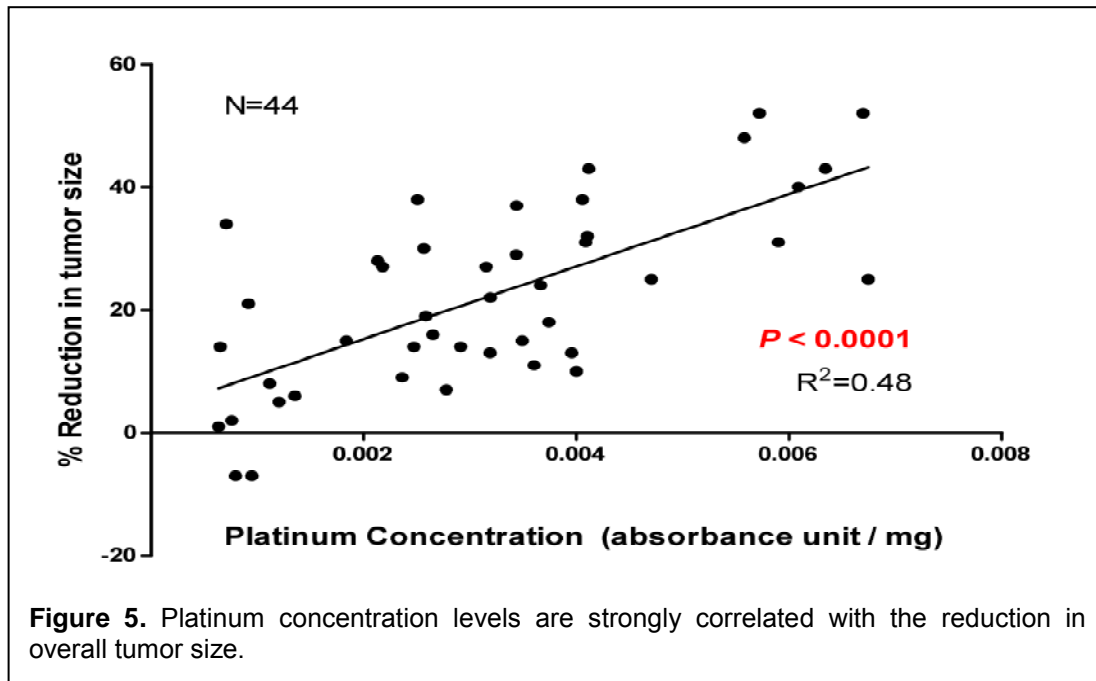
of correlating molecular profiles with survival time, cause-specific survival, time to any relapse, time to development of a new primary lung cancer, and sites of relapse. We will have detailed clinical and molecular risk models for each of these clinical outcomes after analyses are completed during the next project period.



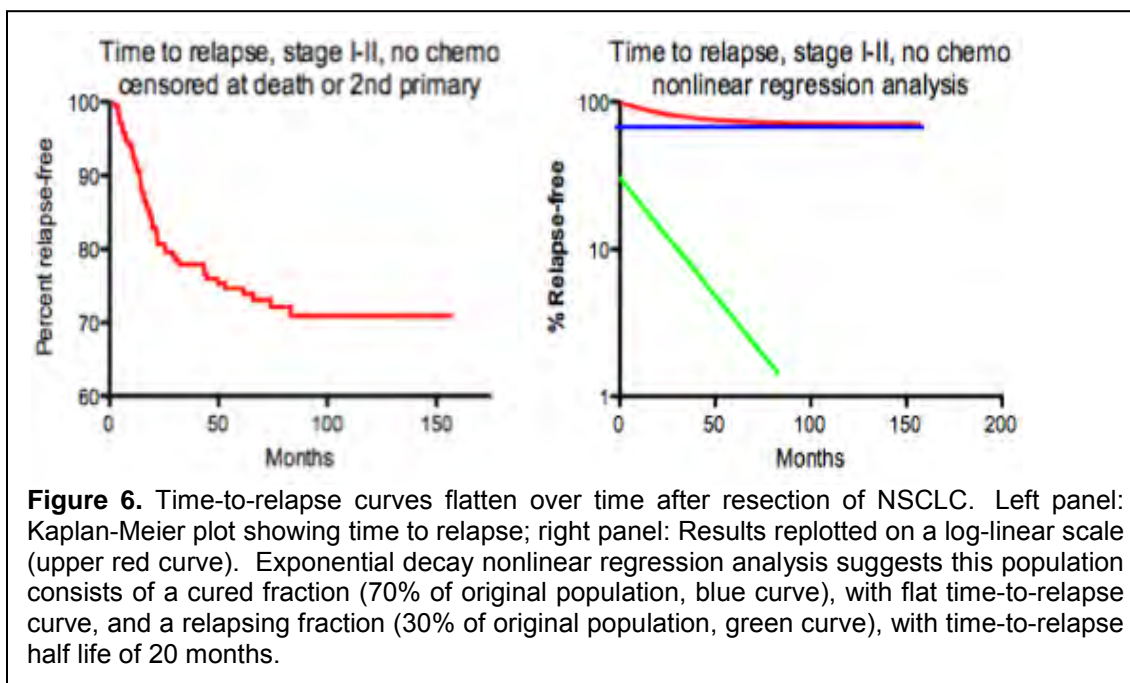
We have prospectively collected fresh-frozen and FFPE tumor tissues on 403 NSCLC patients who have undergone tumor resection, and we banked blood samples on 345 of these cases. The same detailed clinical data have been collected as described above for our tissue bank cases. Data from these prospective cases will be used to validate the risk models generated for our Tissue Bank cases.

We also have detailed information on neoadjuvant and adjuvant chemotherapy received by patients, and multivariate modeling will be used to assess interactions between outcome, molecular risk factors, and adjuvant/neoadjuvant therapies. As platinum is known to remain in tissues for several months after last drug exposure, we have measured platinum concentrations in resected tumor specimens from 44 patients who had received neoadjuvant chemotherapy with cisplatin or carboplatin. We found that the percentage of tumor shrinkage with chemotherapy correlated strongly with tumor platinum concentrations for both cisplatin and carboplatin and for each of adenocarcinomas, squamous cell carcinomas and for patients with either large cell carcinoma or NSCLC not otherwise specified (Figure 5). Despite marked differences in doses between cisplatin and carboplatin, platinum concentrations in tissues were similar, reflecting the reduced rate of uptake of carboplatin into tissues as compared to cisplatin. Studies are underway to assess the observed correlations of tissue platinum concentrations with relapse/survival and to assess correlations between tumor molecular characteristics (e.g., uptake and efflux pumps and DNA repair systems) and platinum concentrations. We have also conducted one of the most detailed reviews yet undertaken of chemotherapy resistance mechanisms in lung cancer, and will be correlating expression of these resistance factors with

tumor platinum concentrations and with probability of relapse and patterns of relapse with (and without) adjuvant therapy.



We previously proposed that nonlinear regression analysis of exponential decay in patient survival curves might yield insights that were not obvious from the standard statistical assessments and Kaplan-Meier plots. Our initial experience with this approach suggests that time-to-relapse curves flatten with time after resection (Figure 6), which is consistent with existence of true cured fraction of patients following surgery, rather than a high proportion of patients having a residual quiescent tumor cell population capable of very late relapse (as seen with breast cancer and some other malignancies). Our assessments also suggest that death from causes other than recurrence of the original lung cancer is a common event in patients with resected NSCLC, and that this factor will reduce the value of overall survival time as an outcome variable in assessing impact of tumor molecular profiles on tumor behavior. Hence, it may be more relevant to use risk models based on time to relapse to select patients for adjuvant therapies than to use models based on overall survival.



### **Key Research Accomplishments**

- Collected extensive clinical follow-up data (including detailed data on relapse patterns) on 272 NSCLC patients who had previously undergone tumor resection.
- Performed extensive molecular analyses of these 272 tumor specimens, in collaboration with Project 3 and the Pathology Core, and have initiated statistical analyses and development of risk models
- Collected prospective fresh-frozen, FFPE tumor tissues and clinical follow-up data on 403 NSCLC patients who have undergone tumor resection.
- Identified CAIX, Nrf2 and Keap1 as independent prognostic factors.
- Correlated the platinum concentration found in patients who received neoadjuvant cisplatin or carboplatin regimens with tumor shrinkage.
- Performed exploratory nonlinear regression analysis of exponential decay in the patient survival curve, and have demonstrated that this approach is feasible and informative.

### **Conclusions**

Sample collection was completed on schedule with more specimens obtained than proposed in our initial application. We anticipate that the completed analyses from this project will have a major impact on our understanding of tumor molecular factors that influence risk of recurrence and patterns of relapse. These analyses will be completed over the next requested period of an unfunded grant extension.

### **Project 3: Molecular Profiling of Non-Small Cell Lung Cancer Tissue Specimens and Serum and Plasma Samples: Correlation with Patient Response and Tumor Resistance to Chemotherapy.**

(Leader: Dr. Ignacio Wistuba; Co-Leaders: Lin Ji and John Minna)

### **Hypothesis:**

In Project 3, we hypothesize that systematic molecular profiling of surgically resected non-small cell lung cancer (NSCLC) tissue specimens using therapeutic target-focused (TTF) and mRNA approaches, along with serum phosphopeptide screening and plasma DNA analysis, will lead to the following results:

1. Validation in patients' tissue specimens of molecular signatures obtained from NSCLC cell lines that are associated with *in vitro* and *in vivo* (xenograft) resistance of NSCLC cell lines to chemotherapeutic and targeted agents.
2. Identification of molecular profiling signatures associated with NSCLC sensitivity or resistance to chemotherapeutic agents that can identify NSCLC patients most likely to respond to a given targeted therapeutic agent.
3. Development and validation of serum phosphopeptide profiles and plasma DNA markers associated with NSCLC patient response and tumor resistance to chemotherapeutic agents.

### **Objectives:**

The greatest obstacle to creating effective treatments for lung cancer is the development of resistance to both chemotherapeutic and targeted agents. In this highly integrated and translational program project, we tackle one of the most clinically significant problems in lung cancer: the prediction of patient response to therapy, especially in the context of tumor resistance to current standard chemotherapies. The main objectives of this project are as follows:

- a) To profile surgically resected tumor tissue specimens obtained from NSCLC patients to validate molecular signatures found in the TTF and mRNA profiles developed in Project 1. These profiles will be compared with molecular signatures obtained from NSCLC cell lines that are associated with *in vitro* and *in vivo* (xenograft) resistance to chemotherapeutic and targeted agents.
- b) By comparing NSCLC tumor specimens (collected in Project 2) from patients who have received preoperative chemotherapy and from those who have not, to validate TTF and mRNA signatures that are found in Project 1 to be associated with resistance to therapy and with the activation of resistance-associated molecular pathways or that are found in Project 1 to be potentially exploitable as new therapeutic targets.
- c) To identify serum and plasma biomarkers as surrogate markers to predict the response of NSCLC patients to neoadjuvant chemotherapy and to predict patient outcome.
- d) To provide tissue- and serum-based molecular profile signatures or markers to Project 2 that can predict the clinical outcome of NSCLC patients who had undergone surgical resection with curative intent, with or without neoadjuvant therapy.

This interdisciplinary research proposal for profiling cell lines, tumor tissue, and serum samples from NSCLC patients requires extensive histopathological, molecular, and immunohistochemical studies, which will be coordinated and/or performed by the Pathology Core (see Pathology Core's report).

### **Specific Aims:**

**Aim 1: To validate, in retrospectively collected NSCLC tumor tissue specimens, the TTF and mRNA profiles predictive of the *in vitro* and *in vivo* (xenograft) resistance of NSCLC cell lines to chemotherapeutic and targeted agents.**

**Summary of proposal:** We will select 150 surgically-resected NSCLC tumor specimens from The University of Texas Lung SPORE (UT-SPORE) Tissue Bank for TTF and mRNA profiling. Using those 150 frozen archival NSCLC tumor tissues, we will perform reverse-phase protein array (RPPA), multiplex bead-based protein analysis (MBA) and Affymetrix U133 Plus 2.0 array to validate the molecular signatures developed in Project 1. Then, we will compare the profile signatures obtained from the NSCLC tumor specimens with the signatures obtained from NSCLC cell lines in Project 1 that predict the *in vitro* and *in vivo* resistance to chemotherapeutic and targeted agents. Finally, using formalin-fixed and paraffin-embedded tissue specimens, we will validate the expression of proteins abnormally represented in the molecular profiling analyses of NSCLC tumor specimens by using tissue microarrays (TMAs) and semiquantitative immunohistochemical (IHC) methods.

### **Summary of Research Findings**

During the fourth year of research, in collaboration with the Pathology Core (I. Wistuba) and the Biostatistics/Bioinformatics Core (J. Lee and K. Coombes), we have analyzed the molecular profiling data of NSCLC and MPM tissue specimens with annotated clinical information, and achieved the following milestones:

- 1) Analyzed the mRNA profiling (Illumina array platform) data obtained from the 209 surgically resected NSCLCs without neoadjuvant therapy and correlated results with NSCLC cell lines profiles and sensitivity to chemotherapy drugs.
- 2) Identified a panel of microRNAs associated with the outcome of NSCLC patients treated with and without adjuvant chemotherapy.
- 3) Analyzed the DNA copy number data (array Comparative Genomic Hybridization, aCGH) obtained from 162 surgically resected NSCLC without neoadjuvant therapy.
- 4) Completed analysis of *KRAS* and *EGFR* mutation status on DNA extracted from the 209 molecularly profiled NSCLC tumors.
- 5) Completed the bioinformatics analysis of the proteomic RPPA profiling data obtained from 209 surgically resected NSCLCs without neoadjuvant therapy.
- 6) Designed a strategy for gene (mRNA), microRNA, and protein signature validation using high-throughput Quantitative Nuclease Protection Assay (qNPA™), Fluidigm™ microfluidic quantitative dynamic array, and IHC methodologies.
- 7) Identified a series of molecular pathways and markers, using gene profiling, as potential novel targets in malignant pleural mesothelioma (MPM) in collaboration with Project 4 (A. Tsao).

The detailed progress update is as follows:

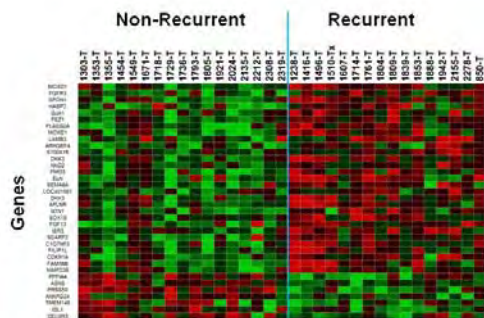
#### **1. mRNA profiling of NSCLC tumors**

During the last year, in collaboration with the Biostatistics/Bioinformatics Core (K. Coombes), we have analyzed the gene expression data obtained from the Affymetrix profiling analysis of the 209 non neoadjuvant-treated tumors. In our preliminary analysis, we indentified a mRNA microarray signature composed of ~40 genes predicting a response of NSCLC tumors to platinum based doublet chemotherapy. From this material, we collected data that has allowed us to construct an mRNA signature predicting survival after treatment with platinum-taxane doublet adjuvant chemotherapy (Figure 7).



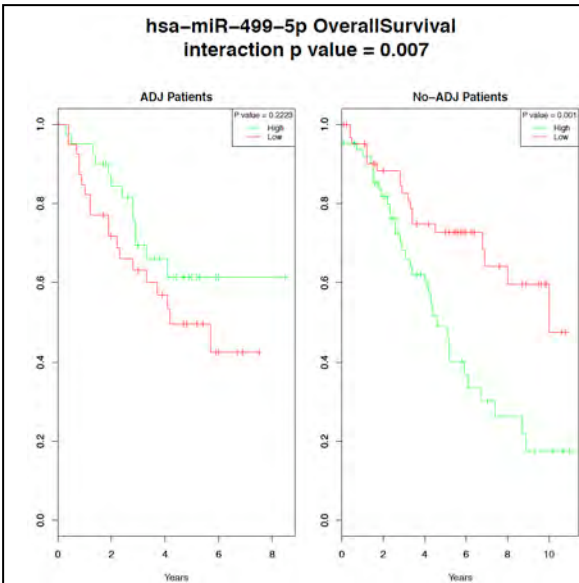
2. microRNA NSCLC tumor tissue profiling.

**Figure 7.** mRNA Expression signature associated with recurrence and non recurrence in NSCLC patients treated with platin-taxane adjuvant chemotherapy. A training set of NSCLCs treated with platin-taxane adjuvant chemotherapy with 16 recurrences and 17 non-recurrences were used to generate a mRNA signature (consisting of ~40 genes) from the Illumina V3 microarray data for mRNA expression predicting these key clinical classes. Red = high gene expression and green = low gene expression

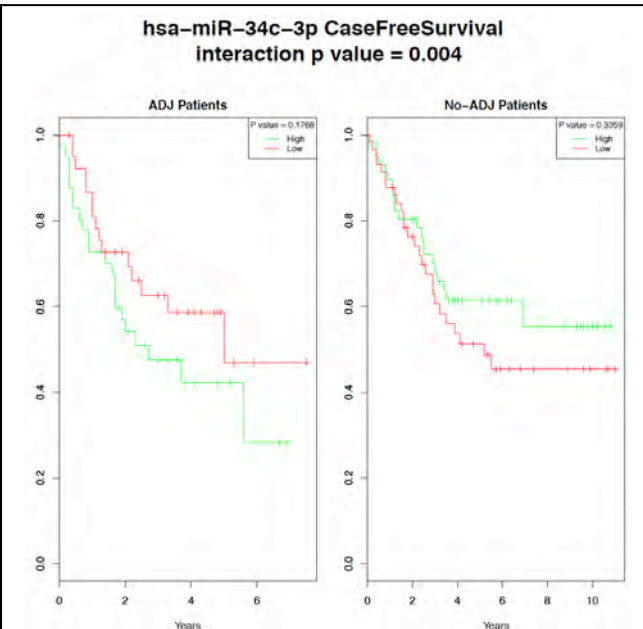


We previously reported the completion of the microRNA profiling of 209 surgically resected chemo-naïve NSCLC tumors on Agilent human v3 microRNA microarray chips. During the past year, we performed the analysis of the data in collaboration with the Bioinformatics Core. We identified a panel of microRNAs that have a statistically significant correlation with the NSCLC patients' recurrence-free as well as overall survival after surgical resection using the Cox proportional hazard regression model. Statistical methods were employed to determine the association of survival (recurrence-free or overall) with a significant interaction between expression and adjuvant treatment. We found that miR-499-5p is significantly associated with overall survival (Figure 8) while miR-34c-3p was associated with recurrence-free survival (Figure 9). Interestingly, patients with high levels of miR-499-5p had a worse prognosis unless they were treated with adjuvant therapy, and those with high levels of miR-34c-3p demonstrated better prognosis if left untreated in the adjuvant setting. We are currently validating the abnormal expression of these microRNAs in RNA extracted from tissue specimens using a quantitative-RT-PCR methodology.

3. DNA copy number (aCGH) analysis of NSCLC tumors. We performed two types of analysis on DNA copy number abnormalities in tumors in order to identify novel copy number variations associated with outcomes of NSCLC patients.



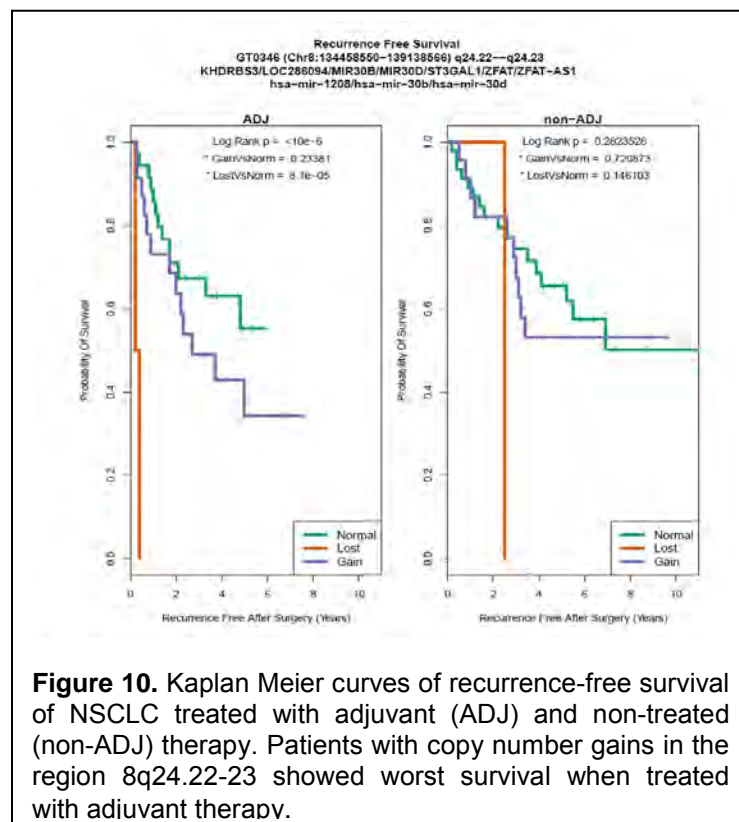
**Figure 8.** miR-499-5p expression is strongly associated with survival.



**Figure 9.** miR-34c-3p expression is strongly associated with survival.



**a) *aCGH of NSCLC primary tumors.*** The bioinformatics analysis of copy number variations (CNVs) selected from 162 surgically resected NSCLCs without neoadjuvant treatment is ongoing. However, we have very interesting preliminary data on two types of comparisons already performed: 1) demonstration of statistically significant differences in the frequency of CNVs across chromosomal regions by histology (adenocarcinoma, [n=115] vs. squamous cell carcinoma [n=47]); and 2) demonstration of statistically significant differences between CNVs and outcomes (recurrence-free survival [RFS] and overall survival [OS]) of patients not treated with adjuvant chemotherapy (prognosis), versus those of patients treated with adjuvant chemotherapy (predictive). In the first analysis, we identified over 250 chromosomal regions showing significant differences in the copy number gains (CNGs) comparing adenocarcinoma with squamous cell carcinoma histologies. Interestingly, in the second type of analysis, we identified a number of regions exhibiting CNGs that associated with prognosis (RFS and OS) in patients not treated with adjuvant therapy. More importantly, several CNGs were predictive of outcome in NSCLC if the patients were treated with adjuvant platinum-based chemotherapy (a representative chromosomal region having predictive effect on adjuvant therapy is depicted in Figure 10).

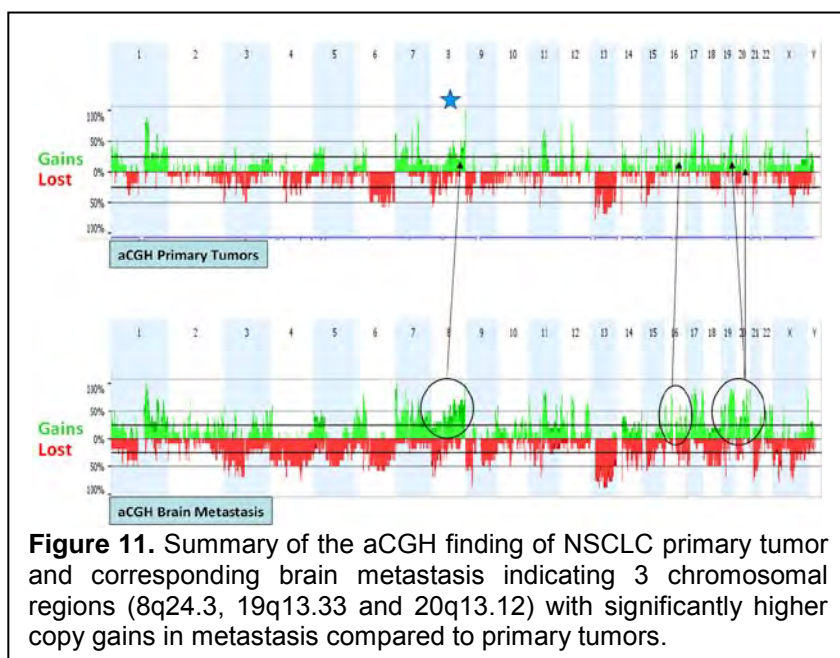


**b) *aCGH of NSCLC primary tumors and corresponding brain metastases.***

In NSCLC, brain metastases (BMs) are estimated to occur in up to 40% of patients. DNA copy number changes are common in cancer and lead to altered expression and function of genes residing within the affected region of the genome. The aim of this study was to compare DNA copy number abnormalities by using array comparative genomic hybridization (aCGH) between primary tumors (PT) and their corresponding BM in NSCLC to identify genomic regions associated with BM development. From surgically resected NSCLC formalin-fixed and paraffin-embedded (FFPE) tissues, we selected 28 paired PTs and BMs (24 adenocarcinomas, and 4 squamous cell carcinomas, SCCs), and 55 additional BMs (43 adenocarcinomas, 2 SCCs, and 10 NSCLCs) specimens for analysis.

Using DNA extracted from FFPE tumor tissues, we performed oligo-based aCGH in 10 paired PT and BM adenocarcinomas. Statistical aberration detection algorithms of data were conducted by aCGH with Nexus Copy Number software v5.0. IHC analysis of two proteins (PSCA and LY6K) coded by genes located in 8q24.3 region was performed in both PT and BM specimens. In the aCGH analysis, multiple chromosomal regions with significant ( $P \leq 0.05$ ) copy number gain and loss were detected. The PTs demonstrated 32 regions (harboring 933 genes) of copy number gain and 16 regions (108 genes) of copy number loss, and the BMs showed 31 regions (1274 genes) with gains and 16 regions (90 genes) with losses. BM demonstrated significantly ( $P \leq 0.01$ ) higher frequency of copy number gains in 3 chromosomal regions: 8q24.3 (BM 100% vs. PT 40%), 19q13.33 (BM 90% vs. PT 20%), and 20q13.12 (BM 60% vs. PT 0%)

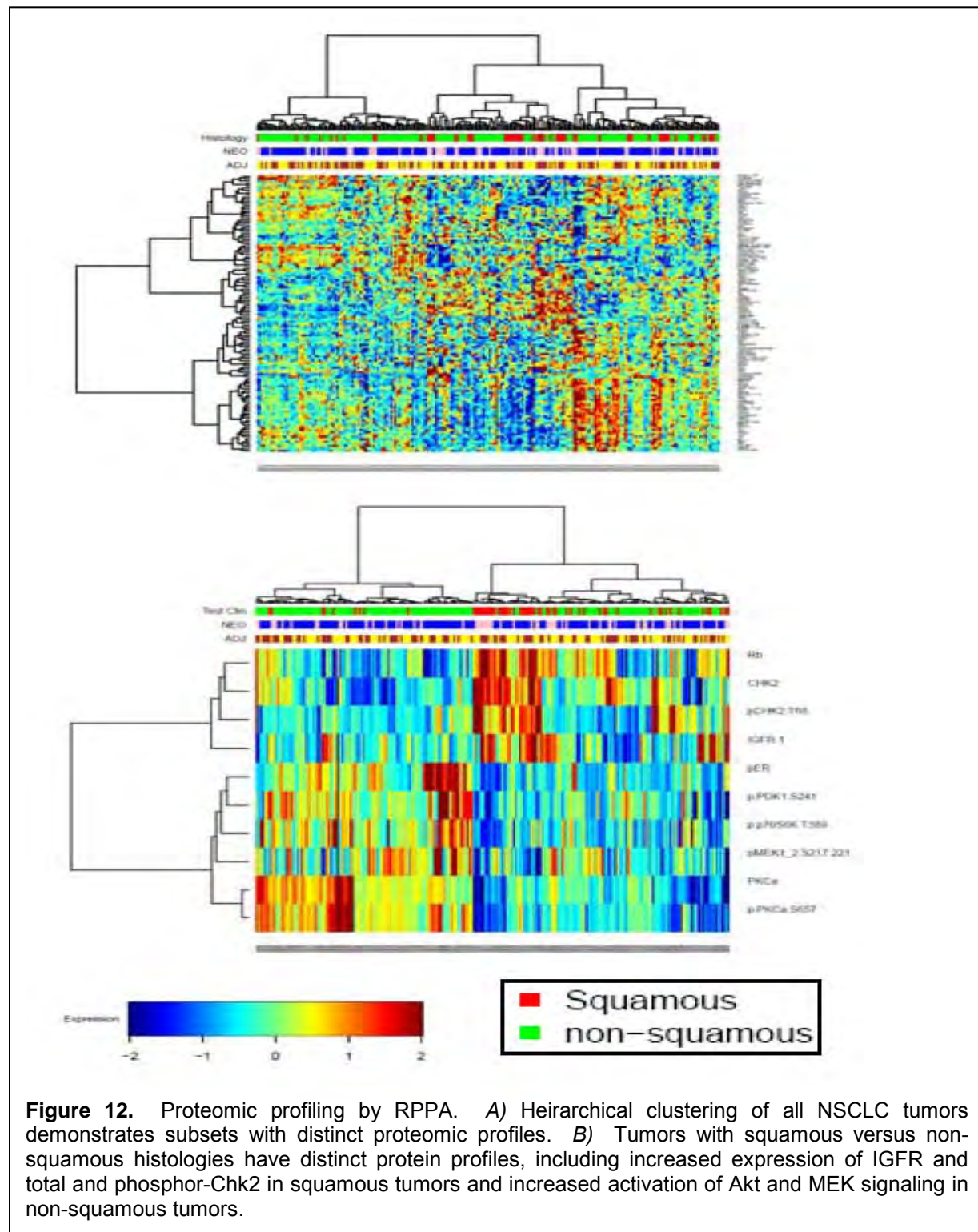
(Figure 11). The 8q24.3 region with copy number gain in tumors harbors 7 genes, including Prostate Stem Cell Antigen (*PSCA*) and Lymphocyte Antigen 6 Complex Locus K (*LY6K*). Interestingly, in our IHC analysis, BMs (n=84; mean score 141.8) showed a significantly ( $P=0.008$ ) higher score of expression of *PSCA* than the corresponding PTs (n=27; mean score 97.8). Similar significant differences were detected when we analyzed only adenocarcinoma samples. No significant differences in the level of IHC expression were detected comparing BMs (n=83; mean score 64) and PTs (n=27; mean score 68.5) for *LY6K*. We conclude that, through aCGH and subsequent protein expression analysis, we have identified that *PSCA* may play an important role in the development of NSCLC brain metastasis. Similarly to prostate cancer, *PSCA* represents a novel potential marker for NSCLC metastasis and therapeutic target for advanced lung tumors. These data were presented in the 2011 AACR Annual Meeting by Galindo et al.



**4. Mutation analysis of NSCLC tumors molecularly profiled.** Mutation analysis of *KRAS* (codons 12 and 13) and *EGFR* (exons 18-21) using pyrosequencing and Sanger sequencing, respectively, have been recently completed on all 209 NSCLCs profiled in this Aim 1. In addition, in collaboration with the Pathology Core, we have prepared additional aliquots of DNA to be examined for 10 additional mutations using the Sequenom® platform. After completion of the mutational analysis, the identified gene mutations will be correlated

with mRNA, microRNA, aCGH, and RPPA data obtained in the same cases.

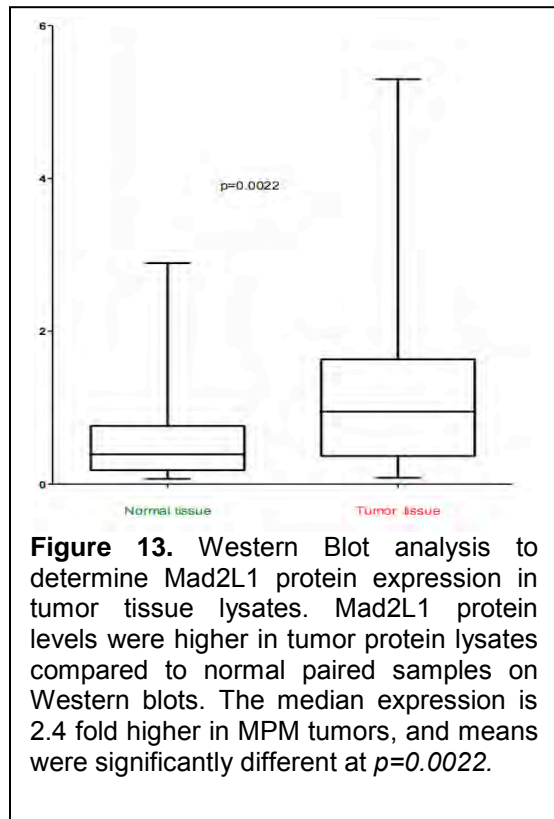
**5. Proteomic RPPA analysis of NSCLC tumors** During the last year, in collaboration with the Project 1 (J. Heymach), tissue samples from 189 tumors from the 209 NSCLCs profiled for mRNA and DNA-CNVs abnormalities were examined for the expression of 120 proteins using RPPA methodology. These included 59 squamous cancers and 156 non-squamous. The data have been subjected to quality control and the expression scores have been normalized using the SuperCurve approach developed by investigators of the Biostatistics/Bioinformatics Core (K. Coombes). Currently, the RPPA data are being correlated with the clinical and pathological characteristics of tumors and patients (Figure 8), particularly with outcome after treatment with adjuvant therapy.



**6. mRNA and microRNA signature validation methodologies.** Last year, we reported our strategy for gene (mRNA), microRNA, and protein signature validation using the following methodologies: a) Quantitative Nuclease Protection Assay (qNPA™; for mRNA and miRNA signatures); b) Fluidigm™ microfluidic quantitative dynamic array; and, c) IHC. In collaboration



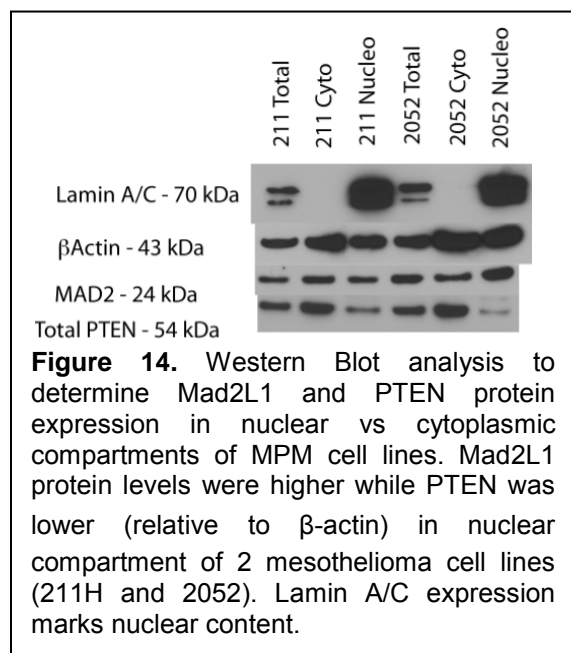
with High-Throughput Genomic (HTG), Inc. (<http://www.htgenomics.com/technology/qnpa>) and the Pathology Core, we continued the development of a multiple qNPA™ assay to test the expression of up to 200 genes using both frozen and FFPE tissues from surgically resected NSCLC tumors. During the last year, we developed a strategy for normalization of the mRNA expression data by optimizing the mRNA expression of up to 20 housekeeping genes using FFPE tissue specimens. In addition, we expanded the number of NSCLC tumor tissue specimens examined for the mRNA expression using the Fluidigm™ methodology to 160 tumors. The data are currently under analysis to correlate expression of mRNA for multiple genes using arrays, qNPA™ and PCR Fluidigm™ methodologies.



Mad2L1 protein in 84 MPM cases in TMAs, and measured the level of protein expression in tumor lysates (Figure 13).

#### 7. MPM tissue specimens and cell lines profiling.

a) MPM Tissue Messenger RNA Profiling and Mitotic Spindle Assembly Checkpoint (MSAC) Pathway Study. We previously reported that gene expression profiling of 53 cases of MPM tumors (along with 38 cases with paired control tissue) had shown significant upregulation of the MSAC pathway. This pathway includes anti-apoptotic molecules like survivin (BIRC5) and many therapeutic targets like Aurora Kinase A (AurKA) and Polo-like Kinase 4 (PLK4) proteins. The key player of this pathway includes the “alarm,” the mitotic arrest deficient-like 1 (Mad2L1/Mad2a) protein, which activates the checkpoint resulting in mitotic arrest until the chromosomes are correctly attached to the spindle microtubules. *Mad2L1* message is upregulated at levels 2.4-fold higher at  $p=0.0022$  in MPM tumors compared to paired controls. Increased expression of *Mad2L1* gene is observed in a variety of human cancers including lung and liver cancer. Also, transgenic mice expressing high levels of *Mad2L1* message and protein exhibit various types of cancers (primarily lung cancers). We validated the microarray results using qPCR, investigated the expression of



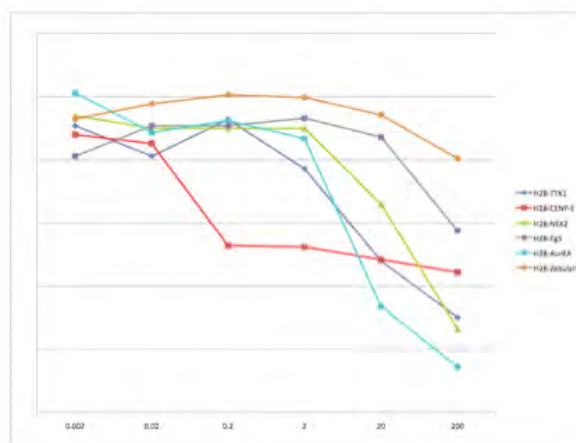
molecular subtypes of MPM tumors based on differential expression of genes. The survival analysis of these tumor subtypes indicated that the tumors with the highest expression of PTEN gene expression showed (relatively) best prognosis with respect to overall survival. Additionally, recently published reports suggest that PTEN has a nuclear role as part of its tumor suppressor function. We intend to analyze the tumor suppressive impact of PTEN expression on the oncogenic role of Mad2L1 within the context of the MSAC pathway. Given the central role played by this pathway in the pathogenesis of pleural mesothelioma, we believe these studies will lead to significant progress in understanding the pathobiology of this malignancy. A manuscript by Suraokar et al. is in preparation describing these data.

#### b) Therapeutic Targets within the MSAC Pathway.

The MSAC pathway is rich in therapeutic targets with drugs available for many of them. We chose 6 kinases, related to the MSAC pathway, based on two criteria: 1) gene expression was significantly upregulated in MPM tumors, and 2) small molecule inhibitors directed against these kinases were commercially available. We tested 6 commercially available drugs targeting Aurora Kinases A and B, Nek2/HEC, CENP-A, CENP-E, and Eg5 and found UA62784, a small molecule inhibitor directed specifically against CENP-E, to be most effective in inhibiting the proliferation of four mesothelioma cancer cell lines, with a median half-maximal inhibitory concentration (IC-50) value of 31 nM (range 0.2

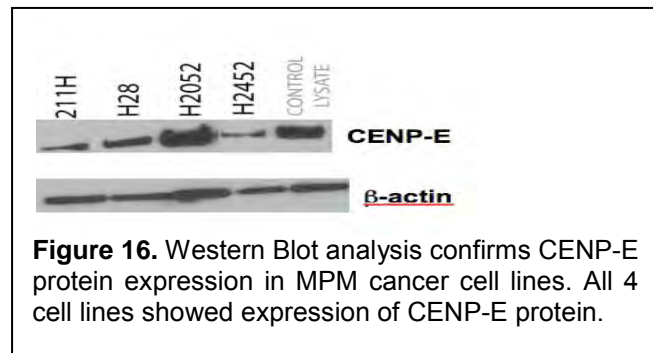
Survival analysis of IHC expression analysis using clinical annotations of the tumor cases indicated worse prognosis (with respect to overall survival) when correlated with high nuclear level of Mad2L1 protein (Figure 14). Multivariate analysis also confirmed that higher nuclear Mad2L1 expression results in a higher hazard ratio. We examined the nuclear and cytoplasmic expression of Mad2L1 protein in two mesothelioma cell lines and found it to be higher (relative to  $\beta$ -actin) than the cytoplasmic level. We also determined the total amount of PTEN, a good prognostic biomarker in mesothelioma, in these compartments and found a dramatically reduced amount of PTEN in the nucleus. We are following these expression studies with additional functional analyses to elucidate the interplay between these two proteins. As reported earlier, our gene expression profiling studies led to the discovery of three novel

**Figure 15.** IHC plots showing typical effect of 6 inhibitors on viability of MPM cancer cell line. H28 cell line showed increased sensitivity to CENP-E inhibitor compared to 5 other drugs. Table showing cumulative IC-50 value range for 4 MPM cell lines.



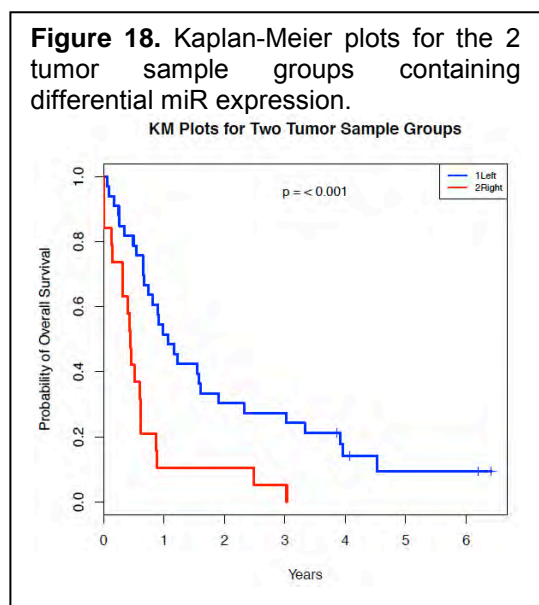
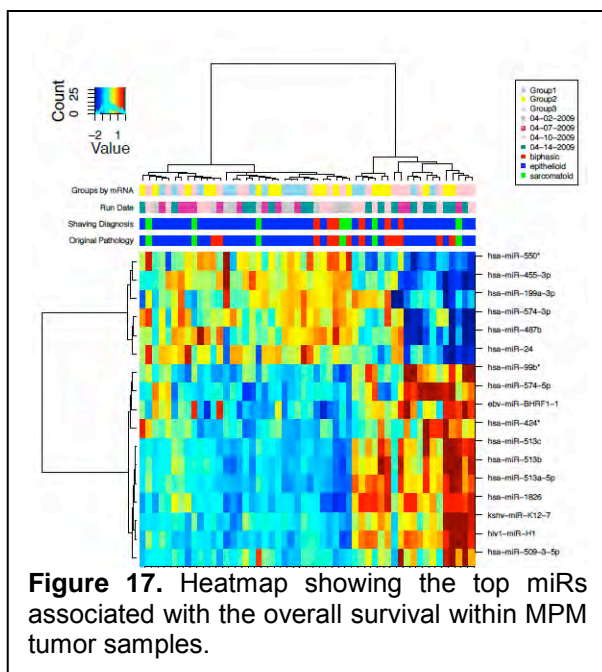
Target	Drug	IC-50
CENP-A	Zebularine	25-300 $\mu$ M
Nek2	INH1	50-200 $\mu$ M
Eg5/KIF11	Monastrol	50-100 $\mu$ M
AurK-A	C1368	2-20 $\mu$ M
TTK/Mps1	SP600125	2-20 $\mu$ M
<b>CENP-E</b>	<b>UA62784</b>	<b>0.02<math>\mu</math>M-0.2 <math>\mu</math>M</b>

nM – 200 nM) (Figure 15). Using Western blot analysis, we found CENP-E protein to be highly expressed in extracts from these cell lines (Figure 16). CENP-E, a 312-kilodalton plus-end directed microtubule-based motor protein, is required for transporting and aligning the



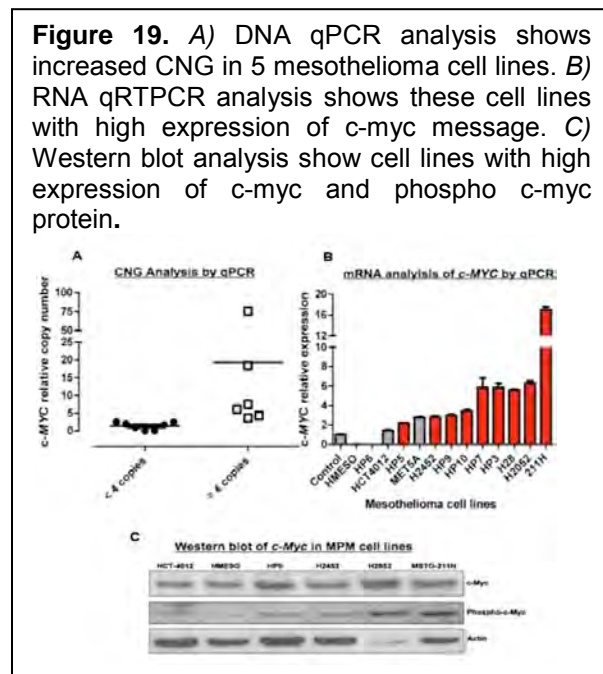
chromosomes on the spindle-midpoint during metaphase and is critically involved in the deployment of the mitotic checkpoint signal. Interestingly, of all these 6 kinases, CENP-E is the one most critically needed for MSAC functioning, thus confirming the critical role played by this pathway and rationalizing a therapeutic strategy targeting it in pleural mesothelioma.

c) MPM Tissue microRNA Profiling and Bioinformatic Analysis. The same 96 samples, which were previously profiled for gene expression, were profiled for global microRNA expression on Agilent human v3 microRNA microarray chips. Bioinformatic analysis performed by Dr. Kevin Coombes, Dr. Lixia Diao, and Dr. Jing Wang show statistically significant correlations between some microRNAs and overall survival using Cox proportional hazard regression model. Their analysis first identified two groups of samples with differing overall survival and differentially expressed miRs (Figure 17). The Kaplan-Meier plots for these two groups show significant differences in overall survival between them (Figure 18). Using the Biomodal analysis developed by Dr. Coombes (which searches for expression of microRNAs using two high points of expression within a set of samples), we identified some miRNAs with interesting expression patterns. For instance, miR-200c effectively stratified most of the epithelioids into two groups with differing expression patterns, while miR-210 expression demarcates (better than any other miR) the tumors from normal tissue. We are currently validating the expression levels of certain miRs in tumor tissue using q-RT-PCR and assessing their expression in our bank of cell lines, and will continue with functional studies in cell lines.

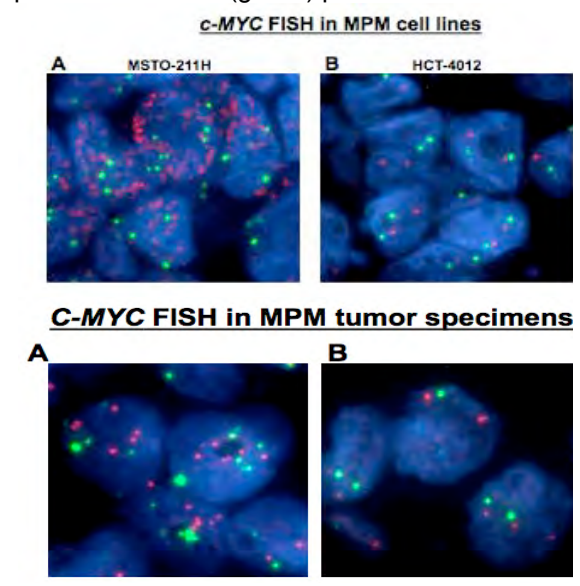


**d) *MPM tissue NextGen Profiling (RNAseq and small RNAseq).*** Six tumor samples (plus 2 control normal samples) were sequenced on SOLID4 at the ncRNA Sequencing Core within the Department of Experimental Therapeutics at MD Anderson Cancer Center. These samples belong to one of the molecular subtypes discovered through gene expression profiling that had upregulated spindle-checkpoint pathway expression and were associated with worse prognosis. The NGS data is currently being analyzed by the Bioinformatics team for mutations in expressed genes within this tumor subset as well as for discovery of novel microRNAs.

**e) *MPM Cell Line Profiling and Functional Analysis.*** Our earlier report included our discovery of amplification of the c-myc locus in MSTO-211H mesothelioma cancer cell line (which was absent in the normal pleural cell line HCT-4012) using Affymetrix SNP 6.0 chip profiling. We



**Figure 20.** FISH analysis using c-myc (red) probe and control (green) probes.



followed these experiments with qPCR on DNA and RNA isolated from these and other mesothelioma cell lines and confirmed an increased copy number of this locus in at least six other cell lines with a corresponding increase in gene expression. Also, overall cell lines with high copy number gain (CNG) had increased expression of the c-myc message and protein, and many of those showed high phospho-c-myc levels (Figure 19). We also confirmed the amplification of c-myc locus in MSTO-211H using FISH probes. We performed FISH analysis on about 80 mesothelioma specimens in TMAs and found a high frequency (21%) of tumors cases with CNG for c-myc locus. These data were presented in the AACR 2011 Annual Meeting by Riquelme et al. (Figure 20).

**Aim 2: To develop TTF and mRNA signatures of NSCLC resistance to chemotherapy, and identify chemoresistance-associated targets/pathways as new therapeutic targets.**

**Summary of proposal:** Whereas Aim 1 focuses on the identification in archived tumor specimens of TTF and mRNA molecular profiles detected in NSCLC cell lines, the main focus of Aim 2 is to determine whether the molecular signatures in the tumor specimens correlate with patient response to neoadjuvant chemotherapy. From the clinical trial in Project 2, we will use specimens from 100 NSCLC patients who received neoadjuvant therapy and had surgical resection with curative intent (cases) and from 200 NSCLC patients who had surgical resection



but did not receive neoadjuvant therapy (controls) to perform RPPA, MBA, and Affymetrix U133 Plus 2.0 array analyses. Then, we will compare the TTF and mRNA profile signatures obtained from these NSCLC tumor specimens with signatures obtained in Project 1 to predict the *in vitro* and *in vivo* resistance of NSCLC cell lines to therapy. Those data will be provided to Project 2 for correlation with clinical characteristics, including prognosis and metastasis. Finally, using formalin-fixed and paraffin-embedded tissue specimens, we will validate the expression of proteins abnormally represented in the molecular profiling analyses in NSCLC tumor specimens from all patients enrolled in Project 2 by using TMAs and semiquantitative IHC methods.

### **Summary of Research Findings**

During the fourth year, in collaboration with the Pathology Core (I. Wistuba) and the Biostatistics/Bioinformatics Core (J. Lee and K. Coombes), we continued the analysis of the molecular profiling data of surgically resected NSCLC specimens obtained from patients who have received neoadjuvant chemotherapy. Our progress included the following:

- 1) Completed analysis of the comprehensive molecular profiling of 40 neoadjuvant-treated NSCLC using mRNA (Illumina), miRNA (Agilent), and DNA aCGH array profiling platforms. In addition, we expanded the mRNA profiling to 63 tumors banked in the Pathology Core.
- 2) Completed the mRNA profiling analysis of 89 frozen tumor samples from the *Intergroupe Francophone de Cancérologie Francophone* (IFCT), a randomized, phase III neoadjuvant chemotherapy trial in NSCLC.
- 3) Expanded the analysis of the role of *KDR* (VEGFR-2) in chemoresistance in NSCLC.

1. Molecular profiling of neoadjuvant-treated NSCLC tumor tissues specimens. During the fourth year of the grant, in collaboration with the Biostatistics/Bioinformatics Core, we analyzed the mRNA (Illumina array; J. Minna) profiles of 63 NSCLCs treated with platinum-based chemotherapy. Our preliminary analysis revealed that 102 genes were differentially expressed in neoadjuvant-treated tumors compared with data obtained from 209 non-treated tumors (cases from Aim 1). Of these, 50 genes were down-regulated and 52 were up-regulated. Interestingly, we found some genes showed histology (adenocarcinoma or squamous cell carcinoma)-specific differential expression in neoadjuvant treated tumors. Although the genes differentially expressed in neoadjuvant-treated tumors comprised several cancer-related pathways, we identified, among others, a “stem-cell” profile in the chemotherapy treated tumors. Currently, we are correlating the gene expression signatures with patient’s pathological response to treatment and outcome, and we are planning *in vitro* studies to mechanistically validate the tumor data using NSCLC cell lines with known chemoresistance characteristics and gene expression profiles examined using Affymetric platform in collaboration with Project 1.

The preliminary analysis of DNA-CNV data obtained from 38 NSCLC treated with neoadjuvant platinum-based chemotherapy showed 161 chromosomal regions with significant CNGs when compared with 138 tumors not treated with such therapy. We are currently correlating the CNV signatures with the patients’ pathological responses to treatment. We are also planning *in vitro* studies to mechanistically validate the tumors’ data using NSCLC cell lines with known chemoresistance characteristics and copy number abnormalities detected by SNP-array analysis in collaboration with Project 1.

Finally, our analysis of the microRNA expression profiles did not reveal statistically significant expression levels of microRNAs when comparing neoadjuvant-treated NSCLC tumors to those of patients who did not receive neoadjuvant treatment.



2. Analysis of tissue and RNA quality of additional neoadjuvant-treated NSCLC tissue sets for profiling studies. As reported in previous years, Dr. Li Mao signed a collaborative agreement with the Intergroupe Francophone de Cancérologie Thoracique (IFCT) to obtain up to 250 frozen lung tumor tissues from patients enrolled in IFCT-0002 clinical trial (a open-labeled, multicenter, randomized phase III study), which was designed to define the best timing of neoadjuvant chemotherapies. The samples are being used to validate our gene expression signature of resistance to platinum-based chemotherapies developed using MD Anderson samples. During the past year, we identified 98 mRNA samples with adequate RNA quality ( $\geq 4$ ) for profiling analysis and tumor malignant cells  $\geq 10\%$  (Table 1). The mRNA Illumina profiling is completed and, currently, the data are being analyzed by the Biostatistics/Bioinformatics Core to validate potential gene expression signatures associated with tumor pathological response and patient outcome (RFS and OS).

**Table 1.** Sample distribution for gene expression profiling with  $\geq 10\%$  of malignant cells and  $RIN \geq 4$ .

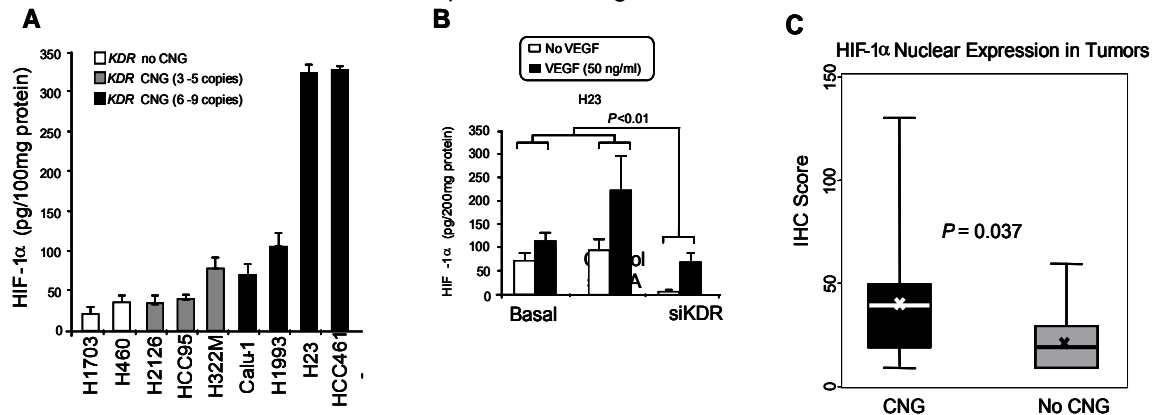
Tumor Response Categories	Number of Cases N=98
Progressive disease	3 (3%)
Stable disease	60 (61%)
Partial response	34 (35%)

multicenter, randomized phase III study), which was designed to define the best timing of neoadjuvant chemotherapies. The samples are being used to validate our gene expression signature of resistance to platinum-based chemotherapies developed using MD Anderson samples. During the past year, we identified 98 mRNA samples with adequate RNA quality ( $\geq 4$ ) for profiling analysis and tumor malignant cells  $\geq 10\%$  (Table 1). The mRNA Illumina profiling is completed and, currently, the data are being analyzed by the Biostatistics/Bioinformatics Core to validate potential gene expression signatures associated with tumor pathological response and patient outcome (RFS and OS).

3. Completion of the data analysis and manuscript submission of additional projects reported last year. During the previous years of the grant, we have developed additional projects to investigate novel biomarkers in NSCLC related or potentially related to resistance to chemotherapy. In one of those studies, we performed additional molecular mechanistic studies to respond to reviewers' suggestions in a manuscript (Yang et al.) submitted to Cancer Research and currently under revision after resubmission with minor comments. A brief description of the major findings of this study is included below.

*KDR* Copy Number Gain Associates with NSCLC Platinum Chemoresistance and HIF-1 $\alpha$  expression In the original work, we showed that the VEGFR-2 gene (*KDR*) shows frequent (32%) copy number gains in NSCLC and *KDR* was associated with patients' poor survival and tumors' angiogenesis. The association we found between *KDR* copy number increase and worse outcome in platinum adjuvant therapy-treated NSCLC patients suggested that it might be a potential biomarker for predicting the efficacy of adjuvant chemotherapy in this disease. Our findings, using NSCLC tissue specimens, were confirmed by the *in vitro* NSCLC cell lines data. During the last year, we have significantly expanded the data and developed a novel mechanistic hypothesis to explain the clinical and *in vitro* results showing an association between *KDR* copy number gain and resistance to platinum drugs. We demonstrated an increased cytotoxicity to platinum drugs and decreased cell migration of NSCLC cell lines with *KDR* copy gain after significant inhibition of VEGFR-2 gene and protein expressions. Then, we demonstrated a significant association between *KDR* copy gain and HIF-1 $\alpha$  expression in both NSCLC tumors and cell lines, which we postulate may explain the association between *KDR* copy number gain and increased tumor angiogenesis, and potentially, resistance to platinum therapies. We specifically showed that *KDR* CNGs were significantly associated with increased levels of nuclear HIF-1 $\alpha$  in both NSCLC tumor specimens and cell lines (Figure 21). Furthermore, *KDR* knockdown experiments using small interfering RNA reduced platinum resistance, cell migration, and HIF-1 $\alpha$  levels in cells bearing *KDR* CNGs, providing evidence for direct involvement of *KDR*.

**Figure 21.** *KDR* copy number gain (CNG) correlated with HIF-1 $\alpha$  expression in NSCLC cell lines and tumor tissue specimens. A) HIF-1 $\alpha$  protein expression determined by ELISA correlated with *KDR* CNG in a series of NSCLC cell lines (cell lines with CNG 6-9 copies versus 3-5 copies and no CNG,  $P < 0.02$ ). B) HIF-1 $\alpha$  expression by ELISA was markedly inhibited by knocking down using si*KDR* in NSCLC H23 cell line with and without stimulation with VEGF. C) Expression of nuclear HIF-1 $\alpha$  in tumors with *KDR* CNG compared with lung cancers without CNG.



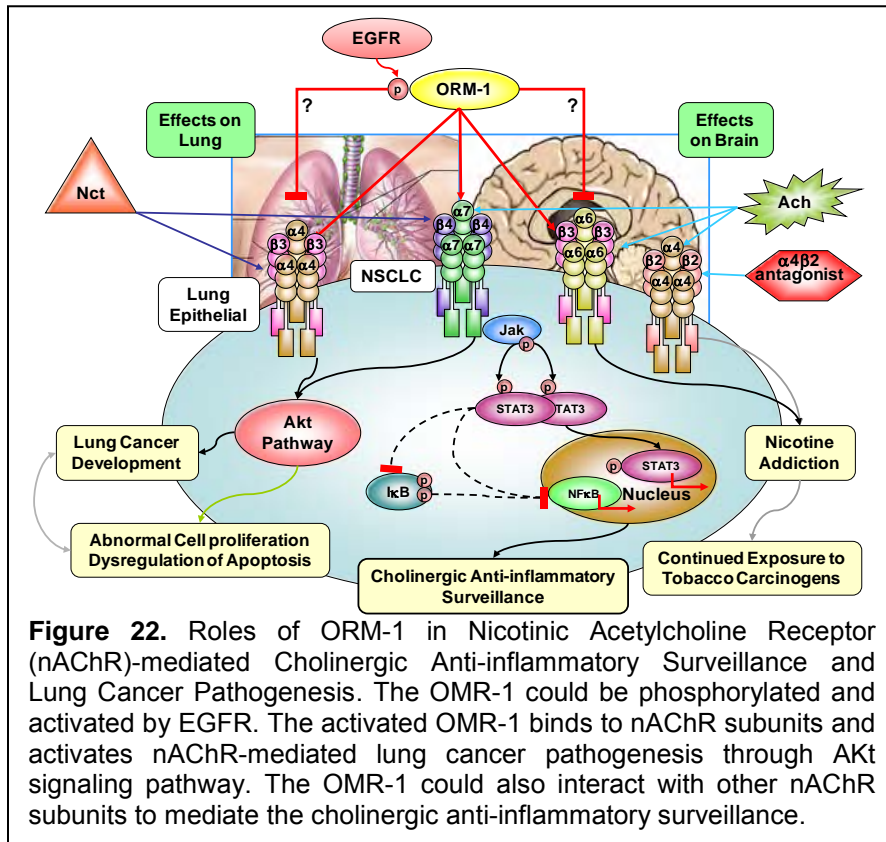
### Aim 3: To identify surrogate serum phosphopeptide profiles and plasma DNA markers associated with NSCLC tumor resistance and patient response to neoadjuvant chemotherapy.

We will identify serum samples from the UT-SPORE Tissue Bank that match the NSCLC tumor resection specimens examined in Aim 1. We will use these serum samples for phosphopeptide profiling and peptide mapping by ProteinChip array-based surface-enhanced laser-desorption/ionization (SELDI) mass spectrometry (MS) and laser desorption/ionization (LDI) mass spectrometry (MS)/MS to compare serum phosphopeptides with TTF and mRNA profiles. The phosphopeptide MS profiles from retrospective specimens will later be used as references and controls for the prospective serum proteomic analysis. As in Aim 2, we will use serum samples collected prospectively in Project 2 from 100 NSCLC cases undergoing neoadjuvant chemotherapy and 200 NSCLC controls undergoing surgery without neoadjuvant chemotherapy, and, when relevant, at the time of relapse. Using these serum specimens, we will perform phosphopeptide profiling on ProteinChip arrays by SELDI-MS to measure the temporal changes in serum phosphopeptides before and after the therapeutic intervention. We will use LDI-QSTAR-MS/MS and liquid chromatography (LC)-MS/MS to identify specific serum phosphopeptides that are determined by SELDI-MS to be relevant to targeted therapeutic response and acquired resistance in lung cancer patients. In addition, we will compare serum phosphopeptide profiles with TTF (RPPA and MBA) profiles, mRNA profiles, and TMAs and IHC analysis developed in Project 1 and in Aims 1 and 2 of this project. This comparison will identify TTF serologic molecular signatures and elucidate the biologic pathways potentially associated with patient response and tumor resistance to targeted therapeutic agents. Finally, in collaboration with Project 2, we will perform correlation analysis of these NSCLC serum phosphopeptide profile signatures with patients' clinical characteristics to predict lung cancer, cancer progression, cancer stages, and overall survival rate; to characterize serum phosphopeptide proteomic patterns and signatures in correlation to tumor recurrence, clinical response to adjuvant chemotherapeutic and targeted agents, and development of resistance; and to identify serum phosphopeptide markers as surrogate predictors of patient outcome.

Moreover, in Aim 3 we will quantify total circulating plasma DNA and methylation-specific DNA in all 300 patients with NSCLC enrolled in the Project 2 clinical trial. The circulating DNA levels will be correlated with patients' clinicopathologic characteristics. Any changes in these levels during chemotherapy and after surgery will be correlated with patient response to neoadjuvant therapy and patient outcome after surgery. The correlation between circulating methylated DNA levels and tumor DNA methylation will also be examined in a selected panel of patients.

### Summary of Research Findings

We used phospho-tyrosine antibody-conjugated super-paramagnetic beads to capture phosphopeptides generated in trypsin-digested serum samples. The captured phospho-tyrosine peptides (pYPs) were separated on a hybrid magnetic plate using a biological sample preparation robot. The affinity-enriched pYPs were then randomly loaded onto SEND ProteinChips with duplicates and analyzed by SELDI-TOF Mass Spectrometry. We used wavelets and the mean spectrum for peak detection and detected more than 600 pYP peaks spanning a M/Z range from 50 to 5500 Dalton. For each peak, we recorded the p-value from an F-test and modeled the set of p-values using a beta-uniform mixture model to estimate the false discovery rate (FDR). We identified 39 pYP peaks with fold changes in detected intensity on SELDI-MS profiles to be significantly (at FDR = 10%) differentially expressed between the normal and lung cancer serum samples. The phosphopeptides detected on SELDI-MS spectra were further identified using a protein chip array-interfaced qSTAR-MS/MS. One of phospho-tyrosine-containing peptides was identified as an Alpha-1-acid glycoprotein 1 precursor (A1AG1) or ORM-1 serum protein. The ORM-1 pYP showed a M/Z peak at 1752.3 Da and was significantly upregulated in lung cancer serum samples with more than 10-fold increase (P = 0.0024) in mass peak intensity. A computer-aided structural and function analysis predicted the potential association of ORM-1 to the nicotinic acetyl choline receptor (nAChRs) and to be a substrate of EGFR tyrosine kinase. We are now performing phosphopeptide profiling and validation of phospho-ORM-1 level in a large group of lung cancer case-control patient serum samples (95) containing: 1) Never-smoker controls (20); 2) Ever-smoker controls (20); 3) Case-Stage I (20); 4) Case-Stage II (15); and 5) Case Stage 3-4 (20) for prediction of lung cancer, stages, and association with tobacco smoking. We will also analyze a group of 64 matched lung collected from PROSPECT program for to identify markers that may predict clinical response to adjuvant therapy or TKIs.



Our results suggest the role of the Phospho-ORM-1 peptide as a novel NACHR-associated protein in lung cancer pathogenesis and smoking-associated carcinogenesis, and as a potential serum marker and target for lung cancer detection and treatment. Identification of OMR-1 as EGFR substrate could place OMR-1 as a potentially critical link between the nACHR-EGFR-Akt signaling pathway in lung cancer development associated with tobacco smoking and other oncogenic stresses. The potential role and mechanism of serum phosphor-ORM-1 in lung cancer pathogenesis is proposed and summarized in Figure 22.

### **Key Research Accomplishments**

- Identified that PSCA may play an important role in the development of NSCLC brain metastasis as a novel potential marker for NSCLC metastasis and therapeutic target for advanced lung tumors.
- Demonstrated that *KDR* CNGs were significantly associated with increased levels of nuclear HIF-1 $\alpha$  in both NSCLC tumor specimens and cell lines.
- Identified phosphorylated ORM-1 as a novel lung cancer serum biomarker that is significantly upregulated in lung cancer with tobacco-smoking history.
- Validated phosphor-ORM-1 protein expression in 80 lung cancer and control serum samples by ELISA and confirmed the significantly upregulated expression of serum phosphor-ORM-1 in late stage lung cancer patients with ever-smoking history.
- Identified the phosphor-ORM-1 protein as a critical ligand of nicotinic acetylcholine receptor (nACHR).
- Demonstrated that OMR-1 is a potential phosphorylation substrate of EGFR.

### **Conclusions**

During the past year, we analyzed the molecular profiling data of NSCLC and MPM tissue specimens with annotated clinical information in Aim 1 and we identified a panel of microRNAs associated to the outcome of NSCLC patients treated with and without adjuvant chemotherapy. Using our results, we designed a strategy for gene (mRNA), microRNA, and protein signature validation using high-throughput qNPA™, Fluidigm™ microfluidic quantitative dynamic array, and IHC methodologies. We also identified a series of molecular pathways and markers, using gene profiling, as potential novel targets in malignant pleural mesothelioma (MPM) in collaboration with Project 4. In Aim 2, we completed the analysis of the molecular profiling data of surgically resected NSCLC specimens obtained from patients who have received neoadjuvant chemotherapy. We identified Phospho-ORM-1 peptide as a novel NACHR-associated protein in lung cancer pathogenesis and smoking-associated carcinogenesis and as a potential serum marker and target for lung cancer detection and treatment in Aim 3. We will continue to analyze this data during the next unfunded research period.

### **Project 4: Target Modulation Following Induction Treatment With Dasatinib in Patients With Malignant Pleural Mesothelioma (MPM) and Identification of New Therapeutic Targets/Strategies for MPM**

(Leaders: Drs. Anne Tsao, Reza Mehran)

#### **Hypothesis:**

We hypothesize that dasatinib, a broad spectrum ATP-competitive inhibitor for oncogenic tyrosine kinases (BCR-ABL, SRC, c-Kit, PDGFR, and ephrin receptor kinases), may be a new therapeutic agent in malignant pleural mesothelioma (MPM). We also believe that conducting

therapeutic target-focused (TTF) molecular and gene profiling (Affymetrix arrays) will lead to development of other novel therapies for MPM.

**Specific aims:**

**Aim 1: Conduct a phase I clinical trial with the primary endpoint of biomarker modulation using dasatinib as induction therapy in patients with resectable MPM.**

**Trial design:** Untreated MPM patients undergo extended surgical staging (ESS) with multiple biopsies to account for tumor heterogeneity. If deemed a surgical candidate for either P/D or EPP, patients receive 4 weeks of oral dasatinib (70 mg BID) followed by pleurectomy/decortication (P/D) or extrapleural pneumonectomy (EPP). If a radiographic response is seen, an additional 2 years of dasatinib maintenance after adjuvant radiotherapy and chemotherapy is given. Serum/blood/platelets/pleural effusion specimens are collected for exploratory analysis of peripheral surrogate biomarkers. The primary endpoint is biomarker modulation of Src Tyr419 immunohistochemistry (IHC) in tumor tissue. Secondary endpoints include response, survival, safety/toxicity, and biomarker modulation.

- 1a. Determine the effects of dasatinib induction therapy on selected tumor biomarkers (activated Src, PDGFR, VEGFR) pre- and post-induction therapy.
- 1b. Determine the modulatory effects of dasatinib on selected biomarkers of survival and apoptosis (PI3K/AKT, bcl-xL, caspases), proliferation (IGFR, Ki-67), angiogenesis (IL-8, bFGF, TNF- $\alpha$ ), epithelial-mesenchymal transition (TNF- $\beta$ , E-cadherin, c-Kit/Slug) and invasion/migration (Ephrin, MMP) in tumor specimens pre- and post- induction therapy.
- 1c. Determine the effects of induction dasatinib therapy on tumor mean vessel density, cell apoptosis, and the proliferation index.
- 1d. Determine the modulatory effects of dasatinib on serum, platelet, and pleural effusion markers of survival (PI3K/AKT, bcl-xL, caspases), proliferation (IGFR, Src), angiogenesis (soluble VEGFR, VEGF, PDGF, IL-8, bFGF, TNF- $\alpha$ ), and invasion/migration (Ephrin, MMP).
- 1e. Determine the drug concentration of dasatinib in tumor and serum.
- 1f. Assess the effects of dasatinib and cytoreductive surgery on the serum mesothelin-related peptide (SMRP) level.
- 1g. Assess the safety and toxicity profile of induction dasatinib in patients with resectable MPM.

**Aim 2: Conduct radiographic correlates of tumor response and clinical outcome with positron-emission technology-computer tomography (PET-CT).**

**Aim 3: Explore and develop new therapeutic targets and treatment strategies for MPM in tumor specimens collected from Specific Aim1 and in MPM cell lines.**

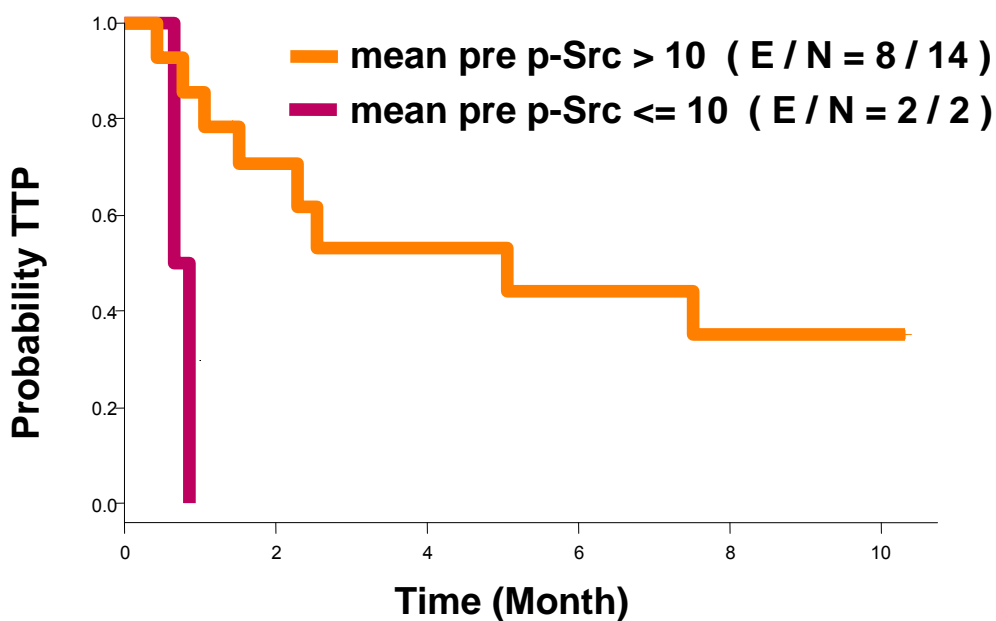
- 3a. Determine key signaling pathways involved in tumor resistance or sensitivity to dasatinib using therapeutic target-focused (TTF) molecular and global gene expression profiling on MPM tumor specimens pre- and post- induction dasatinib therapy.
- 3b. Determine the sensitivity of a panel of MPM cell lines to targeted agents tested in Project 1 via TTF profiling and DATs (drug and therapeutic target siRNA).

**Summary of Research Findings**

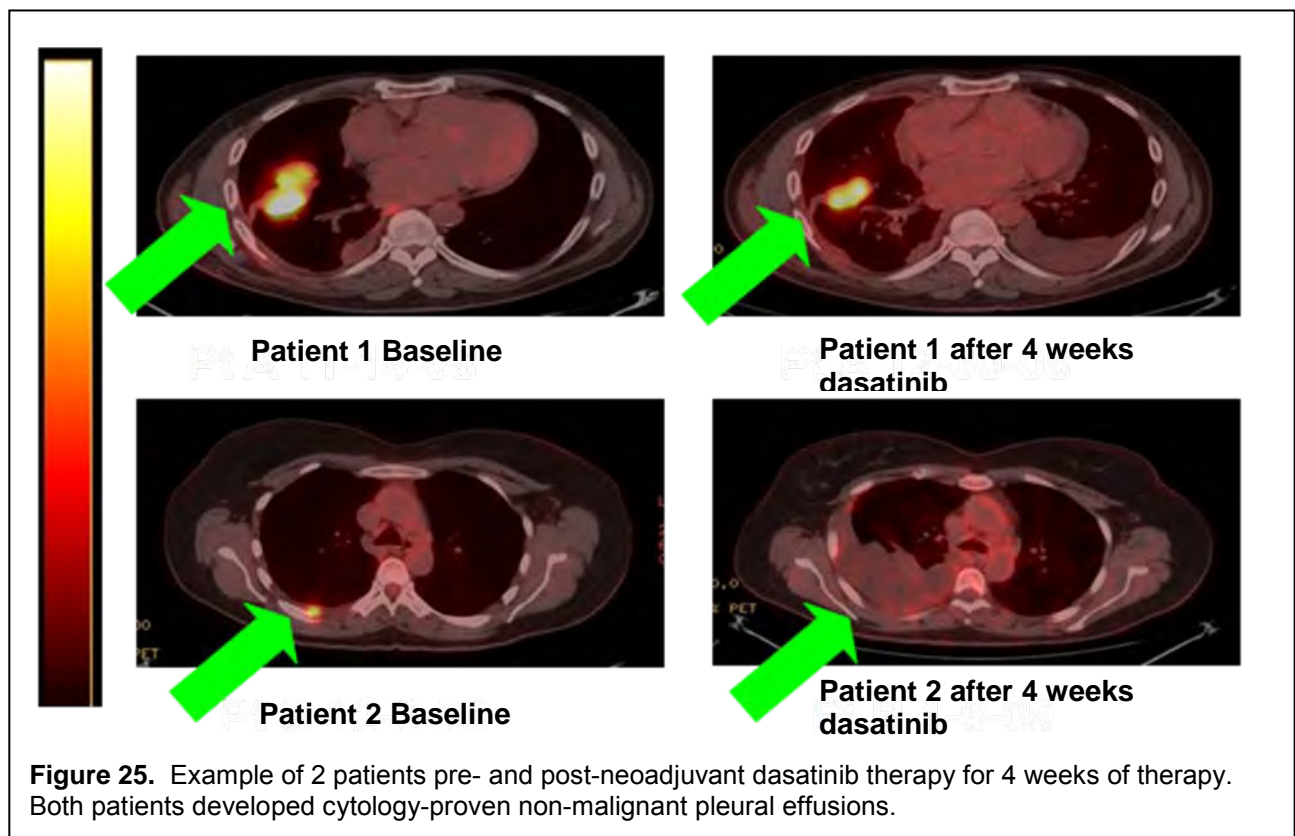
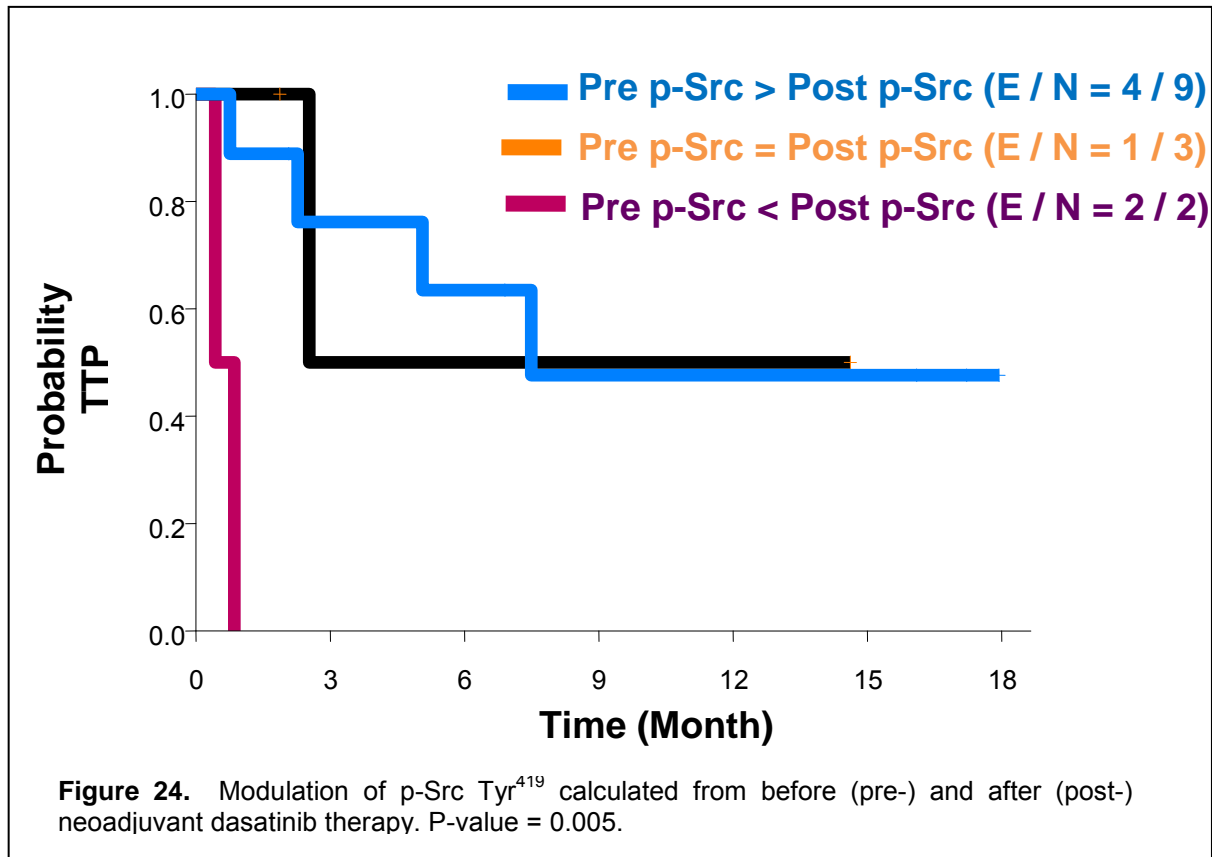
A total of 42 patients have been screened for the trial from April 2008 – May 2011. Of these, 20 patients have successfully enrolled and completed ESS, neoadjuvant dasatinib, and P/D (n=12) or EPP (n=8). Of these 20 patients (16 men and 4 women), 18 had epithelioid histology and 2

had biphasic histology. The main side effects from neoadjuvant dasatinib treatment were grade 1-2: anemia, nausea, vomiting, anorexia, fatigue, and anxiety. Grade 3 toxicities included fluid retention, infection (pneumonia), and hypoxia. There are no grade 4-5 toxicities to date. Post-surgical grade 3 toxicities included anemia, arrhythmia, HTN, and pleural effusion; there was also one grade 4 episode of hyperglycemia. To date, neoadjuvant dasatinib does not add significant toxicity to MPM surgical resection. We will enroll and treat the remaining 4 patients needed to complete this trial within the next project period (unfunded extension requested).

After 4 weeks of neoadjuvant oral dasatinib therapy, there was 1 PD, 15 SD, and 2 minor responses, 1 mixed response, and 1 patient that did not receive the second PET-CT. In the initial analysis of IHC Src Tyr419 in 13 patients (Figure 23), higher baseline levels of p-Src Tyr419 predicted for an improved TTP with dasatinib therapy ( $p=0.008$ ). Also, patients with significant modulation of p-Src Tyr419 after dasatinib therapy demonstrated improved TTP ( $p=0.005$ ) (Figure 24). These findings demonstrate that there is a subpopulation of MPM patients that may derive clinical benefit from oral dasatinib therapy (Figure 25). MPM is a very heterogeneous tumor, and molecular profiling will be necessary to ultimately optimize targeted therapy in this disease. We will continue to perform molecular and global gene expression profiling on the MPM specimens with Project 2 and the Pathology Core during the next project period. Future plans include correlating outcome and tumor p-Src Tyr<sup>419</sup> to peripheral surrogate markers in blood/serum/platelets and pleural effusion and to analyze pathways of resistance in MPM tumors.



**Figure 23.** Baseline levels of IHC p-Src Tyr<sup>419</sup> by time to progression. P-value = 0.008.





### **Key Research Accomplishments**

- Continued to enroll patients to the clinical trial. Four additional patients are needed to complete the trial.
- Produced preliminary evidence to demonstrate that higher baseline levels of p-Src Tyr419 is predictive for improved PFS with dasatinib.
- Demonstrated that modulation of p-SrcTyr419 is a reasonable pharmacodynamic marker for dasatinib treatment.

### **Conclusions**

There is preliminary evidence that a subgroup of MPM patients gain clinical benefit from dasatinib therapy and that baseline p-Src Tyr419 levels in MPM tumor tissue may be predictive of TTP. This report details the first targeted therapy neoadjuvant trial to potentially identify a predictive biomarker in MPM. The novel clinical trial approach is feasible and has the potential to advance the field of MPM in personalized medicine.

### **Project 5: Development of a Novel Multi-Biomarker System Using Quantum Dot Technology for Assessments of Prognosis of NSCLC and Prediction of Outcome of EGFR-Targeted Therapy**

(Leader: Dr. Zhuo (Georgia) Chen; Co-Leaders: Drs. Fadlo Khuri, Dong Shin, Ruth O'Regan, Shi-Yong Sun)

Quantum dots (QDs) provide sharper fluorescent signals than organic dyes and can detect multi-biomarkers simultaneously in the same material, allowing quantification and correlation of molecular signature with cellular response to targeted therapies.

#### **Hypothesis:**

A multi-biomarker system using quantum dot (QD) technology will enhance accuracy in assessment of prognosis of non-small cell lung cancer (NSCLC) and prediction of outcome of epidermal growth factor receptor (EGFR)-targeted therapy.

#### **Specific Aims:**

**Specific Aim 1: Development of QD-Abs and imaging systems for detection and quantification of multi-biomarkers (MBM) using lung cancer cell lines.**

#### **Summary of Research Findings**

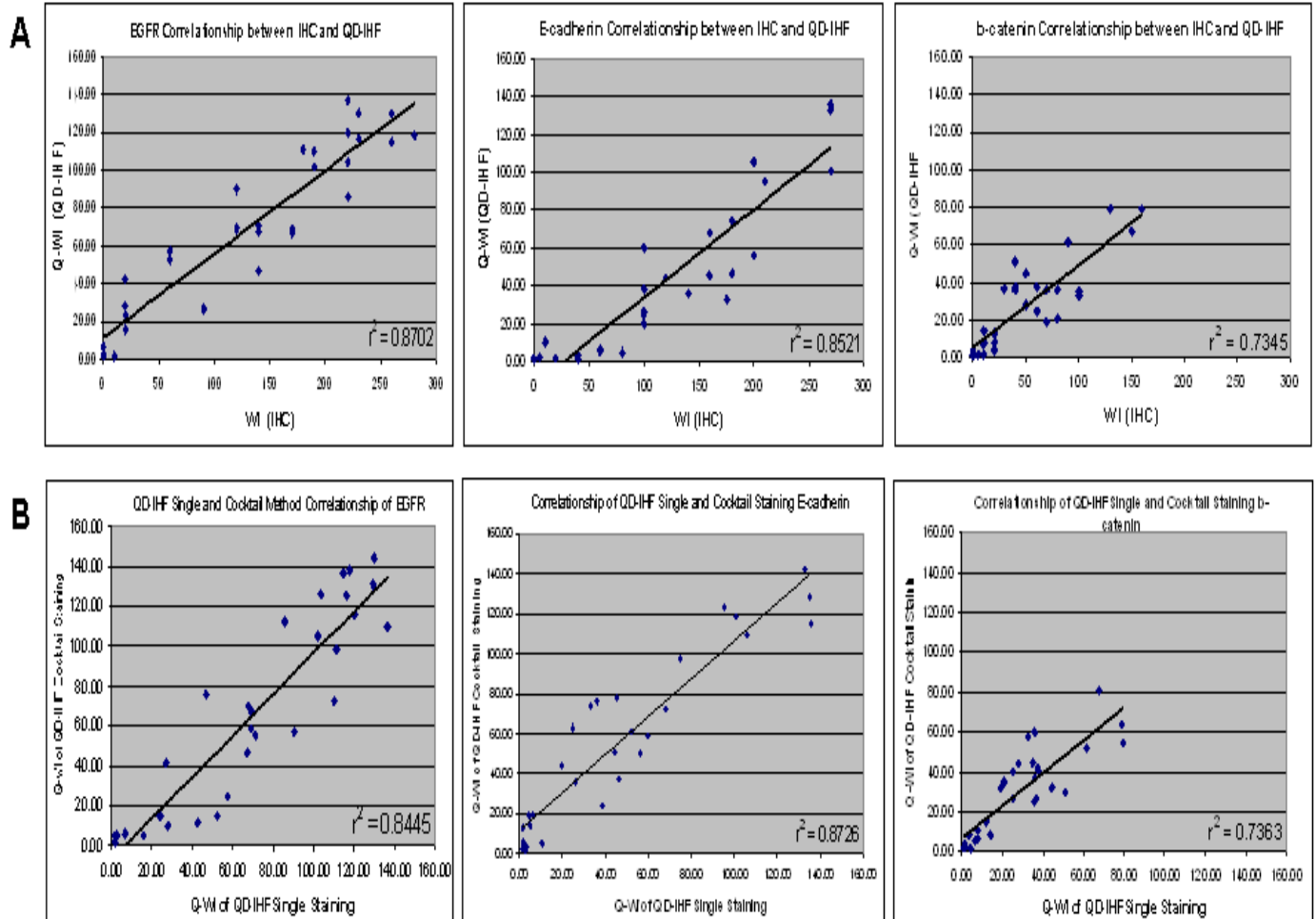
This aim was completed as reported in the previous annual report.

**Specific Aim 2: Verification of QD-Abs for detection and quantification of MBM by comparison with conventional IHC using paraffin-embedded tissues and evaluation of their prognostic value in NSCLC.**

#### **Summary of Research Findings**

We compared QD-antibody (-Ab) staining with conventional IHC in 30 FFPE tumor tissue samples and confirmed a significant correlation between these two methods (Figure 26).





**Figure 26.** Comparison of QD-Ab staining with conventional IHC. A) The single biomarker detection between IHC and QD-IHF was significantly correlated. EGFR:  $p < 0.00001$ ; E-cadherin:  $p < 0.00001$ ; β-catenin:  $p < 0.00001$ . B) Each of the biomarker signals was significantly correlated between the single QD-IHF staining and the same marker stained simultaneously with the multiple QD-IHF. EGFR:  $p < 0.00001$ ; E-cadherin:  $p < 0.00001$ ; β-catenin:  $p < 0.00001$ .

We have worked on two sets of NSCLC tissues, (i) 89 surgical tissue specimens from early stage (T1 and T2) NSCLC and (ii) a tissue array of NSCLC with matched lymph node metastasis ( $n = 34$ , US BIOMAX INC, Cat#LC810). The proposed biomarkers were grouped into two studies. The first study involved EGFR, E-cadherin (E-cad), and β-catenin (β-cat). Their stains by both IHC and IHF-QD have been completed. The second group includes CXCR4, SDF-1, E-cad, p-AKT, and p-ERK IHC staining has been completed and images and quantified data have been acquired. The findings from single biomarkers by IHC studies are summarized as follows:

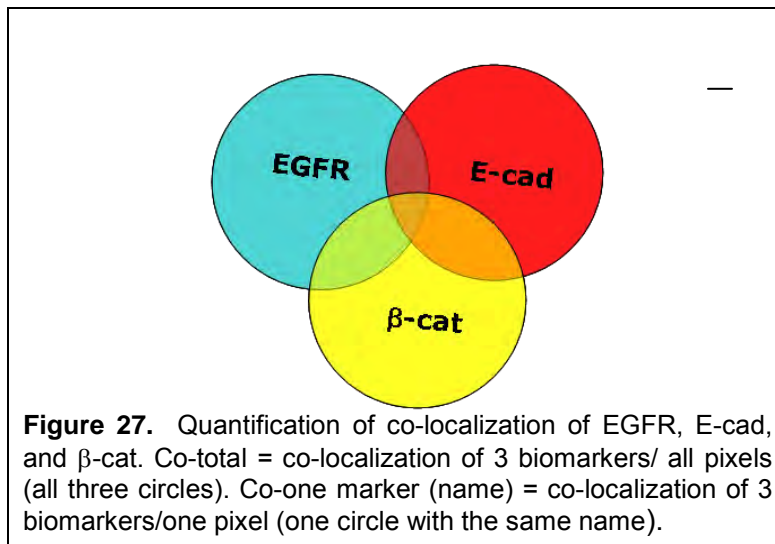
- (i) Expression of EGFR is higher ( $p < 0.0001$ ) and E-cad has less membrane localization in squamous cell carcinoma than in adenocarcinoma.
- (ii) In early stage adenocarcinoma, low expression of E-cad correlated with poor differentiation and lymph node metastasis,  $p = 0.03$  and  $0.01$ , respectively.
- (iii) In early stage adenocarcinoma, high expression of p-AKT was associated with lymph node metastasis,  $p = 0.04$ .

- (iv) In early stage squamous cell carcinoma, a high level of SDF-1 expression was associated with lymph node metastasis and recurrence,  $p = 0.003$  and  $0.02$ , respectively, suggesting the SDF-1/CXCR4/CXCR7 signaling pathway may play a role in tumor progression.
- (v) Nuclear localization of CXCR4 was correlated with high E-cad and low p-AKT expression,  $p = 0.02$  and  $0.001$ , respectively, in all 89 tissue samples.
- (vi) There was no observed correlation between these biomarkers with either disease-free survival or overall survival, since all of the 89 samples are T1 and T2 stage disease.

### **Specific Aim 3: Correlation of the MBM detected by QD-Abs with outcomes of chemotherapies and EGFR- targeted therapy using resectable NSCLC tissues.**

#### **Summary of Research Findings**

Taking advantage of the quantification available with multiplexed QD-IHF, we are able to quantify co-localization of EGFR, E-cad, and  $\beta$ -cat in the same cells. There are two considerations for using the co-values. First, it is known that both EGFR and E-cad are membrane proteins, and activation of EGFR induces internalization and reduction of E-cad. Also, loss of E-cad induces dissociation and internalization of  $\beta$ -cat. Therefore, co-localization of the three proteins represents the true biological relationships. Second, the co-values normalize the variation of the staining intensity due to the quality of tissues and reagents among the different immunostained batches (Figure 27). In general, quantification of QD-IHF by an image system is more objective than conventional IHC. The findings from this study are summarized below:

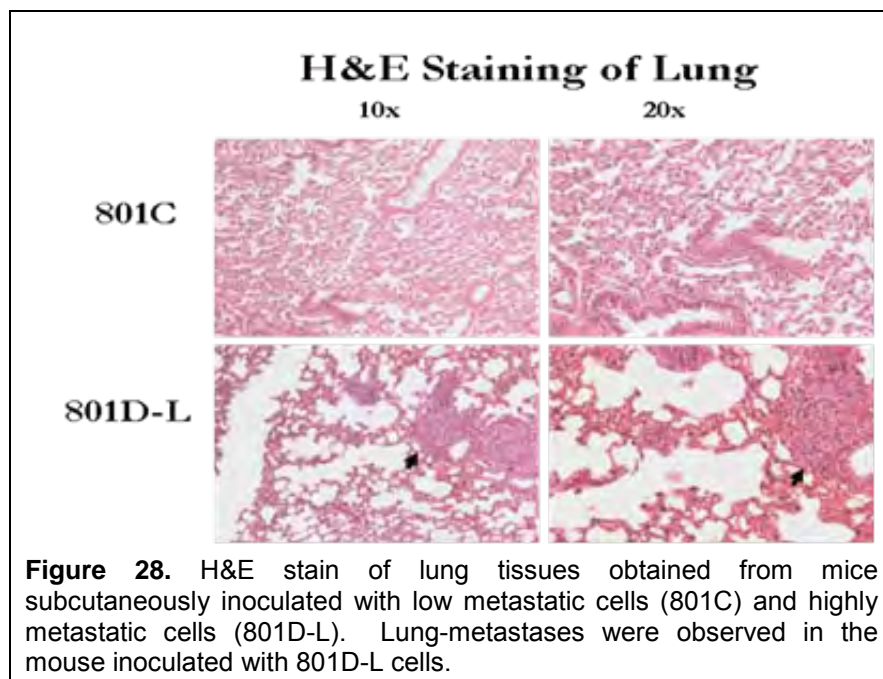


- (i) All of the co-values (Co-EGFR, Co-E-cad, Co- $\beta$ -cat, and Co-Total) are higher in normal lung epithelial tissues than in NSCLC tissues ( $p < 0.0001$ ).
- (ii) Overall, Co-EGFR is associated with smoking ( $p = 0.0011$ ). Both Co-E-cad ( $p = 0.049$ ) and Co- $\beta$ -cat ( $p = 0.044$ ) are associated with alcohol assumption. High Co- $\beta$ -cat is associated with low percentage of 50-month survival ( $p = 0.03$ ).
- (iii) In adenocarcinoma, both Co-E-cad ( $p = 0.024$ ) and Co- $\beta$ -cat ( $p = 0.011$ ) are inversely associated with smoking. Co- $\beta$ -cat is correlated with alcohol assumption ( $p = 0.009$ ) and tumor grade ( $p = 0.029$ ).
- (iv) In squamous carcinoma, Co-EGFR ( $p = 0.002$ ), Co-E-cad ( $p = 0.011$ ), Co- $\beta$ -cat ( $p = 0.003$ ), and Co-total ( $p = 0.003$ ) are correlated with recurrence. Both Co-E-cad ( $p = 0.043$ ) and Co- $\beta$ -cat ( $p = 0.011$ ) are inversely associated with smoking.

Furthermore, when we looked at co-localization of two biomarkers, it was found that:

- (v) The percentage of co-localization of EGFR and  $\beta$ -cat correlated with SDF-1 expression ( $p = 0.0054$ ) in 89 NSCLC tissue samples.
- (vi) As compared with primary lung cancer, the percentage of EGFR- $\beta$ -catenin co-localization was increased in lymph node metastases in 34 pair TMA tissue samples ( $p = 0.0262$ ).

The biological meaning of the EGFR and  $\beta$ -cat interaction is currently under investigation. Based on our findings in Specific Aim 1, we expect that low Co-EGFR and Co-E-cad may predict resistance to EGFR-targeting therapy. However, due to the limited availability of the relevant tissues, the study has not been conducted. We are currently focusing on understanding the correlations of these biomarkers with metastasis and recurrence.



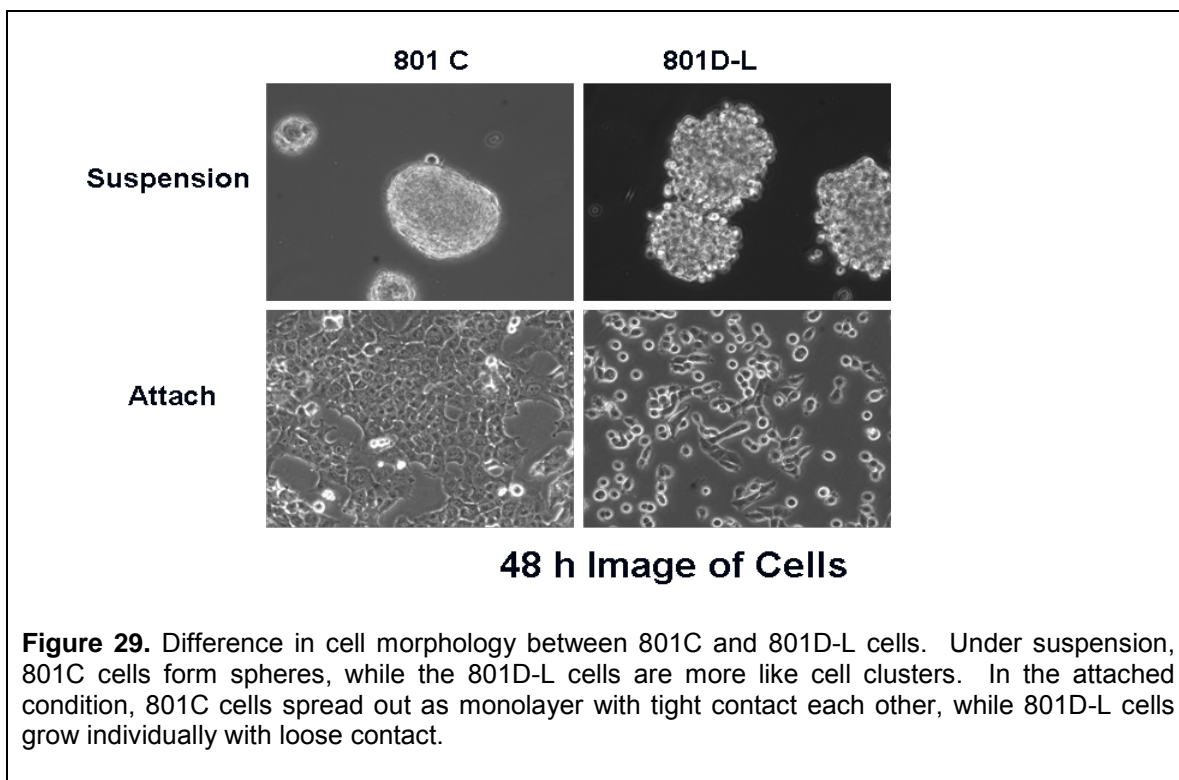
In addition, we recently established a new lung metastasis mouse model using a human large cell lung cancer cell line 801C, and completed a proteomic analysis to compare poorly metastatic cells with highly metastatic cells. The second generation of the *in vivo* selected lung cancer cell line 801D-L showed a higher incidence of lung metastases after subcutaneous inoculation of the cells in nude mice, compared to its parental cells 801C and 801D (Figure 28 and

Table 2). Genetic identity has been determined. Though 801C and 801D-L have the same genetic background, they have different morphology (Figure 29).

**Table 2.** Incidence of Lung Metastases

Cell Type	Number of Mice	Number of Lung Met
801C	8	0
801D	8	1
801D-L	9	9

Primary analysis of the proteomic data using computer software (Ingeuity) has identified top molecular/cellular functions and canonical pathways (Tables 3 and 4), which have provided clues for further molecular analysis to understand the metastatic process of lung cancer. Further analysis of the data and *in vitro* studies are ongoing to further understand the biology behind these observations.



**Table 3.** Top Molecular and Cellular Functions

Function	p- value	No. of Molecules
Cellular assembly and organization	8.8E-05 - 1.5E-05	23
Energy production	1.5E-05 – 1.5E-02	7
Nucleic acid metabolic	1.5E-05 – 3.4E-0.2	12
Small molecule biochemistry	1.5E-0.5 – 3.4E-0.2	28
Cell death	1.7E-0.5 – 3.2E-0.2	25

**Table 4.**Top Canonical Pathways

Pathway	p- value	Ratio
DNA double strand break repair	1.30E-03	2/9
Actin cytoskeleton size	1.37E-03	5/238
Glycine, serine, and threonine metabolism	2.92E-03	3/150
One carbon pool by folate	3.52E-03	2/39
Glycolysis	7.35E-03	3/147

### **Key Research Accomplishments**

- Completed staining, image acquisition, and quantification of the seven biomarkers in the 89 pairs (84 pairs of T1 and T2 samples) of the NSCLC tissues and additional 34 matched NSCLC in a tissue microarray by both IHC and QD-IHF methods.
- Completed initial statistical analyses to correlate the seven biomarkers with clinical characteristics. Our analyses identified an association of several biomarkers with aggressive disease status, such as recurrence and metastasis.

- Established a new lung metastasis xenograft model to further understand the biology of CXCR4, E-cad, EGFR, and  $\beta$ -cat signaling pathways in progression and metastasis of lung cancer.

### **Conclusions**

In the past year, we completed the immunostaining of a total of seven biomarkers, EGFR, E-cad,  $\beta$ -cat, CXCR4, SDF-1, p-AKT, and p-ERK in two sets of NSCLC tissues, including 89 pairs of patient tissue samples from our institution and 34 paired samples in a tissue microarray. Quantification and initial statistical analyses of all seven biomarkers have been completed. We found that quantification of the QD-IHF with the normalized co-values may reduce the quantification error resulting from variations of quality of the FFPE tissues or staining agents that may affect intensity of the IHF signals. Using this method, our data indicated that  $\beta$ -cat and its interaction with EGFR and/or E-cad may play a role in recurrence and metastasis of NSCLC, which was not observed using conventional IHC. We believe that quantification of conventional IHC is subjective and results are less informative regarding possible interactions between protein markers. The further study of the biology behind the observed results from the multiplexed QD-IHF signals will continue in the next project period. We will also try to obtain tissues from patients treated with EGFR-targeting agents to move this project forward towards the identification of optimal biomarker combinations better predict which patients may be resistant to EGFR-targeting therapy.

### **Pathology Core**

(Director: Dr. Ignacio Wistuba)

The Pathology Core is an essential component of the PROSPECT program. The Pathology Core plays an important role by collecting, processing and distributing tissue and serum specimens obtained from clinical trials for non-small cell lung carcinoma (NSCLC) (Project 2) and malignant pleural mesothelioma (MPM; Project 4) for molecular profiles and biomarker analysis.

#### **Our objectives are as follows:**

1. Develop and maintain a repository of tissue and serum specimens from patients with NSCLC and MPM.
2. Process NSCLC cell lines and tissue specimens for histopathologic and molecular analyses.
3. Perform and evaluate immunohistochemical (IHC) analysis in human tumor tissue specimens and mouse xenograft tissues.

**Objective 1. Develop and maintain repository of tissue and serum specimens from patients with NSCLC and malignant pleural mesothelioma (MPM).**

#### **Summary of Research Findings**

Selection of lung cancer and MPM specimens available in Thoracic Malignancy Tissue Bank. This goal was achieved during the second year. During the fourth year we continued the processing and distribution of samples for work related to Projects 2, 3 and 4.

Prospective collection and banking of lung cancer and MPM specimens for various projects. Since the activation of the PROSPECT project on August 2007, the Pathology Core has collected fresh and formalin-fixed tissue specimens from 565 NSCLC and 43 MPM surgically

resected cases (Table 5). These cases represent 85% of surgeries performed in our institution during this period. Snap-frozen normal and tumor tissue have been collected in all cases. The samples have been banked in different conditions, including RNAlater® (Ambion, Austin, TX), dimethyl sulfoxide (DMSO)-preserved samples, and OCT-embedded for frozen sectioning. Blood specimens (serum and PMBC) were collected from 536 out of 712 surgery patients (75%), processed, and banked. Of interest, both tissue and blood specimens have been obtained in 408 cases (58%). To date, 137 cases of NSCLC treated with neoadjuvant chemotherapy have been collected.

**Table 5.** Summary of prospectively collected tumor tissue specimens from NSCLC and MPM cases.

Histology	Total Number of Cases	Last Year Number of Cases
Adenocarcinoma	329	77
Squamous cell carcinoma	130	28
Large cell carcinoma	10	2
Other NSCLC	82	11
No tumor present	14	3
<b>Total Lung Tumors</b>	<b>565</b>	<b>121</b>
<b>Malignant Mesothelioma</b>	<b>43</b>	<b>12</b>

Thoracic Malignancy Tissue Bank Database. For tissue collection and banking, an institutional database with bar coding system has been utilized since inception of this grant. This database has been recently updated to include modules for samples tracking and distribution.

## **Objective 2. Process NSCLC cell lines and tissue specimens for histopathological and molecular analyses.**

### **Summary of Research Findings**

Cell Lines. The establishment of a repository of lung cancer and MPM cell lines was completed during the second year of the grant by the Pathology Core. During the last two years, in collaboration with Project 1 (J. Heymach and J. Minna), we maintained, distributed, and utilized the ~70 NSCLC and 2 normal bronchial epithelial cell lines that we have in the repository. As we reported last year, in collaboration with Project 3 (M. Suraokar and A. Tsao), 21 mesothelioma and mesothelial cell lines have been collected from different sources, maintained, and subsequently characterized and molecularly profiled. During the last year, we have added two additional MPM cell lines to our collection. Additionally, formalin-fixed and paraffin-embedded (FFPE) tumor cell lines pellets have been prepared by the Pathology Core for validation of various in situ techniques, including IHC and fluorescent in situ hybridization (FISH).

Tissue Processing for RNA, DNA and Protein Extractions. During the previous years, we have performed DNA and RNA extractions of frozen tumor and normal tissue from 613 surgically resected chemonaïve NSCLCs, 70 neoadjuvant treated surgically resected NSCLCs, and 76 surgically resected MPMs. In collaboration with Project 1 (J. Heymach), during last year we have completed the extraction of proteins for proteomic reverse phase protein array (RPPA) from 200 NSCLCs that have been molecularly profiled for DNA and RNA changes. Also, DNA was re-extracted from 200 NSCLC tumors profiled in Project 3 for DNA mutation analysis using Sequenom® and Sanger sequencing methodologies. Additionally, mRNA was extracted from 89 additional neoadjuvant-treated NSCLCs in collaboration with Project 3 (I Wistuba) in order to expand the array gene expression data on chemotherapy-treated NSCLC tumors. Finally,



during the last year, mRNA, DNA and proteins were extracted from tumor and normal tissues from 55 surgically resected lung adenocarcinomas for Project 3.

Sample Distribution. During the fourth year, the following samples were distributed by the Pathology Core for molecular profiling to Projects 3 and 4:

*RNA.* Aliquots of RNA (1 µg each) from 53 MPMs have been distributed to Drs. M. Suraokar and I. Wistuba for validation of mRNA and miRNA data obtained in the arrays analyses, and mRNA from 80 neoadjuvant-treated NSCLCs and 55 lung adenocarcinomas to investigators of Project 3.

*DNA.* One aliquot of DNA from 190 NSCLC tumors profiled in Project 3, and from the 55 lung adenocarcinomas from never-smokers processed during the last year were distributed to Project 3 (I. Wistuba) for mutation analysis of 12 genes using Sequenom® methodology as well as Sanger sequencing for *KRAS* (codons 12-13) and *EGFR* (exons 18-21) mutation analyses.

*Protein.* No protein samples were distributed last year.

Molecular signatures validation strategies. During last year, we have continued our collaboration with Project 3 (I. Wistuba) to design a strategy for gene (mRNA) and miRNA signatures validation using the Quantitative Nuclease Protection Assay (qNPA™) and quantitative PCR (qPCR) Fluidigm™ for RNA expression and IHC for protein expression. In collaboration with High-Throughput Genomic (HTG), Inc. (<http://www.htgenomics.com/technology/qnpa>) Project 3 has developed a multiple qNPA™ assays to test the expression of up to 200 genes using both frozen and FFPE tissues from surgically resected NSCLC tumors. During the last year, the Pathology Core completed the processing of FFPE tissue samples from all 249-profiled NSCLC cases for qNPA™ analysis, as well as providing tissue material for optimization of the expression of housekeeping gene arrays needed for data normalization strategies. FFPE tissue sections from 190 surgically resected tumor specimens has been prepared for Project 3 for Fluidigm™ analysis of a panel of 70 genes associated to stem cell features and cancer signaling transduction.

Tissue Microarrays (TMAs). During last year the Pathology Core distributed sections of the MPM TMAs for validation of gene expression data using protein expression IHC methodology for collaboration with investigators of Project 3. Currently, a new set of TMAs containing nearly 90 tumors with well-annotated clinical data is being constructed. In addition, the TMAs containing all 249 NSCLC tumors profiled in project 3 have been constructed and the quality control has been completed. These TMA samples will be used for validation the expression of proteins from genes found to be dysregulated in the gene expression array and proteomic RPPA analyses, as well as for DNA copy number analysis using FISH of chromosomal regions shown to have copy number changes in the aCHG analysis.

MPM Clinical Trial Tissue Collection and Processing. In collaboration with Project 4 (A. Tsao), the Pathology Core has collected, banked, and characterized MPM tumor tissue from 35 patients enrolled in the dasatinib clinical trial who underwent to video-assisted thoracoscopy (VAT) and extrapleural pneumonectomy (EPP). A total of 359 (202 baseline [VAT] and 157 at surgery [EPP]) fresh-frozen and formalin-fixed tumor tissue specimens from 35 patients have been obtained, processed, and histologically characterized by the Pathology Core.

Neuroendocrine (NE) tumor set. In collaboration with Project 1 (J. Heymach) the Pathology Core selected, processed and prepared a TMA including a large set of NE tumors to be used to

validate findings obtained in the profiling of SCLC cell lines. The NE TMA was composed of 96 neuroendocrine tumor specimens, including 25 SCLCs, 22 large cell neuroendocrine carcinomas, 35 atypical cell carcinoids and 65 typical carcinoids. For molecular analysis, these tumors have been fully characterized for histopathological, immunohistochemical and proliferation markers.

**Objective 3. Perform and evaluate immunohistochemical (IHC) analysis in human tumor tissue specimens and mouse xenograft tumor specimens.**

**Summary of Research Findings**

As reported in previous years, the Pathology Core has assisted and performed IHC analysis for over 35 markers using TMAs and whole sections in tumor tissue specimens of NSCLC in collaboration with Projects 2 (D. Stewart) and 3 (I. Wistuba). During the fourth year, the Pathology Core examined the expression of proteins using IHC particularly to validate molecular profiling data, including protein expression of genes overexpressed in MPM gene arrays (surviving, MAD-2, C-ENP) and of genes located in chromosomal regions with copy number increased in NSCLC (PSCA, Ly6K). In addition, the Pathology Core has continued the examination of the expression of total Src and p-Src (Tyr 416) in over 350 MPM tissue samples obtained from patients enrolled in the dasatinib clinical trial for Project 4 (A. Tsao).

**Key Research Accomplishments**

- Collected prospective frozen tissue specimens from 121 NSCLC and 12 MPM cases with annotated clinical information.
- Maintained a NSCLC and MPM cell line repository, and managed the distribution of specimens for molecular profiling in collaboration with Projects 1 and 4.
- Distributed proteins and continued the distribution of nucleic acids (DNA and RNA) from large series of NSCLC and MPM tumor specimens with annotated clinicopathological information for molecular profiling.
- Expanded the mRNA availability of neoadjuvant-treated NSCLCs by extracting mRNA from 89 additional tumors.
- Developed a large cohort of tumor tissue specimens from lung adenocarcinoma arising in never-smoker patients and extracted nucleic acids and proteins for molecular profiling.
- Constructed a NSCLC tumor tissue TMA containing the 249 molecularly profiled (DNA, RNA, proteins) NSCLC tumors with annotated clinical information.
- Collected, processed, and analyzed over 350 MPM tumor tissue specimens from patients enrolled in the dasatinib clinical trial in collaboration with Project 4.
- Contributed to the publication and submission of 6 manuscripts and 6 abstract presentations in scientific meetings.

**Conclusions**

During the fourth grant year, the PROSPECT Pathology Core continued the successful prospectively collection of frozen tissue specimens from 165 NSCLC and 12 MPM surgically resected tumors. The Pathology Core has played an important role in the processing of NSCLC and MPM tissue and cell line specimens for comprehensive molecular profiling, and in the characterization of tissue specimens on the expression of protein expression by immunohistochemistry. Additionally, the Pathology Core has developed and processed tissue for molecular profiling from two important cohorts of NSCLC patients, neoadjuvant-treated tumors and lung adenocarcinoma in never smokers.



## **Biostatistics/Bioinformatics Core**

(Director: Dr. J. Jack Lee; Co-Director: Kevin Coombes)

In close collaboration with the Pathology Core and each of the five main projects, the Biostatistics and Data Management Core (BDMC) for the Department of Defense (DoD) PROSPECT lung cancer research program is a comprehensive, multi-lateral resource for designing clinical and basic science experiments; developing and applying innovative statistical methodology, data acquisition and management, and statistical analysis; and publishing translational research generated by this research proposal. We deliver planned and tailored statistical analyses for rapid communication of project results among project investigators, and by collaborating with all project investigators to facilitate the timely publication of scientific results.

The main objectives of the Biostatistics and Data Management Core are to:

1. Provide the statistical design, sample size, and power calculations for each project.
2. Develop a secure, internet-driven, Web-based database application to integrate data generated by the five proposed projects and the Pathology Core of the PROSPECT research project.
3. Develop a comprehensive, Web-based database management system for tissue specimen tracking and distribution and for a central repository of all biomarker data.
4. Provide all statistical data analyses, including descriptive analysis, hypothesis testing, estimation, and modeling of prospectively generated data.
5. Provide prospective collection, entry, quality control, and integration of data for the basic science, pre-clinical, and clinical studies in the PROSPECT grant.
6. Provide study monitoring and conduct of the neoadjuvant clinical trial that ensures patient safety by timely reporting of toxicity and interim analysis results to various institutional review boards (IRBs), the UTMDACC data monitoring committee, the DoD, and other regulatory agencies.
7. Generate statistical reports for all projects.
8. Collaborate with all project investigators and assist them in publishing scientific results.
9. Develop and adapt innovative statistical and genomic methods pertinent to biomarker-integrated translational lung cancer studies.

## **Summary of Research Findings**

In the fourth funding year, the BDMC continued to work with all project investigators in providing biostatistics and data management support. The accomplishments are summarized below.

### **(A) Biostatistics and Bioinformatics**

We have continued to work with clinical investigators in providing biostatistical support for the development and revision of PROSPECT protocols. We provide statistical report in our monthly project meetings to update the accrual, randomization, demographic data, etc.

We have conducted elaborative database queries and management to define the prospective PROSPECT data set. The data were merged from two sources: the first dataset was downloaded on June 6, 2011, from the PROSPECT database and contains a total of 462 patients; the second dataset was sent by Dr. David Stewart (Project 2 PI) on June 10, 2011, and includes 401 prospective PROSPECT patients, who are all part of the first dataset and had surgery between August 1, 2007 and July 31, 2010. Of the latter 401 patients, 304 patients were diagnosed with NSCLC. The analyses reported in Project 2 and Appendix B1 are based on the data of these 304 patients.

In collaboration with the University of Texas Lung SPORE, we continue to work on developing semantic database models for the kinds of assay data being generated by both PROSPECT projects and the SPORE projects.

Initial analysis of copy number data, gene expression array data, and miRNA data on NSCLC samples from PROSPECT has been completed. The bioinformatics and biostatistics core personnel meet weekly with PROSPECT researchers to prioritize analyses.

## **(B) Data Management**

### **PROSPECT Database Development**

The PROSPECT database development has been heavily modeled on the ReVITALization database effort from the DoD-funded VITAL program, to capitalize on the similarities of required data/data fields and anticipated queries related to these unique databases. To tailor the database for the PROSPECT-specific needs, database extensions were made to allow the collection and management of data from multiple studies conducted by this group, including neoadjuvant studies, adjuvant studies, and standard chemotherapy studies. In addition, the PROSPECT database was developed to extend the ReVITALization database in VITAL to provide additional clinical, pathological, and biomarker data repositories and tissue tracking. In this funding period, we continued our database development efforts and made updates to improve the function and usability of the database. Updated screen shots can be found in Appendix B2.

The SQL Server 2005 database and ASP.NET web application are implemented with VB.net language. Queries and SQL 2005 reports are provided. Secure Socket Layer (SSL) and secured database passwords are used to keep data transaction protected and confidential. The tissue data includes clinical and pathological data.

1) The database's clinical module contains the following Web-based forms:

- Patient Information
- Social History (Alcohol and Smoking history)
- Medical History
- Other Malignancy
- Treatments (Surgery, Chemotherapy, Radiotherapy and Other Treatments)
- Clinical Staging
- Follow up

2) The pathological module contains the following Web-based forms:

- Primary and Metastasis data (Diagnosis and Surgery Specimens)
- Histology
- Staging and Tumor Information: Cancer staging (TNM classification) is automatically determined by the system based on the tumor information provided.
- Tissue Bank (Frozen Tissue and Paraffin)

3) Reports: Several Excel reports are provided for the clinical and pathological modules.

1. Clinical Report
2. Pathological Report
3. Patient Report
4. Accession Report
5. General Information Report

6. Other Malignancy Report
7. Surgery Report
8. Chemotherapy Report
9. Radiotherapy Report
10. Other Treatment Report
11. Staging Report
12. Follow-up Report
13. Histology Diagnosis Report

4) Dictionaries: The database gives control for the users to update dictionaries; however, dictionary deletion is prohibited.

### **Key Research Accomplishments**

- Continued to provide biostatistics and bioinformatics support for the PROSPECT grant.
- Published collaborative papers from data collected in PROSPECT.
- Developed a secured, Web-based database application to assist the study conduct.
- Continued with the database maintenance, training and support as followed:
  - Provided data integrity checking and data correction.
  - Performed periodical database server maintenance and data backup.
  - Provided training and custom support to end users.
  - Cleaned and uploaded data from thoracic surgery database.
  - Added pathological stage field and a checklist in the follow-up page to specify if the recurrence is a local recurrence, second primary tumor or n/a.
  - Added comments for clinical stage, pathological stage and histology.
  - Changed and updated data dictionaries.
  - Updated from 2-stage checkboxes (checked/unchecked) to 3 stage checkboxes (checked/unchecked/null).

### **Conclusions**

In collaboration with clinical investigators, research nurses, Pathology Core, and basic scientists, the Biostatistics and Data Management Core has continued to deliver biostatistics and data management support as proposed.

## **KEY RESEARCH ACCOMPLISHMENTS**

### **PROJECT 1**

- Identified KDR amplification as a marker and mechanism of chemoresistance.
- Identified differences in the downstream signaling promoted by specific KRAS mutants.
- Demonstrated fundamental differences in signaling underlying NSCLC and SCLC, revealing PARP1 and Chk1 as therapeutic targets in SCLC.
- Discovered an EMT signature that predicts resistance to erlotinib as well as PI3K and MEK inhibitors.
- Identified a 5-gene signature, including lipocalin-2 (LCN2) that predicts response to EGFR TKIs in patients with wild-type EGFR.

### **PROJECT 2**

- Collected extensive clinical follow-up data (including detailed data on relapse patterns) on 272 NSCLC patients who had previously undergone tumor resection.
- Performed extensive molecular analyses of these 272 tumor specimens, in collaboration with Project 3 and the Pathology Core, and have initiated statistical analyses and development of risk models
- Collected prospective fresh-frozen, FFPE tumor tissues and clinical follow-up data on 403 NSCLC patients who have undergone tumor resection.
- Identified CAIX, Nrf2 and Keap1 as independent prognostic factors.
- Correlated the platinum concentration found in patients who received neoadjuvant cisplatin or carboplatin regimens with tumor shrinkage.
- Performed exploratory nonlinear regression analysis of exponential decay in the patient survival curve, and have demonstrated that this approach is feasible and informative.

### **PROJECT 3**

- Identified that PSCA may play an important role in the development of NSCLC brain metastasis as a novel potential marker for NSCLC metastasis and therapeutic target for advanced lung tumors.
- Demonstrated that *KDR* CNGs were significantly associated with increased levels of nuclear HIF-1 $\alpha$  in both NSCLC tumor specimens and cell lines.
- Identified phosphorylated ORM-1 as a novel lung cancer serum biomarker that is significantly upregulated in lung cancer with tobacco-smoking history.
- Validated phosphor-ORM-1 protein expression in 80 lung cancer and control serum samples by ELISA and confirmed the significantly upregulated expression of serum phosphor-ORM-1 in late stage lung cancer patients with ever-smoking history.
- Identified the phosphor-ORM-1 protein as a critical ligand of nicotinic acetylcholine receptor (nAChR).
- Demonstrated that OMR-1 is a potential phosphorylation substrate of EGFR.

### **PROJECT 4**

- Continued to enroll patients to the clinical trial. Four additional patients are needed to complete the trial.
- Produced preliminary evidence to demonstrate that higher baseline levels of p-Src Tyr419 is predictive for improved PFS with dasatinib.

- Demonstrated that modulation of p-SrcTyr419 is a reasonable pharmacodynamic marker for dasatinib treatment.

## **PROJECT 5**

- Completed staining, image acquisition, and quantification of the seven biomarkers in the 89 pairs (84 pairs of T1 and T2 samples) of the NSCLC tissues and additional 34 matched NSCLC in a tissue microarray by both IHC and QD-IHF methods.
- Completed initial statistical analyses to correlate the seven biomarkers with clinical characteristics. Our analyses identified an association of several biomarkers with aggressive disease status, such as recurrence and metastasis.
- Established a new lung metastasis xenograft model to further understand the biology of CXCR4, E-cad, EGFR, and  $\beta$ -cat signaling pathways in progression and metastasis of lung cancer.

## **PATHOLOGY CORE**

- Collected prospective frozen tissue specimens from 121 NSCLC and 12 MPM cases with annotated clinical information.
- Maintained a NSCLC and MPM cell line repository, and managed the distribution of specimens for molecular profiling in collaboration with Projects 1 and 4.
- Distributed proteins and continued the distribution of nucleic acids (DNA and RNA) from large series of NSCLC and MPM tumor specimens with annotated clinicopathological information for molecular profiling.
- Expanded the mRNA availability of neoadjuvant-treated NSCLCs by extracting mRNA from 89 additional tumors.
- Developed a large cohort of tumor tissue specimens from lung adenocarcinoma arising in never-smoker patients and extracted nucleic acids and proteins for molecular profiling.
- Constructed a NSCLC tumor tissue TMA containing the 249 molecularly profiled (DNA, RNA, proteins) NSCLC tumors with annotated clinical information.
- Collected, processed, and analyzed over 350 MPM tumor tissue specimens from patients enrolled in the dasatinib clinical trial in collaboration with Project 4.
- Contributed to the publication and submission of 6 manuscripts and 6 abstract presentations in scientific meetings.

## **BIostatISTICS AND DATA MANAGEMENT CORE**

- Continued to provide biostatistics and bioinformatics support for the PROSPECT grant.
- Published collaborative papers from data collected in PROSPECT.
- Developed a secured, Web-based database application to assist the study conduct.
- Continued with the database maintenance, training and support as followed:
  - Provided data integrity checking and data correction.
  - Performed periodical database server maintenance and data backup.
  - Provided training and custom support to end users.
  - Cleaned and uploaded data from thoracic surgery database.
  - Added pathological stage field and a checklist in the follow-up page to specify if the recurrence is a local recurrence, second primary tumor or n/a.
  - Added comments for clinical stage, pathological stage and histology.
  - Changed and updated data dictionaries.

- Updated from 2-stage checkboxes (checked/unchecked) to 3 stage checkboxes (checked/unchecked/null).

## **REPORTABLE OUTCOMES**

### **Publications** (Attached in Appendix A)

Cascone T, Herynk MH, Xu L, Du Z, Kadara H, Nilsson MB, Oborn CJ, Park YY, Erez B, Jacoby JJ, Lee JS, Lin HY, Ciardiello F, Herbst RS, Langley RR, Heymach JV. Upregulated stromal EGFR and vascular remodeling in mouse xenograft models of angiogenesis inhibitor-resistant human lung adenocarcinoma. *Journal of Clinical Investigations*. 2011 Apr 1;121(4):1313-28. doi: 10.1172/JCI42405. PMID: 21436589.

Fujimoto J, Kong M, Lee JJ, Hong WK, Lotan R. Validation of a novel statistical model for assessing the synergy of combined-agent cancer chemoprevention. *Cancer Prev Res (Phila)*. 2010 Aug;3(8):917-28. PMID: 20663979.

Jeong Y, Xie Y, Xiao G, Behrens C, Girard L, Wistuba II, Minna JD, Mangelsdorf DJ. Nuclear receptor expression defines a set of prognostic biomarkers for lung cancer. *PLoS Medicine*. 2010 Dec 14;7(12):e1000378. PMCID: PMC3001894.

Nanjundan M, Byers LA, Carey MS, Siwak DR, Raso MG, Diao L, Wang J, Coombes KR, Roth JA, Mills GB, Wistuba II, Minna JD, Heymach JV. Proteomic profiling identifies pathways dysregulated in non-small cell lung cancer and an inverse association of AMPK and adhesion pathways with recurrence. *Journal of Thoracic Oncology*. 2010 Dec;5(12):1894-904. PMID: 21124077.

Pataer A, Raso MG, Correa AM, Behrens C, Tsuta K, Solis L, Fang B, Roth JA, Wistuba II, Swisher SG. Prognostic significance of RNA-dependent protein kinase on non-small cell lung cancer patients. *Clinical Cancer Research*. 2010 Nov 15;16(22):5522-8. PMCID: PMC3070287.

Stewart DJ. Tumor and host factors that may limit efficacy of chemotherapy in non-small cell and small cell lung cancer. *Critical Reviews in Oncology/ Hematology*. 2010 Sep;75(3):173-234. PMCID: PMC2888634.

Stewart DJ, Behrens C, Roth J, Wistuba II. Exponential decay nonlinear regression analysis of patient survival curves: preliminary assessment in non-small cell lung cancer. *Lung Cancer*. 2011 Feb;71(2):217-23. PMCID: PMC2962880.

Stewart DJ, Nunez M, Behrens C, Swisher S, Roth JA, Heymach J, Wistuba II. Factors associated with membrane carbonic anhydrase IX (mCAIX) immunohistochemistry (IHC) in non-small cell lung cancer (NSCLC). *Journal of Clinical Oncology*. 29: 2011 (suppl; abstr e21125).

Tsuta K, Kalhor N, Raso MG, Wistuba II, Moran CA. Oncocytic neuroendocrine tumors of the lung: histopathologic spectrum and immunohistochemical analysis of 15 cases. *Human Pathology*. 2011 Apr;42(4):578-85. PMID: 21329962.

Tsuta K, Raso MG, Kalhor N, Liu DD, Wistuba II, Moran CA. Histologic features of low- and intermediate-grade neuroendocrine carcinoma (typical and atypical carcinoid tumors) of the lung. *Lung Cancer*. 2011 Jan;71(1):34-41. PMID: 20462655.

Tsuta K, Raso MG, Kalhor N, Liu DC, Wistuba II, Moran CA. Sox10-positive sustentacular cells in neuroendocrine carcinoma of the lung. *Histopathology*. 2011 Jan;58(2):276-85. PMID: 21323953.



Wang J, Byers LA, Yordy JS, Liu W, Shen L, Baggerly KA, Giri U, Myers JN, Ang KK, Story MD, Girard L, Minna JD, Heymach JV, Coombes KR. Blasted cell line names. *Cancer Informatics*. 2010 Oct 14;9:251-5. PMCID: PMC2978931.

**Abstracts** (Attached in Appendix A)

Behrens C, Yuan P, Solis L, Saintigny P, Kadara H, Fujimoto J, Moran C, Swisher SG, Heymach JV, Wistuba II. EZH2 expression is an early event in the pathogenesis of non-small cell lung cancer (NSCLC) and correlates with tumor progression. AACR 102th Annual Meeting, 2011. Abstract# 3196.

Cascone T, Saigal B, Reynolds DM, Erez B, Jacoby J, Nilsson M, Lin HY, Herbst RS, Langley RR, Heymach JV. VEGF inhibitor resistance is associated with stromal EGFR activation and normalized revascularization in an orthotopic model of lung adenocarcinoma. AACR 102th Annual Meeting, 2011. Abstract# 3269.

Galindo HG, Suraokar M, Behrens C, Woods DM, Kalhor N, Aldape KD, Fujimoto J, Herbst RS, Erickson HS, Wistuba II. Identification of prostate stem cell antigen (PSCA) as a potential marker for lung cancer brain metastasis. AACR 102th Annual Meeting, 2011. Abstract# 5166.

Heymach JV, Saintigny P, Kim ES, Byers LA, Lee JJ, Coombes K, Diao L, Wang J, Tran H, Fan YH, Tsao A, Blumenschein Jr GR, Papadimitrakopoulou VA, Tang X, Story M, Xie Y, Girard L, Weinstein J, Mao L, Minna JD, Herbst RS, Lippman SM, Hong WK, Wistuba II. Gene expression signatures predictive of clinical outcome and tumor mutations in refractory NSCLC patients (pts) in the BATTLE trial (Biomarker-integrated Approaches of Targeted Therapy for Lung Cancer Elimination). AACR 102th Annual Meeting, 2011. Abstract# LB-88.

Ihle NT, Herbst RS, Kim ES, Wistuba II, Lee JJ, Blumenschein Jr. GR, Tsao AS, Chen L, Zhang S, Alden CM, Tang X, Liu S, Stewart DJ, Papadimitrakopoulou V, Heymach JV, Tran HT, Hicks ME, Erasmus JJ, Gupta S, Minna JD, Larsen J, Lippman SM, Hong WK, Powis G. Specific forms of mutant KRAS predict patient benefit from targeted therapy in the BATTLE-1 clinical trial in advanced non-small cell lung cancer. AACR 102th Annual Meeting, 2011. Abstract# 955.

Nunez MI, Behrens C, Woods DM, Lin H, Suraokar M, Girard L, Minna J, Lee J, Hofstetter W, Franklin W, Moran CA, Hong WK, Stewart DJ, Wistuba II. High Expression of Folate Receptor Alpha in Lung Cancer Correlates with Adenocarcinoma Histology and EGFR Mutation. United States and Canadian Academy of Pathology 100<sup>th</sup> Annual Meeting 2011. Abstract # 1788.

Nunez MI, Suraokar M, Behrens C, Woods DM, Lin H, Lee J, Mehran RJ, Franklin W, Tsao A, Wistuba II. Folate pathway in malignant pleural mesothelioma (MPM): Novel therapeutic opportunities due to folate receptor alpha overexpression. AACR 102th Annual Meeting, 2011. Abstract# 4121.

Riquelme EM, Suraokar MB, Nunez MI, Gazdar AF, Byers LA, Heymach JV, Mehran RJ, Tsao A, Wistuba II. CNG c-myc in mesothelioma. AACR 102th Annual Meeting, 2011. Abstract# 4031.

Saigal B, Herynk MH, Cascone T, Nilsson M, Khajavi M, Saintigny P, Heymach JV. Estrogen contributes to bevacizumab resistance in xenograft models of non-small cell lung cancer (NSCLC). AACR 102th Annual Meeting, 2011. Abstract# 3273.

Saintigny P, Diao L, Wang J, Girard L, Lin SH, Coombes KR, Liu S, Lee JJ, Weinstein JN, Xie Y, Fan YH, Tang XM, Kim ES, Herbst RS, Tsao A, Blumenschein GR, Mao L, Lippman SM, Minna JD, Hong WK, Wistuba II, Heymach JV. A 5-gene signature (sig) predicts clinical benefit from erlotinib in non-small cell lung cancer (NSCLC) patients (pts) harboring wild-type (wt) EGFR & KRAS. AACR 102th Annual Meeting, 2011. Abstract# 4109.

Wang D, Amin ARM, Peng S, Sangvi C, Shin DM, Eichler JF, Chen ZG, Study of 2, 9-Disecbutyl-1, 10-Phenanthroline as A Novel Anticancer Agent. AACR 102th Annual Meeting, 2011. Abstract# 678.

## **CONCLUSIONS**

**PROJECT 1:** We have made substantial progress towards the overall goals of this project to systematically investigate signaling pathways and potential therapeutic targets using NSCLC cell lines and tumors; and, by correlating these molecular profiles with drug sensitivity phenotypes, to develop markers for predicting response and resistance and to develop strategies for overcoming resistance. We will continue to investigate these findings during the unfunded extension, and we will have a complete report on the identification of candidate therapeutic targets in chemotherapy-resistant cell lines at that time.

**PROJECT 2:** Sample collection was completed on schedule with more specimens obtained than proposed in our initial application. We anticipate that the completed analyses from this project will have a major impact on our understanding of tumor molecular factors that influence risk of recurrence and patterns of relapse. These analyses will be completed over the next requested period of an unfunded grant extension.

**PROJECT 3:** During the past year, we analyzed the molecular profiling data of NSCLC and MPM tissue specimens with annotated clinical information in Aim 1 and we identified a panel of microRNAs associated to the outcome of NSCLC patients treated with and without adjuvant chemotherapy. Using our results, we designed a strategy for gene (mRNA), microRNA, and protein signature validation using high-throughput qNPA™, Fluidigm™ microfluidic quantitative dynamic array, and IHC methodologies. We also identified a series of molecular pathways and markers, using gene profiling, as potential novel targets in malignant pleural mesothelioma (MPM) in collaboration with Project 4. In Aim 2, we completed the analysis of the molecular profiling data of surgically resected NSCLC specimens obtained from patients who have received neoadjuvant chemotherapy. We identified Phospho-ORM-1 peptide as a novel NACHR-associated protein in lung cancer pathogenesis and smoking-associated carcinogenesis and as a potential serum marker and target for lung cancer detection and treatment in Aim 3. We will continue to analyze this data during the next unfunded research period.

**PROJECT 4:** There is preliminary evidence that a subgroup of MPM patients gain clinical benefit from dasatinib therapy and that baseline p-Src Tyr419 levels in MPM tumor tissue may be predictive of TTP. This report details the first targeted therapy neoadjuvant trial to potentially identify a predictive biomarker in MPM. The novel clinical trial approach is feasible and has the potential to advance the field of MPM in personalized medicine.

**PROJECT 5:** In the past year, we completed the immunostaining of a total of seven biomarkers, EGFR, E-cad,  $\beta$ -cat, CXCR4, SDF-1, p-AKT, and p-ERK in two sets of NSCLC tissues, including 89 pairs of patient tissue samples from our institution and 34 paired samples in a tissue microarray. Quantification and initial statistical analyses of all seven biomarkers have been completed. We found that quantification of the QD-IHF with the normalized co-values may reduce the quantification error resulting from variations of quality of the FFPE tissues or staining agents that may affect intensity of the IHF signals. Using this method, our data indicated that  $\beta$ -cat and its interaction with EGFR and/or E-cad may play a role in recurrence and metastasis of NSCLC, which was not observed using conventional IHC. We believe that quantification of conventional IHC is subjective and results are less informative regarding possible interactions between protein markers. The further study of the biology behind the observed results from the multiplexed QD-IHF signals will continue in the next project period. We will also try to obtain tissues from patients treated with EGFR-targeting agents to move this project forward towards

the identification of optimal biomarker combinations better predict which patients may be resistant to EGFR-targeting therapy.

**PATHOLOGY CORE:** During the fourth grant year, the PROSPECT Pathology Core continued the successful prospectively collection of frozen tissue specimens from 165 NSCLC and 12 MPM surgically resected tumors. The Pathology Core has played an important role in the processing of NSCLC and MPM tissue and cell line specimens for comprehensive molecular profiling, and in the characterization of tissue specimens on the expression of protein expression by immunohistochemistry. Additionally, the Pathology Core has developed and processed tissue for molecular profiling from two important cohorts of NSCLC patients, neoadjuvant-treated tumors and lung adenocarcinoma in never smokers.

**BIostatISTICS AND DATA MANAGEMENT CORE:** In collaboration with clinical investigators, research nurses, Pathology Core, and basic scientists, the Biostatistics and Data Management Core has continued to deliver biostatistics and data management support as proposed.

## **APPENDIX A**

### **Abstracts and Publications**

## **APPENDIX B**

### **Biostatistics Workflow and Database Overview**





# Upregulated stromal EGFR and vascular remodeling in mouse xenograft models of angiogenesis inhibitor-resistant human lung adenocarcinoma

Tina Cascone,<sup>1,2</sup> Matthew H. Herynk,<sup>1</sup> Li Xu,<sup>1</sup> Zhiqiang Du,<sup>1</sup> Humam Kadara,<sup>1</sup> Monique B. Nilsson,<sup>1</sup> Carol J. Oborn,<sup>3</sup> Yun-Yong Park,<sup>4</sup> Baruch Erez,<sup>1</sup> Jörg J. Jacoby,<sup>1</sup> Ju-Seog Lee,<sup>4</sup> Heather Y. Lin,<sup>5</sup> Fortunato Ciardiello,<sup>2</sup> Roy S. Herbst,<sup>1</sup> Robert R. Langley,<sup>3</sup> and John V. Heymach<sup>1,5</sup>

<sup>1</sup>Department of Thoracic/Head and Neck Medical Oncology, University of Texas M.D. Anderson Cancer Center, Houston, Texas, USA.

<sup>2</sup>Division of Medical Oncology, "F. Magrassi — A. Lanzara" Department of Clinical and Experimental Medicine, Second University of Naples, Naples, Italy.

<sup>3</sup>Department of Cancer Biology, <sup>4</sup>Department of Systems Biology, and <sup>5</sup>Department of Biostatistics, University of Texas M.D. Anderson Cancer Center, Houston, Texas, USA.

**Angiogenesis is critical for tumor growth and metastasis, and several inhibitors of angiogenesis are currently in clinical use for the treatment of cancer. However, not all patients benefit from antiangiogenic therapy, and those tumors that initially respond to treatment ultimately become resistant. The mechanisms underlying this, and the relative contributions of tumor cells and stroma to resistance, are not completely understood. Here, using species-specific profiling of mouse xenograft models of human lung adenocarcinoma, we have shown that gene expression changes associated with acquired resistance to the VEGF inhibitor bevacizumab occurred predominantly in stromal and not tumor cells. In particular, components of the EGFR and FGFR pathways were upregulated in stroma, but not in tumor cells. Increased activated EGFR was detected on pericytes of xenografts that acquired resistance and on endothelium of tumors with relative primary resistance. Acquired resistance was associated with a pattern of pericyte-covered, normalized revascularization, whereas tortuous, uncovered vessels were observed in relative primary resistance. Importantly, dual targeting of the VEGF and EGFR pathways reduced pericyte coverage and increased progression-free survival. These findings demonstrated that alterations in tumor stromal pathways, including the EGFR and FGFR pathways, are associated with, and may contribute to, resistance to VEGF inhibitors and that targeting these pathways may improve therapeutic efficacy. Understanding stromal signaling may be critical for developing biomarkers for angiogenesis inhibitors and improving combination regimens.**

## Introduction

Tumor growth and metastasis are dependent on the formation of a vascular supply, i.e., angiogenesis (1–3). Most therapeutic efforts directed toward inhibiting the angiogenic process for the treatment of cancer have focused on the VEGF pathway (4–8). The majority of the mitogenic, angiogenic, and permeability-enhancing properties of VEGF are mediated by VEGF receptor-2 (VEGFR2) (8). Several inhibitors of this pathway have received FDA approval and are currently in clinical use; these include bevacizumab (BV; Avastin; Genentech), a monoclonal antibody that blocks human VEGF (9, 10), and small-molecule inhibitors of the VEGFR2 tyrosine kinase (e.g., sorafenib, sunitinib, and pazopanib) (11). The results from phase III clinical trials demonstrated that the addition of BV to standard therapy prolongs progression-free survival (PFS) and/or overall survival, and improves objective tumor responses, in patients with advanced malignancies including non-small-cell lung cancer (NSCLC) and colon cancer (12, 13). However, not all patients benefit from antiangiogenic therapy, and those tumors that initially respond to treatment

will ultimately become refractory and relapse (14, 15). Therefore, the development of more durable cancer therapies requires an improved understanding of the cellular and molecular mechanisms that mediate resistance to antiangiogenic agents.

Recent studies suggest that blockade of the VEGFR2 signaling pathway may prompt some tumors to increase their expression of secondary molecules in order to sustain the neovascularization response (16). Casanovas et al. reported that although anti-VEGFR therapy initially blocks new blood vessel formation and tumor growth in a transgenic model of pancreatic islet cell tumors, both angiogenesis and tumor progression are eventually restored by the increased synthesis of other angiogenic factors from tumor cells (17). There is also evidence suggesting that commonly occurring genetic alterations in tumor cells may uncouple tumor dependency on a vascular blood supply. For example, loss of *p53* enhances the ability of tumor cells to withstand hypoxic conditions (18), which renders *p53*-deficient tumors to be at least partially resistant to antiangiogenic therapy (19). Other tumor cells have been shown to alter their pattern of growth when challenged with antiangiogenic therapy. Instead of recruiting resident ECs to form new vascular networks, these tumor cells meet their metabolic requirements by residing in close proximity to preexisting blood vessels (20). Incomplete target inhibition after treatment with VEGFR antago-

**Conflict of interest:** J.V. Heymach and R.S. Herbst have served on advisory boards for Genentech and AstraZeneca and receive research support from AstraZeneca.

**Citation for this article:** *J Clin Invest.* 2011;121(4):1313–1328. doi:10.1172/JCI42405.



nists has been described in orthotopic models of pancreatic cancer, as well as in patients with this type of cancer and with advanced soft tissue sarcomas (21, 22).

Emerging evidence suggests that stromal cells may also play an important role in mediating resistance to antiangiogenic therapies. Shojaei et al. reported that localization of Gr-1<sup>+</sup>CD11b<sup>+</sup> myeloid cells to various murine tumors rendered the neoplasms refractory to anti-VEGF therapy (23). Myeloid cells provide a rich reserve of angiogenic molecules and possess potent immunosuppressive activity (24), both of which favor tumor progression. Similarly, a recent study evaluating the effects of a neutralizing VEGF antibody in murine lymphoma models demonstrated that tumor-associated fibroblasts upregulate expression of PDGF-C when the VEGFR pathway is blocked, ensuring the continued formation of tumor blood vessels when signaling through this pathway is prohibited (25). Together, these studies provide evidence that both tumor cells and stromal cells contribute to VEGF inhibitor resistance, although their respective contributions remain incompletely characterized and are likely to vary based on molecular features of the tumor and its microenvironment.

We hypothesized that there may be additional stromal and tumor cell mechanisms that contribute to the resistant phenotype. To assess this question, we investigated 3 different models with varying de novo responsiveness to BV. In order to discriminate between tumor (human) and stromal (mouse) genes that may be associated with acquired resistance to BV, we performed species-specific gene expression profiling using vehicle-treated (controls) and BV-resistant xenografts. This approach demonstrated that gene expression changes associated with resistance occurred primarily in stromal cells, highlighted different modes of vascular remodeling that may accompany the emergence of resistance, and led to the identification of what we believe to be a previously unrecognized mechanism for acquired resistance to BV involving upregulation of EGFR signaling in vascular pericytes.

## Results

**NSCLC xenografts exhibit different patterns of resistance to BV.** To investigate the mechanisms by which NSCLC xenografts develop resistance to VEGF blockade, we initially injected male nude mice with either H1975 or A549 human NSCLC adenocarcinoma cells. These models were selected because in prior studies, we observed that A549 xenograft tumors were relatively insensitive to VEGF inhibitors de novo (relative primary resistance), whereas H1975 tumors were more initially responsive to these agents, experiencing significant tumor volume reduction typically lasting more than 1 month (26). Furthermore, the tumor cells contain 2 common alterations associated with EGFR tyrosine kinase inhibitor (TKI) resistance: a T790M EGFR mutation (H1975 model; ref. 27) and a KRas mutation (A549 model; ref. 28). Approximately 3 weeks after tumor cell injection, mice bearing tumors with a mean volume of approximately 270 mm<sup>3</sup> were randomized to receive either vehicle control or BV (see Methods). Animals were treated for 2 weeks (short-term treatment) or until they were euthanized due to tumor burden. Tumors were considered to be resistant when they tripled in volume (i.e., tumor progression) compared with the pretreatment tumor size, and PFS was measured as the time from initiation of treatment until tumor progression. In H1975 tumors, as assessed by tumor volume change ratio ( $\Delta T/\Delta C$ ; see Methods), short-term treatment with BV inhibited tumor growth by 77% compared with vehicle-treated control tumors ( $\Delta T/\Delta C$  23.1%;  $P = 0.015$ , Mann

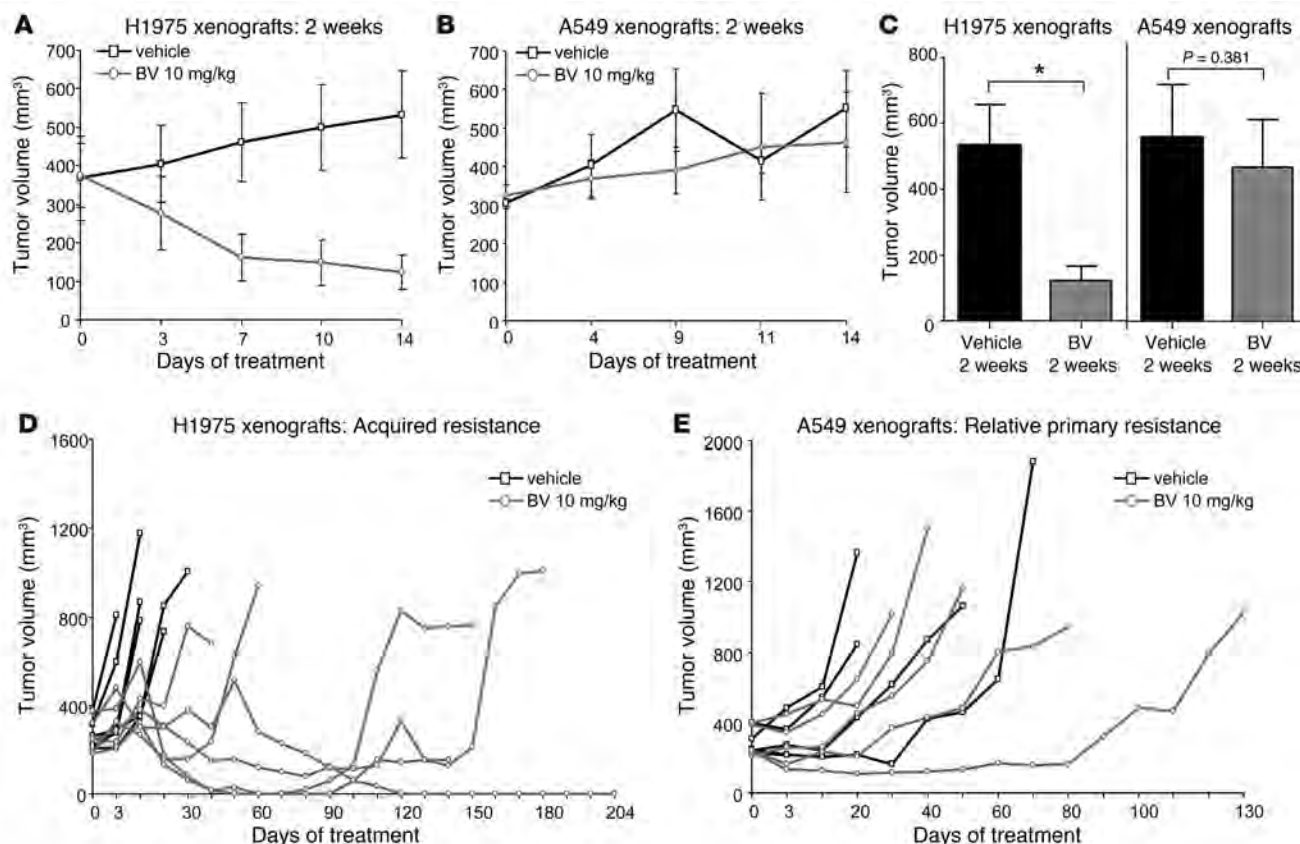
Whitney test; Figure 1, A and C). In A549 xenografts, in contrast, a nonsignificant 16% reduction in tumor growth was observed ( $\Delta T/\Delta C$  83.8%;  $P = 0.381$ , Mann Whitney test; Figure 1, B and C). The individual tumor growth curves shown in Figure 1, D and E, illustrate the growth kinetics of H1975 and A549 xenografts treated with vehicle or BV for a longer period until progression. All H1975 control xenografts progressed within 31 days of treatment onset, with median PFS of 6 days. In contrast, 67% of xenografts (4 of 6) receiving BV developed resistance, and the median PFS was 138 days ( $P = 0.0007$ , log-rank test; Figure 1D). A549 tumors were less responsive to BV and had a median PFS of 40 days compared with 29.5 days in control tumors ( $P = 0.390$ , log-rank test; Figure 1E). These results showed that H1975 tumors were initially responsive to BV therapy, but eventually acquired resistance after prolonged treatment with the drug, whereas A549 tumors demonstrated relative primary resistance to BV.

**Acquired resistance to BV is associated with sustained inhibition of VEGFR2 activation and reduced endothelial apoptosis.** To determine whether acquired resistance to BV is the result of increased VEGFR2 signaling, potentially through increased expression of murine VEGF or another mechanism to bypass blockade of human VEGF by this agent, we evaluated the phosphorylation status of VEGFR2 in control-treated (vehicle progression), BV-sensitive (2 weeks BV treatment), and BV-resistant (BV progression) tumors using immunofluorescence (IF) staining. In control tumors, phosphorylated VEGFR2 (p-VEGFR2) was readily detected on CD31<sup>+</sup> tumor-associated ECs. However, no p-VEGFR2 was detected on the vasculature of BV-sensitive tumors or the BV progression group (Supplemental Figure 1A; supplemental material available online with this article; doi:10.1172/JCI42405DS1). To evaluate changes in stromal (defined here as nontumor cells derived from the host) and tumor-derived VEGF in H1975 BV-resistant tumors, we quantified mouse *Vegfa* and human *VEGFA* mRNA expression by quantitative real-time PCR (qRT-PCR). We observed no change in mouse *Vegfa* mRNA expression in resistant xenografts, whereas human *VEGFA* mRNA levels were increased in resistant tumors, compared with controls ( $P < 0.05$ ; Supplemental Figure 1B). Despite the increase in VEGF ligand, however, VEGFR2 phosphorylation remained suppressed in BV-resistant tumors.

We then assessed whether the acquisition of resistance was associated with changes in endothelial apoptosis. We performed double IF staining for CD31<sup>+</sup> and TUNEL<sup>+</sup> cells in H1975 tumors following short-term BV treatment and BV progression and determined the percentage of apoptotic ECs (CD31<sup>+</sup>TUNEL<sup>+</sup>; Supplemental Figure 1, C and D). The percentage of apoptotic ECs significantly increased following 2 weeks of BV treatment compared with control xenografts ( $P < 0.05$ ). However, at the time of progression, EC apoptosis diminished significantly ( $P < 0.05$  versus short-term BV), to levels comparable to those of vehicle-treated tumors. Thus, EC apoptosis increased while tumors were initially responding to VEGF signaling blockade and returned to levels comparable to those of controls in tumors that acquired BV resistance.

In the same tumors, we also quantified the percentage of total apoptotic cells using laser scanning cytometry (LSC; data not shown). Tumors sensitive to BV showed an increased percentage of total TUNEL<sup>+</sup> cells compared with controls (2 weeks vehicle treatment), whereas no significant changes were observed in BV-resistant tumors compared with controls (vehicle progression).

**Stromal and tumor cell gene expression changes in H1975 BV-resistant xenografts.** To identify changes in stromal and tumor gene expres-



**Figure 1**

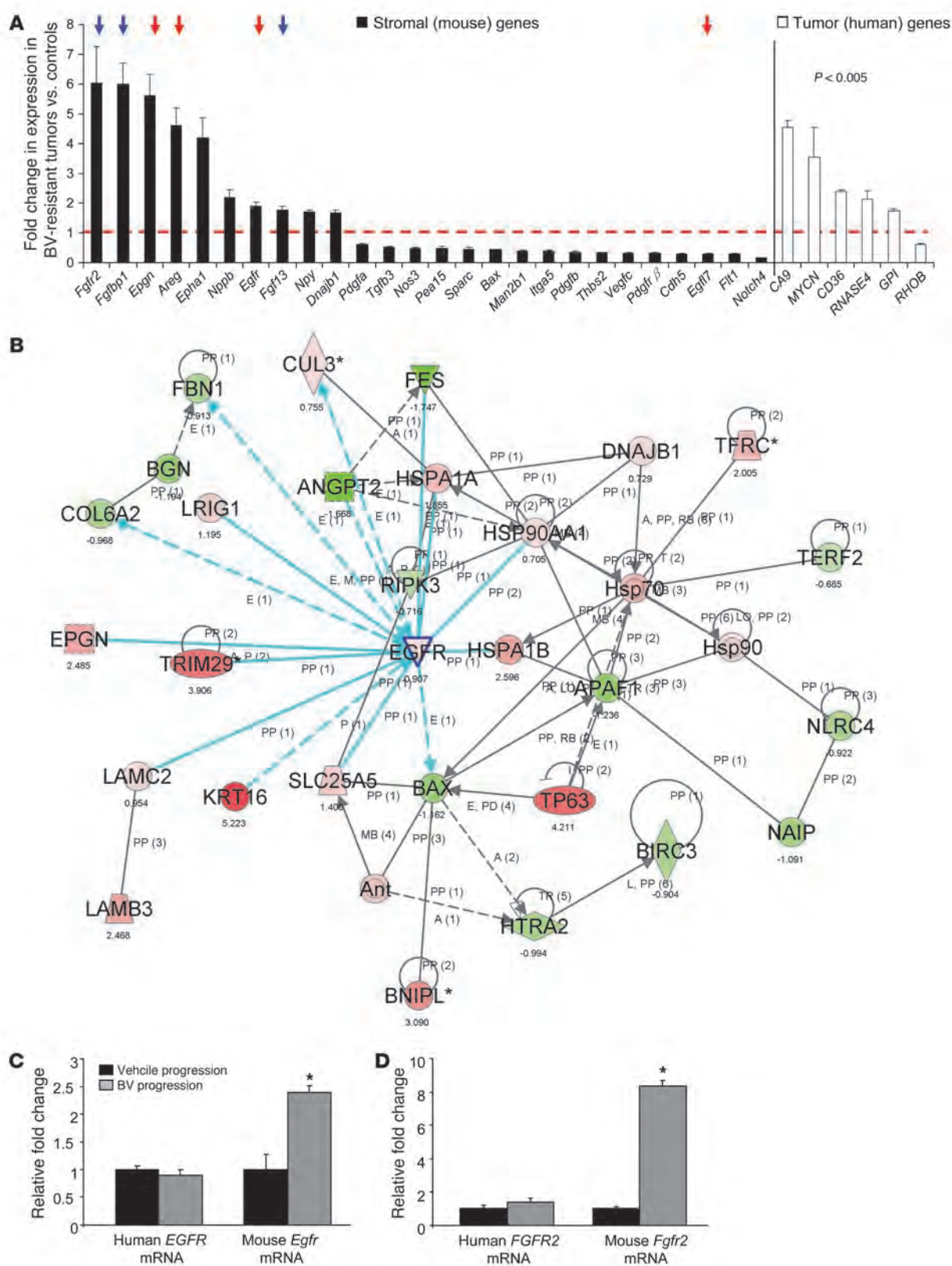
H1975 and A549 NSCLC xenografts show different patterns of resistance to BV treatment. (**A** and **B**) Tumor growth curves of H1975 (**A**;  $n = 5$  per group) and A549 (**B**;  $n = 6$  per group) xenografts receiving vehicle (control) and BV for 2 weeks. (**C**) Mean tumor volume obtained at the last measurement in H1975 and A549 xenografts treated with BV for 2 weeks compared with controls ( $\Delta T/\Delta C$ ).  $*P < 0.05$ , Mann-Whitney test. (**D** and **E**) Individual tumor growth curves of H1975 (**D**;  $n = 6$  per group) and A549 (**E**;  $n = 5$  per group) xenografts treated with vehicle and BV until animals became moribund. Tumors were considered resistant (progression) when tripled in volume compared with the beginning of the treatment.

sion associated with acquired resistance to anti-VEGF therapy, we performed RNA microarray analyses comparing H1975 control and BV-resistant xenografts ( $n = 3$  per group) using Illumina mouse-specific (WG-6 v2) and human-specific (WG-6 v3) expression arrays. Probes in these arrays have been designed to minimize cross-species reactivity; consistent with this, essentially no cross-reactivity was observed in experiments mixing human and mouse cell lines (E.S. Park, unpublished observations). We found that a much larger number of stromal mouse genes were significantly modulated in BV progression versus control vehicle progression xenografts compared with human tumor genes (1,385 stromal genes versus 98 tumor genes), according to the statistical criteria described in Methods. We observed significant changes in the expression of genes involved in angiogenesis, lymphangiogenesis, and hypoxia signaling pathway between BV-resistant and control xenografts. Both *Egfr* and *Fgfr2* genes were upregulated in the stromal compartment, but not in tumor cells, of H1975 BV-resistant tumors compared with controls, as well as stromal molecules and ligands associated with these signaling pathways (e.g., *Epgn*, *Areg*, *Fgf13*, and *Fgfbp1*; Figure 2A and Supplemental Table 1). Among human angiogenic or hypoxia-regulated genes, carbonic anhydrase IX (CA9) was significantly upregulated in BV-resistant tumors (Figure 2A and Supplemental Table 2).

We next sought to identify pathways potentially important in the acquired resistance phenotype. Functional gene-interaction network analyses of gene features differentially expressed between the mouse stroma of BV-resistant and vehicle-treated H1975 xenografts, using Ingenuity Pathway Analysis, revealed significant modulation in the predicted function of a gene neighborhood and interaction network surrounding *Egfr*, based on the number of focus genes and nodes of interaction ( $P < 0.001$ ; Figure 2B). In addition, the modulated gene network associated with *Egfr* expression included downregulated proapoptotic genes, such as the Bcl-2 family member protein *Bax* and apoptotic peptidase activating factor 1 (*Apaf1*). Genes with prosurvival functions, such as the heat shock protein *Dnaib1*, were upregulated.

Next, to validate the changes in expression of the significantly modulated network-hub gene *Egfr*, we assessed the human and mouse mRNA levels using qRT-PCR. Consistent with the microarray data, we observed a 2.5-fold increase in mouse *Egfr* mRNA levels in H1975 BV-resistant xenografts compared with controls ( $P < 0.05$ ; Figure 2C). Human *EGFR* mRNA levels were not significantly different than those of controls. We also validated the stromal expression of *Fgfr2*, which we noted to be upregulated in BV-resistant H1975 tumors in the microarray analysis. A significant increase in mouse *Fgfr2*, but not human *FGFR2*, mRNA







## Figure 2

BV resistance is associated with increased expression of stromal genes involved in angiogenesis. **(A)** Stromal and human angiogenic genes were differentially regulated in H1975 BV-resistant xenografts compared with vehicle controls ( $n = 3$  per group).  $P < 0.005$ , 2-sample  $t$  test with random variance model. Exact permutation  $P$  values for significant genes were computed based on 10 available permutations. Data represent differences in fold change of genes in BV-resistant tumors versus controls. The dashed red line indicates fold change 1 (i.e., no change versus controls). Red and blue arrows indicate *Egfr* and *Fgfr* family member genes, respectively. **(B)** Functional pathway analysis of selected genes and their interaction nodes in a gene network significantly modulated between the BV-resistant and control xenograft mouse stroma. Network score was calculated by the inverse log of the  $P$  value and indicates the likelihood of focus genes in a network being found together not by chance. The selected genes (*Egfr*, *Bax*, and *Dnajb1*) and their interaction segments are highlighted by a blue border. Gene expression variation by at least 1.5-fold is indicated by color (red, upregulated; green, downregulated; gray, NS). **(C and D)** qRT-PCR showing human *EGFR* and mouse *Egfr* **(C)** and human *FGFR2* and mouse *Fgfr2* **(D)** mRNA expression in H1975 xenografts that progressed on vehicle and BV treatments ( $n = 4$  per group). Data are normalized relative to vehicle progression samples and shown as relative fold change. \* $P < 0.05$ ,  $t$  test.

expression was observed in H1975 BV-resistant xenografts compared with controls ( $P < 0.05$ ; Figure 2D).

*EGFR is activated on stromal cells of H1975 and A549 BV-resistant tumors.* Given our observation that mouse *Egfr* mRNA was increased in BV-resistant tumors, we next evaluated EGFR protein expression in H1975 tumors by IF staining using antibodies directed against CD31 and EGFR (Supplemental Figure 2A). Quantification of EGFR staining by LSC analysis revealed that prolonged administration of BV produced a nearly 10-fold increase in the number of EGFR-expressing cells in H1975 BV-resistant tumors compared with control tumors ( $P < 0.01$ ; Figure 3A and Supplemental Figure 2A). We also evaluated EGF ligand by immunohistochemistry (IHC) in H1975 vehicle- and BV-treated xenografts at progression and observed increased levels of EGF immunoreactivity in resistant tumors compared with controls (Supplemental Figure 2B).

We next examined the activation status of EGFR in H1975 and A549 xenografts after treatment with vehicle and BV at progression. Confocal microscopy was used to analyze specimens stained with antibodies directed against CD31 and p-EGFR. As shown in Figure 3B, BV resistance was associated with a marked difference in p-EGFR expression in both H1975 and A549 tumors compared with controls; however, notable differences in the staining pattern were observed between the 2 xenograft models. In the H1975 model, p-EGFR expression was significantly increased on the vascular supporting cells (VSCs) of resistant tumors compared with controls ( $P < 0.001$ ), whereas in A549 BV-resistant xenografts, p-EGFR expression was significantly increased on tumor-associated ECs compared with controls ( $P < 0.05$ ; Figure 3C, right).

To identify the population of VSCs expressing p-EGFR in H1975 BV-resistant tumors, we performed IF staining using antibodies directed against p-EGFR and desmin, a marker for pericytes (Figure 3D). This analysis revealed that the VSCs of H1975 BV-resistant tumors coexpressed p-EGFR and desmin. In addition, the number of pericytes expressing p-EGFR was 8-fold greater in H1975 BV-resistant tumors than in control tumors ( $P < 0.01$ ; Figure 3E). Taken together, our results suggest that upregulation

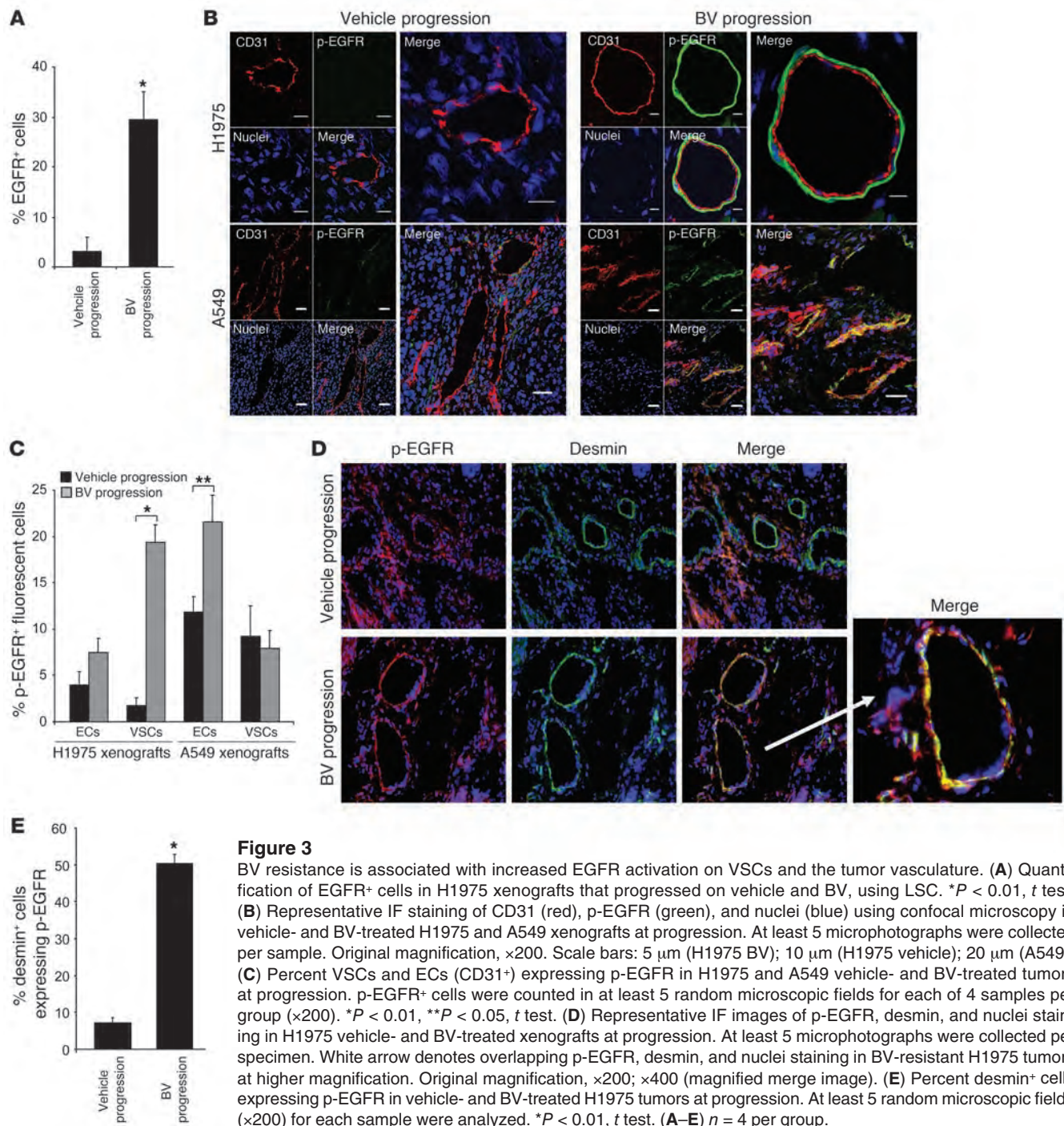
and activation of stromal EGFR is a characteristic feature of BV-resistant tumors in these models and that multiple stromal cell types can express EGFR.

*Increased expression of basic FGF and FGFR2 in H1975 xenografts resistant to BV therapy.* Based on our observation that mouse *Fgfr2* gene expression was increased in the stromal compartment of BV-resistant H1975 tumors, we performed colocalization studies (IF) on H1975 tumors that progressed while receiving vehicle and BV, using antibodies against CD31 and FGFR2 (Figure 4A). We observed a significant increase in FGFR2 protein expression levels in resistant tumors compared with controls ( $P < 0.001$ ; Figure 4B). Furthermore, to assess changes in the FGFR2 ligand, we next measured the plasma concentration of mouse basic FGF (bFGF). We found a 1.5-fold increase in the level of circulating bFGF in BV-resistant tumors compared with controls ( $P = 0.025$ ; Figure 4C). Consistent with these findings, IHC analysis of H1975 control- and BV-treated xenografts at progression demonstrated increased protein expression of bFGF in BV-resistant tumors compared with controls (Figure 4D).

*Resistance to BV is associated with tumor revascularization and morphological changes in the vasculature.* Because the primary mechanism of action of BV is directed against blood vessels, we quantified the microvessel density (MVD) of H1975 and A549 xenografts. We initially assessed changes in the vasculature after short-term treatment. There was a 3-fold MVD reduction in initially sensitive H1975 tumors treated with BV for 2 weeks compared with controls ( $P < 0.01$ ; Figure 5, A and B). Vessel density (as an indicator of relative primary resistance) of A549 tumors treated for 2 weeks did not show significant changes compared with controls. To determine whether the vascular effects observed after 2 weeks of BV therapy persisted in tumors receiving long-term BV treatment, we quantified the MVD in BV-resistant H1975 and A549 tumors (Figure 5, A and B). We found that relative primary and acquired resistance were associated with distinct patterns of tumor vascularization. In H1975 BV-treated xenografts, MVD was significantly higher at progression compared with 2 weeks of treatment ( $P < 0.01$ ), then returned to levels comparable to those of vehicle-treated controls. In A549 BV-resistant xenografts, MVD significantly increased compared with A549 vehicle-treated controls ( $P < 0.05$ ). These data suggest that BV therapy has a marked initial antiangiogenic effect on sensitive H1975 xenografts, but the effect is lost after continued exposure to the drug, and that therapeutic resistance is associated with revascularization at levels comparable with or higher than those in vehicle-treated controls.

Previous studies have demonstrated that antiangiogenic therapy can alter the morphology of the tumor-associated vasculature (29–32). To evaluate the tumor vascularization in greater detail, we measured the vascular tortuosity in vehicle and BV-treated H1975 and A549 xenografts. Short-term administration of BV led to a modest, but not statistically significant, reduction in the vessel tortuosity of H1975 tumors (Figure 5, A and C). However, as these tumors developed BV resistance, we noted a 4-fold reduction in vascular tortuosity compared with controls ( $P < 0.01$ ). These blood vessels were also characterized by large-diameter lumens and a greater degree of pericyte coverage (referred to herein as normalized revascularization). In contrast, in A549 xenografts with relative primary resistance to BV, tumor vascularization was associated with smaller, more tortuous vessels with reduced pericyte coverage compared with controls (referred to herein as sprouting vascularization;  $P < 0.05$ ; Figure 5, A and C). Thus, in these mod-



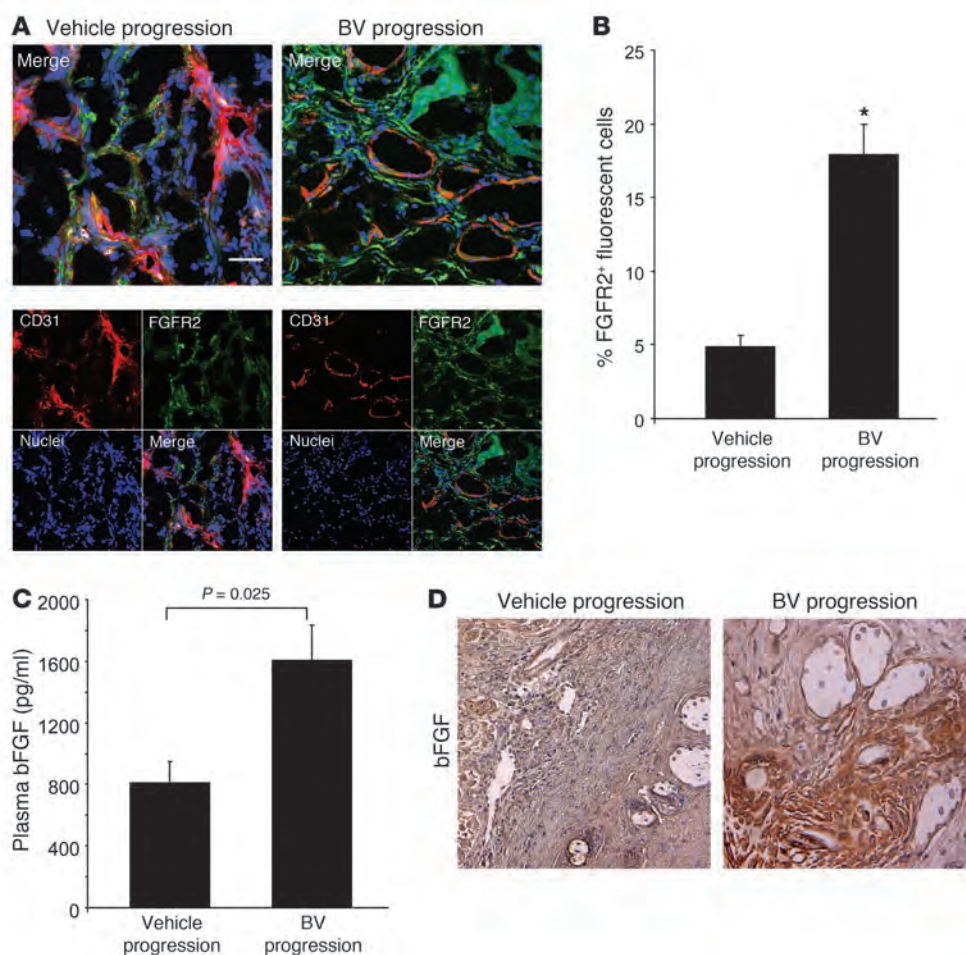


els, acquired resistance and relative primary resistance to BV were associated with distinct patterns of vascular remodeling.

**Dual blockade of EGFR and VEGFR2 signaling pathways delays tumor growth of NSCLC xenografts.** To elucidate whether targeting functioning stromal signaling pathways in BV-resistant tumors abrogates therapeutic resistance, we targeted EGFR using either the EGFR TKI erlotinib in combination with BV, or the dual VEGFR/EGFR inhibitor vandetanib. Both A549 and H1975 tumor cells are known to be resistant to erlotinib and vandetanib in vitro, which is thought to be caused by the presence of a KRas mutation and a

secondary EGFR mutation (T790M), respectively (26–28). Consistent with previous results, erlotinib did not inhibit H1975 tumor growth compared with vehicle, as 5 of 6 xenografts progressed, with a median PFS of 12.5 days ( $P = 0.33$ , erlotinib versus vehicle; Figure 6A). Erlotinib and BV treatment in combination (referred to herein as erlotinib+BV) resulted in prolonged PFS; only 1 of 6 tumors progressed at the end of more than 200 days (median PFS not reached;  $P = 0.0009$ , erlotinib+BV versus vehicle;  $P = 0.19$ , erlotinib+BV versus BV; Figure 6, A and B), although after more than 140 days of treatment, 3 mice died of causes unrelated to



**Figure 4**

Increase in stromal FGFR2 expression in H1975 BV-resistant xenografts. **(A)** Representative IF images of CD31 and FGFR2 staining in H1975 vehicle- and BV-treated H1975 xenografts at progression, using confocal microscopy. At least 5 microphotographs were collected from 4 specimens per group. Original magnification,  $\times 200$ . Scale bar: 20  $\mu\text{m}$ . **(B)** Percent FGFR2<sup>+</sup> fluorescent cells counted in 5 random microscopic fields ( $\times 200$ ) per sample ( $n = 4$  per group).  $*P < 0.001$ ,  $t$  test. **(C)** bFGF levels were measured in plasma of vehicle- and BV-treated H1975 xenografts at progression, using multiplex bead assay ( $n = 4$  per group; each sample tested in duplicate).  $P$  value was calculated using  $t$  test. **(D)** Representative IHC images showing bFGF protein expression in vehicle- and BV-treated H1975 xenografts. At least 5 random microscopic fields were collected from each of 4 specimens per group. Original magnification,  $\times 200$ .

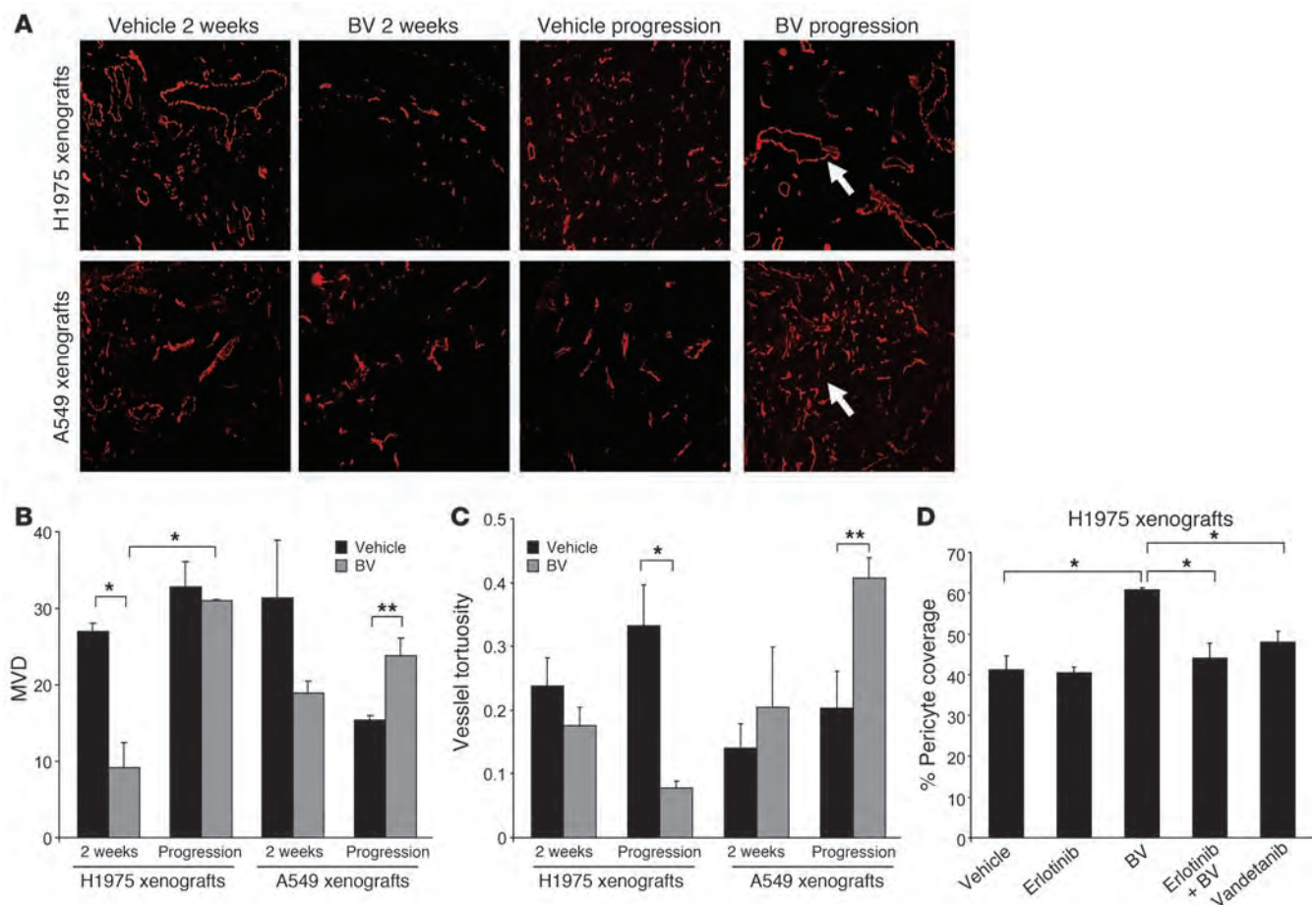
tumor growth. Vandetanib treatment inhibited tumor growth in all tumors, and only 2 of 6 progressed after response, displaying a median PFS of 211 days ( $P = 0.0007$ , vandetanib versus vehicle;  $P = 0.295$ , vandetanib versus BV; Figure 6, A and B).

In A549 xenografts, treatment with erlotinib resulted in a median PFS of 53 days, compared with 29.5 days in vehicle-treated controls ( $P = 0.34$ ; Figure 6C). Over the course of the experiment, 2 tumors progressed on erlotinib+BV treatment (median PFS not reached), and the addition of erlotinib to BV significantly delayed the onset of resistance compared with BV alone ( $P = 0.013$ , erlotinib+BV versus vehicle;  $P = 0.049$ , erlotinib+BV versus BV; Figure 6, C and D). On vandetanib treatment, 1 xenograft progressed after 102 days, and the median PFS was not reached ( $P = 0.017$ , vandetanib versus vehicle;  $P = 0.046$ , vandetanib versus BV; Figure 6, C and D). These findings indicate that EGFR inhibition not only reduced the number of NSCLC xenografts that progressed on therapy compared with BV alone in both our models, but also delayed the onset of resistance to VEGF signaling inhibition in A549 xenografts.

Given the aforementioned EGFR expression in pericytes in the H1975 model, we examined whether targeting EGFR affects vessel maturation and pericyte coverage. Multicolor IF staining was performed using antibodies directed against CD31 and desmin, and pericyte coverage was quantified. In H1975 BV-resistant xenografts, the percentage of blood vessels supported by pericytes was 50% greater than that in control tumors ( $P < 0.01$ ; Figure 5D). However, pericyte coverage was significantly reduced in tumors

receiving long-term treatment with erlotinib+BV or with vandetanib ( $P < 0.01$ ), consistent with EGFR blockade blunting the increase in pericyte coverage accompanying the normalized revascularization observed with BV in this model. In contrast, A549 xenografts that progressed on BV therapy had significantly fewer blood vessels supported by pericytes than did controls ( $P < 0.01$ ; Supplemental Figure 3); nevertheless, long-term administration of erlotinib+BV or of vandetanib also decreased the pericyte coverage in this model compared with controls ( $P < 0.01$ ; Supplemental Figure 3), providing further support for the role of EGFR in tumor-associated stroma.

*Lung adenocarcinoma H441 orthotopic tumors acquire resistance to BV, and tumor growth is delayed with dual EGFR/VEGFR2 inhibition.* To investigate whether the changes associated with BV resistance in subcutaneous models also occur in tumors growing in the lung, we used an established orthotopic model whereby H441 lung adenocarcinoma cells were injected directly into the lung of male nude mice. These cells harbor wild-type EGFR and mutant KRas and were selected because of their moderate tumor cell resistance to EGFR blockade (33), and also because they display optimal growth kinetics when implanted in the mouse lung (34). At 21 days after injection, an initial cohort of 8 mice was euthanized to evaluate mean tumor volume (approximately 60 mm<sup>3</sup>). To evaluate the effects of short-term BV treatment, 2 additional groups of mice were sacrificed after 2 weeks of BV therapy, as in the prior experiments. The remaining animals were then randomized for a



**Figure 5**

Altered patterns of tumor vascular density, tortuosity, and pericyte coverage in BV-resistant xenograft tumors. **(A)** Microphotographs of CD31<sup>+</sup> tumor vessels (red) in H1975 and A549 xenografts treated with vehicle and BV after 2 weeks and at progression. 5–10 microscopic fields were collected from each of 4 specimens per group. Arrows indicate the different vessel morphology in H1975 (top panel) and A549 (lower panel) BV-resistant tumors. Original magnification,  $\times 100$ . **(B and C)** Quantification of MVD **(B)** and vessel tortuosity **(C)** based on CD31-stained tumor sections in H1975 and A549 xenografts treated with vehicle and BV after 2 weeks and at progression. 5 hotspot microscopic fields ( $\times 200$ ) per tumor section were analyzed to quantify MVD; 5 random microscopic fields ( $\times 100$ ) were quantified for vessel tortuosity analysis.  $n = 4$  per group. Units of the y axis for MVD **(B)** represent CD31 + vessels per HPF (high power field). The y axis for vessel tortuosity **(C)** represents the ratio  $T = (L/S) - 1$ . **(D)** Pericyte coverage of H1975 xenografts was quantified as percent CD31<sup>+</sup> vessels with at least 50% coverage of associated desmin<sup>+</sup> cells in at least 5 microscopic fields ( $\times 200$ ) in tumors receiving long-term treatment.  $n = 2$  (vandetanib); 3 (erlotinib); 4 (vehicle, BV, and erlotinib+BV). **(B–D)** \* $P < 0.01$ , \*\* $P < 0.05$ ,  $t$  test.

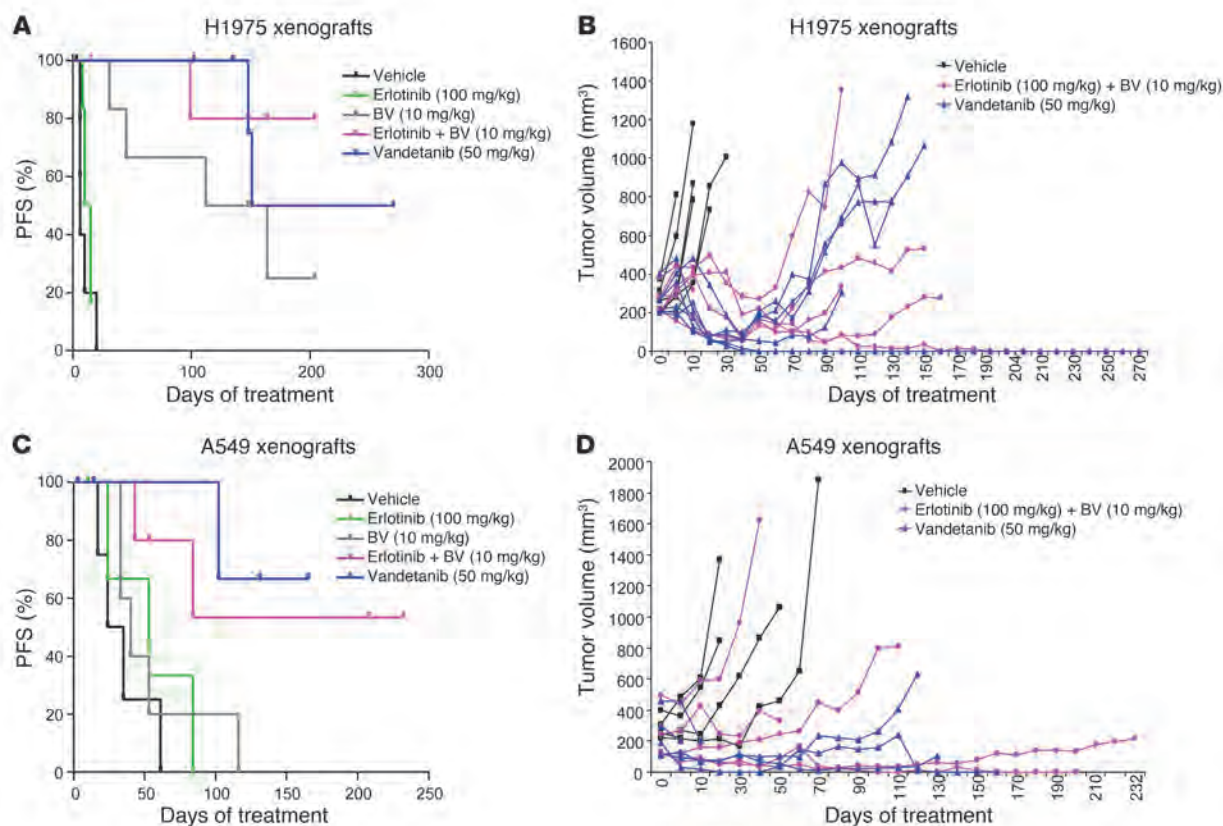
survival analysis ( $n \geq 7$  per group) and treated with vehicle, erlotinib, BV, erlotinib+BV, or vandetanib until moribund, at which time they were euthanized. Survival was defined as the time from treatment onset until sacrifice.

Short-term treatment with BV resulted in significant tumor growth inhibition compared with vehicle-treated tumors ( $\Delta T/\Delta C$  45.7%;  $P = 0.026$ , Mann-Whitney test; Figure 7, A and B). In the long-term treatment analysis, all mice had a large tumor burden at the time of sacrifice (Figure 7C). As shown in Figure 7D and Supplemental Figure 4, erlotinib treatment resulted in a small but significant prolongation of survival compared with vehicle (median survival, 58 versus 50 days;  $P = 0.02$ , log-rank test). The BV group had a longer survival (median, 77 days) compared with erlotinib alone ( $P = 0.00015$ ), and the combination of erlotinib and BV, or vandetanib, significantly prolonged survival (median, 101 days) compared with BV or erlotinib alone ( $P = 0.0001$ , erlotinib+BV

versus erlotinib;  $P = 0.0001$ , erlotinib+BV versus BV;  $P = 0.022$ , vandetanib versus BV; Figure 7D and Supplemental Figure 4, C and D). Similar to our results obtained with the H1975 xenografts, H441 orthotopic tumors were initially sensitive to VEGF signaling pathway blockade, but tumors ultimately progressed. In this orthotopic model, dual targeting of EGFR and VEGF pathways significantly delayed the onset of therapeutic resistance compared with inhibition of either pathway alone.

**Characterization of H441 orthotopic tumor stroma after anti-VEGF therapy and dual EGFR/VEGFR2 inhibition.** We next sought to more completely characterize the vasculature and stroma of BV-resistant H441 tumors. We found a significant decrease in MVD after 2 weeks of BV treatment compared with vehicle controls ( $P = 0.0008$ ; Figure 7E). Consistent with the revascularization observed in the subcutaneous models, tumors resistant to BV or dual VEGFR/EGFR inhibition showed significantly increased MVD compared with BV-sensitive





**Figure 6**

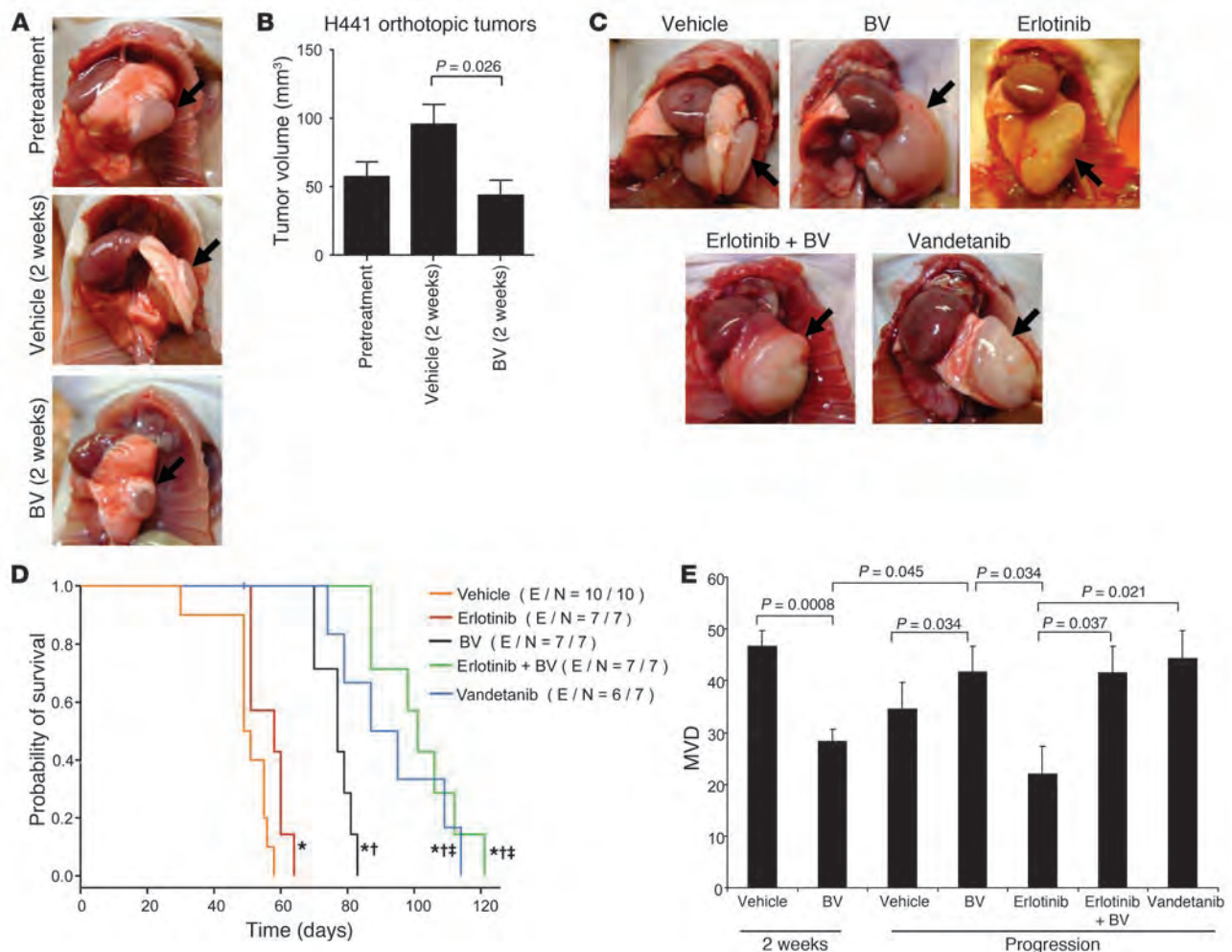
Effect of dual EGFR/VEGFR2 inhibition on H1975 and A549 NSCLC xenograft models. (A and C) Distribution of PFS, shown by Kaplan-Meier plots, and (B and D) individual tumor growth curves of H1975 (A and B) and A549 (C and D) xenografts receiving long-term treatment as indicated. Log-rank test was used to compare statistical differences in survival among treatment groups.

tumors ( $P = 0.045$ ; Figure 7E). Interestingly, in the erlotinib-resistant group, no revascularization was observed; in fact, MVD was significantly lower than in BV-resistant tumors ( $P = 0.034$ ; Figure 7E). These findings indicate that VEGF inhibitor resistance is associated with revascularization in H441 orthotopic tumors.

We next investigated the EGFR signaling pathway in BV-resistant H441 tumors. Protein levels of total EGFR were not significantly different in tumor and endothelium of vehicle and BV-resistant H441 tumors (data not shown). Levels of p-EGFR, however, were significantly increased in H441 BV-resistant tumors compared with vehicle-treated tumors ( $P = 0.039$ ; Figure 8, A and B), and, consistent with the H1975 subcutaneous model of acquired resistance, the activated receptor colocalized with the stroma, supporting large, normalized vessels in BV-resistant tumors. Furthermore, in tumors resistant to VEGFR/EGFR targeting, the levels of p-EGFR were strongly decreased compared with either vehicle-treated or BV-resistant tumors ( $P = 0.0001$ , erlotinib+BV versus vehicle;  $P = 0.0008$ , erlotinib+BV versus BV;  $P = 0.011$ , vandetanib versus vehicle;  $P = 0.009$ , vandetanib versus BV; Figure 8, A and B), demonstrating persistent EGFR blockade with treatment. Given these results, we next quantified the percentage of pericyte coverage of the blood vessels supplying H441 orthotopic tumors, as an index of vessel maturation. As shown in Figure 8, C and D, BV-resistant tumors had significantly increased pericyte coverage compared with controls and BV-sensitive tumors ( $P = 0.003$ , BV

progression versus vehicle progression;  $P < 0.0001$ , BV progression versus BV 2 weeks). Moreover, in tumors that progressed while receiving erlotinib alone, erlotinib+BV, or the dual inhibitor vandetanib, the pericyte coverage was reduced to levels comparable to vehicle-treated tumors ( $P = 0.001$ , erlotinib versus BV;  $P = 0.054$ , erlotinib+BV versus BV;  $P = 0.007$ , vandetanib versus BV; Figure 8, C and D). These findings support our earlier observation that stromal EGFR contributed to acquisition of resistance to VEGF inhibition through signaling activation on VSCs. However, we also noted in BV-resistant H441 tumors a substantial amount of p-EGFR IF staining localized far from the CD31<sup>+</sup> vascular structures (Figure 8A), which indicates that apart from VSCs, other components of the tumor stroma may undergo significant changes and contribute to the resistant phenotype, at least in this model. Furthermore, it is worth noting that increases in FGFR2 gene and protein levels were not observed in BV-resistant orthotopic tumors (data not shown), which indicates that there were differences between the orthotopic and subcutaneous models.

*Inflammatory cells and tumor-associated fibroblasts in BV-resistant tumors.* Because bone marrow-derived inflammatory cells and tumor-associated fibroblasts have previously been shown to play a role in mediating angiogenesis and refractoriness to VEGF blockade (23, 25, 35, 36), we next evaluated the infiltration of inflammatory macrophages and myofibroblasts in the stroma of both our models of acquired resistance. We performed double IF staining



**Figure 7** Orthotopic H441 NSCLC tumor growth and MVD after VEGF blockade or dual EGFR/VEGFR pathway inhibition. (**A** and **B**) Representative photographs (**A**) and mean tumor volume obtained at the last measurement (**B**) of H441 orthotopic tumors before or after 2 weeks of treatment. Arrows denote tumor mass in the lung.  $n = 8$  (pretreatment); 9 (vehicle); 10 (BV).  $P$  value was calculated using Mann-Whitney test. (**C**) Representative photographs of H441 orthotopic tumors after long-term administration.  $n = 10$  (vehicle); 7 (erlotinib, BV, and erlotinib+BV); 6 (vandetanib). Arrows denote tumor mass in the lung. (**D**) Kaplan-Meier plots showing survival distribution in H441 orthotopic tumor-bearing mice treated as indicated. Number of events (E) per number in each group (N) is indicated. \* $P < 0.05$  versus vehicle, † $P < 0.01$  versus erlotinib, ‡ $P < 0.05$  versus BV, log-rank test. (**E**) MVD quantification in H441 orthotopic tumors.  $n = 4$  (erlotinib); 5 (vehicle 2 weeks and vandetanib); 6 (BV 2 weeks and vehicle progression); 7 (BV progression and erlotinib+BV). Statistical values were calculated using  $t$  test. Units in the  $y$  axis for MVD represent CD31 + vessels per HPF.

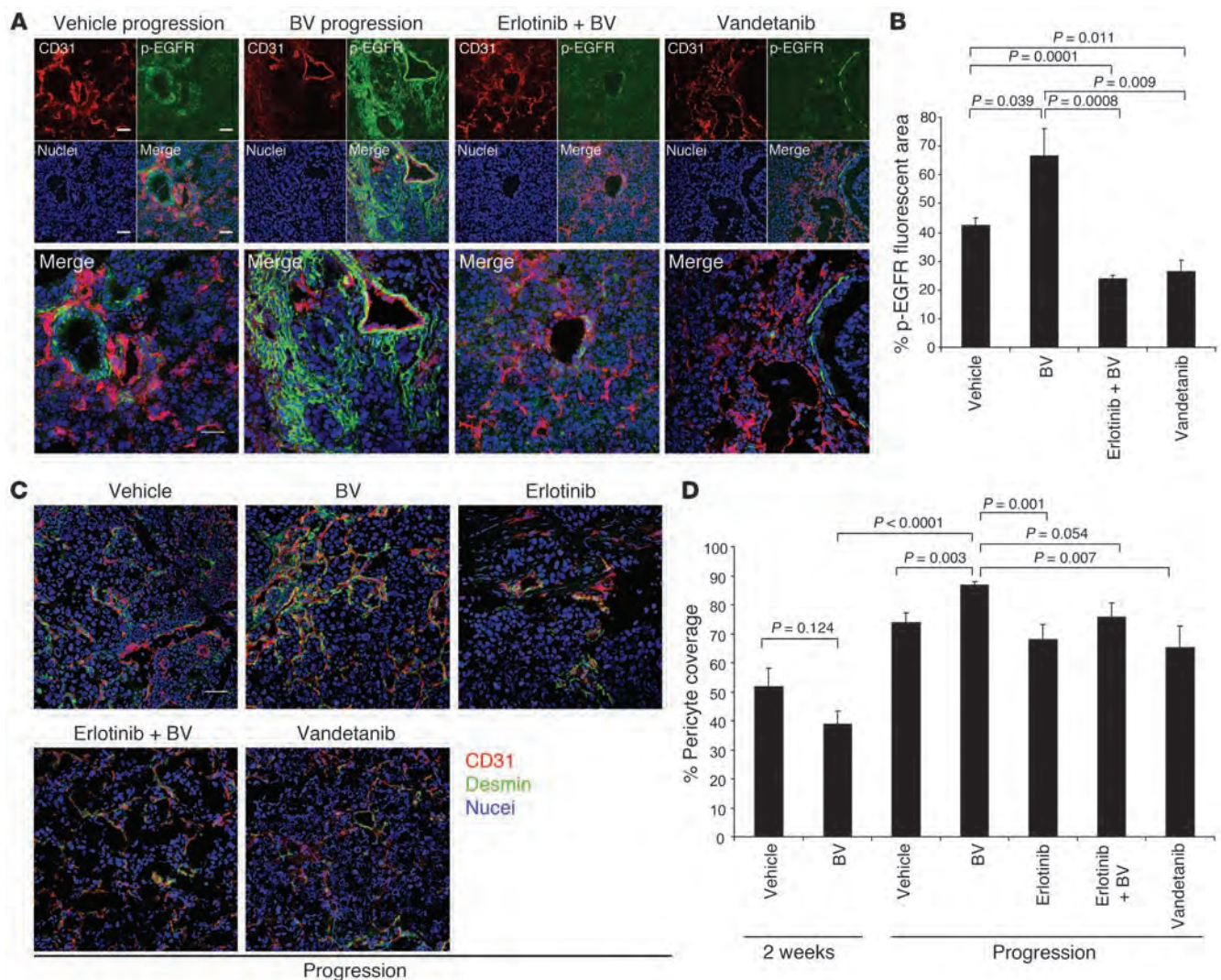
to identify F4/80<sup>+</sup> macrophages (Supplemental Figure 5A) and  $\alpha$ -SMA<sup>+</sup> fibroblasts and myofibroblasts (Supplemental Figure 5C) in both H1975 subcutaneous and H441 orthotopic tumors with BV resistance. As shown in Supplemental Figure 5, B and D, there were no significant differences in overall levels of these markers between vehicle- and BV-treated tumors at progression in either model. In vehicle-treated H441 tumors, the  $\alpha$ -SMA staining pattern suggested a dense and desmoplastic stroma. Conversely, this pattern was no longer observed in BV-resistant tumors:  $\alpha$ -SMA consistently localized in rounded, well-demarcated areas, indicating a pattern characteristic of, but not limited to, perivascular cells in this model. In fact, given the different localization pattern of  $\alpha$ -SMA between BV-resistant orthotopic tumors and vehicle-treated tumors, we cannot rule out the possibility of potential changes in other cell populations of the lung microenvironment, such as

mesenchymal or other stromal cells, that might contribute to the onset of resistance to VEGF inhibition.

## Discussion

Early reports examining the effects of VEGF blockade and other antiangiogenic therapies raised the hopes that these agents may substantially slow or stop tumor growth, and that therapeutic resistance to these agents would be less likely to occur, at least in part, because the target was diploid and not prone to the same genetic instability as tumor cells (37, 38). However, both preclinical studies and clinical experience in lung cancer and other solid tumors (12, 17, 39–43) indicate that the vast majority of solid tumors either exhibit primary (intrinsic) resistance or will eventually acquire resistance to the effects of antiangiogenic therapy. Although to date most studies of therapeutic resistance to anticancer drugs have





**Figure 8**

EGFR is activated in H441 BV-resistant tumors, and dual EGFR/VEGFR inhibition reduces pericyte coverage. **(A)** Representative microphotographs of CD31 (red), p-EGFR (green), and nuclei (blue) fluorescent staining in H441 tumors that progressed on vehicle, BV, erlotinib+BV, and vandetanib treatments, using confocal microscopy. At least 5 microphotographs were collected from all the tumor specimens in each group. Original magnification,  $\times 200$ . Scale bar: 50  $\mu$ m. **(B)** Percent p-EGFR fluorescent area in H441 tumors that progressed while on the indicated therapies, as determined using Alpha Innotech Software. 5–10 random microphotographs ( $\times 200$ ) of red (CD31), green (p-EGFR), and blue (nuclei) fluorescence were collected from 5 (vehicle and BV), 6 (erlotinib+BV), and 4 (vandetanib) specimens per group. *P* values were calculated using *t* test. **(C)** Representative IF images of CD31, desmin, and nuclei in H441 tumors that progressed while on the indicated treatments, using confocal microscopy. At least 5 microphotographs were collected from all the tumor specimens per group. Original magnification,  $\times 200$ . Scale bar: 50  $\mu$ m. **(D)** Percent pericyte coverage in H441 tumors was quantified in at least 5 microscopic fields ( $\times 200$ ) of tumor specimens. *n* = 4 (erlotinib); 5 (vehicle 2 weeks and vandetanib); 6 (BV 2 weeks and vehicle progression); 7 (BV progression and erlotinib+BV). *P* values were calculated using *t* test.

focused on the role of tumor cells, recent studies have suggested that host factors, including tumor stroma, may play an important role in resistance to angiogenesis inhibitors (14, 15, 23, 25, 42, 44).

In this study, we used mouse- and human-specific profiling of human NSCLC xenografts in mice to investigate stromal and tumor cell changes occurring in tumors that acquired resistance to BV. This analysis revealed that changes in gene expression, and particularly changes in angiogenesis-related genes, occurred predominantly in stromal and not tumor cells. This observation reinforces the notion that tumor stroma may play an important

— and potentially dominant, in at least some circumstances — role in VEGF inhibitor resistance.

Pathway analyses highlighted that among these stromal changes, there were multiple genes in the *Egfr* and *Fgfr2* pathways that were upregulated in resistant tumors (e.g., *Epgn*, *Areg*, *Fgf13*, and *Fgfbp1*) and that the EGFR pathway appeared to be a central gene interaction pathway. EGFR and FGFR2 upregulation was confirmed using species-specific RT-PCR as well as IHC. As noted below, upregulation of the bFGF/FGFR2 pathway has previously been observed by our group and others in VEGF inhibitor resistance



(16, 17, 45), but to our knowledge, a role for stromal EGFR has not been reported previously. We therefore investigated this pathway in greater detail using 3 models: subcutaneous and orthotopic models of acquired resistance (H1975 and H441, respectively) and a model of relative primary resistance (A549). Tumor cells from all 3 models are known to be relatively resistant to EGFR blockade in vitro (26, 33).

In both models of acquired BV resistance, there was a significant increase in activated EGFR that largely, but not exclusively, localized on VSCs, which were predominantly pericytes (Figures 3, 5, and 8). No significant p-EGFR was detectable on VSCs of control tumors. This was accompanied by an increase in pericyte coverage and a pattern of less tortuous, normalized revascularization in the BV-resistant tumors. Dual inhibition of VEGFR and EGFR pathways reduced pericyte coverage of tumor vessels compared with BV alone, which indicates that EGFR signaling plays a functional role in pericyte coverage of tumor vessels in the models studied. Dual targeting also significantly delayed the emergence of resistance and prolonged survival in the H441 model, with similar trends observed in the H1975 model (Figures 6 and 7). To our knowledge, this is the first evidence demonstrating a potential role for EGFR signaling in pericytes or other stromal cell populations of the tumor microenvironment in resistance to VEGF pathway inhibition in murine models of NSCLC.

Consistent with our observation regarding EGFR in tumor pericytes, a recent study found that the EGFR TKI gefitinib significantly suppressed tumor-associated pericyte function (46). During the revisions of this manuscript, other investigators reported a role for the stromal heparin-binding *Egf/Egfr* (Hb-Egf/Egfr) signaling pathway in the progression of a pancreatic neuroendocrine tumor model of EGFR-targeted inhibition (47). The authors demonstrate that stromal cell-derived Hb-Egf activates the EGFR pathway in perivascular cells, contributing to increased pericyte coverage and angiogenesis. These reports provide further support for a role of EGFR signaling in pericyte function in tumor revascularization.

A recent study has identified a role for PDGF-C expressed by tumor-associated fibroblasts in VEGF inhibitor resistance (25) and in attenuating tumor response to anti-VEGF treatment in a model of glioblastoma (48). PDGFR signaling in pericytes has also been implicated in vessel maturation, and recent evidence indicates that VEGF signaling suppresses pericyte PDGFR signaling, inhibiting vessel maturation (49). Somewhat surprisingly, we did not observe upregulation of any PDGFRs or ligands. In contrast, we noted modest but statistically significant downregulation of the stromal genes *Pdgfra*, *Pdgfb*, and *Pdgfrb*. Given the role of the PDGF family in multiple tumor processes, including pericyte recruitment and function (50, 51), it appears that pericyte-expressed EGFR may play a complimentary or compensatory role in the increased pericyte coverage observed in the acquired resistance models. Although the current study does not address this issue, it will be interesting to determine whether increased pericyte EGFR signaling in the H441 model (in the absence of increased EGFR gene or protein levels) is driven by increased ligand production or by reduced VEGFR-driven inhibition of signaling, as observed for pericyte PDGFR.

In the A549 model, stromal EGFR was also upregulated in BV-resistant tumors, but was localized exclusively to tumor endothelium, not VSCs. As expected, dual VEGFR/EGFR inhibition did not reduce pericyte coverage in this model, but did significantly delay the emergence of resistance compared with BV alone (Figure 6). This observation highlights that a signaling pathway may play dif-

ferent roles in tumor stroma depending on the cellular context. Studies examining EGFR distribution on endothelium suggest that it is restricted to blood vessels supplying pathologic tissues (52), where it activates angiogenic programs (53). Others have reported that EGFR is activated on endothelium when tumor cells express EGFR ligands, such as TGF- $\alpha$  or EGF (54, 55).

Activation of the bFGF/FGFR2 pathway has previously been shown to be a critical regulator of the angiogenic switch (56) and to be upregulated in response to antiangiogenic therapy (17). We observed an approximately 6-fold increase in stromal *Fgfr2* gene expression in tumors with acquired resistance and, consistent with this finding, an increase in the number of FGFR2-expressing cells in these tumors. This immunoreactivity appeared to be largely, but not exclusively, on tumor endothelium. This suggests that the FGFR2 pathway may promote VEGF-independent endothelial survival, as previously observed in other preclinical models (57, 58), although we cannot rule out the possibility that it plays a role in other nonendothelial stromal cells. Circulating levels of bFGF were also elevated in the plasma of mice bearing BV-resistant tumors. This observation is notable in light of our recent observation that acquired resistance to chemotherapy and BV in colorectal cancer patients is associated with an increase in circulating bFGF (45), which suggests that similar mechanisms may be occurring in cancer patients.

The mechanisms underlying regulation of tumor stromal genes altered in resistant tumors remain to be established and are likely to differ in the various stromal cell types. Expression of many of the genes, including *CAIX*, *FGFR2* (59), and *EGFR* family members, is known to be regulated by hypoxia or to correlate with expression of HIF1 $\alpha$ , as previously reviewed (60). One possible explanation is that BV therapy initially triggers a substantial decrease in tumor MVD and increases tumor hypoxia (61), inducing upregulation of hypoxia-dependent pathways. It is worth noting, however, that BV resistance was not associated with significant increases in many stromal genes known to be upregulated by hypoxia, and many of the genes upregulated in BV resistance are not known to be regulated by hypoxia. Hypoxia is therefore likely to be only one of many factors — both host and tumor cell dependent — likely to affect the resistant tumor and its microenvironment. These regulators of the stromal response merit further investigation.

Resistance to VEGF inhibition was also associated with different patterns of vascular remodeling in the models of acquired and primary resistance. In the H1975 model of acquired resistance, short-term treatment with BV during the sensitive phase initially induced a reduction in MVD; an increase in EC apoptosis, as observed in other studies (29, 30, 32, 62–65); and tumor shrinkage. This was followed by the development of resistance, marked by a pattern of normalized revascularization with increased MVD, reduced EC apoptosis, and a higher degree of pericyte coverage (Figure 5 and Supplemental Figure 1). These effects appeared to be VEGFR2 independent, as VEGFR2 phosphorylation remained inhibited in resistant tumors. Similar normalized revascularization was observed in the H441 orthotopic model (Figures 7 and 8). Prior studies have indicated that pericyte coverage may exert a protective effect on tumor endothelium (66, 67), potentially through the production of factors promoting endothelial survival and VEGF independence. Our findings were consistent with this hypothesis and revealed pericyte EGFR signaling to be a potential mediator of this effect.

In the A549 model of relative primary resistance, a distinct pattern of disorganized sprouting revascularization was observed in resistant tumors. This was marked by decreases in pericyte cover-





age with BV treatment and increased vessel tortuosity in resistant tumors. Unlike the acquired resistance models, stromal p-EGFR was upregulated in tumor endothelium, which suggests that the endothelium may be able to switch its dependence from VEGFR- to EGFR-driven endothelial proliferation and angiogenesis in the BV-resistant A549 xenografts, resulting in sprouting revascularization. It is worth noting that in an earlier study, we observed a similar switch (from EGFR- to VEGFR-dependent tumor endothelium) in a melanoma model (68), supporting the feasibility of this proposed mechanism. Endothelial EGFR signaling may explain, at least in part, the intrinsic relative resistance of these tumors to VEGF blockade, as well as our prior observation that A549 cells display EGFR TKI resistance *in vitro*, but show moderate sensitivity to EGFR inhibition when grown as xenografts (26). Other pathways that may contribute to this vascular phenotype are currently under investigation, including regulators of EC motility (e.g., HGF/c-MET) and vessel maturation (e.g., Ang-2/Tie-2). Nevertheless, this model provides evidence that there are distinct patterns of vascular remodeling that can accompany VEGF inhibitor resistance-associated tumor revascularization.

This study has a number of clinical implications for the use of VEGF inhibitors in NSCLC and other tumor types. First, it suggests that dual inhibition of the VEGFR and EGFR pathways may delay the emergence of therapeutic resistance in NSCLC. Consistent with this possibility, a recent phase III study (ATLAS) comparing the use of BV combined with erlotinib versus BV alone as maintenance therapy after chemotherapy demonstrated a significant, but modest, PFS improvement with an observed hazard ratio of 0.72 ( $P = 0.001$ ; refs. 69, 70). Combined VEGFR/EGFR inhibition (via BV with erlotinib or vandetanib) has also demonstrated significantly improved PFS compared with EGFR inhibition alone (71–73). These studies showed a significant delay in tumor progression while treatment with VEGFR/EGFR inhibition was ongoing; however, significant improvements in overall survival were not observed. The explanation for this lack of durable clinical benefit is not known, but it is possible that once the dual inhibition is discontinued, these 2 pathways, or other alternative escape pathways, rapidly emerge.

The results of the present study may not be broadly generalizable to other tumor types or regimens containing chemotherapy. In a randomized phase III trial in colorectal cancer, the addition of the EGFR monoclonal antibodies panitumumab (74) or cetuxumab (75) to BV and chemotherapy showed trends toward worse clinical outcomes. Furthermore, in a recent study of colorectal cancer patients treated with BV plus chemotherapy, we observed increases in plasma bFGF, HGF, PDGF, and several myeloid factors prior to development of progressive disease (45); in contrast, in our model, bFGF was the sole factor that significantly increased. This suggests that resistance mechanisms may be disease or regimen specific.

Second, these findings raise the possibility that combinations of VEGF inhibitors with drugs targeting other potential stromal resistance pathways — such as FGFR2 — may improve treatment efficacy. Third, they suggest that the analysis of both tumor cell and stromal markers — not just tumor cell markers alone — may provide important clinical information. Fourth, they suggest that analysis of vascular patterns in VEGF inhibitor-resistant tumors may provide information regarding the underlying mechanisms of resistance.

In summary, our findings suggest that in NSCLC models, gene expression changes associated with VEGF inhibitor resistance occur predominantly in tumor stromal cells, not tumor cells, pro-

viding further evidence that tumor stroma may play an important — and potentially dominant — role in VEGF inhibitor resistance. Primary and acquired resistance may be associated with distinct patterns of vascularization, described here as normalized and sprouting patterns, and distinct patterns of stromal signaling. Finally, we identify what we believe to be a novel role for pericyte EGFR signaling in VEGF inhibitor resistance. It is worth noting, however, that although combinations of VEGF and EGFR pathway inhibition have shown promise in NSCLC, therapeutic resistance nevertheless continues to emerge, which indicates that additional resistance mechanisms remain to be uncovered.

## Methods

**Subcutaneous *in vivo* studies.** All animal studies reported were approved by M.D. Anderson Cancer Center's animal care committee, which is fully accredited by the Association for Assessment and Accreditation of Laboratory Animal Care (AAALAC International). To generate tumor xenografts, A549 and H1975 tumor cells ( $2.0 \times 10^6$ ) in 100  $\mu$ l HBSS were injected into the subcutaneous flanks of 4- to 8-week-old male athymic nude mice (NCI-nu). Body weights and tumor volumes were recorded twice weekly. Tumor volumes were calculated as  $\pi/6 \times a^2 \times b$ , where  $a$  is the smaller measurement of the tumor and  $b$  is the larger one, and expressed in cubic millimeters. When the tumor volumes reached an average of approximately 270 mm<sup>3</sup>, mice were randomly assigned to one of the following treatment groups: (a) control i.p. injection of vehicle (PBS) twice weekly and oral (p.o.) administration of vehicle daily; (b) i.p. injection of BV (10 mg/kg) twice weekly; (c) erlotinib (100 mg/kg) p.o. daily; (d) erlotinib p.o. daily plus BV i.p. twice weekly; (e) vandetanib (50 mg/kg) p.o. daily ( $n = 6$  [H1975] and 5 [A549] per group). Animals were sacrificed due to tumor burden. The log-rank test was performed to compare survival curves between different treatment groups using GraphPad Prism version 5.00 for Windows (GraphPad Software). For short-term treatment studies, H1975 ( $n = 5$  per group) and A549 ( $n = 6$  per group) tumor-bearing animals were treated for 2 weeks with vehicle and BV (10 mg/kg) and then sacrificed. The last tumor measurement was used to calculate  $\Delta T/\Delta C$  (change in tumor volume relative to change in control, expressed as a percentage), as previously described (76). Tumor tissues from short- and long-term *in vivo* experiments were collected for IHC studies. Tumors were excised, a portion was fixed in formalin and embedded in paraffin, and another portion was embedded in OCT (Miles Inc.) and rapidly frozen in liquid nitrogen. Additional tumor sections for molecular studies were snap-frozen in liquid nitrogen. Staining with H&E was used to confirm the presence of tumor in each sample included in the analysis.

**RNA microarray analysis.** Total RNA was extracted from snap-frozen tissues using the mirVana miRNA Isolation Kit (Ambion) according to the manufacturer's protocol. Biotin-labeled cRNA samples for hybridization were prepared using Illumina Total Prep RNA Amplification Kit (Ambion Inc.). Total RNA (1  $\mu$ g) was used for the synthesis of cDNA, followed by amplification and biotin labeling. Each of 1.5  $\mu$ g of biotinylated cRNAs was hybridized to both mouse WG-6v2 and human WG-6v3 Expression BeadChips (Illumina) at the same time for analysis of murine and human transcripts. Signals were developed by Amersham fluorolink streptavidin-Cy3 (GE Healthcare). Gene expression data were collected using an Illumina bead Array Reader confocal scanner (BeadStation 500GXDW; Illumina Inc.). Data were analyzed using the BRB-ArrayTools Version 3.7.0 Beta platform (<http://linus.nci.nih.gov/BRB-ArrayTools.html>). A log base-2 transformation was applied to the data set prior to data normalization. A median array was selected as the reference array for normalization, and statistical significance was set at  $P < 0.01$ . To evaluate the expression of genes involved in response to hypoxia, lymphangiogenesis, and angiogenesis in



BV-resistant xenografts versus controls, a list of 269 genes used in previous publications was compared (77). Genes differentially expressed between groups were determined applying univariate *t* test with estimation of the false discovery rate (FDR). Genes were determined using selection criteria of  $P < 0.005$  and fold change of 1.5 or larger. Functional gene-interaction network analysis of genes differentially expressed between the mouse stroma of BV-resistant and vehicle-treated H1975 xenografts was performed using Ingenuity Pathways Analysis.

**Accession numbers.** Microarray data have been deposited into NCBI GEO (accession no. GSE26644).

**IF.** Frozen tissue sections were used to evaluate CD31, p-VEGFR2, EGFR, and desmin expression. Specimens were sectioned (8–10  $\mu$ M thickness), mounted onto positively charged slides, and air-dried for 30 minutes. Tissue fixation was performed using 3 sequential immersions in ice-cold acetone, acetone-chloroform 50:50 (v/v), and acetone (5 minutes each). Slides were incubated in protein block solution containing 4% fish gelatin for 20 minutes at room temperature and then incubated overnight at 4°C with a 1:500 dilution of rat anti-mouse CD31. Sections were rinsed with PBS and then incubated for 1 hour with a goat anti-rat Alexa Fluor 594 antibody (diluted 1:1,200). Samples were rinsed with PBS, incubated for 20 minutes with protein block, and then incubated with primary antibody against p-VEGFR2 (diluted 1:400), or EGFR (diluted 1:100) or desmin (diluted 1:400) at 4°C overnight. Samples were rinsed 3 times with PBS and then incubated for 1 hour with goat anti-rabbit Alexa Fluor 488 antibody (diluted 1:1,200). After rinsing, sections were incubated with Hoechst stain (diluted 1:10,000 in PBS; Polysciences Inc.) for 2 minutes to visualize cell nuclei. Slides were mounted with a glycerol/PBS solution containing 0.1 mol/l propyl gallate (Sigma-Aldrich) to minimize fluorescent bleaching. IF microscopy was performed using a Zeiss Axioplan fluorescence microscope (Carl Zeiss Inc.) equipped with a 100-W Hg lamp and narrow bandpass excitation filters. Representative images were obtained using a cooled charge-coupled device Hamamatsu C5810 camera (Hamamatsu Photonics) and Optimas software (Media Cybernetics).

**Confocal microscopy.** Confocal microscopy was used in protein localization studies of CD31 and p-EGFR and of CD31 and total FGFR2 in subcutaneous murine models, and of CD31 and desmin, CD31 and p-EGFR, and F4/80 and  $\alpha$ -SMA staining in orthotopic tumors, as previously described (78). Frozen tissues for confocal microscopy were sectioned (8–12  $\mu$ m) and mounted on positively charged slides. IF staining for p-EGFR or total FGFR2 and CD31 was carried out as described above, with the exception that the Alexa Fluor 594 fluorophore used for CD31 detection was replaced with a Cy5 antibody, and the Alexa Fluor 488 fluorophore used to visualize p-EGFR or FGFR2 or desmin was replaced with a Cy3 antibody. Sytox green (diluted 1:10,000 in PBS) was used to visualize cell nuclei. Confocal fluorescence images were collected using a Zeiss LSM 510 laser scanning microscope (Carl Zeiss Inc.) equipped with an argon laser (458/477/488/514 nm, 30 mW), HeNe laser (413 nm, 1 mW and 633 nm, 5 mW), LSM 510 control and image acquisition software, and appropriate filters (Chroma Technology Corp.).

**Determination of MVD, vessel tortuosity, and pericyte coverage.** Tumor MVD was determined as previously described (79). In brief, we examined tumors microscopically to identify hot spots by low magnification ( $\times 100$ ), and the mean MVD was quantified as the total number of CD31<sup>+</sup> structures observed in at least 5 higher-magnification microscopic fields per tumor ( $\times 200$ ). For each group, tumors from 4 mice receiving short- and long-term treatment were used. As previously described (80), the tortuosity of blood vessel was calculated as  $(L/S) - 1$ , where *L* is the length of the vessel of interest and *S* is the straight-line distance between its endpoints. Vessel length was evaluated in 4 samples per treatment group by tracing along the midline of the blood vessels that showed up in a longitudinal cut within

an image ( $\times 100$ ), and the number of pixels was converted into distance in millimeters with NIH ImageJ (version 1.34; <http://rsb.info.nih.gov/ij/>). To determine the extent of pericyte coverage on the tumor vasculature, tumor sections were stained for CD31 (red) and desmin (green) as described above. 5 fields per tumor were randomly identified at original magnification  $\times 200$ , and those blood vessels at least 50% covered by green desmin-positive cells were considered to be positive for pericyte coverage.

**Plasma bFGF concentration analysis.** bFGF levels were measured in the plasma of tumor-bearing animals by multiplex bead assay (BioRad and Millipore) in a 96-well plate according to the manufacturer's protocol. Concentrations were calculated based on a standard curve derived by performing 6 serial dilutions of a protein standard in assay diluent. Plasma samples were tested in duplicate, and the mean value was used for analysis.

**Orthotopic lung adenocarcinoma model.** Male 8-week-old athymic Ncr (*nu/nu*) mice were maintained in a specific pathogen-free mouse colony in accordance with regulations and standards of the Department of Agriculture and the Department of Health and Human Services. Mice were anesthetized with a combination of ketamine HCl (86 mg/kg) and xylazine (17 mg/kg) in normal saline; 100  $\mu$ l solution per 10 g body weight was injected i.p. Mice were then placed in the right lateral decubitus position. The skin overlying the left chest wall in the midaxillary line was prepped with alcohol and incised ( $\sim 7$  mm), and the underlying chest wall was visualized. Logarithmically growing H441 cells ( $1 \times 10^6$  cells in single-cell suspensions of greater than 95% viability as determined by Trypan blue exclusion) in 50  $\mu$ l HBSS containing 50  $\mu$ g growth factor-reduced Matrigel (BD Bioscience) were injected into the left thorax at the lateral dorsal axillary line and into the left lung. After tumor cell inoculation, the skin incision was clipped, and the mice were turned to the left lateral decubitus position and observed until fully recovered. No anesthesia or surgery-related deaths occurred. 3 weeks after H441 tumor cell injection, 8 mice were euthanized for evaluation of baseline tumor volume ( $n = 8$ ). Animals were sacrificed when moribund. Orthotopic tumors were photographed, and tissues were collected for IHC studies.

**Alpha Innotech IF quantification.** Alpha Innotech software (version 3.000) was used to quantify the IF signal in 5–10 random microscopic fields, depending on the tumor size, captured from at least 4 tumor specimens per group analyzed. Each microphotograph was collected using the same original magnification to obtain equal-sized images. 2 equally sized circles (area, 25,000 pixels) were randomly distributed on each microphotograph, and blue, red, and green pixel sums, averages, and background-corrected averages were obtained. The background-corrected fluorescent area of interest (green for p-EGFR, red for F4/80 and  $\alpha$ -SMA) was normalized relative to the blue (nuclei) area for each analyzed microphotograph, and the mean ratio from all the images of each tumor specimen was calculated per treatment group.

**Reagents, tumor cell lines, conditions, qRT-PCR, IHC, and LSC.** See Supplemental Methods.

**Statistics.** Unless otherwise indicated, data are mean  $\pm$  SEM. Distribution of PFS was estimated by the Kaplan-Meier method. Log-rank (Mantel-Cox) test was performed to test the difference in survival between groups. For comparison of continuous variables between 2 groups, 2-tailed Student's *t* test and Mann-Whitney-Wilcoxon test were used. A *P* value less than 0.05 was considered significant.

## Acknowledgments

This study was supported in part by the Department of Defense BATTLE W81XWH-06-1-0303, Department of Defense PROSPECT award W81XWH-07-1-03060, University of Texas Southwestern Medical Center, University of Texas M.D. Anderson Cancer Center Lung SPORE NIH grant P50 CA070907 and NCI grant



P30CA016672, and research support from AstraZeneca. J.V. Heymach is a Damon Runyon-Lilly Clinical Investigator supported in part by Damon Runyon Cancer Research Foundation grant CI 24-04 and is also supported by the Physician Scientist Program at M.D. Anderson Cancer Center. We gratefully acknowledge Donna Reynolds (University of Texas M.D. Anderson Cancer Center) for providing us with cut tissue sections and helping with IHC protocols; Michael Worley (University of Texas M.D. Anderson Cancer Center) for editing the manuscript; Anderson Ryan, Julianne Jürgensmeier, and Lee Ellis for helpful scientific discussions; and AstraZeneca for providing vandetanib. Research in the laboratory

of F. Ciardiello is supported by a grant from the Associazione Italiana per la Ricerca sul Cancro (AIRC).

Received for publication January 21, 2010, and accepted in revised form January 26, 2011.

Address correspondence to: John V. Heymach, Departments of Thoracic/Head and Neck Medical Oncology and Cancer Biology, University of Texas M.D. Anderson Cancer Center, Unit 432, 1515 Holcombe Blvd., Houston, Texas 77030, USA. Phone: 713.792.6363; Fax: 713.792.1220; E-mail: jheymach@mdanderson.org.

- Folkman J, Shing Y. Angiogenesis. *J Biol Chem*. 1992;267(16):10931–10934.
- Folkman J. Tumor angiogenesis: therapeutic implications. *N Engl J Med*. 1971;285(21):1182–1186.
- Carmeliet P, Jain RK. Angiogenesis in cancer and other diseases. *Nature*. 2000;407(6801):249–257.
- Ferrara N, Gerber HP, LeCouter J. The biology of VEGF and its receptors. *Nat Med*. 2003;9(6):669–676.
- Ferrara N, Davis-Smyth T. The biology of vascular endothelial growth factor. *Endocr Rev*. 1997;18(1):4–25.
- Ellis LM, Hicklin DJ. VEGF-targeted therapy: mechanisms of anti-tumour activity. *Nat Rev Cancer*. 2008;8(8):579–591.
- Kerbel RS. Tumor angiogenesis. *N Engl J Med*. 2008;358(19):2039–2049.
- Jain RK, di Tomaso E, Duda DG, Loeffler JS, Sorensen AG, Batchelor TT. Angiogenesis in brain tumours. *Nat Rev Neurosci*. 2007;8(8):610–622.
- Ferrara N, Hillan KJ, Gerber HP, Novotny W. Discovery and development of bevacizumab, an anti-VEGF antibody for treating cancer. *Nat Rev Drug Discov*. 2004;3(5):391–400.
- Dvorak HF. Vascular permeability factor/vascular endothelial growth factor: a critical cytokine in tumor angiogenesis and a potential target for diagnosis and therapy. *J Clin Oncol*. 2002;20(21):4368–4380.
- Chung AS, Lee J, Ferrara N. Targeting the tumour vasculature: insights from physiological angiogenesis. *Nat Rev Cancer*. 2010;10(7):505–514.
- Sandler A, et al. Paclitaxel-carboplatin alone or with bevacizumab for non-small-cell lung cancer. *N Engl J Med*. 2006;355(24):2542–2550.
- Hurwitz H, et al. Bevacizumab plus irinotecan, fluorouracil, and leucovorin for metastatic colorectal cancer. *N Engl J Med*. 2004;350(23):2335–2342.
- Crawford Y, Ferrara N. Tumor and stromal pathways mediating refractoriness/resistance to anti-angiogenic therapies. *Trends Pharmacol Sci*. 2009;30(12):624–630.
- Ebos JM, Lee CR, Kerbel RS. Tumor and host-mediated pathways of resistance and disease progression in response to antiangiogenic therapy. *Clin Cancer Res*. 2009;15(16):5020–5025.
- Bergers G, Hanahan D. Modes of resistance to anti-angiogenic therapy. *Nat Rev Cancer*. 2008;8(8):592–603.
- Casanovas O, Hicklin DJ, Bergers G, Hanahan D. Drug resistance by evasion of antiangiogenic targeting of VEGF signaling in late-stage pancreatic islet tumors. *Cancer Cell*. 2005;8(4):299–309.
- Graeber TG, et al. Hypoxia-mediated selection of cells with diminished apoptotic potential in solid tumours. *Nature*. 1996;379(6560):88–91.
- Yu JL, Rak JW, Coomber BL, Hicklin DJ, Kerbel RS. Effect of p53 status on tumor response to antiangiogenic therapy. *Science*. 2002;295(5559):1526–1528.
- Leenders WP, et al. Antiangiogenic therapy of cerebral melanoma metastases results in sustained tumor progression via vessel co-option. *Clin Cancer Res*. 2004;10(18 pt 1):6222–6230.
- Davis DW, et al. Pharmacodynamic analysis of target inhibition and endothelial cell death in tumors treated with the vascular endothelial growth factor receptor antagonists SU5416 or SU6668. *Clin Cancer Res*. 2005;11(2 pt 1):678–689.
- Heymach JV, et al. Phase II study of the antiangiogenic agent SU5416 in patients with advanced soft tissue sarcomas. *Clin Cancer Res*. 2004;10(17):5732–5740.
- Shojaei F, et al. Tumor refractoriness to anti-VEGF treatment is mediated by CD11b+Gr1+ myeloid cells. *Nat Biotechnol*. 2007;25(8):911–920.
- Ferrara N. Role of myeloid cells in vascular endothelial growth factor-independent tumor angiogenesis. *Curr Opin Hematol*. 2010;17(3):219–224.
- Crawford Y, et al. PDGF-C mediates the angiogenic and tumorigenic properties of fibroblasts associated with tumors refractory to anti-VEGF treatment. *Cancer Cell*. 2009;15(1):21–34.
- Naumov GN, et al. Combined vascular endothelial growth factor receptor and epidermal growth factor receptor (EGFR) blockade inhibits tumor growth in xenograft models of EGFR inhibitor resistance. *Clin Cancer Res*. 2009;15(10):3484–3494.
- Kobayashi S, et al. EGFR mutation and resistance of non-small-cell lung cancer to gefitinib. *N Engl J Med*. 2005;352(8):786–792.
- Pao W, et al. KRAS mutations and primary resistance of lung adenocarcinomas to gefitinib or erlotinib. *PLoS Med*. 2005;2(1):e17.
- Jain RK. Normalization of tumor vasculature: an emerging concept in antiangiogenic therapy. *Science*. 2005;307(5706):58–62.
- Batchelor TT, et al. AZD2171, a pan-VEGF receptor tyrosine kinase inhibitor, normalizes tumor vasculature and alleviates edema in glioblastoma patients. *Cancer Cell*. 2007;11(1):83–95.
- Greenberg JJ, Cheres DA. VEGF as an inhibitor of tumor vessel maturation: implications for cancer therapy. *Expert Opin Biol Ther*. 2009;9(11):1347–1356.
- Jain RK. Normalizing tumor vasculature with anti-angiogenic therapy: A new paradigm for combination therapy. *Nat Med*. 2001;7(9):987–989.
- Mukohara T, et al. Differential effects of gefitinib and cetuximab on non-small-cell lung cancers bearing epidermal growth factor receptor mutations. *J Natl Cancer Inst*. 2005;97(16):1185–1194.
- Jacoby JJ, et al. Treatment with HIF-1alpha antagonist PX-478 inhibits progression and spread of orthotopic human small cell lung cancer and lung adenocarcinoma in mice. *J Thorac Oncol*. 2010;5(7):940–949.
- Shojaei F, et al. G-CSF-initiated myeloid cell mobilization and angiogenesis mediate tumor refractoriness to anti-VEGF therapy in mouse models. *Proc Natl Acad Sci U S A*. 2009;106(16):6742–6747.
- Shojaei F, Zhong C, Wu X, Yu L, Ferrara N. Role of myeloid cells in tumor angiogenesis and growth. *Trends Cell Biol*. 2008;18(8):372–378.
- Boehm T, Folkman J, Browder T, O'Reilly MS. Antiangiogenic therapy of experimental cancer does not induce acquired drug resistance. *Nature*. 1997;390(6658):404–407.
- Kerbel RS. Inhibition of tumor angiogenesis as a strategy to circumvent acquired resistance to anti-cancer therapeutic agents. *Bioessays*. 1991;13(1):31–36.
- Heymach JV, et al. Randomized phase II study of vandetanib alone or with paclitaxel and carboplatin as first-line treatment for advanced non-small-cell lung cancer. *J Clin Oncol*. 2008;26(33):5407–5415.
- Broxterman HJ, Lankelma J, Hoekman K. Resistance to cytotoxic and anti-angiogenic anticancer agents: similarities and differences. *Drug Resist Updat*. 2003;6(3):111–127.
- Kerbel RS, et al. Possible mechanisms of acquired resistance to anti-angiogenic drugs: implications for the use of combination therapy approaches. *Cancer Metastasis Rev*. 2001;20(1–2):79–86.
- Ellis LM, Hicklin DJ. Pathways mediating resistance to vascular endothelial growth factor-targeted therapy. *Clin Cancer Res*. 2008;14(20):6371–6375.
- Heymach JV, Sledge GW, Jain RK. Tumor angiogenesis. In: Hong WK, et al., eds. *Holland-Frei Cancer Medicine* 8. Shelton, Connecticut, USA: People's Medical Publishing House-USA; 2010:149–169.
- Ferrara N. Pathways mediating VEGF-independent tumor angiogenesis. *Cytokine Growth Factor Rev*. 2010;21(1):21–26.
- Kopetz S, et al. Phase II trial of infusional fluorouracil, irinotecan, and bevacizumab for metastatic colorectal cancer: efficacy and circulating angiogenic biomarkers associated with therapeutic resistance. *J Clin Oncol*. 2010;28(3):453–459.
- Iivanainen E, et al. The EGFR inhibitor gefitinib suppresses recruitment of pericytes and bone marrow-derived perivascular cells into tumor vessels. *Microvasc Res*. 2009;78(3):278–285.
- Nolan-Stevaux O, et al. Differential contribution to neuroendocrine tumorigenesis of parallel Egfr signaling in cancer cells and pericytes. *Genes and Cancer*. 2010;1(2):125–141.
- di Tomaso E, et al. PDGF-C induces maturation of blood vessels in a model of glioblastoma and attenuates the response to anti-VEGF treatment. *PLoS One*. 2009;4(4):e5123.
- Greenberg JJ, et al. A role for VEGF as a negative regulator of pericyte function and vessel maturation. *Nature*. 2008;456(7223):809–813.
- Pietras K, Pahl J, Bergers G, Hanahan D. Functions of paracrine PDGF signaling in the proangiogenic tumor stroma revealed by pharmacological targeting. *PLoS Med*. 2008;5(1):e19.
- Ostman A, Heldin CH. PDGF receptors as targets in tumor treatment. *Adv Cancer Res*. 2007;97:247–274.
- Amin DN, Hida K, Bielenberg DR, Klagsbrun M. Tumor endothelial cells express epidermal growth factor receptor (EGFR) but not ErbB3 and are responsive to EGF and to EGFR kinase inhibitors. *Cancer Res*. 2006;66(4):2173–2180.
- Cheng H, et al. Construction of a novel constitutively active chimeric EGFR to identify new targets for therapy. *Neoplasia*. 2005;7(12):1065–1072.
- Wu W, et al. Expression of epidermal growth factor (EGF)/transforming growth factor-alpha by human lung cancer cells determines their response to EGF receptor tyrosine kinase inhibition in the lungs of mice. *Mol Cancer Ther*. 2007;6(10):2652–2663.
- Kuwait T, et al. Phosphorylated epidermal growth factor receptor on tumor-associated endothelial cells is a primary target for therapy with tyrosine





- kinase inhibitors. *Neoplasia*. 2008;10(5):489–500.
56. Kandel J, Bossy-Wetzel E, Radvanyi F, Klagsbrun M, Folkman J, Hanahan D. Neovascularization is associated with a switch to the export of bFGF in the multistep development of fibrosarcoma. *Cell*. 1991;66(6):1095–1104.
57. Paris F, et al. Endothelial apoptosis as the primary lesion initiating intestinal radiation damage in mice. *Science*. 2001;293(5528):293–297.
58. Karsan A, Yee E, Poirier GG, Zhou P, Craig R, Harlan JM. Fibroblast growth factor-2 inhibits endothelial cell apoptosis by Bcl-2-dependent and independent mechanisms. *Am J Pathol*. 1997;151(6):1775–1784.
59. Giatromanolaki A, et al. Relation of hypoxia inducible factor 1 alpha and 2 alpha in operable non-small cell lung cancer to angiogenic/molecular profile of tumours and survival. *Br J Cancer*. 2001;85(6):881–890.
60. Semenza GL. Targeting HIF-1 for cancer therapy. *Nat Rev Cancer*. 2003;3(10):721–732.
61. Franco M, et al. Targeted anti-vascular endothelial growth factor receptor-2 therapy leads to short-term and long-term impairment of vascular function and increase in tumor hypoxia. *Cancer Res*. 2006;66(7):3639–3648.
62. Roland CL, et al. Inhibition of vascular endothelial growth factor reduces angiogenesis and modulates immune cell infiltration of orthotopic breast cancer xenografts. *Mol Cancer Ther*. 2009;8(7):1761–1771.
63. Kim KJ, et al. Inhibition of vascular endothelial growth factor-induced angiogenesis suppresses tumour growth in vivo. *Nature*. 1993;362(6423):841–844.
64. Willett CG, et al. Direct evidence that the VEGF-specific antibody bevacizumab has antivascular effects in human rectal cancer. *Nat Med*. 2004;10(2):145–147.
65. Tong RT, Boucher Y, Kozin SV, Winkler F, Hicklin DJ, Jain RK. Vascular normalization by vascular endothelial growth factor receptor 2 blockade induces a pressure gradient across the vasculature and improves drug penetration in tumors. *Cancer Res*. 2004;64(11):3731–3736.
66. Lu C, et al. Impact of vessel maturation on anti-angiogenic therapy in ovarian cancer. *Am J Obstet Gynecol*. 2008;198(4):477.e1–477.e9.
67. Bergers G, Song S, Meyer-Morse N, Bergsland E, Hanahan D. Benefits of targeting both pericytes and endothelial cells in the tumor vasculature with kinase inhibitors. *J Clin Invest*. 2003;111(9):1287–1295.
68. Amin DN, Bielenberg DR, Lifshits E, Heymach JV, Klagsbrun M. Targeting EGFR activity in blood vessels is sufficient to inhibit tumor growth and is accompanied by an increase in VEGFR-2 dependence in tumor endothelial cells. *Microvasc Res*. 2008;76(1):15–22.
69. Miller VA, O'Connor P, Soh C, Kabbinnar F. A randomized, double-blind, placebo-controlled, phase IIIb trial (ATLAS) comparing bevacizumab (B) therapy with or without erlotinib (E) after completion of chemotherapy with B for first-line treatment of locally advanced recurrent, or metastatic non-small cell lung cancer (NSCLC). *J Clin Oncol*. 2009;27(suppl):S18.
70. Kabbinnar FF, et al. Overall survival (OS) in ATLAS, a phase IIIb trial comparing bevacizumab (B) therapy with or without erlotinib (E) after completion of chemotherapy (chemo) with B for first-line treatment of locally advanced, recurrent, or metastatic non-small cell lung cancer (NSCLC). *J Clin Oncol*. 2010;28(suppl):Abstract 7526.
71. Natale RB, et al. Vandetanib versus gefitinib in patients with advanced non-small-cell lung cancer: results from a two-part, double-blind, randomized phase II study. *J Clin Oncol*. 2009;27(15):2523–2529.
72. Herbst RS, et al. Phase II study of efficacy and safety of bevacizumab in combination with chemotherapy or erlotinib compared with chemotherapy alone for treatment of recurrent or refractory non small-cell lung cancer. *J Clin Oncol*. 2007;25(30):4743–4750.
73. Hainsworth J, Herbst R. A phase III, multicenter, placebo-controlled, double-blind, randomized clinical trial to evaluate the efficacy of bevacizumab (Avastin) in combination with erlotinib (Tarceva) compared with erlotinib alone for treatment of advanced non-small cell lung cancer after failure of standard first-line chemotherapy (BETA). *J Thor Oncol*. 2008;3:S302.
74. Hecht JR, et al. A randomized phase IIIB trial of chemotherapy, bevacizumab, and panitumumab compared with chemotherapy and bevacizumab alone for metastatic colorectal cancer. *J Clin Oncol*. 2009;27(5):672–680.
75. Punt CJ, et al. Randomized phase III study of capecitabine, oxaliplatin, and bevacizumab with or without cetuximab in advanced colorectal cancer (ACC), the CAIRO2 study of the Dutch Colorectal Cancer Group (DCCG). *J Clin Oncol*. 2008;26(suppl):180s.
76. Bao R, et al. Targeting heat shock protein 90 with CUDC-305 overcomes erlotinib resistance in non-small cell lung cancer. *Mol Cancer Ther*. 2009;8(12):3296–3306.
77. Van den Eynden GG, et al. Differential expression of hypoxia and (lymph)angiogenesis-related genes at different metastatic sites in breast cancer. *Clin Exp Metastasis*. 2007;24(1):13–23.
78. Kuwai T, et al. Intratumoral heterogeneity for expression of tyrosine kinase growth factor receptors in human colon cancer surgical specimens and orthotopic tumors. *Am J Pathol*. 2008;172(2):358–366.
79. Weidner N, Semple JP, Welch WR, Folkman J. Tumor angiogenesis and metastasis—correlation in invasive breast carcinoma. *N Engl J Med*. 1991;324(1):1–8.
80. Stockmann C, et al. Deletion of vascular endothelial growth factor in myeloid cells accelerates tumorigenesis. *Nature*. 2008;456(7223):814–818.

# Cancer Prevention Research



## Validation of a Novel Statistical Model for Assessing the Synergy of Combined-Agent Cancer Chemoprevention

Junya Fujimoto, Maiying Kong, J. Jack Lee, et al.

*Cancer Prev Res* 2010;3:917-928. Published OnlineFirst August 4, 2010.

**Updated Version** Access the most recent version of this article at:  
doi:[10.1158/1940-6207.CAPR-10-0129](https://doi.org/10.1158/1940-6207.CAPR-10-0129)

**Cited Articles** This article cites 33 articles, 16 of which you can access for free at:  
<http://cancerpreventionresearch.aacrjournals.org/content/3/8/917.full.html#ref-list-1>

**Citing Articles** This article has been cited by 1 HighWire-hosted articles. Access the articles at:  
<http://cancerpreventionresearch.aacrjournals.org/content/3/8/917.full.html#related-urls>

**E-mail alerts** [Sign up to receive free email-alerts](#) related to this article or journal.

**Reprints and Subscriptions** To order reprints of this article or to subscribe to the journal, contact the AACR Publications Department at [pubs@aacr.org](mailto:pubs@aacr.org).

**Permissions** To request permission to re-use all or part of this article, contact the AACR Publications Department at [permissions@aacr.org](mailto:permissions@aacr.org).

## Research Article

## Validation of a Novel Statistical Model for Assessing the Synergy of Combined-Agent Cancer Chemoprevention

Junya Fujimoto<sup>1</sup>, Maiying Kong<sup>2</sup>, J. Jack Lee<sup>2</sup>, Waun Ki Hong<sup>1</sup>, and Reuben Lotan<sup>1</sup>

## Abstract

Lung cancer is the leading cause of cancer death, developing over prolonged periods through genetic and epigenetic changes induced and exacerbated by tobacco exposure. Many epigenetic changes, including DNA methylation and histone methylation and acetylation, are reversible. The use of agents that can modulate these aberrations are a potentially effective approach to cancer chemoprevention. Combined epigenetic-targeting agents have gained interest for their potential to increase efficacy and lower toxicity. The present study applied recently developed statistical methods to validate the combined effects of the demethylating agent 5-aza-2-deoxycytidine (5-AZA-CdR, or AZA, or decitabine) and the histone deacetylase inhibitor suberoylanilide hydroxamic acid (SAHA or vorinostat). This validation compared AZA alone with SAHA alone and with their combinations (at later or earlier time points and in varying doses) for inhibiting the growth of cell lines of an *in vitro* lung carcinogenesis system. This system comprises isogenic premalignant and malignant cells that are immortalized (earlier premalignant), transformed (later premalignant), and tumorigenic human bronchial epithelial cells [immortalized BEAS-2B and its derivatives 1799 (immortalized), 1198 (transformed), and 1170-I (tumorigenic)]. AZA alone and SAHA alone produced a limited (<50%) inhibition of cell growth, whereas combined AZA and SAHA inhibited cell growth more than either agent alone, reaching 90% inhibition under some conditions. Results of drug interaction analyses in the  $E_{\max}$  model and semiparametric model supported the conclusion that drug combinations exert synergistic effects (i.e., beyond additivity in the Loewe model). The present results show the applicability of our novel statistical methodology for quantitatively assessing drug synergy across a wide range of doses of agents with complex dose-response profiles, a methodology with great potential for advancing the development of chemopreventive combinations. *Cancer Prev Res*; 3(8); 917–28.

©2010 AACR.

## Introduction

Lung cancer is the leading cause of cancer death in the United States (1). The severe morbidity and mortality from lung cancer have not been reduced, and the overall 5-year survival rate is a discouraging ~15%, which has not

improved substantially (despite advances in various treatment modalities) over the past 20 years (2). For these reasons, novel approaches for preventing and treating lung cancer are urgently needed (2).

Activation of oncogenes or amplification or mutations in growth-factor signaling molecules, along with deletions, loss of expression, or diminished function of tumor-suppressor genes, are hallmarks of cancer development (3, 4). Epigenetic events are also implicated in cancer development, including the silencing of critical genes by aberrant methylation of CpG islands in gene promoter regions and by changes in chromatin structure resulting from alterations in the state of histone acetylation (5). Certain compounds that modulate DNA methylation [e.g., DNA methyltransferase inhibitors including 5-aza-2'-deoxycytidine (5-AZA-CdR, or AZA, or decitabine) and 5-azacytidine (azacitidine)] or inhibit histone deacetylation [e.g., histone deacetylase (HDAC) inhibitors including suberoylanilide hydroxamic acid (SAHA, or vorinostat), butyrate derivatives, depsipeptide, and valproic acid] can reactivate the expression of epigenetically silenced genes and induce differentiation or apoptosis of malignant cells (5). Furthermore, phase II and III clinical trials of AZA and

**Authors' Affiliations:** Departments of <sup>1</sup>Thoracic/Head and Neck Medical Oncology and <sup>2</sup>Biostatistics, The University of Texas M.D. Anderson Cancer Center, Houston, Texas

**Note:** J. Fujimoto and M. Kong contributed equally to this study and are co-first authors. J.J. Lee and R. Lotan contributed equally to this study and are co-corresponding authors.

Current address for M. Kong: Department of Bioinformatics and Biostatistics, School of Public Health and Information Sciences, University of Louisville, Louisville, KY 40292.

**Corresponding Authors:** Reuben Lotan, Department of Thoracic/Head and Neck Medical Oncology-Unit 432, The University of Texas M.D. Anderson Cancer Center, 1515 Holcombe Boulevard, Houston, TX 77030. Phone: 713-792-8467; Fax: 713-745-5656; E-mail: rlotan@mdanderson.org or J. Jack Lee, Department of Biostatistics-Unit 1411, The University of Texas M.D. Anderson Cancer Center, 1515 Holcombe Boulevard, Houston, TX 77030. Phone: 713-794-4158; Fax: 713-563-4243; E-mail: jjlee@mdanderson.org.

doi: 10.1158/1940-6207.CAPR-10-0129

©2010 American Association for Cancer Research.

phase III trials of several HDAC inhibitors have produced promising results in several neoplastic settings (6). Combinations of modulators of DNA methylation and HDAC inhibitors have been shown to exert more than additive effects or synergistic effects in certain preclinical studies with cultured tumor cell lines (7, 8).

Comprehensive experiments to establish synergistic, antagonistic, or additive interactions are very difficult to perform *in vivo* because the assessment of synergy requires many challenging animal experiments to measure responses to single and combined agents over different dose ranges and time periods. Therefore, many studies have used *in vitro* cell systems that usually are fully malignant (e.g., refs. 9, 10). Information on agent effects in premalignancy requires the availability of cells that represent distinct stages of carcinogenesis. An excellent *in vitro* lung carcinogenesis cell system based on isogenic cell lines has been developed from the well-characterized BEAS-2B cell line, which was derived by immortalizing normal human bronchial epithelial (HBE) cells through simian vacuolating virus 40 (SV40) T/Adeno12 virus (11). The three cell lines, 1799 (immortalized), 1198 (transformed), and 1170-I (tumorigenic), were then derived from BEAS-2B cells after subcutaneous growth as xenotransplants in nude mice. 1198 and 1170-I were isolated after *in vivo* exposure of BEAS-2B transplants to cigarette smoke condensate (12). The full complement of cell lines reflects a spectrum of neoplasia from early premalignancy (BEAS-2B) to midstage premalignancy (1799) to advanced premalignancy (transformed 1198) to malignancy (1170-I). This *in vitro* human lung carcinogenesis model offers opportunities to identify new agents or combinations of agents that affect early and/or late stages of lung carcinogenesis and are potentially relevant to human lung cancer chemoprevention and therapy. We previously used this cell system to test the efficacy of combined celecoxib and fenretinide (13).

The standard median-effect equation for analyzing a two-drug combination (14, 15) is limited in its ability to address the complex dose-response pattern of chemopreventive combinations involving various doses and schedules. This complexity is underscored by the dose-response pattern of increasing doses of single agents, which can involve a monotonic relationship (increasing response) until a plateau effect is reached, or can involve a U-shaped curve; that is, increasing activity up to a point where activity begins to decrease again with higher doses. Such nonmonotonic dose-response relationships may relate to the body's regulatory mechanism to maintain homeostasis and can be observed with natural agents. Therefore, we used the  $E_{\max}$  model to address the potential plateau effect of increasing doses of DNA methylation modulators and HDAC inhibitors and extended the semi-parametric model (which is a recently developed theoretical model for assessing two drugs given simultaneously) to examine the complex drug interaction contour of different doses and schedules of our two-drug combinations (16, 17). Our present study validated this novel statistical

methodology for quantitating the synergy indicated by previous qualitative analyses for the interaction between AZA and SAHA in suppressing the growth of premalignant and malignant HBE cells *in vitro*. The significance of this work is heightened by the growing, crucial potential of cancer chemoprevention with agent combinations (18).

## Materials and Methods

### Cells and cell culture

A collection of isogenic cells comprising an *in vitro* lung carcinogenesis model that includes immortalized (BEAS-2B and 1799), transformed (1198), and tumorigenic (1170-I) human HBE cells was obtained from Dr. Klein-Szanto (Fox Chase Cancer Center, Philadelphia, PA). BEAS-2B and 1799 cells were grown in keratinocyte serum-free medium (K-SFM, Gibco, Invitrogen Corporation) containing epidermal growth factor (5 ng/mL) and bovine pituitary extract (50 µg/mL) at 37°C in a humidified atmosphere of 95% air and 5% CO<sub>2</sub>. 1198 and 1170-I cells were maintained in K-SFM with 3% fetal bovine serum (HyClone). However, in some experiments, 1198 and 1170-I cells were cultured in serum-free K-SFM supplemented with epidermal growth factor and bovine pituitary extract as above. The four cell lines have been submitted for short tandem repeat (STR) genotyping (Powerplex 1.2 to the Johns Hopkins CORE Fragment Analysis Facility, Baltimore, MD) and the results obtained on November 9, 2009, have indicated that all cell lines had an identical STR pattern as expected because all were derived from the BEAS-2B. The STR profile was as follows: AMEL: X, Y; CSF1PO: 9, 12; D13S317: 13, 13; D16S539: 12, 12; D5S818: 12, 13; D7S820: 10, 13; TH01: 7, 9.3; TPOX: 6, 11; vWA: 17, 18. This pattern was distinct from those of all cell lines listed in the American Type Culture Collection STR Database for Human cell lines in a search done on November 16, 2009 (<http://www.atcc.org/CulturesandProducts/CellBiology/STRProfileDatabase/tabid/174/Default.aspx>).

### Reagents

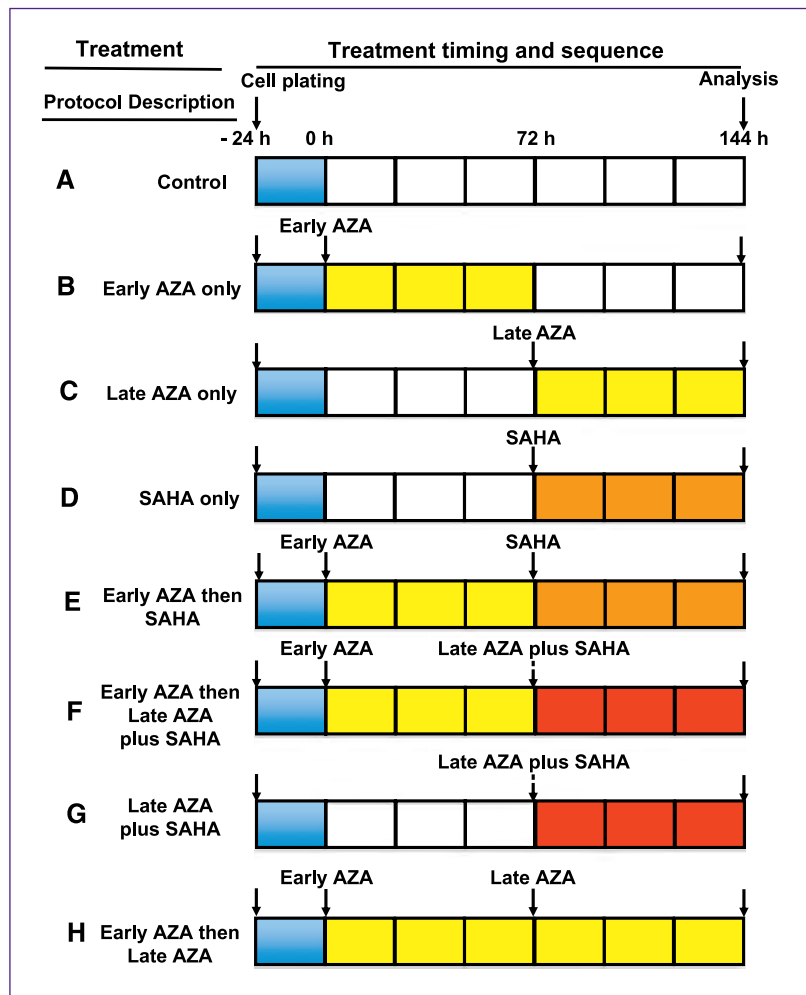
SAHA was purchased from the Midwest Research Institute. It was dissolved in DMSO and diluted into growth medium before cell exposure. AZA was purchased from Sigma Chemical Co. It was also dissolved in DMSO at a concentration of 10 mmol/L, and aliquots were stored at -80°C. The stock solutions were diluted to the desired concentrations with culture medium before their use, keeping the final concentration of DMSO <0.1%.

### Single agents: protocol and dose-response/growth inhibition model

The effects of AZA and SAHA as single agents were examined following an experimental design that is described pictorially in Fig. 1 (groups B–D). The cells were harvested by trypsinization from subconfluent stock cultures and seeded in 96-well plates at a density of 3,000 per well



**Fig. 1.** Graphic outline of the different protocols used for cell treatment with 5-AZA-CdR and SAHA in terms of scheduling, combining, and sequencing.



24 hours before treatment (time designated as -24 hours) to allow them to attach to the surface of the dishes. BEAS-2B and 1799 immortalized cells were analyzed for single-agent effects in their optimal growth medium, which is serum-free, whereas 1198 transformed cells and 1170-I tumorigenic cells were analyzed in both their optimal growth medium, which contains 5% serum, as well as in the same serum-free medium as the immortalized cells. AZA was added to untreated cells either at time 0 hour (Fig. 1; designated as early AZA) or 72 hours later (late AZA) or at both times. SAHA was added to untreated cells only at 72 hours. Cell numbers in triplicate wells were estimated at time 144 hours by the colorimetric sulforhodamine B assay with reagents purchased from Sigma-Aldrich using an automated plate reader (model MR5000, Dynatech Laboratories, Inc.), and the values were used to calculate the percentage of growth inhibition (%GI) using equation A:

$$\% \text{ GI} = (1 - A_t/A_c) \times 100 \quad (\text{A})$$

where  $A_t$  and  $A_c$  are the optical densities in treated and control cultures within the same plate, respectively (19).

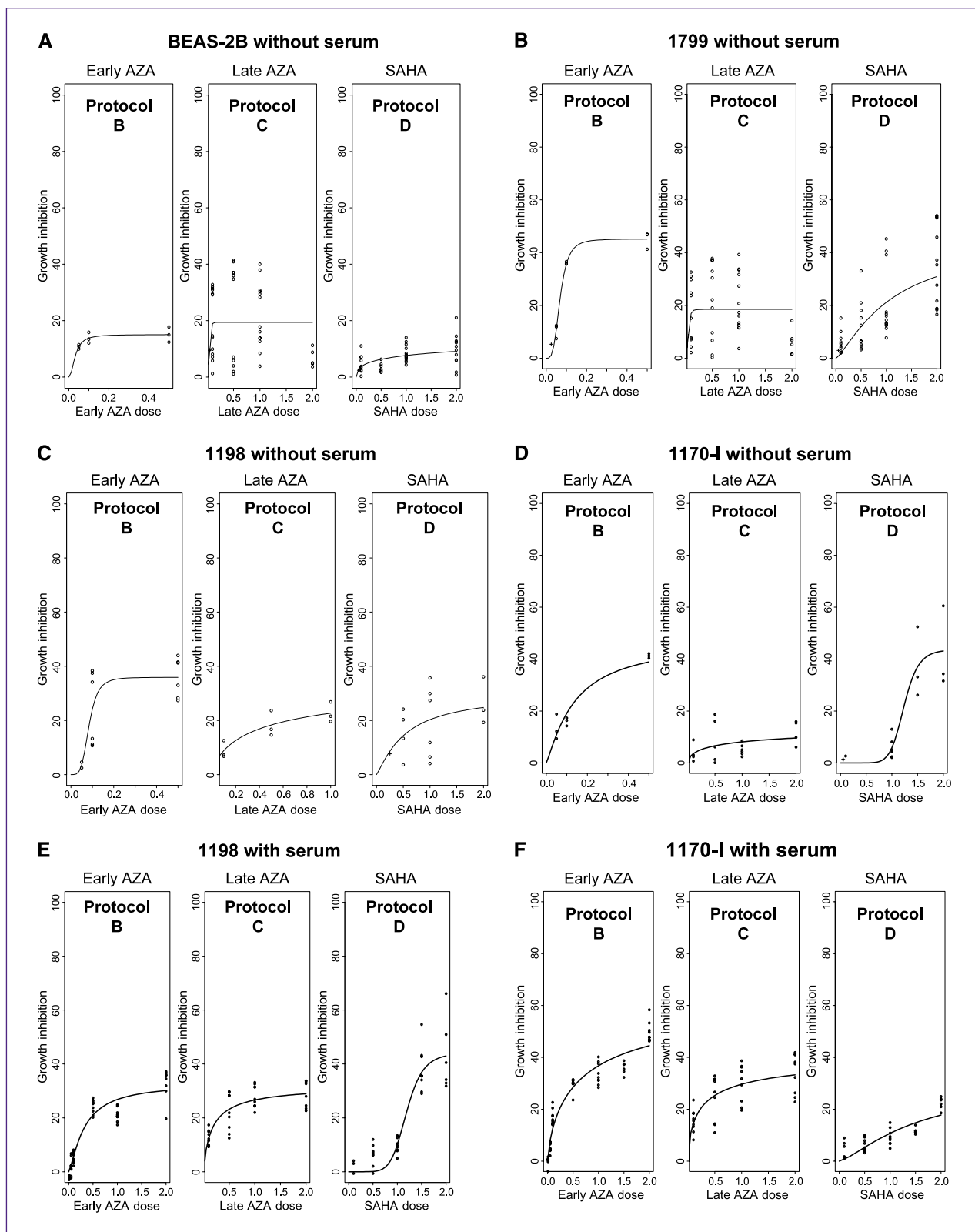
The percentage of growth inhibition versus the dose levels for early AZA, late AZA, and SAHA when used alone were plotted in Fig. 2A to F. In each figure panel, the solid line is the fitted dose-growth inhibition curve for each single agent based on the following  $E_{\max}$  model (20):

$$y = \frac{E_{\max} (d/ED_{50})^m}{1 + (d/ED_{50})^m} \quad (\text{B})$$

In the  $E_{\max}$  model (Eq. B),  $E_{\max}$  is the maximum growth inhibition attributable to the single agent,  $ED_{50}$  is the dose required to produce 50% of the maximal growth inhibition ( $0.5E_{\max}$ ), and  $d$  is the dose level that produces growth inhibition  $y$ . Note that the  $E_{\max}$  model does not require 100% growth inhibition as the dose of the drug increases to infinity. It reflects the nature of many chemopreventive agents; that is, as the dose continues to increase, the effect may reach a plateau.

#### Combined agents: growth inhibition and statistical method to assess synergy

The protocols used for treating cells with combinations of AZA and SAHA are depicted in Fig. 1 (protocols E, F,



**Fig. 2.** Dose-response curves of treating immortalized, transformed, and tumorigenic human bronchial epithelial cells with 5-AZA-CdR or SAHA as single agents. Cells were grown without serum (A, B, C, and D) or with serum (E and F) and treated with the indicated single agents according to protocols B, C, and D (see Fig. 1), where the growth inhibition was calculated relative to the growth of cells under protocol A (no treatment).

and G). In protocol E, AZA was added to cells at time 0 hour (early AZA) and SAHA was added 72 hours later. In protocol F, AZA was added at time 0 hour (early AZA), and a combination of AZA (late AZA) and SAHA was added 72 hours later. In protocol G, a combination of AZA (late AZA) and SAHA was added at 72 hours. We did not include an early SAHA treatment followed by AZA in the protocol because demethylation is a prolonged process (requiring DNA replication and incorporation of AZA), whereas HDAC inhibition is a rapid process that occurs within hours. Protocol H was a control for consecutive treatment of cells with early AZA and late AZA without SAHA. The cells were harvested 144 hours after treatment initiation, and growth inhibition was estimated as described above. To examine the growth inhibition for different combined doses, we summarized the mean and SEM for the observed growth inhibition at each combination dose. For each fixed early AZA dose level (range 0–0.5  $\mu\text{mol/L}$  without serum and range 0–2.0  $\mu\text{mol/L}$  with serum), we plotted the growth inhibition versus late AZA at each of the dose levels for SAHA (0–2  $\mu\text{mol/L}$ ), as shown in Fig. 3A to F. These plots enabled us to examine when the maximal growth inhibitions were obtained and how the growth inhibitions vary as dose levels for early AZA, late AZA, and SAHA increase. We decided to use the Loewe additivity model (15) for this analysis because we have recently shown that this model is one of the best general reference models for evaluating drug interactions. The Loewe additivity model (Eq. C) for three drugs can be described as

$$\frac{d_1}{D_{y,1}} + \frac{d_2}{D_{y,2}} + \frac{d_3}{D_{y,3}} = 1 \quad (\text{C})$$

where  $(d_1, d_2, d_3)$  is the combination dose of early AZA, late AZA, and SAHA in the mixture that produces a growth inhibition  $\gamma$  under additivity;  $D_{y,1}$ ,  $D_{y,2}$ , and  $D_{y,3}$  are the respective doses of early AZA, late AZA, and SAHA that result in the growth inhibition  $\gamma$  when used alone. The Loewe additivity model can be equivalently written as

$$d_1 + \frac{D_{y,1}}{D_{y,2}}d_2 + \frac{D_{y,1}}{D_{y,3}}d_3 = D_{y,1}$$

where the ratio  $D_{y,1}/D_{y,2}$  is called the relative potency of drug 2 versus drug 1. Thus, the growth inhibition produced by drug 2 at dose level  $d_2$  is the same as the growth inhibition produced by drug 1 alone at dose level  $D_{y,1}d_2/D_{y,2}$ . Similarly, the growth inhibition produced by drug 3 at dose level  $d_3$  is the same as the growth inhibition produced by drug 1 alone at dose level  $D_{y,1}d_3/D_{y,3}$ . Thus, without drug interaction, the growth inhibition produced by the combination dose  $(d_1, d_2, d_3)$  should be the same as the growth inhibition produced by drug 1 alone at dose level  $d_1 + \frac{D_{y,1}}{D_{y,2}}d_2 + \frac{D_{y,1}}{D_{y,3}}d_3$ ; that is,  $D_{y,1}$ . Based on the estimated dose–growth inhibition curve for each single drug and the Loewe additivity model, one may predict

the additive growth inhibition at a combination dose by solving  $\gamma$  in Eq. C. Synergy occurs when the actual growth inhibition is more than the predicted growth inhibition, whereas antagonism occurs when the actual growth inhibition is less than the predicted growth inhibition.

To obtain an overall picture of drug interactions for the combination doses of early AZA, late AZA, and SAHA, we extend the semiparametric model (17) to assess the growth inhibition beyond additivity for the three drug combinations. To this end, we first obtained the differences of the observed growth inhibitions and the predicted growth inhibition at each observed combination dose  $(d_{1i}, d_{2i}, d_{3i})$  ( $i = 1, \dots, n$ ). Based on this information, we can then estimate the function  $f(d_1, d_2, d_3)$ , the growth inhibition beyond additivity, for any combination dose  $(d_1, d_2, d_3)$  by using the thin plate splines (21), where  $f(d_1, d_2, d_3)$  can be expressed as

$$f(d_1, d_2, d_3) = \gamma_0 + \gamma_1 d_1 + \gamma_2 d_2 + \gamma_3 d_3 + \sum_{k=1}^K v_k \eta(\|(d_1, d_2, d_3)^T - (\kappa_{1k}, \kappa_{2k}, \kappa_{3k})^T\|)$$

where

$$\eta(\|(d_1, d_2, d_3)^T - (\kappa_{1k}, \kappa_{2k}, \kappa_{3k})^T\|) = \sqrt{(d_1 - \kappa_{1k})^2 + (d_2 - \kappa_{2k})^2 + (d_3 - \kappa_{3k})^2}$$

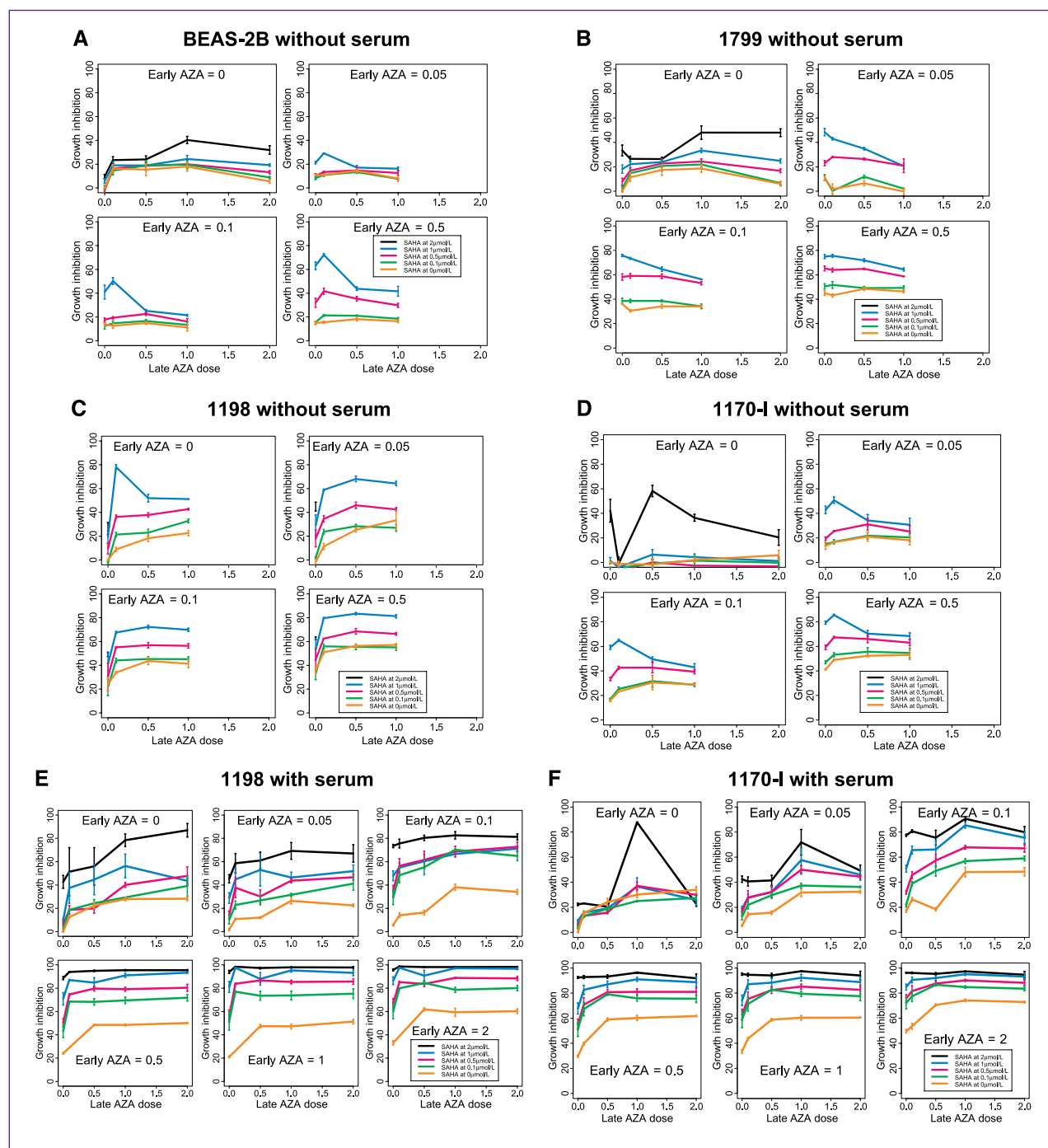
and  $(\kappa_{1k}, \kappa_{2k}, \kappa_{3k})$  ( $k = 1, \dots, K$ ) are the knots for the thin plate spline, which are selected as all the different observed combination doses. We used the technique developed by Kong and Lee (17) to estimate the function  $f(d_1, d_2, d_3)$ . In addition, we constructed a 95% confidence interval for  $f(d_1, d_2, d_3)$ . Thus, different patterns of drug interactions can be clearly identified.

In short, the  $E_{\text{max}}$  model (20) was applied to describe the dose–growth inhibition relationship of early AZA, late AZA, or SAHA used alone. The predicted additive growth inhibition for combinations was calculated based on the Loewe additivity model and the marginal dose–growth inhibition curves. After that, the growth inhibition beyond additivity was determined by applying the semiparametric model (17) such that the patterns of drug interactions (i.e., synergy, additivity, or antagonism) over all experimental combinations can be characterized.

## Results

### Single agents

The dose–response curve for each single drug calculated using  $E_{\text{max}}$  model in S-PLUS are presented in Fig. 2A–F. When early AZA, late AZA, and SAHA were used alone, the estimated maximum growth inhibitions ( $E_{\text{max}}$ ) of BEAS-2B cells were 15%, 19%, and 19%, respectively (Fig. 2A). Note that these estimated maximum growth inhibitions are obtained based on the  $E_{\text{max}}$  model (E2),



**Fig. 3.** Dose-response curves of treating immortalized, transformed, and tumorigenic human bronchial epithelial cells with combinations of 5-AZA-CdR and SAHA. Cells were grown without serum (A, B, C, and D) or with serum (E and F) and treated with the indicated agents according to protocols E, F, G, and H (see Fig. 1). Growth inhibition was calculated relative to the growth of cells under protocol A (no treatment).

which may be larger than the maximum observed growth inhibition. The estimated maximum growth inhibitions of 1799 cells for early AZA, late AZA, and SAHA used alone were 45%, 19%, and 45%, respectively (Fig. 2B). Treatment of 1198 cells with early AZA, late AZA, and SAHA

alone in medium without serum (Fig. 2C) resulted in estimated maximum growth inhibitions of 36%, 36%, and 30%, respectively. Similar results (33%, 33%, and 44%, respectively) were observed when 1198 cells were treated with these agents in medium with serum (Fig. 2E). Treatment

of 1170-I cells with early AZA, late AZA, and SAHA alone resulted in estimated maximum growth inhibitions of 47%, 16%, and 44%, respectively, in medium without serum (Fig. 2D) and 55%, 42%, and 30%, respectively, in the presence of serum (Fig. 2F).

The four cell lines exhibited dose-dependent inhibition of growth, which was variable among the different cell lines and between the two agents and growth media. For most cell lines, the growth inhibition to AZA peaked at low doses (e.g., 0.5  $\mu\text{mol/L}$ ) and was not improved much with increased agent dose up to 2  $\mu\text{mol/L}$ . In contrast, most cell lines showed progressive increase in growth inhibition by SAHA as the dose of this agent increased up to 2  $\mu\text{mol/L}$ . The presence of serum increased the sensitivity of 1198 cells to late AZA and SAHA (Fig. 2C and E), whereas serum increased the sensitivity of 1170-I cells to early AZA and late AZA (Fig. 2F).

### Combined agents

Because, with a few exceptions, AZA alone and SAHA alone were not very potent (<50% growth inhibition), we examine the possibility that a combination of the two agents, which reverse epigenetic gene silencing by distinct mechanisms, may produce additive or synergistic effects on growth inhibition. The dose-response curves for the drug combinations administered according to protocols E to H (Fig. 1) are presented in Fig. 3A to F. When the Loewe additivity model was applied to these results for each cell line under each condition (growth with or without serum), we obtained the predicted growth inhibitions for each combination dose. We then estimated the growth inhibition beyond additivity by applying the semiparametric model as described in Materials and Methods. The differences of the observed growth inhibitions and their predicted growth inhibitions (namely, residuals) based on the pure additivity model were plotted versus the predicted growth inhibitions in panel 1s of Fig. 4A to F, and the residuals based on the semiparametric model were plotted versus the predicted growth inhibitions in panel 2s of Fig. 4A to F. When the residuals based on the pure additivity model are small and centered around zero, the result suggests that the pure additivity model fits the data well. Positive residuals from the pure additivity model indicate synergistic combinations whereas negative residuals illustrate antagonistic effects.

By examining panel 1s of all six data sets, we conclude that the additivity model could not adequately describe the observed growth inhibition data. Most residuals from the pure additivity model lie in the positive regions, suggesting synergistic effects. After applying the semiparametric method for modeling the combination data, the resulting residuals are centered around zero, as shown in panel 2s of the corresponding figures. Furthermore, Fig. 5 shows the corresponding contour plots of the residuals beyond additivity using the semiparametric model. Each panel displays the contour plot of the beyond additivity growth inhibition of SAHA and late AZA by conditioning on early AZA. More detailed descriptions on the

patterns of drug interactions for each individual cell lines are described below.

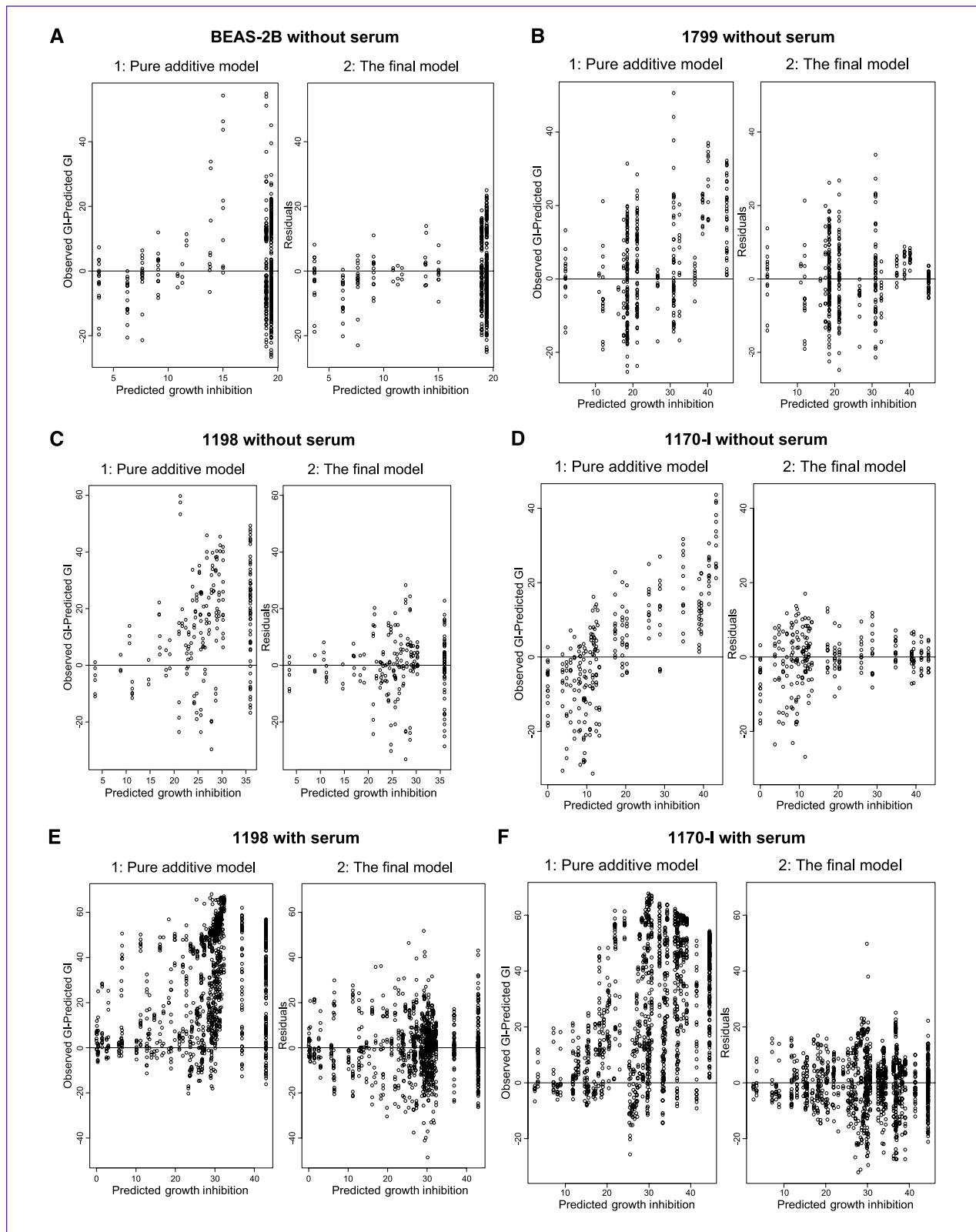
**Immortalized BEAS-2B and 1799 cells treated with early AZA, late AZA, and SAHA combinations in serum-free medium.** Growth inhibition of BEAS-2B cells (Fig. 3A) and 1799 cells (Fig. 3B) increased as early AZA increased up to 0.5  $\mu\text{mol/L}$  and SAHA increased up to 1.0  $\mu\text{mol/L}$ . The figure also indicates that the combination of both agents even at low doses, for example, early AZA at 0.5  $\mu\text{mol/L}$ , late AZA at 0.1  $\mu\text{mol/L}$ , and SAHA at 1  $\mu\text{mol/L}$ , can achieve more than 70% growth inhibition of BEAS-2B cells, whereas any single agent only achieved <20% growth inhibition. In 1799 cells, late AZA had no enhancing effect but the combination of early AZA at 0.5  $\mu\text{mol/L}$  and SAHA at 1  $\mu\text{mol/L}$  achieved nearly 80% growth inhibition compared with <45% by any single agent.

The residuals based on the Loewe additivity model versus the predicted growth inhibition are presented in Fig. 4A.1 and B.1 for BEAS-2B and 1799 cells, respectively. Many of the differences, particularly for higher predicted growth inhibitions, are above zero, suggesting that this pure additivity model does not describe the data adequately. Applying the semiparametric model to each of the data sets, residual plots in Fig. 4A.2 for BEAS-2B cells and Fig. 4B.2 for 1799 cells show that the residuals are centered around zero, indicating that the semiparametric model is a better model to describe these experimental data. We have also drawn the contour plot for the growth inhibitions beyond additivity at each fixed-dose early AZA level as shown in Fig. 5A for BEAS-2B cells and in Fig. 5B for 1799 cells. Panels 1, 2, and 3 in each figure show that the combination doses in the areas above the thick solid curves (in light blue) are synergistic, the combination doses in the areas below the thick solid curves and above the thick dashed lines (uncolored) are additive, and the combination doses in the area under the thick dashed lines (in light pink) are antagonistic. The combination doses with early AZA at 0.5  $\mu\text{mol/L}$  (panel 4) are mostly synergistic.

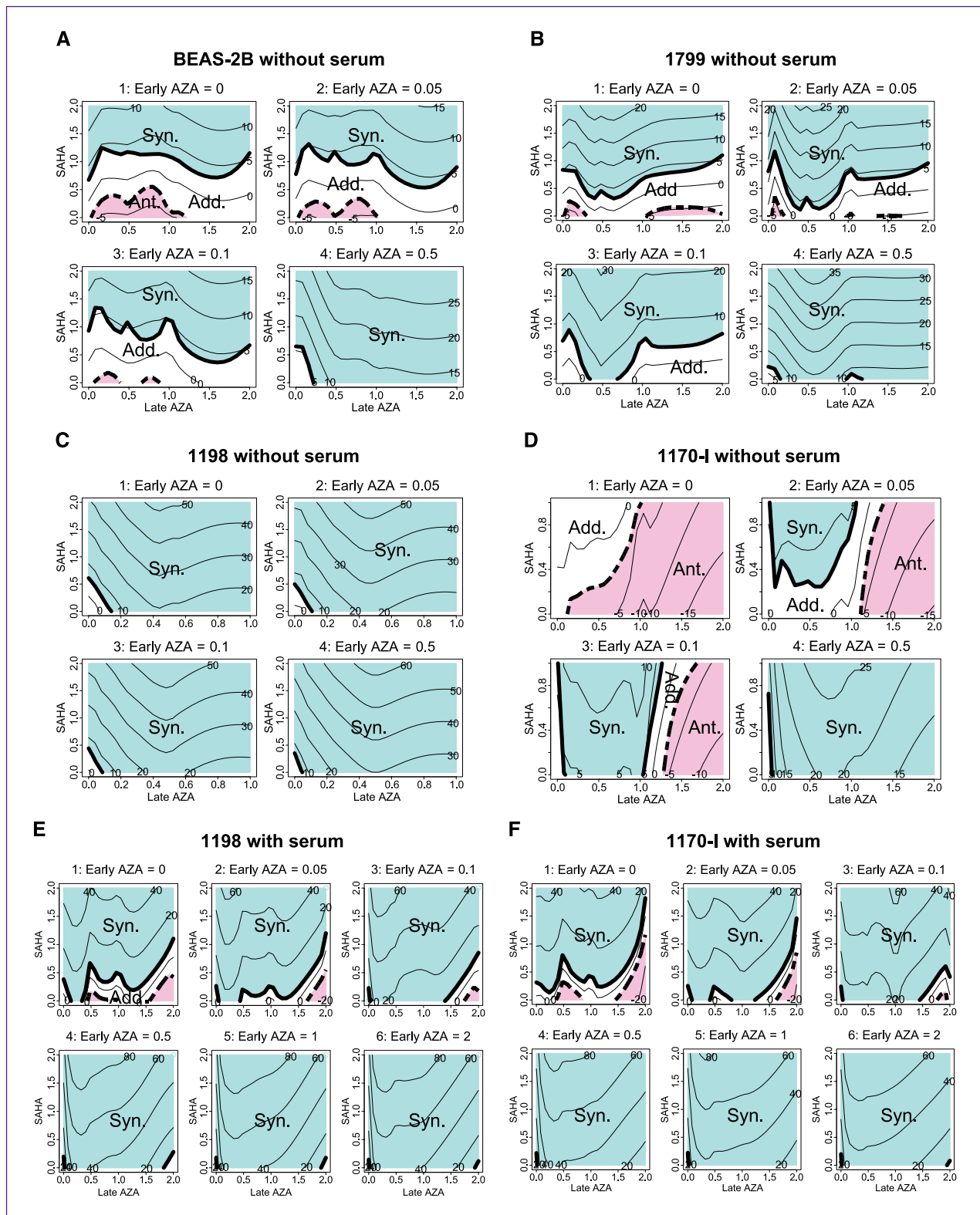
**Transformed 1198 cells treated with early AZA, late AZA, and SAHA or their combination in serum-free and serum-supplemented media.** We found that in 1198 cells grown in serum-free medium, growth inhibition increased as early AZA increased up to 0.5  $\mu\text{mol/L}$  as well as SAHA increased up to 1  $\mu\text{mol/L}$  (Fig. 3C). Further enhancement of growth inhibition was achieved when a small dose of late AZA (e.g., 0.1  $\mu\text{mol/L}$ ) was added, but no further inhibition was obtained by increasing the late AZA dose to 1  $\mu\text{mol/L}$  (Fig. 3C). The combination of 0.5  $\mu\text{mol/L}$  early AZA, 0.1  $\mu\text{mol/L}$  late AZA, and 1  $\mu\text{mol/L}$  SAHA achieved almost 80% growth inhibition, whereas the best single agent could only achieve <36% growth inhibition.

When 1198 cells were treated in serum-supplemented medium, growth inhibition increased as early AZA increased up to 2  $\mu\text{mol/L}$ , late AZA increased to 1  $\mu\text{mol/L}$ , and SAHA increased up to 2  $\mu\text{mol/L}$  (Fig. 3E). Increasing the early AZA doses above 0.5  $\mu\text{mol/L}$  did not improve its growth-inhibitory effects in combination with 0.5, 1, and





**Fig. 4.** A-F, panel 1 shows the plots of the difference between observed and predicted growth inhibition on the Y axis versus predicted growth inhibition on the X axis based on the pure additivity model, whereas panel 2 shows the plots of the difference between observed and fitted growth inhibition on the Y axis versus the predicted growth inhibition on the X axis based on the semiparametric model.



**Fig. 5.** Contour plots for the growth inhibitions beyond additivity of the indicated cell lines at each fixed dose level of early AZA with SAHA doses on the Y axis and the late AZA doses on the X axis. The combination doses in the light-blue areas are synergistic (Syn.); the combination doses in the uncolored areas are additive (Add.); and the combination doses in the light-pink areas are antagonistic (Ant.). For the cells grown in serum-free medium (A–D), when the dose level for early AZA is nonzero, the experimental dose range for late AZA is 0 to 1  $\mu\text{mol/L}$ , and the dose range for SAHA is 0 to 1  $\mu\text{mol/L}$ .



2  $\mu\text{mol/L}$  SAHA. The combination doses of early AZA (0.5  $\mu\text{mol/L}$ ), late AZA (0.1  $\mu\text{mol/L}$ ), and SAHA (1  $\mu\text{mol/L}$ ) achieved 90% growth inhibition, whereas, under the same condition, each single agent could only achieve <44% growth inhibition (Figs. 2E and 3E).

Based on the Loewe additivity model, we obtained the predicted additive growth inhibition for each combination dose as previously described. For 1198 cells treated in the absence (Fig. 4C.1) and in the presence of serum (Fig. 4E.1), most of the residuals based on the Loewe additivity model were found to be above zero, indicating that the additive model is not adequate for describing the data. However, the semiparametric model was found to be a better model to describe the experimental data as indicated by the finding that the residuals from the semiparametric model are centered around zero in Fig. 4C.2 and E.2.

Contour plots for the growth inhibitions without and with serum beyond additivity at each fixed dose level for early AZA indicated the type of drug interactions (Fig. 5C and E, respectively). In each panel, the combination doses in the area above the thick solid curve (light-blue area) are synergistic. Figure 5C and E indicates that most of the combination doses of SAHA, late AZA, and early AZA are synergistic.

**Tumorigenic 1170-I cells treated with combinations of early AZA, late AZA, and SAHA in serum-free and serum-supplemented media.** Treatment of 1170-I cells with combination of agents in serum-free medium showed that the response from 0.1 to 1  $\mu\text{mol/L}$  SAHA was improved by pretreatment with early AZA in the dose range from 0.05 to 0.5  $\mu\text{mol/L}$  (Fig. 3D). Addition of late AZA at a low dose level of 0.1  $\mu\text{mol/L}$  had a small effect on growth inhibition; however, addition of late AZA at 0.5  $\mu\text{mol/L}$  or beyond did not increase growth inhibition. The combination of 0.5  $\mu\text{mol/L}$  early AZA, 0.1  $\mu\text{mol/L}$  late AZA, and 1  $\mu\text{mol/L}$  SAHA achieved 80% growth inhibition, whereas any single agent could only achieve <47% growth inhibition (Fig. 2D).

When 1170-I cells were treated in the presence of serum, their sensitivity to the combination treatment increased relative to the serum-free treatment. Growth inhibition increases as early AZA dose increased up to 0.5  $\mu\text{mol/L}$  and SAHA dose increased up to 2  $\mu\text{mol/L}$ . The addition of late AZA enhanced the growth-inhibitory effects when early AZA doses were 0, 0.05, or 0.1  $\mu\text{mol/L}$ , but only slightly for early AZA dose at 0.5  $\mu\text{mol/L}$  and beyond, reaching plateaus for late AZA dose at 0.5  $\mu\text{mol/L}$  and beyond (Fig. 3F). The efficacy of the combination of early AZA and SAHA reached a plateau after early AZA doses >0.5  $\mu\text{mol/L}$ . Figure 3F also indicates that the combination of 0.5  $\mu\text{mol/L}$  early AZA and 2  $\mu\text{mol/L}$  SAHA achieved 85% growth inhibition, which was much higher than any single agent could achieve.

Under the additive model, Fig. 4D.1 shows that there were some negative residuals when the predicted growth inhibition was small. Moreover, most residuals in Fig. 4D.1 (in the absence of serum) and F.1 (in the presence of serum) were positive, indicating that the additive model had failed to describe the data well. In contrast, the residual plots based on the semiparametric model (Fig. 4D.2 and F.2) show that the residuals are centered around zero,

indicating that the semiparametric model describes the experimental data well. The contour plots for the growth inhibitions beyond additivity at each fixed dose level for early AZA are shown in Fig. 5D and F for cells treated in serum-free and serum-supplemented medium, respectively. In each panel in Fig. 5D, the combination doses in the light-blue areas are synergistic, the combination doses in the light-pink areas are antagonistic, and the combination doses in the uncolored areas are additive. When tumorigenic 1170-I cells were treated in serum-free medium (Fig. 5D.1), in the absence of early AZA, the concurrent combination of SAHA and late AZA are antagonistic or additive. The addition of a low dose of late AZA following early AZA enhanced the synergistic effect (Fig. 5D). In the presence of serum, most of the combination doses of early AZA, late AZA, and SAHA were synergistic except when the early AZA and SAHA are both low; for example, early AZA  $\leq 0.05$   $\mu\text{mol/L}$  and SAHA  $\leq 0.5$   $\mu\text{mol/L}$  (Fig. 5F).

It is noted that the dose range for late AZA is 0 to 1  $\mu\text{mol/L}$  and the dose range for SAHA is 0 to 1  $\mu\text{mol/L}$  for cells grown in serum-free medium (Fig. 5A–D) when the dose level for early AZA is nonzero. Although the statistical model provides estimates in the entire dose range, the extrapolations beyond the actual data range should be done with caution.

## Discussion

Although complex, the present findings clearly indicate that combining AZA with SAHA synergistically inhibited growth in most settings (versus results of either agent alone) and that increasing SAHA doses (within the studied range) almost always increased growth inhibition. We also found in regard to the AZA-SAHA combinations that the dose-response (growth inhibition) pattern of late AZA varied between combinations with lower-concentration early AZA (<0.5  $\mu\text{mol/L}$ ) and higher-concentration early AZA ( $\geq 0.5$   $\mu\text{mol/L}$ ; the concentration range of early and late AZA was 0–2  $\mu\text{mol/L}$ ). As evidenced by these data, early and late AZA were evaluated as two different drugs, illustrating the applicability of our model to three-drug combinations and its value for finding complex, subtle synergistic effects. Furthermore, the overall growth-inhibition results validate our novel statistical method for quantitatively assessing drug synergy (over a wide range of doses and different schedules and medium conditions) with comparisons that can be tested for significance. Although effective chemopreventively (in immortalized BEAS-2B or 1799 cells and transformed 1198 cells) or therapeutically (in malignant 1170-I cells), this method is especially important for assessing the complex dose-response relationships of chemopreventive combinations. Another advantage of the method for chemoprevention is its ability to analyze synergistic interactions between agents or doses with relatively modest effects.

Several agent combinations are more effective than single agents in treating certain cancers (9, 22–24). It is thought that future strategies will focus on synergistic drug

combinations that can enhance efficacy by targeting several alternative pathways and decrease side effects (e.g., by lowering constituent-agent doses). These fundamental principles of combination approaches are applicable to both therapy and chemoprevention and to cytotoxic and noncytotoxic agents. Epigenetic therapy targets different chromatin modifications (e.g., methylation and acetylation) to reach an effective reversal of epigenetic alterations (25). The use of HDAC inhibitors and demethylating agents in chemoprevention has received increasing attention as the role of epigenetic alteration at early stages of cancer development has been recognized (26–28). Indeed, combinations of demethylating agents (mostly decitabine) and HDAC inhibitors (phenyl butyrate, valproic acid, SAHA) have shown enhanced activity relative to single agents in various preclinical studies (7, 29, 30), and some combinations have been tested in animal models and clinical trials (31, 32). For example, short-term, low-dose AZA decreased the incidence of tobacco carcinogen-induced lung neoplasms by 30%, the HDAC inhibitor phenylbutyrate alone was ineffective, and combined AZA and phenylbutyrate reduced these neoplasms by >50% in female mice, suggesting that the combination effect was more than additive (29). In another mouse model, a combination of AZA and the HDAC inhibitor valproic acid was more effective than either agent alone in preventing the development of spontaneous medulloblastoma and rhabdomyosarcoma in *Patched (Ptch)* heterozygous mice (30). These studies used a single dose of each agent and thus precluded the determination of additivity or synergy for the combinations. Even previous *in vitro* studies, however, suggested a synergistic interaction between decitabine and HDAC inhibitors, absent any formal quantitative analysis (33) or with calculations of the combination index (CI; refs. 7, 8, 34).

We did not address the mechanisms by which AZA, SAHA, and their combination inhibited cancer cell growth because we focused this investigation on the nature of the interactions between these epigenetic modulators. We and others have shown previously that SAHA and AZA can modulate the expression of genes involved in cell cycle progression and apoptosis induction by both the mitochondrial and death-receptor pathways (35); these effects could mediate these agents' synergistic inhibitory effects on cell growth in the system reported here as well.

Studying the effects of 48-hour treatment with AZA or SAHA or both combined in breast carcinoma MDA-MB-231 cells, Beltran et al. (8) generated dose-effect curves and median-effect plots of cell proliferation, using a median-effect equation,  $E_{\max} = 1$ , that can be considered a special case of the  $E_{\max}$  model. The median-effect dose ( $ED_{50}$ ) and slope ( $m$ ) were calculated from the median-effect plots and introduced into the isobologram equation for the calculating the CI (14, 15). They found CI values between 0.5 and 1, indicating a synergistic effect.

Kumagai et al. (7) analyzed the *in vitro* effects of the combination of AZA and SAHA on pancreatic cancer cells. Their colorimetric 3-(4,5-dimethylthiazol-2-yl)-2,5-diphenyltetrazolium bromide assay showed that treatment for

96 hours with SAHA (2.5  $\mu\text{mol/L}$ ) plus AZA (1  $\mu\text{mol/L}$ ) in medium with 10% fetal bovine serum decreased cell growth of the pancreatic cancer cell lines PANC-1 by 31% and AsPC-1 by 16% (versus control). These levels of growth inhibition were much higher than those accomplished with each agent alone at the same concentrations. They then used the CI to evaluate the nature of the interaction between the two agents (29). The CIs were 0.54 (<1.0) for PANC-1 and 0.48 (<1.0) for AsPC-1. Because both CIs were <1, the authors concluded that combined AZA and SAHA had synergistic antiproliferative effects on these pancreatic cancer cells.

A major contribution of this report is in extending and applying novel statistical methods to complex combined-agent studies. Single chemopreventive agents usually have a limited ability to inhibit growth. Chou and Talalay's median-effect equation (14) assumes that growth inhibition reaches 100% at a certain (increased) dose, which is not always true. Hence, we applied the  $E_{\max}$  model to address the phenomenon of a plateau dose, past which growth inhibition does not advance toward 100%. We plotted additivity in the Loewe model and then compared this plot with that of overall activity to determine whether Loewe additivity provided an adequate fit of the data. Many combination doses produced positive residual plots, indicating drug synergy. We then applied the semiparametric model proposed by Kong and Lee (17) to model combination drug effects beyond additivity. Furthermore, many older methods require fixed ratios of doses in combinations (also known as the ray design) for calculating the CI (14, 34). In contrast, our method can be applied to any dose ratios and thus can present an overall picture of drug interactions for the entire range of experimental doses. The patterns of drug interactions based on our approach are fully determined by the experimental data without any presumed parametric models. By examining growth inhibition over all combined doses (Fig. 3) and the patterns of drug interactions (Fig. 5), we can identify low doses with highly synergistic combination effects on growth inhibition.

Although translating *in vitro* data to the clinic requires caution, our results have clinical implications in demonstrating that low doses of AZA (<0.5  $\mu\text{mol/L}$ ) and SAHA (<1  $\mu\text{mol/L}$ ) can effectively suppress the proliferation of immortalized lung cells and cells representing later premalignant and malignant lung epithelial lesions. Our results also indicate that early administration of AZA greatly enhances the effect of combined AZA and SAHA. Low combined doses of these agents were effective and have the potential to decrease adverse effects of the higher dose that either agent alone would need to be effective; this reduction in toxicity is an important advantage for chemoprevention, where side effects should be minimal or absent.

In conclusion, the present findings suggest that combined demethylating agents and HDAC inhibitors may be a rational approach for clinical cancer chemoprevention or therapy trials in the lung. These results also validate our novel statistical method for quantitatively assessing drug synergy. We succeeded in assessing the complex

dose-response relationship of chemopreventive combinations and in analyzing synergistic interactions between doses with relatively modest single-agent effects, and this methodology has great potential for advancing the development of cancer chemoprevention with combined agents, one of the most important directions of this field.

## Disclosure of Potential Conflicts of Interest

No potential conflicts of interest were disclosed.

## References

- Jemal A, Siegel R, Ward E, et al. Cancer statistics, 2008. *CA Cancer J Clin* 2008;58:71–96.
- Herbst RS, Heymach JV, Lippman SM. Lung cancer. *N Engl J Med* 2008;359:1367–80.
- Hanahan D, Weinberg RA. The hallmarks of cancer. *Cell* 2000;100:57–70.
- Sato M, Shames DS, Gazdar AF, Minna JD. A translational view of the molecular pathogenesis of lung cancer. *J Thorac Oncol* 2007;2:327–43.
- Jones PA, Baylin SB. The epigenomics of cancer. *Cell* 2007;128:683–92.
- Okii Y, Aoki E, Issa JP. Decitabine—bedside to bench. *Crit Rev Oncol Hematol* 2007;61:140–52.
- Kumagai T, Wakimoto N, Yin D, et al. Histone deacetylase inhibitor, suberoylanilide hydroxamic acid (Vorinostat, SAHA) profoundly inhibits the growth of human pancreatic cancer cells. *Int J Cancer* 2007;121:656–65.
- Beltran AS, Sun X, Lizardi PM, Blancafort P. Reprogramming epigenetic silencing: artificial transcription factors synergize with chromatin remodeling drugs to reactivate the tumor suppressor mammary serine protease inhibitor. *Mol Cancer Ther* 2008;7:1080–90.
- Li T, Ling YH, Goldman ID, Perez-Soler R. Schedule-dependent cytotoxic synergism of pemetrexed and erlotinib in human non-small cell lung cancer cells. *Clin Cancer Res* 2007;13:3413–22.
- Giovannetti E, Lemos C, Tekle C, et al. Molecular mechanisms underlying the synergistic interaction of erlotinib, an epidermal growth factor receptor tyrosine kinase inhibitor, with the multitargeted antifolate pemetrexed in non-small-cell lung cancer cells. *Mol Pharmacol* 2008;73:1290–300.
- Reddel RR, Ke Y, Gerwin BI, et al. Transformation of human bronchial epithelial cells by infection with SV40 or adenovirus-12 SV40 hybrid virus, or transfection via strontium phosphate coprecipitation with a plasmid containing SV40 early region genes. *Cancer Res* 1988;48:1904–9.
- Klein-Szanto AJ, Iizasa T, Momiki S, et al. A tobacco-specific N-nitrosamine or cigarette smoke condensate causes neoplastic transformation of xenotransplanted human bronchial epithelial cells. *Proc Natl Acad Sci U S A* 1992;89:6693–7.
- Schroeder CP, Kadara H, Lotan R, et al. Involvement of mitochondrial and Akt signaling pathways in augmented apoptosis induced by a combination of low doses of celecoxib and N-(4-hydroxyphenyl) retinamide in premalignant human bronchial epithelial cells. *Cancer Res* 2006;66:9762–70.
- Chou TC, Talalay P. Quantitative analysis of dose-effect relationships: the combined effects of multiple drugs or enzyme inhibitors. *Adv Enzyme Regul* 1984;22:27–55.
- Chou TC. Assessment of synergistic and antagonistic effects of chemotherapeutic agents *in vitro*. *Contrib Gynecol Obstet* 1994;19:91–107.
- Lee JJ, Kong M, Ayers GD, Lotan R. Interaction index and different methods for determining drug interaction in combination therapy. *J Biopharm Stat* 2007;17:461–80.
- Kong M, Lee JJ. A semiparametric response surface model for assessing drug interaction. *Biometrics* 2008;64:396–405.
- Sporn MB, Hong WK. Clinical prevention of recurrence of colorectal

## Grant Support

The David Workman award from the Samuel Waxman Cancer Research Foundation (W.K. Hong and R. Lotan), grants DAMD17-02-1-0706 and W81XWH-07-1-0306 from the Department of Defense (W.K. Hong, J.J. Lee, and R. Lotan), and grant CA16672 from the National Cancer Institute.

The costs of publication of this article were defrayed in part by the payment of page charges. This article must therefore be hereby marked advertisement in accordance with 18 U.S.C. Section 1734 solely to indicate this fact.

Received 06/08/2010; accepted 06/09/2010; published OnlineFirst 07/27/2010.

- adenomas by the combination of difluoromethylornithine and sulindac: an important milestone. *Cancer Prev Res* 2008;1:9–11.
- Skehan P, Storeng R, Scudiero D, et al. New colorimetric cytotoxicity assay for anticancer-drug screening. *J Natl Cancer Inst* 1990;82:1107–12.
  - Ting N. Dose finding in drug development. New York: Springer; 2006.
  - Green PJ, Silverman BW. Nonparametric regression and generalized linear models: a roughness penalty approach. London: Chapman & Hall/CRC; 1993.
  - Kano Y, Tanaka M, Akutsu M, et al. Schedule-dependent synergism and antagonism between pemetrexed and docetaxel in human lung cancer cell lines *in vitro*. *Cancer Chemother Pharmacol* 2009;64:1129–37.
  - Raynal NJ, Charbonneau M, Momparler LF, Momparler RL. Synergistic effect of 5-aza-2'-deoxycytidine and genistein in combination against leukemia. *Oncol Res* 2008;17:223–30.
  - Nagai S, Takenaka K, Sonobe M, Wada H, Tanaka F. Schedule-dependent synergistic effect of pemetrexed combined with gemcitabine against malignant pleural mesothelioma and non-small cell lung cancer cell lines. *Chemotherapy* 2008;54:166–75.
  - Altucci L, Minucci S. Epigenetic therapies in hematological malignancies: searching for true targets. *Eur J Cancer* 2009;45:1137–45.
  - Kelloff GJ, Lippman SM, Dannenberg AJ, et al. Progress in chemoprevention drug development: the promise of molecular biomarkers for prevention of intraepithelial neoplasia and cancer—a plan to move forward. *Clin Cancer Res* 2006;12:3661–97.
  - Issa JP. Cancer prevention: epigenetics steps up to the plate. *Cancer Prev Res* 2008;1:219–22.
  - Sharma S, Kelly TK, Jones PA. Epigenetics in cancer. *Carcinogenesis* 2010;31:27–36.
  - Belinsky SA, Klinge DM, Stidley CA, et al. Inhibition of DNA methylation and histone deacetylation prevents murine lung cancer. *Cancer Res* 2003;63:7089–93.
  - Ecke I, Petry F, Rosenberger A, et al. Antitumor effects of a combined 5-aza-2'-deoxycytidine and valproic acid treatment on rhabdomyosarcoma and medulloblastoma in P14 mutant mice. *Cancer Res* 2009;69:887–95.
  - Gore SD, Hermes-DeSantis ER. Future directions in myelodysplastic syndrome: newer agents and the role of combination approaches. *Cancer Control* 2008;15 Suppl:40–9.
  - Bisht M, Kenealy M, Johnstone R, Rasheed W, Prince HM. Epigenetic targets in hematological malignancies: combination therapies with HDACis and demethylating agents. *Expert Rev Anticancer Ther* 2007;7:1439–49.
  - Cameron EE, Bachman KE, Myohanen S, Herman JG, Baylin SB. Synergy of demethylation and histone deacetylase inhibition in the re-expression of genes silenced in cancer. *Nat Genet* 1999;21:103–7.
  - Zhao L, Wientjes MG, Au JL. Evaluation of combination chemotherapy: integration of nonlinear regression, curve shift, isobologram, and combination index analyses. *Clin Cancer Res* 2004;10:7994–8004.
  - Gillenwater AM, Zhong M, Lotan R. Histone deacetylase inhibitor suberoylanilide hydroxamic acid induces apoptosis through both mitochondrial and Fas (Cd95) signaling in head and neck squamous carcinoma cells. *Mol Cancer Ther* 2007;6:2967–75.

# Proteomic Profiling Identifies Pathways Dysregulated in Non-small Cell Lung Cancer and an Inverse Association of AMPK and Adhesion Pathways with Recurrence

Meera Nanjundan, PhD,\* Lauren Averett Byers, MD, MS,† Mark S. Carey, PhD,‡  
Doris R. Siwak, PhD,‡ Maria Gabriela Raso, MD,§ Lixia Diao, PhD, Jing Wang, PhD,  
Kevin R. Coombes, PhD, Jack A. Roth, MD,¶ Gordon B. Mills, MD, PhD,‡ Ignacio I. Wistuba, MD,§  
John D. Minna, MD,# and John V. Heymach, MD, PhD†\*\*

**Introduction:** The identification of key pathways dysregulated in non-small cell lung cancer (NSCLC) is an important step toward understanding lung pathogenesis and developing new therapeutic approaches.

**Methods:** Toward this goal, reverse-phase protein lysate arrays (RPPA) were used to compare signaling pathways between NSCLC tumors and paired normal lung tissue from 46 patients and assess their association with clinical outcome.

**Results:** After RPPA quantification of 63 proteins and phosphoproteins, tissue pairs were randomized to a training set ( $n = 25$  pairs) and test set ( $n = 21$  pairs). In the training set, 15 protein markers were differentially expressed between tumors and normal lung ( $p \leq 0.01$ ), including markers in the PI3K/AKT and p38 MAPK signaling pathways (e.g., p70S6K, S6, p38, and phospho-p38), as well as caveolin-1 and  $\beta$ -catenin. A four-protein signature (p70S6K, cyclin B1, pSrc(Y527), and caveolin-1) independent of histology classified specimens as tumor versus normal with a predicted accuracy of

83%, sensitivity of 67%, and specificity of 100%. The signature was validated in the test set, correctly classifying all normal tissues and 14 of 21 tumor tissues. RPPA results were confirmed by immunohistochemistry for caveolin-1 and p70S6K. In tumors from patients with resected NSCLC, expression of proteins in the energy-sensing AMPK pathway (pLKB1, AMPK, p-Acetyl-CoA, pTSC2), adhesion, EGFR, and Rb signaling pathways was inversely associated with NSCLC recurrence.

**Conclusions:** These data provide evidence for dysregulation of several pathways including those involving energy sensing and adhesion that are potentially associated with NSCLC pathogenesis and disease recurrence.

**Key Words:** NSCLC, Proteomics, Recurrence, AMPK, Adhesion.

(*J Thorac Oncol.* 2010;5: 1894–1904)

Lung cancer is the leading cause of cancer death in the United States, with a 5-year overall survival of 16% for all stages.<sup>1</sup> Although chemotherapy is the standard treatment for advanced or metastatic non-small cell lung cancer (NSCLC), overall response rates do not exceed 20 to 30% with current front-line therapy.<sup>1–3</sup> Newer targeted agents show promise in combination with traditional cytotoxic chemotherapy but still only benefit a small subset of biologically susceptible patients. Therefore, a better understanding of the signaling pathways that are dysregulated in NSCLC has the potential to contribute to improved outcomes.

Defects in cell signaling pathways play a critical role in cancer cell growth, survival, invasion, and metastasis. An important goal of proteomics is to provide a map of the signaling pathways that are dysregulated in tumor cells as compared with normal cells. These aberrations could identify novel predictors of response or identify novel targets for therapy. Protein profiling is an important complement to other molecular profiling techniques such as gene expression analysis because proteins are the immediate effector molecules and, unlike transcriptional profiling, protein profiling can quantify post-translational modifications (e.g., phosphorylation status) that are intimately linked with activation of signaling proteins such as the receptor tyrosine kinases. In

\*Department of Cell Biology, Microbiology, and Molecular Biology, University of South Florida, Tampa, Florida; Departments of †Thoracic and Head and Neck Medical Oncology, ‡Systems Biology, §Pathology, ¶Bioinformatics and Computational Biology, and ¶Thoracic and Cardiovascular Surgery, University of Texas M.D. Anderson Cancer Center, Houston; #Hamon Center for Therapeutic Oncology Research and Simmons Cancer Center, University of Texas Southwestern Medical Center, Dallas; and \*\*Department of Cancer Biology, University of Texas M.D. Anderson Cancer Center, Houston, Texas.

Disclosure: This work was supported by the University of Texas Southwestern Medical Center and M. D. Anderson Cancer Center SPORC grant P50 CA070907; Department of Defense grant W81XWH-07-1-0306 01 (PP-1B); CCSG functional proteomics core grant P30 CA016672; and Kleberg Center for Molecular Markers as well as the CA06294 grant awarded by the National Cancer Institute. John V. Heymach is a Damon Runyon-Lilly Clinical Investigator supported in part by the Damon Runyon Cancer Research Foundation (CI 24-04). Lauren Averett Byers is supported in part by the AACR-AstraZeneca-Prevent Cancer Foundation Fellowship for Translational Lung Cancer Research.

Address for correspondence: Lauren Averett Byers, MD, Department of Thoracic and Head and Neck Medical Oncology, University of Texas M. D. Anderson Cancer Center, 1515 Holcombe Blvd, Unit 0432, Houston, TX 77030. E-mail: lbyers@mdanderson.org

The first two authors contributed equally to the study.

Copyright © 2010 by the International Association for the Study of Lung Cancer

ISSN: 1556-0864/10/0512-1894



addition, protein profiling directly characterizes potential drug targets and provides potential predictive markers, because most drugs act directly on protein function.

To date, only a few studies report the use of proteomic technologies to assess protein expression in lung tumors. Several groups have used matrix-assisted laser desorption ionization mass spectrometry<sup>4,5</sup> or electrospray ionization mass spectrometry, often in combination with 2D gel electrophoresis, of a small number of samples to identify potential tumor markers in lung cancers including cytokeratins, annexin II, cathepsin D, HSP27, stathmin, and MnSOD.<sup>5</sup> Matrix-assisted laser desorption ionization time-of-flight was also shown to distinguish tumor tissues from normal, deriving a 25-signal proteomic signature associated with poor outcome.<sup>6–8</sup> However, mass spectrometry technology is not widely used in clinical applications because of the large volume of sample required, relatively low throughput, high cost, and relative lack of sensitivity in detecting low-abundance proteins important for cellular functions.

In this study, we compare key signaling proteins from prosurvival, mitogenic, apoptotic, and growth regulatory pathways between paired NSCLC tumor and normal lung specimens using reverse-phase protein array (RPPA). RPPA is a quantitative, high-throughput assay that allows broad and simultaneous profiling of therapeutically relevant signaling networks.<sup>9–11</sup> The technique has been successfully used in other malignancies such as breast cancer to identify signaling pathway abnormalities, pharmacodynamic markers, and proteins associated with therapeutic resistance.<sup>12–14</sup>

In this report, we show that 15 proteins were significantly differentially expressed between normal lung and NSCLC tumors, including those involved in cell scaffolding, PI3K/AKT, and MAPK signaling. Among these, we found a four-protein signature (caveolin-1, p70S6K, cyclin B1, and pSrc(527)) able to distinguish tumors from normal lung. These findings were then validated in an independent set of paired tumors, and results for caveolin-1, cyclin B1, and p70S6K were confirmed by immunohistochemistry (IHC). In addition, protein expression analysis identified an association between tumor recurrence and alterations in the energy sensing AMPK pathway, adhesion pathways, EGFR pathway, and Rb (total and phosphorylated) levels. These results suggest that a 4-marker signature can aid in the diagnosis of NSCLC as well as point to potential targets for NSCLC treatment.

## RESULTS

### Proteomic Markers Differentiate NSCLC Tumors from Normal Lung

Sixty-three proteins and phosphoproteins were selected for analysis based on their involvement in key signaling pathways or cellular functions, including the (1) PI3K pathway, (2) MAPK pathway, (3) LKB1 pathway, (4) JAK/STAT pathway, (5) apoptosis, (6) cell polarity, (7) tyrosine kinase pathways including EGFR, (8) nuclear receptor pathway, and (9) cell cycle regulation. Protein markers were quantified by RPPA in 46 paired tumor and normal tissues from resected lung specimens.

Forty percent of the patient samples were arrayed in duplicate in different areas of each slide to assess reproducibility. For each protein, the Pearson correlation between duplicate samples was calculated. The median correlation coefficient across all protein markers was 0.734 (corresponding to a  $p$  value of  $3.0 \times 10^{-5}$ ). Duplicate samples were then averaged and unsupervised hierarchical clustering performed for all patient specimens with all 63 RPPA markers. Clustering demonstrated a clear division between normal lung and tumor specimens (Figure 1). Reproducibility for individual proteins quantified by RPPA was validated by the clustering of repeat antibody staining such as phospho-p38, pLKB1, and cyclin D1 being nearest neighbors on unsupervised hierarchical clustering (Figure 1).

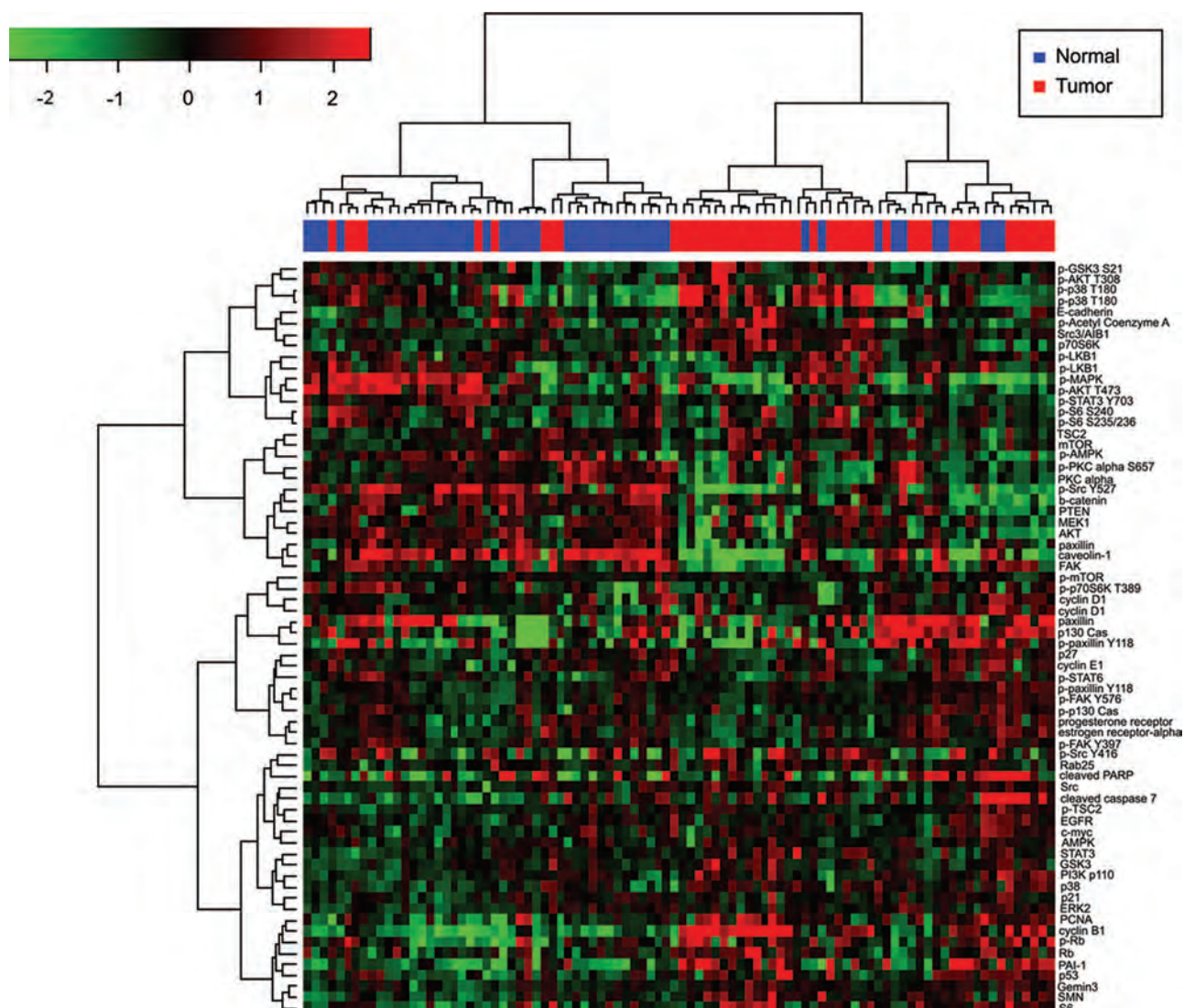
To further analyze specific factors most strongly distinguishing normal lung from NSCLC, paired samples were then randomly divided into a training set ( $n = 25$  pairs) and test set ( $n = 21$  pairs) for further analysis. Among the training set, using a conservative cutoff to account for multiple testing (false discovery rate [FDR]  $< 1\%$ , corresponding to a  $p$  value  $\leq 0.005$ ), 15 markers were expressed at significantly different levels in tumor and normal tissue by two-sample  $t$  test (Table 1, Figure 2). Several of these markers reflected changes in the PI3K/AKT and p38 MAPK signaling pathways. For example, total Akt ( $p = 0.002$ ) was increased in tumors relative to normal lung tissue, as were total and phospho-p38 ( $p = 9.9 \times 10^{-5}$  and 0.003, respectively), PAI1 ( $p = 1.87 \times 10^{-5}$ ), and p70S6Kinase and S6 ( $p = 9.3 \times 10^{-6}$  and 0.0014, respectively). Compared with normal tissue, tumors also demonstrated a decrease in the scaffolding protein caveolin and in  $\beta$ -catenin. Src pathway activity was elevated in tumors, as reflected by decreased phosphorylation of the autoinhibitory site pSrc(Y527), as previously described.<sup>15</sup>

Although total Akt decreased in tumors compared with normal lung, the level of pAkt T308 relative to total Akt increased significantly ( $p = 0.0004$ ) (Figure 2B), suggesting a shift toward Akt pathway activation in tumors. Similarly, the decrease in total FAK noted in tumor samples was associated with a relative increase in pFAK Y576 ( $p = 2.67 \times 10^{-5}$ ) and pFAK Y397 (0.008) (Figure 2B). Because FAK is a downstream target of Src, this observation is consistent with increased activity of the Src pathway in NSCLC tumors, as reflected by decreased phosphorylation of the autoinhibitory Src site (pSrc(Y527)). Of note, tumors were well balanced in histology between adenocarcinomas ( $n = 24$ ) and squamous cell carcinomas ( $n = 22$ ), and among the 15 markers differing between normal and tumor tissue, only PAI1 was also differentially expressed between histologies (higher in squamous cell carcinomas,  $p = 0.0044$ ).

### Four-Marker Signature Differentiates NSCLC from Normal Lung

We then tested whether a marker set of proteins differentially expressed between tumor and lung could be identified that could correctly classify an independent set of samples. To determine the optimal number of markers to be combined, we computed the sensitivity, specificity, positive predictive value, and negative predictive value for combining the top 2 up to the top 10 markers. The top four markers (caveolin-1, pSrc(Y527), cyclin B1, and p70S6K) were selected for the





**FIGURE 1.** Unsupervised hierarchical clustering identifies distinct protein expression patterns between normal lung and non-small cell lung cancer (NSCLC) tumors. Levels of 63 proteins and phosphoproteins were determined by reverse-phase protein lysate arrays in paired normal lung (blue) and NSCLC (red) samples from 46 patients. Unsupervised hierarchical clustering separated samples into two main groups based on differences in protein expression. One group contained a majority of the tumor samples (red), whereas the other contained mostly normal lung (blue), indicating major differences in protein expression between tumor and normal lung, even within an individual patient. Replicate proteins, such as p-p38(T180), pLKB1, and cyclin D1, clustered next to each other.

model because they resulted in a predicted accuracy of 0.833, sensitivity of 0.667, specificity of 1.000, positive predictive value of 1.000, and negative predictive value of 0.750, which was superior to using only the top 2 to 3 markers and was as good as the predictions for the top 5 to 10 markers (Supplemental Table 3, <http://links.lww.com/JTO/A36>).

### Validation of the Four-Marker NSCLC Signature

The ability of the four-marker signature to classify tumor versus normal lung tissue was then tested by diagonal linear discriminant analysis. In the training set, the signature correctly classified all 25 normal samples and 22 of 25 tumor

samples (Figure 3A). The four markers were then used to classify the 21 paired samples in the test set. In this set, all normal samples and 14 of 21 tumor samples were correctly classified (Figure 3B). The receiver operating characteristic plot demonstrates good performance of the model, with an area under the curve of  $0.961 \pm 0.031$  (Figure 3C).

### Validation of RPPA Protein Markers by IHC in Paraffin-Embedded Samples

Of the four markers in the NSCLC signature, antibodies optimized to detect caveolin-1, p70S6K, and cyclin B1 in paraffin-embedded samples by IHC were available for validation of the RPPA results. Caveolin-1, p70S6K, and cyclin

**TABLE 1.** Proteins and Phosphoproteins Differentially Expressed Between Normal Lung and NSCLC

Protein Marker	Mean of Normal Lung (log 2)	Mean of Tumor (log 2)	Difference (log 2)	T Score	p
Adhesion/invasion					
Caveolin	8.79	5.03	−3.76	−8.43	5.04E-11
pSrc(Y527)	2.30	0.01	−2.29	−5.97	2.80E-07
PAI1	−3.75	−1.85	1.90	4.75	1.87E-05
Paxillin	4.54	3.46	−1.08	−4.65	2.63E-05
FAK	3.29	2.20	−1.09	−3.35	0.002
β-catenin	3.88	3.00	−0.88	−3.09	0.003
PI3K/Akt pathway					
p70s6kinase	1.79	2.65	0.86	4.96	9.25E-06
S6	−4.64	−3.73	0.91	3.39	0.001
AKT	2.67	1.88	−0.79	−3.29	0.002
P38 MAPK/ERK					
p38	0.46	1.19	0.73	4.25	9.93E-05
p38 p180	−0.24	0.91	1.16	3.10	0.003
Other					
Cyclin B1	−3.36	−0.68	2.68	6.38	6.67E-08
SMN	2.03	2.64	0.60	3.11	0.003
Src3/AIB1	−1.02	−0.35	0.67	4.85	1.33E-05
Gemin3	−0.75	−0.37	0.38	2.92	0.005

Protein abbreviations listed in Supplemental Table 2.

B1 levels were quantified by IHC in formalin-fixed paraffin-embedded (FFPE) tissue in 39 of the 46 paired normal and tumor samples and compared with levels in the stroma, alveoli, and bronchial epithelium using paired *t* tests. Expression levels were scored as the percentage of tumor cells staining positive (0–100%) times the intensity of staining (0 through 3+), giving a possible range of IHC levels from 0 to 300. Tumor cell and alveolar stroma staining was successfully scored in all 39 samples. One patient specimen could not be scored for alveoli staining because of insufficient tissue, and 14 lacked sufficient tissue for bronchial epithelial staining. IHC scores are shown in Supplemental Table 4 (<http://links.lww.com/JTO/A36>).

Consistent with the results observed by RPPA, caveolin-1 levels were highest in normal alveolar stromal tissue, which was 15-fold higher than levels measured in tumor cytoplasm (median in alveolar stroma 300 versus median in tumor cytoplasm 20.0,  $p = 2.2 \times 10^{-16}$ ) and 30-fold higher than in tumor membrane (median in tumor membrane 10.0,  $p = 2.2 \times 10^{-16}$ ) (Table 2). Caveolin-1 levels in membrane of normal alveoli were also significantly higher than those of tumor membrane (eight-fold higher in alveoli,  $p = 0.013$ ). Although basal cells in the bronchial epithelium expressed high levels of caveolin-1 by IHC, expression was low in other strata of bronchial epithelium, resulting in an overall low IHC score among bronchial epithelial cells compared with other tissues.

Levels of p70S6K and cyclin B1 were then quantified in cytoplasm from tumor tissue, normal alveoli, and bronchial epithelial. Consistent with the RPPA measurements, p70S6K and cyclin B1 were significantly higher in tumor as compared with alveoli ( $p = 1.24 \times 10^{-13}$  and  $4.18 \times 10^{-6}$ , respectively). The median level of p70S6K in patient tumors was 60.0. In

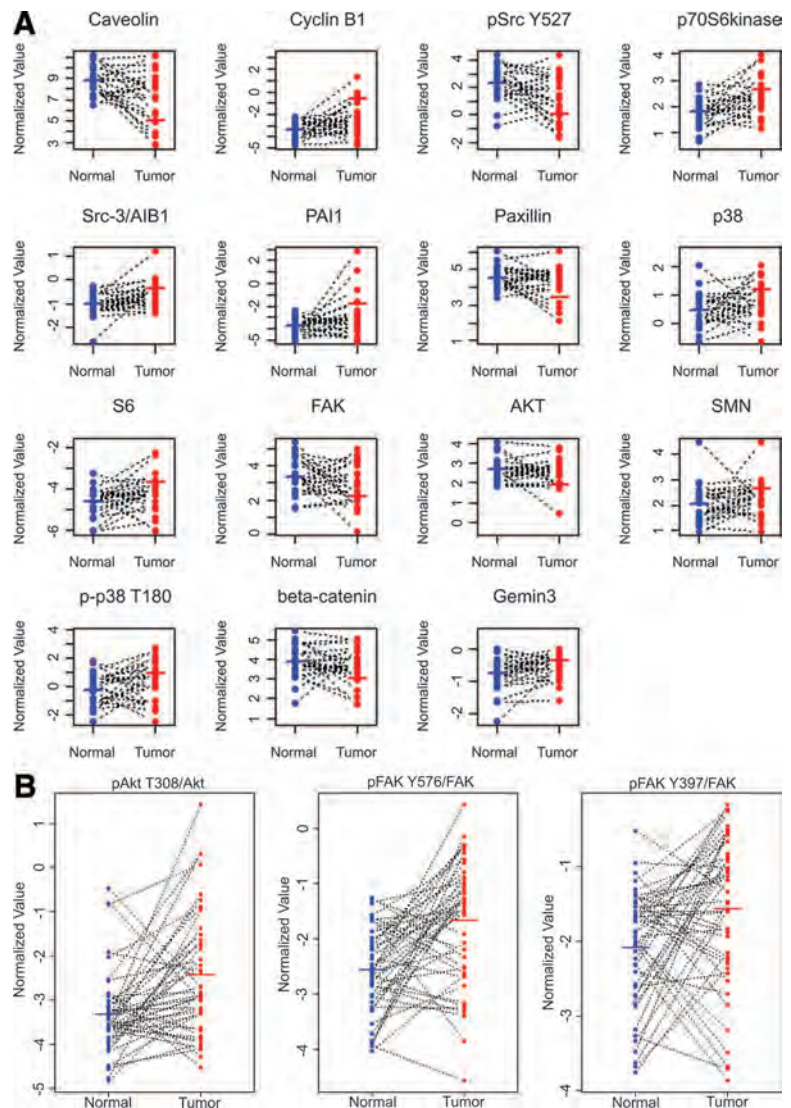
contrast, p70S6K was not detected in any normal alveoli sample. Tumors also had higher levels of p70S6K compared to bronchial epithelium (median in tumor 60.0, median in bronchial epithelium 50.0,  $p = 0.039$ ). No cyclin B1 was detectable in any normal tissue sample (alveoli or bronchial epithelium). Cyclin B1 levels ranged from 0 to 210 in tumor samples (median 20.0) (Table 2).

### Correlation of RPPA Markers with Clinicopathological Features Identifies Lower Tumor pAMPK in Current Smokers

Using data from all 46 patients, tumor levels of each protein were then correlated with clinicopathological features and outcome data. For each patient, the protein levels in the tumor specimens were first normalized using the paired normal lung tissue and then compared between clinical groups by *t* test or analysis of variance (ANOVA). None of the protein markers were significantly associated with age, gender, overall stage (I–IV), T stage, or N stage. To analyze the possible interaction between smoking status and protein expression, current smokers ( $n = 22$ ) were compared with former smokers ( $n = 22$ ). Phospho-AMPK was lower in current smokers, as compared with former smokers (median in current smokers −0.968, median in former smokers 0.605,  $p = 0.001$ ). None of the RPPA markers were significantly different in normal lung tissue between current and former smokers.

### NSCLC Recurrence Associated with Decreased AMPK Pathway Proteins, Adhesion Markers, and Total and Phospho-Rb

Protein markers were then compared between patients with ( $n = 19$ ) and without ( $n = 27$ ) NSCLC recurrence by ANOVA. At a FDR of 30% (corresponding  $p < 0.019$ ), six



**FIGURE 2.** Identification of proteins differentially expressed between paired normal lung and non-small cell lung cancer tumor samples. *A*, Protein and phosphoprotein levels for 63 markers were compared between normal tissue (blue) and tumor tissue (red) from patients who underwent surgical resection of their tumors. Protein levels were compared between the two groups by *t* test and those with *p* value <0.005 (false discovery rate <1%) are shown. *B*, The ratio of phospho- to total protein levels are shown for Akt and FAK.

markers were significantly different between patients with and without recurrence. At an FDR of 50%, seven additional markers that were associated with recurrence were identified ( $p = 0.066-0.119$ ) (Table 3). Patients with recurrence had downregulation of markers in the AMPK signaling pathway, as indicated by decreased levels of total AMPK and pTSC2 and increased acetyl-CoA (normally inhibited by AMPK). pLKB1, an upstream activator of AMPK, was also higher in patients without recurrence, although this did not reach statistical significance.

Recurrence was also associated with a trend toward lower levels of adhesion-associated molecules paxillin (both total and phosphorylated), p-p130 Cas, and STAT3. Lower levels of EGFR pathway signaling components (total EGFR, pAKT(T308), and ERK2) and Rb (total and phosphorylated) were also associated with recurrence.

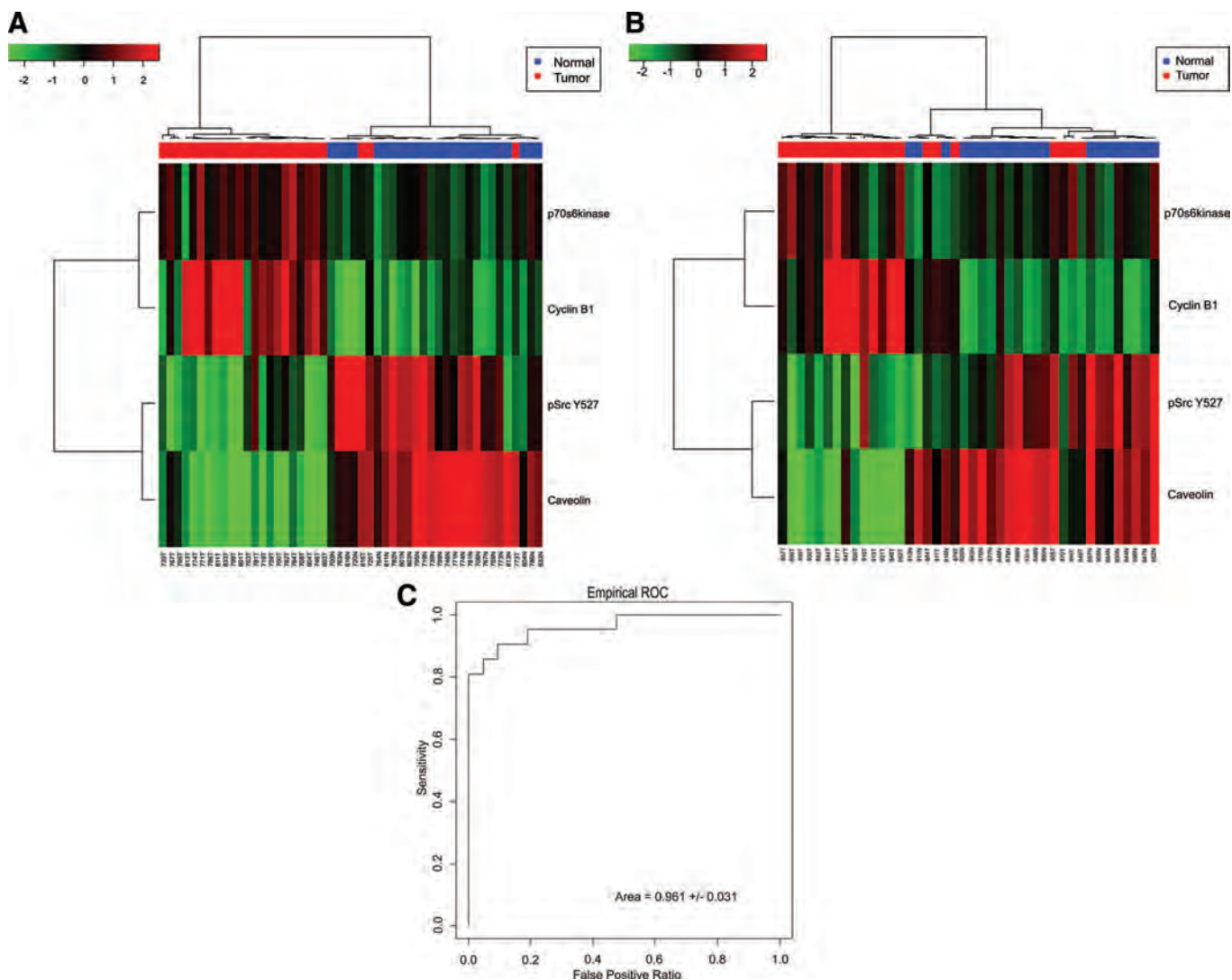
The difference in RPPA markers in patients with and without recurrence was also analyzed by stage. As expected, recurrences were more common in patients with higher stage disease (recurrences in 8/20 stage I patients, 4/15 stage II, 5/9

stage III, and 2/2 stage IV). Because of the small number of patients, those with stage I/II and III/IV were grouped for analysis. No RPPA markers were significantly different in stage I/II patients with and without recurrence. However, in stage III/IV patients, three markers were significantly different at an FDR of 40% ( $p < 0.008$ ) and nine markers at an FDR of 50% ( $p < 0.05$ ). Five of these nine markers were the same as in the analysis of all stages together, including AMPK pathway markers (total AMPK, pTSC2, and ACoA), EGFR, and Rb. Two additional markers also in the AMPK pathway that were identified by the analysis of stage III/IV patients were downstream targets of TSC2, pS6(Y240), and pS6(Y235). The two markers not seen in the previous analysis of all stages together were p21 and cMyc, both lower in patients with recurrence.

### Improved Cause-Specific Survival Associated with Elevated pTSC2

The association between cause-specific survival and protein markers was also analyzed. At an FDR of 30%





**FIGURE 3.** A four-marker proteomic signature discriminates tumor from normal lung tissue. *A*, The receiver operating characteristic curve shows good performance of the model to correctly classify tumor and normal tissues. *B*, Two-way hierarchical clustering of the normal (blue) and tumor (red) tissues from the training set shows that these tissues are well differentiated by levels of the four markers (p70S6K, cyclin B1, pSrc(Y527), and caveolin). *C*, Similarly, the four markers also separate normal (blue) from tumor (red) in the test set.

(corresponding  $p < 0.0064$ ), pTSC2 was again noted to be a favorable prognostic marker ( $p = 0.00012$ ) with higher levels in patients who were either alive at the end of the study or censored based on death from a non-NSCLC-related cause. ERK2 was also associated with longer cause-specific survival ( $p = 0.012$ , corresponding FDR  $< 50\%$ ). No protein markers were associated with overall survival. However, this analysis was limited by the high number of deaths among patients without disease recurrence (9/27 patients). When cause-specific survival was analyzed by stage, no markers were associated with shorter survival in patients with stage I/II disease. However, in stage III/IV patients, downregulation of pLKB1, an upstream activator of AMPK, and pS6(Y235) were significantly associated with shorter cause-specific survival.

There was a trend toward improved outcome with higher levels of paxillin (total and phospho), p-p130 Cas, STAT3, and pAkt in stage III/IV patients, although this did not reach significance ( $p = 0.07$ – $0.19$ ).

## DISCUSSION

RPPA was used to assess the protein levels and activation status of signal transduction pathways implicated in lung cancers. We analyzed 46 paired tumors and matched normal tissue to identify differences in protein expression between these tissues. Compared with their paired normal lung samples, tumors expressed lower levels of caveolin-1 and  $\beta$ -catenin, increased invasion markers (e.g., PAI1), and higher levels of PI3K/AKT and p38 MAPK pathway components. Although a large number

**TABLE 2.** Immunohistochemistry Scores from Paired Samples Demonstrate Higher Caveolin-1 in Normal Lung and Higher p70S6K and Cyclin B1 in NSCLC Tumors

	Tumor		Alveoli		Alveolar Stroma	Bronchial Epithelium	
IHC Scores	Cytoplasm	Membrane	Cytoplasm	Membrane		Cytoplasm	Membrane
Caveolin							
Mean	43.1	47.3	24.0	79.0	300	6.6	8.0
Median	20.0	10.0	20.0	80.0	300	5.0	5.0
P70S6K							
Mean	63.6		0			48.3	
Median	60.0		0			50.0	
Cyclin B1							
Mean	20.0		0			0	
Median	35.2		0			0	

IHC, immunohistochemistry; NSCLC, non-small cell lung cancer.

**TABLE 3.** Protein Markers Associated with Recurrent NSCLC

		Mean (log 2)		Median (log 2)		<i>p</i>
		No	Yes	No	Yes	
AMPK pathway proteins	AMPK	0.259	−0.123	0.302	−0.192	0.066
	p-Acetyl-CoA	0.385	1.480	0.247	1.365	0.010
	pTSC2	0.392	−0.169	0.354	−0.099	0.003
Adhesion markers	STAT3	0.456	0.008	0.260	0.074	0.089
	Paxillin	−0.719	−1.348	−0.602	−1.426	0.084
	p-paxillin (Y118)	0.117	−0.195	0.094	−0.223	0.075
	p-p130 Cas (Y241)	0.023	−0.394	0.123	−0.377	0.102
EGFR pathway proteins	EGFR	0.342	−0.278	0.157	−0.292	0.009
	pAKT (T308)	0.373	−0.279	0.327	−0.072	0.010
	ERK2	0.248	−0.236	0.289	−0.488	0.014
	p-PKCalpha (S657)	−0.513	−1.105	−0.945	−1.044	0.112
Total and phospho-Rb	Rb	1.011	−0.097	0.768	−0.301	0.005
	p-Rb	1.050	0.148	1.421	0.364	0.119

NSCLC, non-small cell lung cancer.

of proteins and phosphoproteins were differentially expressed in tumor versus normal tissues, a signature of only four markers was sufficiently robust to distinguish normal lung from tumor in our test set, suggesting that these proteins contain significant information content. These discriminators were p70S6K, cyclin B1, pSrc(Y527), and caveolin-1. Of note, these four markers were not associated with histology or smoking status.

Among the four markers in the NSCLC signature, caveolin-1 (decreased in tumor tissue) is a scaffolding protein present in plasma membrane caveolae microdomains rich in signaling molecules.<sup>16</sup> Caveolin-1 has previously been shown to be a tumor suppressor that is downregulated in lung cancer cell lines relative to normal bronchial epithelial cells,<sup>16</sup> and its expression differs by tumor stage and tumor type.<sup>17,18</sup> In addition, we also observed reduced levels of  $\beta$ -catenin relative to normal lung.  $\beta$ -catenin, which associates with caveolin-1, may be associated with malignant transformation<sup>19</sup> and progression of pulmonary adenocarcinoma.<sup>19</sup> Because caveolin-1 can stabilize  $\beta$ -catenin, reduced caveolin-1 levels promote  $\beta$ -catenin degradation.<sup>20</sup>

We then correlated protein levels in resected tumors with clinical outcomes. In this analysis, we observed an association between elevated expression of proteins in the energy-sensing AMPK pathway and decreased recurrence, longer cause-specific survival, and smoking status. Recurrence was also less common in patients with increased levels of adhesion markers, EGFR pathway markers, and Rb (total and phosphorylated). For example, total and phospho-paxillin (a scaffolding protein) and FAK (a tyrosine kinase localized at focal adhesions) were lower in tumor tissue of patients with subsequent disease recurrence. In addition, p-p130 Cas (another scaffolding protein) was also lower in patients with recurrence.

The analyses correlating protein levels with clinical parameters also demonstrated that downregulation of markers in the energy-sensing AMPK pathway was associated with worse clinical outcome and with smoking status. Specifically, lower levels of AMPK and pTSC2 (a downstream target of AMPK) and higher p-Acetyl-CoA (normally inhibited by AMPK) were associated with recurrent NSCLC, whereas



higher pTSC2 was associated with longer cause-specific survival. pAMPK levels were lower in current smokers as compared with former smokers.

These findings are consistent with previous studies that have shown that inactivating mutations of the tumor suppressor LKB1, which is upstream of AMPK, are seen more frequently in smokers and poorly differentiated NSCLC tumors (versus well or moderately differentiated tumors)<sup>21</sup> and are associated with a shorter latency, more frequent metastasis, and accelerated pulmonary tumorigenesis.<sup>22</sup> Also, in support of these observations are preclinical studies that showed that rosiglitazone, an activator of AMPK, inhibits NSCLC cell line growth and that this effect can be reversed by siRNA against AMPK.<sup>23</sup> Similarly, in another study, doubling time of A549, a NSCLC cell line with mutant LKB1, was significantly increased when wild-type LKB1 was reintroduced.<sup>24</sup> In addition, induction of AMPK and its reciprocal inactivation of the mTOR pathway has been implicated as a mechanism through which certain chemopreventive agents may act in NSCLC.<sup>25</sup> Together, these results suggest that this pathway may act to suppress tumor growth and/or malignant spread.

Finally, increased expression of protein markers in the EGFR pathway was also associated with a lower frequency of NSCLC recurrence. This is in keeping with clinical studies that have shown an association between activating mutations in EGFR and EGFR protein levels and improved clinical outcomes.<sup>26,27</sup> Similar results were observed when analyses of recurrence and/or cause-specific survival were performed in stage III/IV patients. However, none of the RPPA markers were associated with outcome in stage I/II patients. There are at least two possible explanations for this. First, it is possible that because stage I/II patients had relatively fewer recurrences, it was not possible to detect differences between these groups. Another explanation is that the changes in the tumor that increase the likelihood of recurrence occur later in the development/growth of lung cancer and therefore are more likely to be detected in a more advanced-stage tumor, compared with an earlier stage tumor. The association of protein markers with clinical outcome warrants further evaluation both in determining prognosis and in predicting response to targeted therapies.

Among the four protein markers in the NSCLC signature, RPPA results for caveolin-1, cyclin B1, and p70S6K were validated by IHC, which also demonstrated higher caveolin-1 in normal lung tissue (particularly in alveolar stroma); higher p70S6K in tumor cells; and cyclin B1 staining exclusive to tumor cells. The validation of RPPA results by IHC is particularly important for two reasons. First, although RPPA is a powerful technique for high-throughput screening of large numbers of patient samples (up to 1000) in parallel to identify prognostic or predictive protein biomarkers, it is not the optimal platform for rapid testing of individual patient samples. In addition, while RPPA is currently optimized for frozen tissue, it is much more common for available patient tumor tissue to be paraffin embedded. Therefore, the correlation of protein levels quantified in frozen tissue by RPPA with those in paraffin-embedded tissue by IHC has important clinical implications

because IHC is readily available in clinical pathology laboratories and could be immediately available to assess validated protein markers in FFPE samples from patients with NSCLC. Specifically, the validation of RPPA finding by IHC demonstrates the feasibility of using IHC of FFPE samples (such as tissue from diagnostic biopsies) to assess protein markers identified by RPPA in the future for diagnostic purposes or for treatment selection.

This study demonstrates that proteomic profiling using RPPA technology can identify dysregulated signaling events in NSCLC, which is an important step toward identifying biomarkers and targets that could potentially improve the outcomes for this and other cancers. Indeed, proteins associated with PI3K/AKT, MAPK, and Src signaling pathways were differentially expressed between normal lung and NSCLC tumors, and a model using only four of the proteins was capable of distinguishing tumors from normal lung (p70S6K, cyclin B1, pSrc(Y527), and caveolin-1). The differences in levels of potential protein targets between tumor and normal tissues further supports the concept that molecularly targeted drugs in NSCLC could preferentially target the tumor tissue with more limited direct effect on normal lung.

In addition, proteomic profiling identified pathways whose relative expression levels in tumor tissue was associated with recurrence. In particular, lower levels of the AMPK, EGFR, and Rb pathways were associated with recurrent disease. These studies support the potential of RPPA to identify differentially expressed protein biomarkers of relevance to lung cancer. These markers, if validated in further studies, have prognostic implications and may serve as potential drug targets aiding in the development of future therapeutic strategies.

## MATERIALS AND METHODS

### Human NSCLC Tumors and Normal Lung Tissue

Forty-six paired normal lung and NSCLC tumor samples were obtained from surgical specimens in the M. D. Anderson Cancer Center Thoracic Tissue Bank (Supplemental Table 1, <http://links.lww.com/JTO/A36>). In all cases, histology quality control was performed by a thoracic pathologist on frozen tissues. Tumor samples were included in the analysis if the percentage of malignant cells present in the sample were  $\geq 70\%$ . Normal lung samples from the same patients were reviewed to confirm that they contained no malignant cells. Twenty-two of the tumors were squamous cell carcinomas and 24 were adenocarcinomas. The median age of the patients from whom the tumors had been excised was 67 years (range, 48–81 years); 22 (48%) were women, and 44 (96%) were former or current smokers. Six (13%) patients had stage IA cancer, 14 (30%) stage IB, 2 (4%) stage IIA, 13 (28%) stage IIB, 3 (7%) stage IIIA, 6 (13%) stage IIIB, and 2 (4%) stage IV. Nineteen patients (41%) have subsequently had recurrent disease versus 27 (59%) who remain without evidence of disease at last contact. Of note, nine patients without NSCLC recurrence have died of other causes.

## Protein Lysate Preparation and Reverse-Phase Lysate Array

Protein lysate was prepared from frozen sections of tumor tissues as previously described.<sup>28</sup> Briefly, lysis buffer (1% Triton X-100, 50 mM HEPES [pH 7.4], 150 mM NaCl, 1.5 mM MgCl<sub>2</sub>, 1 mM EGTA, 100 mM NaF, 10 mM NaPPi, 10% glycerol, 1 mM phenylmethylsulfonyl fluoride, 1 mM Na<sub>3</sub>VO<sub>4</sub>, and 10 µg/mL aprotinin) was added to the samples and homogenized, followed by microcentrifugation at 14,000 rpm for 10 minutes.

Cleared supernatants were collected, followed by protein quantification using the BCA reaction kit (Pierce Biotechnology, Inc., Rockford, IL). All samples were normalized to the same starting concentration of 1 mg/ml, which were then mixed with SDS sample buffer without bromophenol blue (three parts cell lysate plus one part 4× SDS sample buffer, which contained 35% glycerol, 8% SDS, 0.25 M Tris-HCl [pH 6.8]). Before using the 4× SDS buffer, 10% 2-mercaptoethanol was added. The samples were boiled for 5 minutes. Then, the samples (each in duplicate) were serially diluted from the starting concentration of 1 mg/ml (1:2–1:16) with dilution buffer (three parts lysis buffer:one part 4× SDS + 2-mercaptoethanol). To each of the diluted samples, an equal amount of 80% glycerol/2× Ca<sup>2+</sup>- and Mg<sup>2+</sup>-free phosphate buffered saline solution was added, after which the diluted samples were transferred to 384-well plates. RPPA was produced and analyzed as previously described, with slight modifications.<sup>29</sup> Protein lysate arrays were printed on nitrocellulose-coated glass FAST Slides (GE Whatman, Piscataway, NJ) by a GeneTAC G3 arrayer (Digilab Inc., Holliston, MA) with forty-eight 200-µm-diameter pins arranged in a 4 × 12 format. Forty-eight grids were printed at each slide with each grid containing 24 dots. Protein dots were printed in duplicate with five concentrations. Arrays were produced in batches of 15, and occasional low-quality arrays (e.g., with many spot dropouts) were discarded.

Antibody staining of each array was performed at room temperature using an automated BioGenex autostainer (San Ramon, CA). Briefly, each array was incubated with a specific primary antibody, and signal was detected using the Dako Catalyzed Signal Amplification system according to the manufacturer's recommended procedure (DakoCytomation California, Inc., Carpinteria, CA). The full list of primary antibodies used in the experiment is outlined in Supplemental Table 2 (<http://links.lww.com/JTO/A36>) (inclusive of antibody dilutions). Please refer to Tibes et al.<sup>11</sup> for details regarding antibody optimization and validation.

The primary antibodies used in the key signaling pathways were extensively validated via Western blots, where band quality and correlation of protein levels with RPPA were determined. In brief, the microarray slides were precleared with Reblot mild stripping solution (Millipore, Billerica, MA) for 5 minutes and then with a general blocking agent (I-block, Foster City, CA) for 30 minutes. The slides were then blocked for endogenous peroxidase, avidin, biotin, and protein for 5 minutes each. After the blocking procedure, the slides were incubated with primary antibody and secondary antibody (diluted in DAKO antibody diluent with background-reducing compo-

nents) for 20 minutes each. Signal amplification was accomplished by incubating slides with streptavidin-biotin complex, biotinyl-tyramide, and streptavidin-peroxidase for 15 minutes each; signal detection was enabled by addition of 3,3'-diaminobenzidine tetrahydrochloride chromogen for 5 minutes. Between steps, each slide was washed with RPPA TBST (25 mM Tris, pH 7.6, 300 mM NaCl, 0.1% Tween-20). Spot images were quantified using imaging analysis with an HP Scanjet 8200 scanner (Hewlett Packard, Palo Alto, CA) with a 256-shade grayscale at 600 dots per inch.

Forty percent were printed in duplicate in serial dilutions on a single slide, which is then probed with a validated antibody that recognizes a unique protein or phosphoprotein and the amount of antibody binding to each sample is quantified. The high capacity of RPPA reduces interassay variability (as would be seen if each sample was analyzed independently by Western or similar techniques), with the use of multiple replicates further increasing quantitation thus allowing for statistically robust and reproducible comparisons to be made between samples.

## RPPA Data Processing and Statistical Analysis

RPPA data was quantified using a SuperCurve method that detects changes in protein level by MicroVigene software (VigeneTech, Carlisle, MA) and an R package developed in house.<sup>30</sup> Briefly, the SuperCurve method generates a common logistic curve for each antibody by pooling spot intensity data (obtained from MicroVigene) from all samples on the slide. Individual dilution series numbers for each sample are then mapped onto the SuperCurve for quantification. After quantification, data were logarithm transformed (base 2) for further processing and analyses. Then, median-control normalization was applied on the dataset. The statistical analyses were performed using R (version 2.7.0).

Differences in sample loading were adjusted by normalizing each sample using a whole antibody set approach (available as a script in the R package). This approach, which is patterned after gene microarray approaches, was chosen because comparison of actual sample dilutions with single housekeeping genes (such as  $\beta$ -actin or GAPDH) or total protein stains (such as colloidal gold) and statistical analyses of relatively invariant proteins (including total Akt, ERK2, GSK3, and p38) indicated greater variability and less consistency than with the whole set approach.

Before analysis, duplicate samples were averaged. Then, two-sample *t* tests were used to compare protein levels between normal and tumor tissue. Adjusting for multiple testing, we applied a beta-uniform mixture to model the resulting *p* values computed from the test statistic applied and assessed the FDR to identify significant differentially expressed genes.<sup>31,32</sup> In this investigation, we used an FDR of 1% as cutoff to identify markers significant differentially expressed between normal and tumors samples. Next, diagonal linear discrimination analysis algorithm was applied to build a statistical model for classification and prediction. Sensitivity, specificity, positive predictive value, and negative predictive value were computed from diagonal linear discrimination analysis results. Markers selected by this method were then validated in the test set of 21 paired samples.

For correlations between clinicopathological features or clinical outcomes and protein marker levels, clinical and protein data from all 46 patients were used. For each protein marker, tumor levels were first normalized to levels in matched normal lung tissue from the same patients. Normalized tumor protein levels were then correlated with clinical features and outcomes using *t* test (for gender and N stage), ANOVA (smoking status, overall pathologic stage, T stage, and recurrence), Cox proportional hazard ratio (cause-specific survival and overall survival), and linear regression (age).

### IHC for Caveolin, p70S6K, and Cyclin B1

Thirty-nine of the 46 paired normal and tumor samples had FFPE tissue available for testing by IHC. Each case was represented by three 1-mm diameter tissue cores per tumor and normal (bronchial epithelium and alveoli) site in a tissue microarray. Tissue microarray histology sections (5- $\mu$ m thick) were deparaffinized, hydrated, and heated in a steamer for 30 minutes with Dako Target Retrieval solution pH 6.0 for antigen retrieval (Dako North America, Inc., Carpinteria, CA). Peroxide blocking was done with 3% H<sub>2</sub>O<sub>2</sub> in methanol at room temperature for 15 minutes, followed by 10% fetal bovine serum in TBST for 30 minutes.

Slides were incubated at room temperature for 90 minutes with primary antibody against caveolin-1 (BD Transduction Laboratories, San Jose, CA; dilution 1:500), cyclin B1, and p70S6K (Cell Signaling, Danvers, MA; dilution 1:300) and then probed for 30 minutes with the secondary antibody Envision Dual Link Plus (DAKO, Carpinteria, CA). Staining was developed with 0.05% DAB (DAKO) and counterstained with hematoxylin. Staining was quantified by multiplying the percentage of cells staining positive by the intensity of staining (0, 1+, 2+, or 3+). Levels between tissue types in each patient were then compared by paired *t* test.

### ACKNOWLEDGMENTS

Supported by the University of Texas Southwestern Medical Center and M. D. Anderson Cancer Center SPORE NIH grant P50 CA070907; Department of Defense grant W81XWH-07-1-0306 01 (PP-1B); CCSG functional proteomics core grant P30 CA016672; and Kleberg Center for Molecular Markers. The content is solely the responsibility of the authors and does not necessarily represent the official views of the National Cancer Institute or the National Institutes of Health.

### REFERENCES

- American Cancer Society. Cancer Facts & Figures 2008. Atlanta, GA: American Cancer Society, 2008.
- Hoang T, Xu R, Schiller JH, et al. Clinical model to predict survival in chemonaïve patients with advanced non-small-cell lung cancer treated with third-generation chemotherapy regimens based on eastern cooperative oncology group data. *J Clin Oncol* 2005;23:175–183.
- Schiller JH, Harrington D, Belani CP, et al. Comparison of four chemotherapy regimens for advanced non-small-cell lung cancer. *N Engl J Med* 2002;346:92–98.
- Scagliotti GV, Parikh P, von Pawel J, et al. Phase III study comparing cisplatin plus gemcitabine with cisplatin plus pemetrexed in chemotherapy-naïve patients with advanced-stage non-small-cell lung cancer. *J Clin Oncol* 2008;26:3543–3551.
- Chen G, Gharib TG, Huang CC, et al. Proteomic analysis of lung adenocarcinoma: identification of a highly expressed set of proteins in tumors. *Clin Cancer Res* 2002;8:2298–2305.
- Yanagisawa K, Shyr Y, Xu BJ, et al. Proteomic patterns of tumour subsets in non-small-cell lung cancer. *Lancet* 2003;362:433–439.
- Kikuchi T, Carbone DP. Proteomics analysis in lung cancer: challenges and opportunities. *Respirology* 2007;12:22–28.
- Yanagisawa K, Tomida S, Shimada Y, et al. A 25-signal proteomic signature and outcome for patients with resected non-small-cell lung cancer. *J Natl Cancer Inst* 2007;99:858–867.
- Sheehan KM, Calvert VS, Kay EW, et al. Use of reverse phase protein microarrays and reference standard development for molecular network analysis of metastatic ovarian carcinoma. *Mol Cell Proteomics* 2005;4:346–355.
- Petricoin EF, Zoon KC, Kohn EC, et al. Clinical proteomics: translating benchside promise into bedside reality. *Nat Rev Drug Discov* 2002;1:683–695.
- Tibes R, Qiu Y, Lu Y, et al. Reverse phase protein array: validation of a novel proteomic technology and utility for analysis of primary leukemia specimens and hematopoietic stem cells. *Mol Cancer Ther* 2006;5:2512–2521.
- Chu I, Arnaout A, Loiseau S, et al. Src promotes estrogen-dependent estrogen receptor alpha proteolysis in human breast cancer. *J Clin Invest* 2007;117:2205–2215.
- Hennessy BT, Lu Y, Poradosu E, et al. Pharmacodynamic markers of perifosine efficacy. *Clin Cancer Res* 2007;13:7421–7431.
- Berns K, Horlings HM, Hennessy BT, et al. A functional genetic approach identifies the PI3K pathway as a major determinant of trastuzumab resistance in breast cancer. *Cancer Cell* 2007;12:395–402.
- Byers LA, Sen B, Saigal B, et al. Reciprocal regulation of c-Src and STAT3 in non-small cell lung cancer. *Clin Cancer Res* 2009;15:6852–6861.
- Racine C, Belanger M, Hirabayashi H, et al. Reduction of caveolin 1 gene expression in lung carcinoma cell lines. *Biochem Biophys Res Commun* 1999;255:580–586.
- Ho CC, Kuo SH, Huang PH, et al. Caveolin-1 expression is significantly associated with drug resistance and poor prognosis in advanced non-small cell lung cancer patients treated with gemcitabine-based chemotherapy. *Lung Cancer* 2008;59:105–110.
- Kato T, Miyamoto M, Kato K, et al. Difference of caveolin-1 expression pattern in human lung neoplastic tissue. Atypical adenomatous hyperplasia, adenocarcinoma and squamous cell carcinoma. *Cancer Lett* 2004;214:121–128.
- Awaya H, Takeshima Y, Amatya VJ, et al. Loss of expression of E-cadherin and beta-catenin is associated with progression of pulmonary adenocarcinoma. *Pathol Int* 2005;55:14–18.
- Lu Z, Ghosh S, Wang Z, et al. Downregulation of caveolin-1 function by EGF leads to the loss of E-cadherin, increased transcriptional activity of beta-catenin, and enhanced tumor cell invasion. *Cancer Cell* 2003;4:499–515.
- Matsumoto S, Iwakawa R, Takahashi K, et al. Prevalence and specificity of LKB1 genetic alterations in lung cancers. *Oncogene* 2007;26:5911–5918.
- Ji H, Ramsey MR, Hayes DN, et al. LKB1 modulates lung cancer differentiation and metastasis. *Nature* 2007;448:807–810.
- Han S, Roman J. Rosiglitazone suppresses human lung carcinoma cell growth through PPARgamma-dependent and PPARgamma-independent signal pathways. *Mol Cancer Ther* 2006;5:430–437.
- Zhou J, Huang W, Tao R, et al. Inactivation of AMPK alters gene expression and promotes growth of prostate cancer cells. *Oncogene* 2009;28:1993–2002.
- Jin Q, Feng L, Behrens C, et al. Implication of AMP-activated protein kinase and Akt-regulated survivin in lung cancer chemopreventive activities of deguelin. *Cancer Res* 2007;67:11630–11639.
- Eberhard DA, Johnson BE, Amler LC, et al. Mutations in the epidermal growth factor receptor and in KRAS are predictive and prognostic indicators in patients with non-small-cell lung cancer treated with chemotherapy alone and in combination with erlotinib. *J Clin Oncol* 2005;23:5900–5909.
- Deeb G, Wang J, Ramnath N, et al. Altered E-cadherin and epidermal growth factor receptor expressions are associated with patient survival in lung cancer: a study utilizing high-density tissue microarray and immunohistochemistry. *Mod Pathol* 2004;17:430–439.
- Zhang Q, Bhola NE, Lui VW, et al. Antitumor mechanisms of combined



- gastrin-releasing peptide receptor and epidermal growth factor receptor targeting in head and neck cancer. *Mol Cancer Ther* 2007;6:1414–1424.
29. Cheng KW, Lu Y, Mills GB. Assay of Rab25 function in ovarian and breast cancers. *Methods Enzymol* 2005;403:202–215.
30. Hu J, He X, Baggerly KA, et al. Non-parametric quantification of protein lysate arrays. *Bioinformatics* 2007;23:1986–1994.
31. Benjamini Y, Hochberg Y. Controlling the false discovery rate: a practical and powerful approach to multiple testing. *J R Stat Soc Ser B* 1995;57:289–300.
32. Pounds S, Morris SW. Estimating the occurrence of false positives and false negatives in microarray studies by approximating and partitioning the empirical distribution of p-values. *Bioinformatics* 2003;19:1236–1242.

[ASCO](#) | [Conquer Cancer Foundation](#) | [Cancer.Net](#) | [Journal of Clinical Oncology](#) | [Journal of Oncology Practice](#)

JUNE 3-7, 2011 | MCCORMICK PLACE | CHICAGO, ILLINOIS

- [Home 2011 Abstracts](#)
- [Search Abstracts](#)
- [Express Print Abstracts](#)
- [Browse Abstracts](#)
- [Back to Annual Meeting Home](#)
- [Planning Committee Disclosures PDF](#)

0

## Abstract Types

### CRA

Clinical Review Abstract

### LBA

Late-breaking Abstract

### TPS

Trials in Progress-Poster Session

### e

Publication-only Abstract

### ^

Abstracts granted an exception in accordance with ASCO's Conflict of Interest Policy

## Factors associated with membrane carbonic anhydrase IX (mCAIX) immunohistochemistry (IHC) in non-small cell lung cancer (NSCLC).

Publication-only abstracts (abstract number preceded by an "e"), published in conjunction with the 2011 Annual Meeting **but not presented at the Meeting**, can be found online only.

The publication-only abstracts are not included in the print or USB versions of the *ASCO Annual Meeting Proceedings Part I*, but they are citable to the *Journal of Clinical Oncology* as a supplement (see citation on left).

Sub-category:

[Prognostic Factors](#)

Category:

Tumor Biology



Meeting:  
[2011 ASCO Annual Meeting](#)

Abstract No:  
 e21125

Citation:  
 J Clin Oncol 29: 2011 (suppl; abstr e21125)

Author(s): D. J. Stewart, M. Nunez, C. Behrens, S. Swisher, J. A. Roth, J. Heymach, I. I. Wistuba;  
 University of Texas M. D. Anderson Cancer Center, Houston, TX

### [Abstract Disclosures](#)

Abstract:

**Background:** CAIX reduces cell acidity, is upregulated by HIF1a, and correlates with HIF1a and with poor prognosis in some cancers but not others. We found in multivariate analysis that mCAIX but not cytoplasmic (c) CAIX (cCAIX) correlated with relapse in stage I-II NSCLC (Proc AACR, 2010). **Methods:** In 308 resected NSCLCs (stage I, II, III, IV in 188, 61, 46 and 9 patients) we used IHC to assess CAIX and other markers of hypoxia, proliferation, etc. IHC scores (0-300) were calculated by multiplying stain intensity (0-3) by % cells staining. We used nonparametric statistics to assess factors correlating with mCAIX scores. **Results:** Median mCAIX scores were lower in adeno vs squamous NSCLC (5 vs 65,  $p < 0.0001$ ) and correlated inversely with % papillary adeno present ( $r -0.17$ ,  $p 0.02$ ). mCAIX correlated with tumor diameter ( $r 0.19$ ,  $p 0.0008$ ) but not with node stage (N0 vs N1-2, 30 vs 20,  $p 0.93$ ). mCAIX correlated with nuclear (n) Ki67 ( $r 0.20$ ,  $p 0.0005$ ), mitoses ( $r 0.18$ ,  $p 0.001$ ) and necrosis ( $r 0.20$ ,  $p 0.0006$ ) but not apoptosis ( $r 0.05$ ,  $p 0.38$ ). mCAIX did not correlate with nHIF1a ( $r -0.01$ ,  $p 0.84$ ) and paradoxically correlated inversely with cHIF1a ( $r -0.14$ ,  $p 0.02$ ) and cVEGF ( $r -0.13$ ,  $p 0.03$ ), but did correlate with the hypoxia-induced transcription factor cSHARP2 ( $r 0.18$ ,  $p 0.002$ ). cCAIX did correlate with cHIF1a, but only in tumors  $< 5$  cm ( $r 0.14$ ,  $p 0.04$ ) and N0 patients ( $r 0.17$ ,  $p 0.01$ ). mCAIX was higher with EGFR wild type vs mutant (20 vs 0,  $p 0.006$ ) and Notch amplified vs not (120 vs 21.25,  $p 0.0006$ ), and did not vary with KRAS mutation (5 vs 15.83,  $p 0.76$ ). There was a trend to lower mCAIX in well vs moderately/poorly differentiated tumor (5 vs 30,  $p 0.06$ ). mCAIX correlated negatively with the tumor suppressors cRB ( $r -0.13$ ,  $p 0.03$ ), cP16 ( $r -0.12$ ,  $p 0.03$ ), nP16 ( $r -0.13$ ,  $p 0.03$ ) and nP14 ( $r -0.12$ ,  $p 0.04$ ). **Conclusions:** In NSCLC mCAIX expression correlates with tumor type, subtype, size, proliferation and necrosis, and varies inversely with tumor suppressor genes. mCAIX did not correlate with HIF1a. cCAIX only correlated with cHIF1a in small and N0 tumors. Variable findings between studies with respect to CAIX importance may depend on tumor type, size and stage, and on whether mCAIX is assessed separately from cCAIX. Support: DoD # W81XWH-07-1-0306.

► Other Abstracts in this Sub-Category:

1. [A pilot study of tumor-derived exosomes as diagnostic and prognostic markers in breast cancer patients receiving neoadjuvant chemotherapy.](#)

Meeting:[2011 ASCO Annual Meeting](#) Abstract No: TPS248 First Author: R. E. Raab  
Category:Tumor Biology - [Prognostic Factors](#)

2. [ACRIN 6691 monitoring and predicting breast cancer neoadjuvant chemotherapy response using diffuse optical spectroscopic imaging \(DOSI\).](#)

Meeting:[2011 ASCO Annual Meeting](#) Abstract No: TPS249 First Author: B. J. Tromberg  
Category:Tumor Biology - [Prognostic Factors](#)

3. [Effect of IGF1R protein expression on benefit to adjuvant trastuzumab in early-stage HER2+ breast cancer in NCCTG N9831 trial.](#)

Meeting:[2011 ASCO Annual Meeting](#) Abstract No: 10503 First Author: M. M. Reinholz  
Category:Tumor Biology - [Prognostic Factors](#)  
[More...](#)

[Terms & Conditions](#) | [Privacy Policy](#) | [Sponsor](#) | [Contact Us](#) | [Relationships with Industry](#) | [Site Map](#)  
© 2005-2011 American Society of Clinical Oncology (ASCO). All rights reserved worldwide. | 2318  
Mill Road, Suite 800, Alexandria, VA 22314 | phone: (571) 483-1300



Original contribution

# Oncocytic neuroendocrine tumors of the lung: histopathologic spectrum and immunohistochemical analysis of 15 cases<sup>☆</sup>

Koji Tsuta MD, PhD<sup>a,c</sup>, Neda Kalhor MD<sup>a</sup>, Maria Gabriela Raso MD<sup>a</sup>, Ignacio I. Wistuba MD<sup>a,b</sup>, Cesar A. Moran MD<sup>a,\*</sup>

<sup>a</sup>Department of Pathology, The University of Texas MD Anderson Cancer Center, Houston, TX 77030, USA

<sup>b</sup>Department of Thoracic/Head and Neck Medical Oncology, The University of Texas MD Anderson Cancer Center, Houston, TX 77030, USA

<sup>c</sup>Division of Clinical Laboratory, National Cancer Center Hospital, Tokyo, 104-0045, Japan

Received 18 August 2009; revised 17 October 2009; accepted 23 October 2009

## Keywords:

Neuroendocrine carcinoma;  
Oncocytic;  
Mitochondria

**Summary** Oncocytic neuroendocrine tumor of the lung is rare. To reveal the clinicopathologic features of oncocytic neuroendocrine tumor, we reviewed surgical resections from 80 patients diagnosed with carcinoid tumors and 35 high-grade neuroendocrine carcinomas. We discovered 7 cases from the 80 carcinoid tumors and added 8 patients from personal consultation files. There were no statistically significant differences among the clinical features (such as age, location, and survival). Although most oncocytic neuroendocrine tumors were low-grade neuroendocrine carcinomas, we found that they could be of any grade. Tumor cells showed an ample amount of granular oncocytic cytoplasm and had a round-to-oval nucleus with coarse chromatin. Two cases mainly consisted of small-sized to medium-sized cells resembling plasma cells. This tumorous area intermingled with the conventional oncocytic area. Other histologic features were a large conspicuous nucleolus in 9 cases and the presence of giant cells in 8 cases. In the 80 carcinoid cases, bone formation ( $P = .034$ ), the presence of giant cells ( $P = .021$ ), and tumor cells with a conspicuous nucleolus ( $P = .021$ ) were more frequently observed. Immunohistochemical analysis revealed that oncocytic cells were positive for antimitochondria antibody. In conclusion, most of the tumors were low-grade neuroendocrine carcinomas, but we found that oncocytic neuroendocrine tumor can display features of high-grade neuroendocrine carcinoma. The oncocytic change was induced by accumulation of mitochondria. Although this variant does not differ in clinical features of nononcocytic neuroendocrine tumors, histologic features of the oncocytic neuroendocrine tumor can be a potential cause of diagnostic error.

© 2011 Published by Elsevier Inc.

## 1. Introduction

Bronchopulmonary neuroendocrine tumors comprise about 20% of all lung tumors and represent a spectrum of tumors arising from neuroendocrine cells. The different types of bronchopulmonary neuroendocrine carcinomas are separated into 4 subgroups in increasing order of biologic

<sup>☆</sup> This work was supported in part by the grant from the US Department of Defense PROSPECT W81XWH-07-1-0306.

\* Corresponding author. Department of Pathology, Unit 85, The University of Texas MD Anderson Cancer Center, 1515 Holcombe Boulevard, Houston, TX 77030, USA.

E-mail address: cesarmoran@mdanderson.org (C. A. Moran).

aggressiveness: low-grade typical carcinoids (TCs), intermediate-grade atypical carcinoids (ACs), high-grade large cell neuroendocrine carcinomas (LCNECs), and small cell lung carcinomas. Although these subgroups share structural, morphological, immunohistochemical, and ultrastructural features, the treatment modalities and prognoses differ for each type [1].

Eosinophilic cytoplasmic change can be induced by the accumulation of mitochondria, neurosecretory granules, lysosomes, secretory (exocrine) granules, cytoplasmic filaments, and smooth endoplasmic reticulum, and it is generally accepted that oncocytic tumors are due to intracytoplasmic accumulation of mitochondria. Small numbers of oncocytic cells are found in normal parathyroid glands, salivary glands, mucous glands of the aerodigestive tract, and the pancreas. A wide spectrum of benign and malignant oncocytic tumors can arise in various organs of the neuroendocrine system. Most of the reported cases of oncocytic neuroendocrine tumors (ONTs) have been oncocytic carcinoid tumors, and no oncocytic LCNECs have been reported [2].

Although focal oncocytic change is commonly observed in carcinoid tumors, carcinoid tumors consisting almost entirely of oncocytic cells are relatively uncommon [3,4]. Oncocytic carcinoid tumors have been reported in the nasopharynx [5], thymus [6], lung, pancreas [7], kidney [8], and urinary bladder [9]. Oncocytic carcinoid tumor of the lung has been reported in 11 single-case reports [10-20] and 1 case in a series analysis of carcinoid tumors [3].

We report the clinicopathologic features of 15 cases of ONT; to our knowledge, this constitutes the largest series of these rare tumors and is the first report of oncocytic LCNEC.

## 2. Materials and methods

### 2.1. Case selection

We retrospectively reviewed tumor specimens from 80 patients diagnosed with low-grade to intermediate-grade neuroendocrine carcinomas and 35 high-grade neuroendocrine carcinomas between 1990 and 2005. We obtained the tumor specimens from cases deposited in the files of The University of Texas MD Anderson Cancer Center (Houston, TX) Lung SPORE Tissue Bank with approval by the institutional review board. We collected the patients' demographic and clinical information including age, sex, smoking history, presenting symptoms, treatment modalities, site of any tumor recurrence, duration of recurrence or survival, tumor location (which lobe and whether central or not), and maximum tumor size (in centimeters).

Histologic diagnosis was based on the classification schema of the latest edition of the World Health Organization classification [1]. Neuroendocrine carcinomas of the lung

sometimes contain eosinophilic cells, so we set a cutoff value for ONTs of 50% or more tumor cells, showing oncocytic cytoplasmic change. Using this cutoff, 7 cases of ONT were discovered. We also added 8 cases of ONT (7 cases of carcinoid tumors and 1 case of LCNEC) from the personal files of one of the authors (C. A. M.).

### 2.2. Histologic examination

All available hematoxylin-eosin-stained slides were examined for each case and were assessed with clinical details blinded for each patient. We evaluated the histologic features of the infiltrative growth of the adjacent normal architecture and the presence of pleural invasion, blood or lymphatic vessel invasion, and neoplastic necrosis. The stroma between the tumor nests was mainly composed of capillary or fibrous tissue and the presence of bone formation. Cytologic features that we evaluated included the nuclear-to-cytoplasmic ratio, cell size, the presence of giant tumor cells ( $\geq 1$  cell per 10 high-power fields), the presence of conspicuous nucleolus, and the chromatin pattern, which was categorized as fine granular or coarse.

### 2.3. Immunohistochemical and ultrastructural examination

Immunohistochemical analyses were performed in the 7 cases from MD Anderson Cancer Center. Heat-induced epitope retrieval was performed using Target Retrieval Solution (Dako, Carpinteria, CA). We used primary antibodies against chromogranin A (1:100, DAK-A3; Dako), synaptophysin (1:200, polyclonal; Dako), CD56 (1:200, 123C3.D5; Neomarkers, Fremont, CA), mitochondria (1:100, 1273; Chemicon, Temecula, CA), thyroid transcription factor-1 (TTF-1) (1:100, 8G7G3/1; Dako), and Ki-67 (1:100, MIB1; Dako) using the EnVision-Plus (Dako) detection system.

We evaluated the immunostaining results for chromogranin A, synaptophysin, CD56, mitochondria, and TTF-1 on a 4-point scale, with 1+ indicating reactivity in 5% to 25% of the tumor cell population, 2+ in 26% to 50% of cells, 3+ in 51% to 75% of cells, and 4+ in  $>76\%$  of cells. Staining in rare, scattered, individual cells ( $<5\%$ ) was considered to indicate a negative result. Ki-67 immunoreactivity was evaluated in positive nuclei of the highest labeling region (so-called hot spots) of 1000 tumor nuclei. Disagreements in histologic and immunohistochemical results were resolved by means of a joint review of the slides using a multiheaded microscope.

Standard transmission electron microscopy was performed on tissue from the paraffin blocks in 1 case (case no. 14).

### 2.4. Statistical analysis

We performed all statistical analyses using SPSS version 12.0 software for Windows (SPSS, Chicago, IL). We used

the Wilcoxon rank sum test to analyze the continuous variables and Fisher exact test to analyze other clinicopathologic data. We considered  $P \leq .05$  to indicate significance. We calculated disease-free survival curves using the Kaplan-Meier method, and we compared the curves using the log-rank test.

### 3. Results

#### 3.1. Clinical features of ONT

The clinicopathologic summary of our 15 cases of ONT is shown in Table 1. Ten patients were men, and 5 were women. The patients' mean age (at the time of diagnosis) was 46.3 years (range, 32-75 years). Tumor sizes ranged from 1.0 to 6.0 cm (mean, 3.10 cm). Tumors were located in the right upper lobe in 4 patients, the right lower lobe in 2 patients, the left upper lobe in 2 patients, and the left lower lobe in 7 patients. Tumors were located in the central portion of the lung in 12 patients and in the intermediate or peripheral portion in 3 patients. Lymph node metastasis was observed in 1 patient with a TC tumor. The mean follow-up time for 14 patients was 54.2 months (range, 12-107 months), with 12 still alive at the time of this report. Of 14 patients, 2 died of other causes.

#### 3.2. Histologic features

The ONTs that we discovered consisted of 11 cases of TC, 3 cases of AC, and 1 case of LCNEC. Percentages of oncocyctic components in tumors ranged from 50% to 100% (mean, 81.3%). Tumors in 7 (40%) of 15 cases contained only oncocyctic cells. ONT showed variable growth

patterns, the most frequently observed pattern organoid in 7 cases, and 4 cases each had solid growth or pseudogland patterns (Fig. 1A). Neoplastic necrosis was observed in 1 case each of AC and LCNEC. Mitotic counts of more than or equal to 2 cells, 10 high-power fields were found in 2 cases of AC and 1 case of LCNEC.

Most of the tumor cells showed an ample amount of granular oncocyctic cytoplasm and had round-to-oval nuclei with coarse chromatin (Fig. 1B). However, 2 cases consisted of mainly small-sized to medium-sized tumor cells with an eccentrically placed nucleus and moderate-to-abundant eosinophilic cytoplasm and thus resembled plasma cells. The nucleus of these cells showed fine granular chromatin without nucleolus (Fig. 1C). This tumorous area intermingled with the conventional oncocyctic area. A large conspicuous nucleolus was observed in 9 (60%) of 15 cases, and 8 cases contained giant cells with bizarre nuclei (Fig. 1D).

The 1 case of metastasis in the lymph node consisted of oncocyctic tumor cells that resembled those of the primary tumor site. The primary site contained 80% oncocyctic cells, but the metastatic lymph node consisted of only oncocyctic cells (Fig. 2A and B).

The oncocyctic LCNEC showed large solid nests with massive necrosis (Fig. 3A and B). The oncocyctic cells of LCNEC were slightly larger than those in nononcocyctic areas. Tumor cells showed an ample amount of granular oncocyctic cytoplasm and had round-to-oval nuclei with coarse chromatin; giant cells were present.

#### 3.3. Immunohistochemical and ultrastructural findings

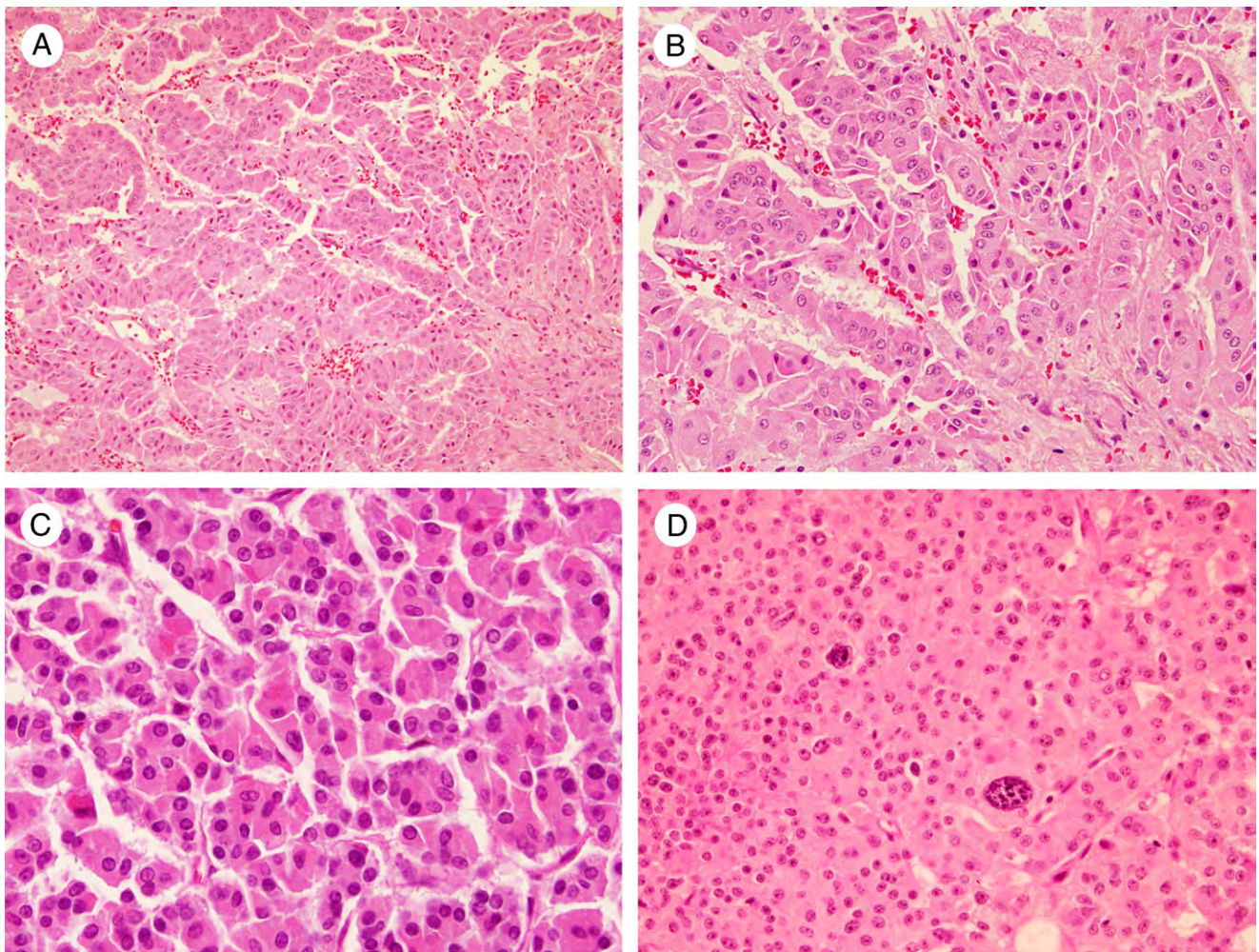
Immunohistochemical results of ONT are shown in Table 2. All 7 consecutively identified cases were positive

**Table 1** Clinicopathologic summary of present 15 cases of oncocyctic neuroendocrine tumor

No.	Sex	Age (y)	Size (cm)	Site	LN	Diag	Outcome	Mitosis/ 10 HPF	ONC cell (%)	Chromatin	Nucleo	Bone	Giant cell	
1	M	45	1.0	LLL	C	N0	TC	Alive	0	50	Fine	—	+	—
2	F	45	2.8	LLL	C	N0	TC	Alive	0	50	Coarse	—	+	+
3	M	40	2.5	RLL	C	N0	TC	Alive	0	50	Fine	—	—	—
4	M	48	3.0	RUL	P	N0	LCNEC	Death	37	50	Coarse	+	—	+
5	M	50	5.0	LUL	I	N0	TC	Alive	0	80	Coarse	+	—	+
6	M	32	6.0	LLL	C	N2	TC	Alive	0	80	Coarse	+	+	+
7	F	33	2.9	LUL	C	N0	TC	Alive	0	80	Coarse	+	+	+
8	F	42	2.5	RLL	C	N0	AC	Alive	1	80	Coarse	—	—	—
9	F	47	2.8	LLL	C	N0	TC	Alive	0	100	Coarse	+	—	+
10	M	49	2.5	LLL	C	N0	TC	N/A	0	100	Coarse	—	—	+
11	M	52	2.8	RUL	C	N0	TC	Alive	0	100	Coarse	+	—	—
12	F	48	3.0	RUL	C	N0	TC	Alive	0	100	Coarse	+	—	—
13	M	50	4.5	LLL	C	N0	TC	Alive	0	100	Fine	—	—	—
14	M	75	2.5	RUL	I	N0	AC	Death	2	100	Coarse	+	—	—
15	M	38	2.8	LLL	C	N0	AC	Alive	5	100	Coarse	+	—	+

Abbreviations: LN indicates lymph node metastasis; Diag, diagnosis; HPF, high power field; ONC, oncocyctic cell; Nucleo, nucleolus; M, male; F, female; N/A, not assessed; RUL, right upper lobe; RML, right middle lobe; RLL, right lower lobe; LUL, left upper lobe; LLL, left lower lobe; C, central portion.





**Fig. 1** Microscopic features of an ONT. A, The tumor arranged by organoid and trabecular cluster. (hematoxylin-eosin–stained, original magnification  $\times 10$ ). B, Tumor cells showing an ample amount of granular oncocytic cytoplasm with round-to-oval nuclei with coarse chromatin. Some tumor cells had a large conspicuous nucleolus (hematoxylin-eosin–stained, original magnification  $\times 40$ ). C, Two cases showed small-sized to medium-sized tumor cells with an eccentrically placed nucleus and moderate-to-abundant eosinophilic cytoplasm and thus resembled plasma cells. The nuclear chromatin showed fine granular without nucleolus (hematoxylin-eosin–stained, original magnification  $\times 40$ ). D, Some cases showed scattered giant cells with bizarre nucleus in the tumor nests (hematoxylin-eosin–stained, original magnification  $\times 40$ ).

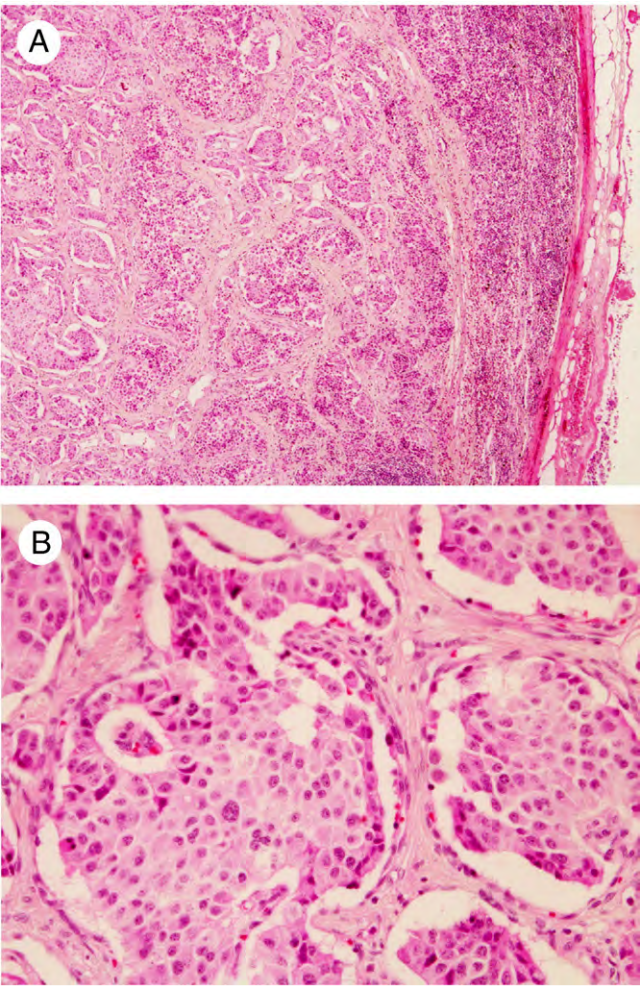
for the 3 neuroendocrine markers. However, the distribution of positive cells for the 3 neuroendocrine markers varied. Among the markers, CD56 tended to stain diffusely. The immunoreactivity of antimitochondrial antibody was observed in all cases (Fig. 4). Most of the oncocytic cells showed diffuse granular staining. However, the correlation between hematoxylin-eosin–stained oncocytic cells and intensity of reactivity for antimitochondria antibody was not always observed. Both conventional oncocytic cells and plasmacytoid-like cells were positive for antimitochondrial antibody. All cases were negative for TTF-1. The mean proliferative index assessed by Ki-67 staining of TC and AC was 0.87% (range, 0.3%–1.9%) and 9.9% (only 1 case), respectively.

Electron microscope studies demonstrated numerous mitochondria that occupied most of the cell cytoplasm. A large number of neurosecretory type of granules were also present.

### 3.4. Clinicopathologic features of 80 consecutively resected carcinoid tumors

We detected 7 cases of ONT from 80 cases of low-grade to intermediate-grade neuroendocrine carcinomas but not in 35 cases of high-grade neuroendocrine carcinomas. Thus, we consecutively analyzed 80 resected samples to determine the clinicopathologic differences between ONTs and non-ONTs. There were no statistical differences between the clinical features of patients with oncocytic compared to nononcocytic carcinoid tumors (Table 3). Furthermore, there was no statistical difference ( $P = .85$ ) in a 5-year recurrence-free survival of patients with ONT (100%) compared to patients with non-ONT (89.4%). Among histologic features, bone formation ( $P = .034$ ), the presence of giant tumor cells ( $P = .021$ ), and tumor cells with a conspicuous nucleolus ( $P = .021$ ) were more frequently observed in ONTs than in non-ONTs.

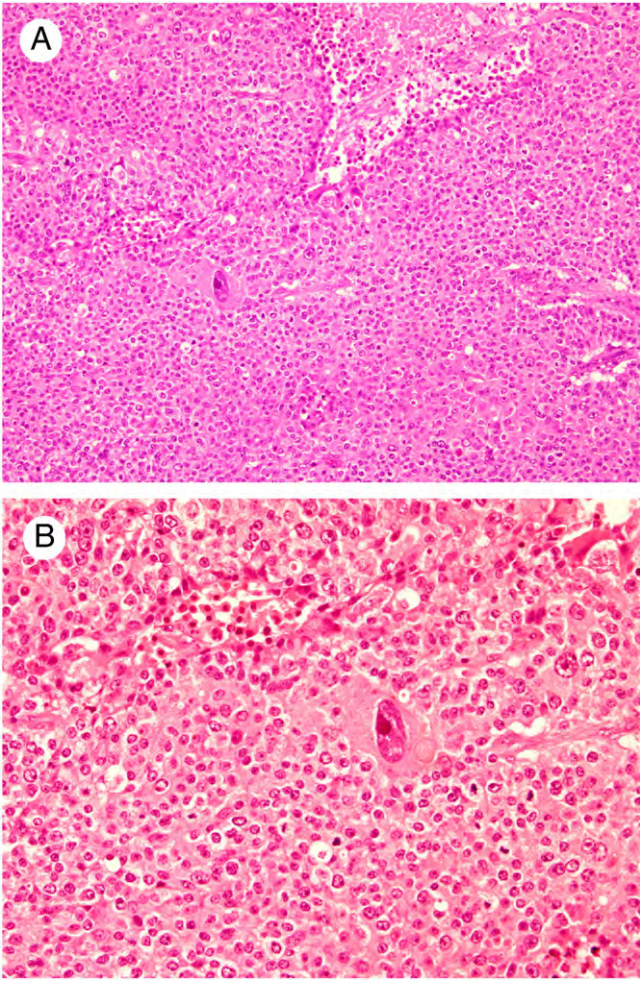




**Fig. 2** The microscopic features of oncocytic carcinoid tumor of lymph node metastasis. A, The lymph node was almost replaced by the tumor cells (hematoxylin-eosin–stained, original magnification ×4). B, All the tumor cells consisted of the oncocytic cells. (hematoxylin-eosin–stained, original magnification ×20).

**3.5. Clinicopathologic features of 12 previously reported cases of ONT**

Clinicopathologic features of the 12 previously reported cases of ONT are listed in Table 4: 8 cases of TC, 1 case of AC, and 3 of probable TC (there was no mention of mitosis or necrosis). Six patients were men, 4 were women, and 2 did

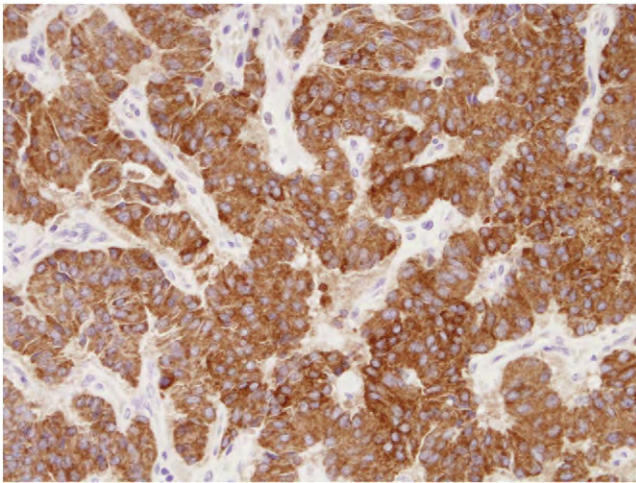


**Fig. 3** The microscopic features of oncocytic LCNEC. A, The tumor was arranged as a large solid nest with coagulative necrosis (hematoxylin-eosin–stained, original magnification ×10). B, The tumor cells contained moderate amounts of eosinophilic cytoplasm with a large pleomorphic nucleus and coarse chromatin. This photomicrograph shows some mitotic figures and giant cells with bizarre nucleus (hematoxylin-eosin–stained, original magnification ×20).

not document sex. The patients’ mean age was 55.6 years (range, 44–80 years). Tumor sizes ranged from 2.0 to 17.5 cm (mean, 4.8 cm; median, 3.0 cm). Tumors were located in the right upper lobe in 2 patients, the middle lobe in 1 patient, the right lower lobe in 4 patients, the left upper lobe in 2 patients,

Table 2 Immunohistochemical results of ONT						
No.	Chromogranin A	Synaptophysin	CD56	TTF-1	Mitochondria	Ki-67 (%)
1	4+	3+	3+	0	3+	0.6
2	2+	3+	2+	0	1+	0.8
5	2+	2+	3+	0	2+	0.8
6	3+	2+	2+	0	2+	0.8
7	2+	1+	3+	0	4+	1.9
13	2+	1+	4+	0	4+	0.3
14	3+	2+	3+	0	4+	9.9





**Fig. 4** Oncocytic area showing granular cytoplasmic positivity for antimitochondrial antibody (original magnification  $\times 20$ ).

and the left lower lobe in 1 patient. One tumor was located in a left main bronchus, and the tumor location was not reported in 1 patient. Lymph node status was recorded for 2 patients, and metastasis was not observed. Clinical follow-up data were recorded for 3 patients: 1 patient was reported at autopsy to have died of another cause, and 2 patients were alive at 24 months.

The proportion of oncocytic components was recorded for 5 patients: in 4 cases, the oncocytic component predominated, and 1 case was pure. Ultrastructural analysis was performed for 10 patients, and results showed that 4 cases had a mixture of neuroendocrine cells and oncocytic cells, and 6 patients had a homogenous distribution of tumor cells with hyperplasia of numerous mitochondria and neurosecretory granules in the cytoplasm. No immunohistochemical analysis for antimitochondrial antibody was done.

#### 4. Discussion

ONT of the lung is a rare tumor, and only 12 cases have been previously reported. We report the clinicopathologic features of 15 cases of ONT (12 of TC, 2 of AC, and 1 of LCNEC). In our experience (based on 80 cases), the incidence of oncocytic carcinoid tumor is about 8.8%. Compared with previous reports, we found that ONTs span the histologic spectrum from low-grade to intermediate-grade (TC or AC) and high-grade neuroendocrine carcinomas (LCNEC). Thus, this constitutes the largest series of these rare tumors and, to our knowledge, the first report of oncocytic LCNEC.

Although an eosinophilic cytoplasmic change can be induced by accumulation of mitochondria, neurosecretory granules, lysosomes, secretory (exocrine) granules, cytoplasmic filaments, and smooth endoplasmic reticulum, all of the reported cases of oncocytic carcinoid of the lung have reported the presence of abundant mitochondria in the cytoplasm. We found that most of the oncocytic cells in all of

our analyzed cases also showed strong granular immunoreactivity to antimitochondrial antibody in the cytoplasm. Because all nucleated cells have mitochondria in their cytoplasm, immunohistochemical positivity with this antibody does not have any specificity. However, a correlation between strong granular cytoplasmic reactivity for this antibody and an electron microscopic view of packed mitochondria has been reported [21]—a finding that we also corroborated by performing ultrastructural analysis in 1 case in which we found numerous mitochondria that occupied most of the cell cytoplasm. These results indicate that these oncocytic changes in ONT are induced by an accumulation of mitochondria, which mirrors what has been reported by others.

Histologic features of ONT compared to those of non-ONTs were an ample amount of granular oncocytic cytoplasm, conspicuous nucleolus, the presence of giant tumor cells, and bone formation. Most of the previously reported histologic features of ONT had an ample amount of granular oncocytic cytoplasm and nucleomegaly with prominent nucleoli, and some cases contained multinucleated giant cells. These histologic features resemble those of non-small cell carcinomas, possibly squamous cell carcinoma. Furthermore, recently reported oncocytic primary adenocarcinoma of the lung also enters into the differential diagnosis [22]. Our results indicate that neuroendocrine markers should be added to immunohistochemical panels when diagnosing oncocytic lesions. We also observed plasmacytoid-like cells in 2 cases. Plasmacytoid carcinoid tumors have not been reported as a subtype of neuroendocrine carcinomas. Furthermore, we found that the plasmacytoid-like areas intermingled with conventional oncocytic areas, and immunohistochemical analysis for antimitochondrial antibody showed strong positivity. These results indicated that plasmacytoid-like cells are part of the morphological diversity of ONT.

Bone formation was observed in 4 of 7 low-grade to intermediate-grade ONTs, and we found a significant correlation ( $P = .034$ ) between bone formation and oncocytic morphology and not with non-ONTs. However, the 12 previously reported cases of ONT did not report bone formation. Bone formation is one of the characteristics of low-grade to intermediate-grade neuroendocrine carcinomas, and the incidence has been reported to be 10% to 25% [3]. In reports of bone formation in low-grade to intermediate-grade neuroendocrine carcinomas, there has been no mention of a correlation with oncocytic change. The exact mechanism of bone formation in neuroendocrine carcinoma is unknown.

The hypothesis of oncocytic change is that mitochondrial pathology is an important factor in aging and degenerative diseases. Various features of mitochondrial DNA make it more likely to be defective than nuclear DNA, and with advancing age, an accumulation of genetic errors in mitochondrial DNA results in “mitochondrial respiratory failure” and compensatory mitochondrial hyperplasia [23]. However, our data from consecutive cases of carcinoid

**Table 3** Clinicopathologic features about 7 cases of ONT compared to 73 cases of non-ONT

		Oncocytic		<i>P</i>
		(-)	(+)	
Diagnosis	Typical	62 (85%)	6 (86%)	1.00
	Atypical	11 (15%)	1 (14%)	
Age	(y)	54.99	47.14	.351
Sex	Male	47 (64%)	2 (29%)	.075
	Female	26 (16%)	5 (71%)	
Symptom	None	46 (63%)	4 (57%)	.471
	Present	24 (17%)	3 (43%)	
Smoking	Never	28 (41%)	4 (57%)	.684
	Former	30 (43%)	2 (29%)	
	Present	11 (16%)	1 (14%)	
Location	Central	44 (60%)	5 (71%)	.700
	Noncentral	29 (40%)	2 (29%)	
Tumor size	(cm)	2.90	3.53	.797
Lymph node metastasis	Absent	56 (78%)	6 (86%)	1.00
	Present	16 (22%)	1 (14%)	
Pathological stage	I and II	61 (85%)	6 (86%)	1.00
	III and IV	11 (15%)	1 (14%)	
Infiltrative growth	Absent	29 (40%)	4 (57%)	.439
	Present	44 (60%)	3 (43%)	
Pleural invasion	Absent	72 (99%)	7 (100%)	1.00
	Present	1 (1%)	0	
Blood-vessel invasion	Absent	42 (58%)	4 (57%)	1.00
	Present	31 (42%)	3 (43%)	
Lymph-vessel invasion	Absent	46 (63%)	5 (71%)	1.00
	Present	27 (37%)	2 (29%)	
Neoplastic necrosis	Absent	68 (93%)	7 (100%)	1.00
	Present	5 (7%)	0	
Stroma	Capillary	52 (71%)	5 (71%)	1.00
	Fibrous	21 (29%)	2 (29%)	
Bone formation	Absent	61 (84%)	4 (57%)	.034
	Present	12 (16%)	3 (43%)	
Nuclear-cytoplasmic ratio	Low to moderate	51 (70%)	7 (100%)	.181
	High	22 (30%)	0	
Cell size	Small to medium	43 (59%)	2 (29%)	.230
	Large	30 (41%)	5 (71%)	
Giant cell	Absent	62 (85%)	3 (43%)	.021
	Present	11 (15%)	4 (57%)	
Chromatin pattern	Fine	45 (62%)	2 (29%)	.118
	Coarse	28 (38%)	5 (71%)	
Nucleolus	Inconspicuous	62 (85%)	3 (43%)	.021
	Conspicuous	11 (15%)	4 (57%)	

tumors showed no age differences between patients with oncocytic carcinoid tumors and those with nononcocytic carcinoid tumors. The average age of the previously reported 12 patients was 55.6 years. The median and mean age for the patients with surgically managed carcinoid tumors were 59 and 55 years, respectively (range, 12-91 years) [24]. These results revealed that age does not affect oncocytic change.

Unfavorable outcomes (recurrence, death, and lymph node metastasis) and histologic features of tumor aggressiveness (the presence of pleural, blood, or lymphatic vessel invasion) of oncocytic carcinoid tumors did not reveal any differences in nononcocytic carcinoid tumors. A high Ki-67

index is a known unfavorable factor in pulmonary carcinoid tumors [25]. Among the cases we studied, the mean Ki-67 index was 0.87% in oncocytic TC and 9.9% in oncocytic AC, both of which are within the range of previously reported Ki-67 index [26]. These results indicate that the tumor aggressiveness of ONT is based on the tumor grade of neuroendocrine tumors.

In conclusion, we have described 15 cases of ONT. Most of the tumors were low-grade neuroendocrine carcinoma (TC), but we found that ONT can also display features of high-grade neuroendocrine carcinoma. ONT showed diffuse positivity with antimitochondrial antibody. Although this

**Table 4** Summary of reported 12 cases of oncocytic carcinoid tumor

Sex	Age (y)	Size	Site	LN meta	Diag	Outcome	Oncocytic %	EM	Ref
NOD	58	3.0	LUL	NOD	Carcinoid	NOD	NOD	Mixture	19
M	69	3.0	RML, C	NOD	Carcinoid	Autopsy	Predominant	Mixture	22
M	43	4.0	Left main bronchus	NOD	TC	Alive, 24 mo	Predominant	Mixture	1
M	52	6.0	RLL, C	NOD	TC	NOD	NOD	Homogenous	20
F	55	2.0	RLL	NOD	TC	NOD	NOD	Homogenous	9
F	44	3.0	RLL	NOD	Carcinoid	NOD	NOD	Mixture	6
NOD	NOD	NOD	NOD	NOD	TC	NOD	Pure	NOD	8
M	47	6.0	LUL	NOD	TC	NOD	NOD	Homogenous	11
F	80	3.6	LLL, C	NOD	TC	NOD	Predominant	Homogenous	16
M	48	2.3	RUL, C	N0	TC	Alive, 24 mo	NOD	Homogenous	17
F	49	2.5	RUL, C	NOD	TC	NOD	NOD	Homogenous	2
M	66	17.5	RLL, C	N0	AC	NOD	Predominant	N/A	13

Abbreviations: EM indicates electron microscopy; Ref, reference; NOD, not documented.

tumor variant does not differ in clinical features and prognostic differences from non-ONTs, the presence of conspicuous nucleolus and the presence of giant cells can be a potential cause of diagnostic error.

## Acknowledgment

The authors would like to thank Susan Cweren and Denise Woods for their skillful technical assistance and Virginia M. Mohlere for her skillful English editing.

## References

- [1] Travis WD, Colby T, Corrin B, et al. Tumors of the lung. In: Kleihues P, Sobin LH, editors. WHO classification of tumors. Pathology and genetics of tumors of the lung, pleura, thymus and heart. Lyon (France): IARC press; 2004. p. 9-124.
- [2] Nappi O, Ferrara G, Wick MR. Neoplasms composed of eosinophilic polygonal cells: an overview with consideration of different cytomorphologic patterns. *Semin Diagn Pathol* 1999;16: 82-90.
- [3] Hasleton PS, al-Saffar N. The histological spectrum of bronchial carcinoid tumours. *Appl Pathol* 1989;7:205-18.
- [4] Colby TV, Koss MN, Travis WD. Typical and atypical carcinoid tumors. In: Colby TV, Koss MN, Travis WD, editors. In tumors of the lower respiratory tract. Third series. Washington, DC: Armed Forces Institute of Pathology; 1995. p. 294-309.
- [5] Stanley RJ, DeSanto LW, Weiland LH. Oncocytic and oncocytoid carcinoid tumors (well-differentiated neuroendocrine carcinomas) of the larynx. *Arch Otolaryngol Head Neck Surg* 1986;112:529-35.
- [6] Moran CA, Suster S. Primary neuroendocrine carcinoma (thymic carcinoid) of the thymus with prominent oncocytic features: a clinicopathologic study of 22 cases. *Mod Pathol* 2000;13:489-94.
- [7] Carstens PH, Cressman Jr FK. Malignant oncocytic carcinoid of the pancreas. *Ultrastruct Pathol* 1989;13:69-75.
- [8] Hannah J, Lippe B, Lai-Goldman M, Bhuta S. Oncocytic carcinoid of the kidney associated with periodic Cushing's syndrome. *Cancer* 1988;61:2136-40.
- [9] McCabe JE, Das S, Dowling P, Hamid BN, Pettersson BA. Oncocytic carcinoid tumour of the bladder. *J Clin Pathol* 2005;58:446-7.
- [10] Sajjad SM, Mackay B, Lukeman JM. Oncocytic carcinoid tumor of the lung. *Ultrastruct Pathol* 1980;1:171-6.
- [11] Sklar JL, Churg A, Bensch KG. Oncocytic carcinoid tumor of the lung. *Am J Surg Pathol* 1980;4:287-92.
- [12] Scharifker D, Marchevsky A. Oncocytic carcinoid of lung: an ultrastructural analysis. *Cancer* 1981;47:530-2.
- [13] Alvarez-Fernandez E, Folque-Gomez E. Atypical bronchial carcinoid with oncocytoid features. Its ultrastructure, with special reference to its granular content. *Arch Pathol Lab Med* 1981;105:428-31.
- [14] Kuwahara T, Maruyama K, Mochizuki S, Seki Y, Sawada K. Oncocytic carcinoid of the lung. An ultrastructural observation. *Acta Pathol Jpn* 1984;34:355-9.
- [15] Ghadially FN, Block HJ. Oncocytic carcinoid of the lung. *J Submicrosc Cytol* 1985;17:435-42.
- [16] Matsumoto S, Muranaka T, Hanada K, Takeo S. Oncocytic carcinoid of the lung. *Radiat Med* 1993;11:63-5.
- [17] Ogino S, al-Kaisi N, Abdul-Karim FW. Cytopathology of oncocytic carcinoid tumor of the lung mimicking granular cell tumor. A case report. *Acta Cytol* 2000;44:247-50.
- [18] Okuda K, Sano M. Oncocytic carcinoid of the lung. *Jpn J Thorac Cardiovasc Surg* 2005;53:393-6.
- [19] Arora R, Mathur SR, Aron M, et al. Oncocytic carcinoid tumor of the lung: a case report of diagnostic pitfall in filter membrane preparation of bronchial washings. *Acta Cytol* 2007;51:907-10.
- [20] McIntire M, Shah ND, Kim AW, Gattuso P, Liptay MJ. Cytologic imprints of giant atypical bronchopulmonary carcinoid tumor of the lung with extensive oncocytic component. *Diagn Cytopathol* 2008;36: 887-90.
- [21] Shintaku M, Honda T. Identification of oncocytic lesions of salivary glands by anti-mitochondrial immunohistochemistry. *Histopathology* 1997;31:408-11.
- [22] Solis LM, Raso MG, Behrens C, Wistuba I, Moran CA. Primary oncocytic adenocarcinoma of the lung: clinicopathological and immunohistochemical study of 16 cases. *Mod Pathol* 2009;36A:22.
- [23] Linnane AW, Marzuki S, Ozawa T, Tanaka M. Mitochondrial DNA mutations as an important contributor to ageing and degenerative diseases. *Lancet* 1989;1:642-5.
- [24] Travis WD, Giroux DJ, Chansky K, et al. The IASLC Lung Cancer Staging Project: proposals for the inclusion of bronchopulmonary carcinoid tumors in the forthcoming (seventh) edition of the TNM classification for lung cancer. *J Thorac Oncol* 2008;3: 1213-23.
- [25] Costes V, Marty-Ané C, Picot MC, et al. Typical and atypical bronchopulmonary carcinoid tumors: a clinicopathologic and KI-67-labeling study. *HUM PATHOL* 1995;26:740-5.
- [26] Rugge M, Fassan M, Clemente R, et al. Bronchopulmonary carcinoid: phenotype and long-term outcome in a single-institution series of Italian patients. *Clin Cancer Res* 2008;14:149-54.





# Histologic features of low- and intermediate-grade neuroendocrine carcinoma (typical and atypical carcinoid tumors) of the lung

Koji Tsuta<sup>a,d</sup>, Maria G. Raso<sup>b</sup>, Neda Kalhor<sup>a</sup>, Diane D. Liu<sup>c</sup>, Ignacio I. Wistuba<sup>a,b</sup>, Cesar A. Moran<sup>a,\*</sup>

<sup>a</sup> Department of Pathology, The University of Texas M. D. Anderson Cancer Center, Houston, TX, USA

<sup>b</sup> Department of Thoracic/Head and Neck Medical Oncology, The University of Texas M. D. Anderson Cancer Center, Houston, TX, USA

<sup>c</sup> Department of Biostatistics, The University of Texas M. D. Anderson Cancer Center, Houston, TX, USA

<sup>d</sup> Division of Clinical Laboratory, National Cancer Center Hospital, Tokyo, Japan

## ARTICLE INFO

### Article history:

Received 10 November 2009

Received in revised form 5 February 2010

Accepted 1 April 2010

### Keywords:

Typical carcinoid

Atypical carcinoid

Mitosis

Necrosis

Recurrence-free survival

Neuroendocrine carcinoma

## ABSTRACT

**Background:** Determining the differential diagnosis between typical (TCs) and atypical carcinoid tumors (ACs) is imperative, as the distinction between TCs and ACs is currently based on histologic criteria that are not always correlated with the unfavorable clinical outcomes.

**Patients and methods:** We conducted a retrospective study of patients who were diagnosed with carcinoid tumors between 1990 and 2005 at M. D. Anderson Cancer Center. We reviewed the slides for the following pathologic features: infiltrative growth; pleural, blood, or lymphatic vessel invasion; tumor stroma; presence of active fibroblastic proliferation; chromatin pattern; presence of nucleolus; and nuclear pleomorphism. We also evaluated the necrotic patterns. Finally, we evaluated three methods for calculating the number of mitoses: randomly selected, the most mitotically active in 10 high-power fields (HPFs), or overall mean mitotic count.

**Results:** Our cohort consisted of 80 patients (68 with TCs and 12 with ACs). Older age ( $P=0.002$ ), pathologic stage III or IV disease ( $P=0.04$ ), active fibroblastic proliferation ( $P=0.041$ ), and comedo-like necrosis ( $P=0.001$ ) were significantly associated with tumor recurrence or patient's death. Among the three mitotic counting methods, the overall mean number of mitoses was significantly correlated with recurrence-free survival ( $P<0.0001$ ). Our criteria for distinguishing AC from TC included the presence of comedo-like necrosis and/or an overall mean number of mitoses  $\geq 0.2$ /HPF.

**Conclusions:** Using an overall mean number in counting mitoses and detecting comedo-like necrosis is important for classifying lung carcinoid tumors.

© 2010 Published by Elsevier Ireland Ltd.

## 1. Introduction

Bronchopulmonary neuroendocrine tumors comprise about 20% of all lung carcinomas and represent a spectrum of tumors arising from neuroendocrine cells. The different types of bronchopulmonary neuroendocrine carcinomas share structural, morphologic, immunohistochemical, and ultrastructural features, and they are separated into four subgroups in increasing order of biologic aggressiveness: low-grade (typical carcinoids; TCs), intermediate-grade (atypical carcinoids; ACs), and high-grade (large-cell neuroendocrine carcinomas; LCNECs), or (small-cell lung carcinomas). TCs and ACs account for approximately 1–2% of all primary lung carcinomas [1,2].

Although TCs are generally regarded as low-grade carcinomas, approximately 10–23% [3] of cases metastasize to the regional lymph nodes at presentation, with the 5-year overall survival rates ranging from 82% to 100% for patients with TCs [4,5]. In contrast, approximately 40–50% of ACs metastasize to the regional lymph nodes at presentation, with the 5-year overall survival rates ranging from 25% to 78% for patients with ACs [2,5–9].

Conventional carcinoid tumors are composed of homogeneous cellular proliferation with an organoid and trabecular structure. Tumor cells are composed of small- to medium-sized, round to polygonal cells with a scant to moderate amount of eosinophilic cytoplasm and centrally located round to oval nuclei with fine granular chromatin. Histologic atypia, such as nuclear atypia, prominent nucleoli, and pleomorphism, is more common in AC than TC, but these features are sometimes observed in TC [6,7,10]. Therefore, the unfavorable clinical outcomes and atypical histologic features associated with these lung carcinoid tumors are unreliable for distinguishing TCs from ACs.

\* Corresponding author at: Department of Pathology, Unit 85, The University of Texas M. D. Anderson Cancer Center, 1515 Holcombe Boulevard, Houston, TX 77030, USA. Tel.: +1 713 792 8134; fax: +1 713 745 3740.

E-mail address: [CesarMoran@mdanderson.org](mailto:CesarMoran@mdanderson.org) (C.A. Moran).

Arrigoni et al. [11] first defined ACs as carcinoid tumors with (1) 1 mitosis/1–2 high-power fields (HPFs) or 5–10 mitoses/10 HPF; (2) necrosis; (3) pleomorphism, hyperchromasia, or an abnormal nuclear/cytoplasmic ratio; and (4) areas of increased cellularity with disorganization. In 1998, Travis et al. [6] proposed that LCNECs be classified in a separate category from ACs, as this poorly differentiated high-grade carcinoma was characterized by a neuroendocrine appearance under light microscopy. These criteria have been applied to the latest World Health Organization classification [10]. With the establishment of diagnostic criteria for LCNEC, the definition of AC was then restricted to tumors with a mitotic rate of 2–10 mitoses per 2 mm<sup>2</sup> (10 HPF) or the presence of necrosis.

Differentiating ACs from TCs or LCNECs is clinically important because the treatment modalities and prognoses for these types of tumors are different. However, the distinction between ACs and TCs is currently based only on the histologic evaluation of mitotic count and necrosis. In this study, we sought to retrospectively evaluate the various histologic features of ACs and TCs and relate these to their outcomes (i.e., tumor recurrence, patient death, or lymph node metastasis). Furthermore, we revised the relevance of the patterns of necrosis and mitotic counting methods.

## 2. Materials and methods

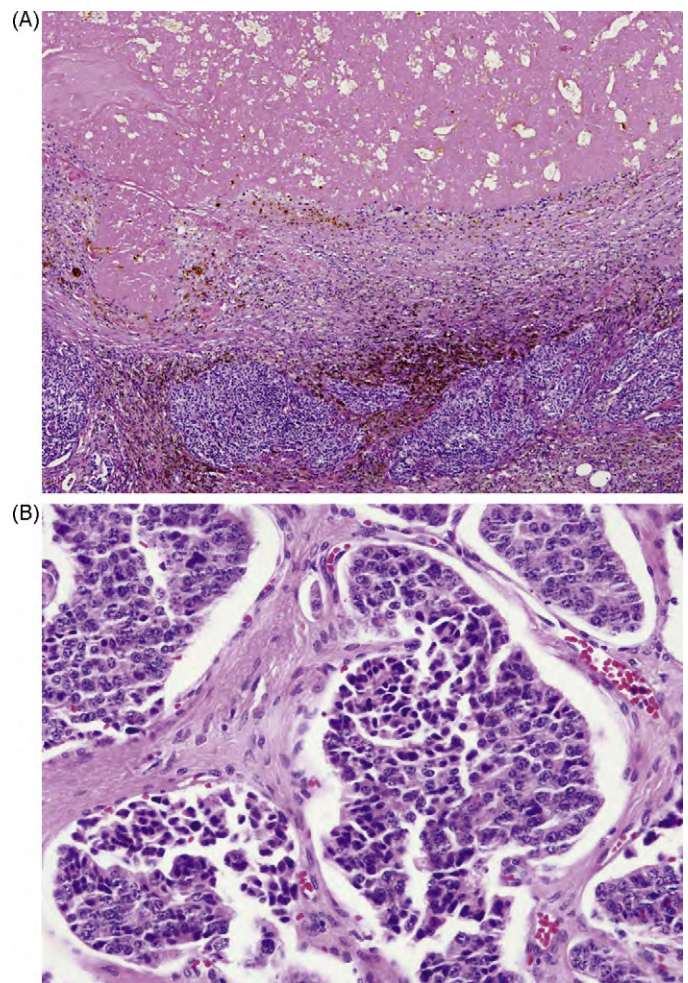
### 2.1. Case selection

We retrospectively reviewed the tumor specimens from patients who were surgically resected and diagnosed with TC or AC between 1990 and 2005. We obtained the tumor specimens from cases deposited in the files of the University of Texas M. D. Anderson Cancer Center (Houston, TX, USA) Lung SPORE Tissue Bank, which was approved by the institutional review board. We reviewed the pathologic records of the specimens and all available hematoxylin and eosin (HE)-stained slides, some special stains, and the immunohistochemical and/or ultrastructural analyses available. We collected the patients' clinical information, including age, gender, smoking history, presenting symptoms, treatment modalities, site of any tumor recurrence, duration of recurrence or survival, tumor location (which lobe and whether central or not), maximum tumor size (in cm), and pathologic disease stage (p-stage).

### 2.2. Histologic examination

All available HE-stained slides for each case were examined by two pathologists (K.T. and C.A.M.); each pathologist was blinded to the clinical details of each patient. We evaluated the pathologic features of tumor invasiveness, including the infiltrative growth of the adjacent normal architecture, presence of pleural invasion, and presence of blood or lymphatic vessel invasion. The stroma between the tumor nests was mainly composed of capillary or fibrous tissue. We also observed active fibroblastic proliferation [12]. We then evaluated the histologic features of the tumor cells, including the chromatin pattern (i.e., fine granular or coarse) and the presence or absence of nucleolus and nuclear pleomorphism (i.e., whether there was more than a 3-fold variation in nuclear size that did not include the presence of giant cells).

We then evaluated the necrotic pattern, such as the presence or absence of comedo-like necrosis (necrosis present within the center of tumor nest) and coagulative necrosis (necrosis involving one or more whole tumor nests and/or forming bridging necrosis) (Fig. 1A). We also evaluated the histologic features suggesting tumor damage, such as pyknotic cells (i.e., foci of dyscohesive cells) with somewhat pyknotic nuclei and condensed, shrunken-appearing cytoplasm without karyorrhexis, eosinophilic debris, or apoptosis (Fig. 1B), cholesterol cleft, stromal hemorrhage, and psammoma bodies.



**Fig. 1.** (A) Massive coagulative necrosis surrounded by thick fibrous tissue with a hemosiderin deposition. The outermost portion of the necrosis consisted of tumor cells. (B) Foci of dyscohesive cells with somewhat pyknotic nuclei and condensed, shrunken-appearing cytoplasm without karyorrhexis, eosinophilic debris, or apoptosis observed in tumor nests.

or apoptosis (Fig. 1B), cholesterol cleft, stromal hemorrhage, and psammoma bodies.

### 2.3. The mitotic counting method

After all slides were reviewed on an Olympus CX31 microscope (Olympus; Tokyo, Japan), the mitoses were counted on one representative slide. This microscope's standard field of view number is 20 (0.2 mm<sup>2</sup>); therefore, an HPF magnification of 400× equals to 0.2 mm<sup>2</sup>. To determine the most suitable mitotic counting method, we studied three methods: (1) the number of mitoses in a randomly selected 10-HPF area counted; (2) the number of mitoses in the most mitotically active 10-HPF areas (so called hot spots) counted; or (3) the mean number of mitoses in the whole section calculated (the number of mitoses divided by the number of HPFs in the whole section). To avoid overcounting the number of mitoses at the telophase, two adjoining mitotic figures were counted as one mitosis.

### 2.4. Statistical analysis

We performed all statistical analyses using SPSS version 12.0 software for Windows (SPSS; Chicago, IL). We used the Wilcoxon rank-sum test to analyze the continuous variables and Fisher's



exact test to analyze lymph node metastasis. We calculated the recurrence-free survival (RFS) curves using the Kaplan–Meier method, and we compared the curves using the log-rank test. We considered a  $P$ -value of  $\leq 0.05$  to be significant in two tailed analysis.

### 3. Results

#### 3.1. Clinical features

We reviewed the tumor specimens from 88 patients with an original diagnosis of lung carcinoid tumors. We excluded 5 patients who received therapy preoperatively (4 who received neoadjuvant chemotherapy and 1 who received YAG laser ablation). Furthermore, we excluded 3 patients who had high mitotic activity and massive necrosis; their diagnosis was then changed to LCNEC based on the latest World Health Organization criteria [10]. Therefore, our final cohort consisted of 80 patients with lung carcinoid tumors, including 68 patients with TCs and 12 with ACs. The patients' mean age (at the time of diagnosis) was 54.3 years (range, 19–80 years). The presenting symptoms were documented in 27 out of 77 patients. Smoking history was documented in 76 cases; 32 patients were never smokers, 32 were former smokers, and 12 were present smokers. The tumor was located in the right-upper lobe in 11 patients, the middle lobe in 10, the right-lower lobe in 26, the left-upper lobe in 13, and the left-lower lobe in 19, and 1 patient had a hilar lesion. The tumor was located in the central portion of the lung in 49 patients or in the intermediate or peripheral portion in 31 patients. A preoperative biopsy and/or cytologic diagnostic procedure were carried out in 69 patients, including the diagnoses were not tumorous lesions.

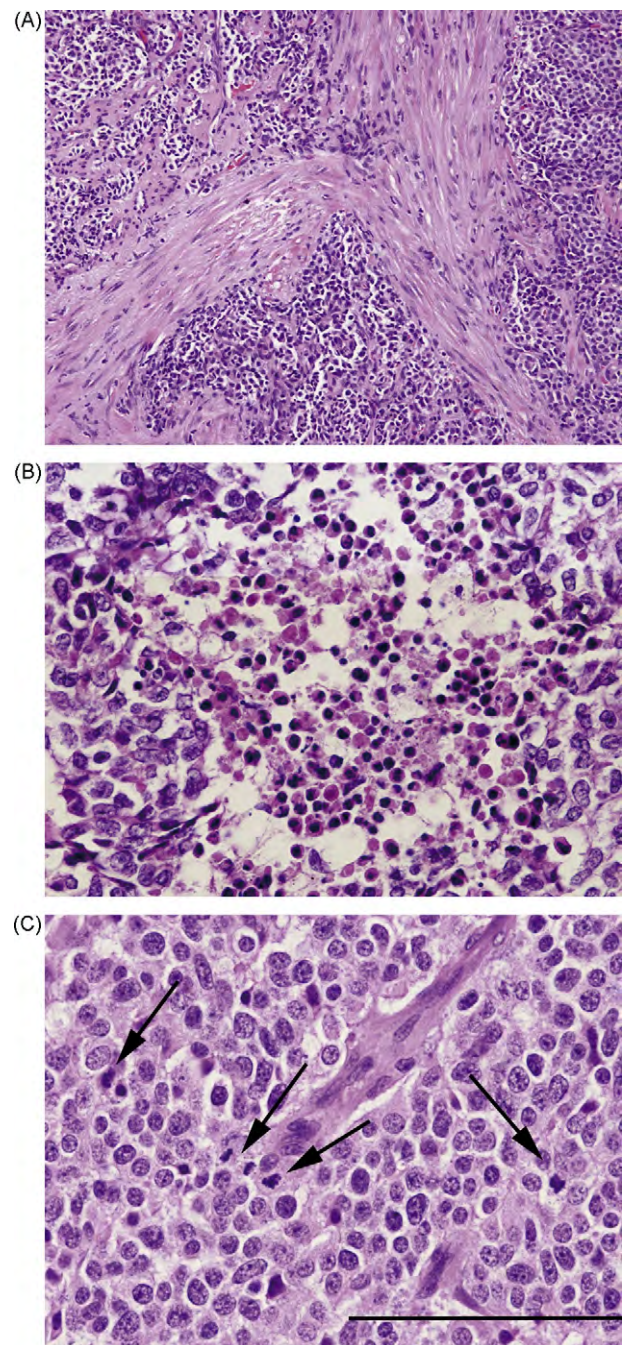
The tumor sizes ranged from 1.0 to 13.0 cm (mean, 2.96 cm). Lymph node status was recorded in 79 patients, and metastasis was observed in 17. Sixty-one cases had p-stage I disease, 6 had p-stage II disease, 11 had p-stage III disease, 1 had p-stage IV disease, and 1 case was unstaged.

Tumor recurrence was observed in 6 of 80 patients (2 cases of liver recurrence and 1 case each of kidney, brain, chest wall, and subclavicular lymph node recurrence). The mean follow-up time for all 80 patients was 68 months (range, 1–197 months), with 74 still alive at the time of this report. Only 1 patient died of a tumor progression, and 5 died of other causes.

#### 3.2. Histologic factors

We reviewed an average of 4.7 (range, 1–16) HE-stained slides for each case. Infiltrative growth was observed in 47 cases. Blood-vessel, lymph-vessel, and pleural invasion were observed in 34 cases, 29 cases, and 1 case, respectively. Capillary rich stroma was observed in 57 cases, and fibrous rich stroma was observed in 23 cases. Active fibroblastic proliferation was observed in 38 cases (Fig. 2A). We found a fine chromatin pattern in 47 cases and a coarse chromatin pattern in 33 cases. We also observed a conspicuous nucleolus in 15 cases and nuclear pleomorphism in 13 cases. We found other unusual histologic features of the tumors, such as bone formation in 16 cases and granulomatous inflammation in 2 cases.

We found comedo-like necrosis in 5 cases and coagulative necrosis in 10 cases (Fig. 2B), and we found both comedo-like and coagulative necrosis in 2 cases. All but 1 patient with coagulative necrosis had undergone preoperative biopsy. Pyknotic cells, cholesterol cleft, hemorrhage, and psammoma bodies were observed in 54 cases, 4 cases, 29 cases, and 13 cases, respectively.



**Fig. 2.** (A) Bundles of spindle-shaped fibroblasts are shown between tumor nests (magnification,  $10\times$ ). (B) The tumor had a large solid nest with comedo-like necrosis (magnification,  $20\times$ ). (C) Although this case showed 5 mitoses in 1 high-power field (HPF), this photomicrograph area is smaller than 1 HPF ( $0.2\text{ mm}^2$ ) and corresponded to a  $0.134\text{ mm}^2$  area. Because this image was captured using the Olympus DP-70 system (Tokyo, Japan), this photomicrograph showed 4 mitotic figures, indicated by the arrows (2 in prophase, 1 in metaphase, and 1 in telophase). This case's mitotic count in the most mitotically active area was 15 mitoses/10 HPF, but the average mitosis was 0.18 mitoses/HPF. This patient was alive at 45 months with no evidence of tumor recurrence (bar =  $200\text{ }\mu\text{m}$ ).

#### 3.3. Mitotic count

We reviewed a mean of 341.6 HPF (range, 44–762 HPF) per case. The number of mitoses ranged from 0 to 115, with a mean of 10.9 per case. The number of mitoses in 1 HPF exceeded 2 in 26 cases, and the highest recorded mitotic count in 1 HPF was 5 (Fig. 2C). The mean number of mitoses in the randomly selected 10-HPF

areas was 0.45 mitoses/10 HPF (range, 0–6 mitoses/10 HPF), and the mean number of mitoses in the most mitotically active 10-HPF areas was 5.73 mitoses/10 HPF (range, 0–25 mitoses/10 HPF). The overall mean number of mitoses was 0.04 mitoses/1 HPF (range, 0–0.32 mitoses/1 HPF).

Both the presence of comedo-like necrosis and an overall mean number of mitoses of  $\geq 0.2$  mitoses/1 HPF were observed in 3 cases. These cases corresponded to 60% of cases bearing comedo-like necrosis and 60% of cases having an overall mean number of mitoses  $\geq 0.2$  mitoses/1 HPF.

#### 3.4. Clinicopathologic features based on unfavorable outcomes

We next evaluated whether there was an association between the patients' clinicopathologic factors and tumor recurrence, patient death, and/or lymph node metastasis (Table 1). An older age ( $P=0.002$ ), p-stage III or IV disease ( $P=0.0029$ ), pleural invasion ( $P<0.0001$ ), and the presence of active fibroblasts ( $P=0.0184$ ) were significantly associated with tumor recurrence or patient death. All patients with tumor specimens that exhibited an active fibroblastic proliferation had undergone a preoperative biopsy and/or cytologic diagnostic procedure. Blood-vessel invasion ( $P=0.0417$ ), lymph-vessel invasion ( $P=0.0017$ ), coarse chromatin pattern ( $P=0.0304$ ), conspicuous nucleolus ( $P=0.0085$ ), and nuclear pleomorphism ( $P=0.0019$ ) were significantly associated with lymph node metastasis.

#### 3.5. Evaluation of necrotic patterns based on the patients' unfavorable outcomes and RFS

We then sought to determine if there was a correlation between the tumor specimens' necrotic patterns and histologic features suggesting tumor damage and the patients' unfavorable outcomes (Table 2). Only the presence of comedo-like necrosis was significantly associated with tumor recurrence or patient death ( $P<0.0001$ ).

#### 3.6. Evaluation of mitotic count based on the patients' unfavorable outcomes, RFS, and OS

We investigated whether there was a correlation between the results of three mitotic counting methods and the patients' unfavorable outcomes and RFS (Table 3). For specimens in which the number of mitoses in a randomly selected 10-HPF area was counted, the presence of 2–10 mitoses/10 HPF appeared to be significantly associated with tumor recurrence or patient death ( $P=0.003$ ). In addition, the 5-year RFS rates for the specimens with 0–1 mitoses/10 HPF and 2–10 mitoses/10 HPF were 94.2% and 58.3%, respectively (Fig. 3A). However, when we individualized each case and correlated the number of mitotic figures with the 5-year RFS rates, we obtained the following information: 0 mitoses = 95.1%; 1 mitotic figure = 87.5%; 2 mitotic figures = 75.0%; 3 mitotic figures = 100%. Based on these data, we analyzed changing the cut off number of mitosis from 0–3 to 4–10. The 5-year RFS rates for the specimens with 0–3 mitoses/10 HPF and 4–10 mitoses/10 HPF were 93.1% and 0%, respectively ( $P=0.002$ ).

For specimens in which the number of mitoses in the most mitotically active 10-HPF area was counted, this method showed tendency with tumor recurrence or patient death ( $P=0.0575$ ). The 5-year RFS rates for specimens with 0–1 mitoses/10 HPF, 2–10 mitoses/10 HPF, and more than 11 mitoses/10 HPF were 95.5%, 94.6%, and 75.2%, respectively ( $P=0.0575$ ; Fig. 3B). Once again, when we individualized each case and correlated the number of mitotic figures with the 5-year RFS rates, we obtained the following information: 0 mitoses = 100%; 1 mitotic figure = 90.0%; 2 mitotic figures = 100%; and 3 mitotic figures = 100%. Based on these

data, we analyzed changing the cut off number of mitosis from 0–3 to 4 or more. The 5-year RFS rates for the specimens with 0–3 mitoses/10 HPF and 4 or more mitoses/10 HPF were 97.4% and 83.4%, respectively ( $P=0.024$ ).

For specimens in which the overall mean number of mitoses was calculated, the value of  $\geq 0.2$  mitoses per 1 HPF was significantly associated with tumor recurrence or patient death ( $P<0.0001$ ). The 5-year RFS rates for specimens with an overall mean mitosis  $<0.2$  and a mean mitosis  $\geq 0.2$  were 95.9% and 0%, respectively (Fig. 3C). Multivariate analysis was not performed because of the small number of events (recurrence and death) in our patient population. Based on the 5-year RFS rates, we considered that the overall mean mitotic counting method was the most useful. Furthermore, we also found that the criteria on the number of mitosis should be selected based on the counting methods (0–3 and 4–10 in randomly selected areas and 0–3 and  $\geq 4$  in the most mitotically active areas).

Although there were few deaths, we analyzed 5-year OS rates. For specimens in which the number of mitoses was counted in a randomly selected 10-HPF area, the 5-year OS rates with 0–1 mitoses/10 HPF and 2–10 mitoses/10 HPF were 100% and 96.6%, respectively ( $P=0.0033$ ; Fig. 3D). For specimens in which the number of mitoses in the most mitotically active 10-HPF area was counted, the 5-year OS rates for specimens with 0–1 mitoses/10 HPF, 2–10 mitoses/10 HPF, and  $>11$  mitoses/10 HPF were 100%, 95.5%, and 82.1%, respectively ( $P=0.1471$ ; Fig. 3E). For specimens in which the overall mean number of mitoses was calculated, the 5-year OS rates for specimens with an overall mean mitosis  $<0.2$  and a mean mitosis  $\geq 0.2$  were 98.7% and 0%, respectively ( $P<0.0001$ ; Fig. 3F).

#### 3.7. New recommended definition for AC

Based on these results, we recommend that the definition for AC include comedo-like necrosis and/or an overall mean number of mitosis of  $\geq 0.2$ . Based on this definition, we observed AC in 7 cases rather than the 12 cases specified in the records. The 5-year RFS rates for patients with TC and AC by this new definition were 97.2% and 0%, respectively ( $P<0.0001$ ; Fig. 4). We observed lymph node metastasis in 14 patients with TC and 3 patients with AC; however, there was no significant difference between these two rates ( $P=0.166$ ).

## 4. Discussion

Our results favor a new histological definition for AC. In this study, we found that the overall mean number of mitoses was superior to calculate the number of mitoses in a randomly selected 10-HPF area or in the most mitotically active 10-HPF area. Furthermore, the presence of comedo-like necrosis was significantly associated with tumor recurrence and patient death when compared to the presence of coagulative necrosis.

A high mitotic count is generally reported as an unfavorable factor in patients with tumors. In general, selecting the most mitotically active 10-HPF area is the preferred method for calculating mitotic counts [13–15]. Most of the articles on pulmonary neuroendocrine tumors, including the first publication on the definition of LCNEC, counted the mitoses in the most mitotically active areas [7,16,17]. Our results indicated that the mitotic counts in both ACs and TCs were distributed heterogeneously. Surprisingly, 21 of 26 cases with a mitotic count exceeding 2 mitoses in only 1 HPF showed no tumor recurrence or patient death. When compared with a randomly selected 10-HPF area or the most mitotically active 10-HPF area,  $\geq 2$  mitoses in only 1 HPF had the least selection bias to go beyond the diagnostic criteria for TC. Furthermore, when we selected the most mitotically active areas, 20 cases went

**Table 1**  
Correlation between clinicopathological factors and unfavorable outcomes.

	Recurrence/death		P-value <sup>a</sup>	Lymph node metastasis		P-value <sup>b</sup>
	(–)	(+)		(–)	(+)	
Original diagnosis						
Typical	63	5	<0.0001	55	12	0.1192
Atypical	7	5		7	5	
Age (years)	52.5	67.1	0.002	54.1	54.4	1.00
Gender						
Female	45	4	0.1944	38	10	0.8536
Male	25	6		24	7	
Symptom						
None	43	7	0.8271	38	11	0.5524
Present	24	3		23	4	
Smoking						
Never	31	1	0.0767	27	4	0.5267
Former	25	7		24	8	
Present	10	2		10	2	
Location						
Central	44	5	0.3645	38	11	0.7971
Non-central	26	5		24	6	
Tumor size (cm)	2.92	3.23	0.936	3.05	2.69	0.9952
Lymph node metastasis						
Absent	55	7	0.4563	–	–	–
Present	14	3		–	–	
Pathologic stage						
I and II	61	6	0.0029	–	–	–
III and IV	8	4		–	–	
Infiltrative growth						
Absent	29	4	0.4805	27	5	0.4051
Present	41	6		35	12	
Blood-vessel invasion						
Absent	46	3	0.088	39	6	0.0417
Present	27	7		23	11	
Lymph-vessel invasion						
Absent	46	5	0.2246	45	5	0.0017
Present	24	5		17	12	
Pleural invasion						
Absent	70	9	<0.0001	61	17	1.00
Present	0	1		1	0	
Stroma						
Capillary rich	52	5	0.1467	43	13	0.7649
Fibrous rich	18	5		19	4	
Active fibroblastic proliferation						
Absent	40	2	0.0184	34	7	0.3179
Present	30	8		28	10	
Chromatin pattern						
Fine	40	7	0.5614	40	6	0.0304
Coarse	30	3		22	11	
Nucleolus						
Inconspicuous	57	8	0.7714	54	10	0.0085
Conspicuous	13	2		8	7	
Nuclear pleomorphism						
Absent	59	8	0.5684	56	10	0.0019
Present	11	2		6	7	

<sup>a</sup> Log-rank test.

<sup>b</sup> Fisher's exact test.

beyond the diagnostic criteria for AC. These results indicated that the latest WHO criteria for diagnosing ACs is strict only evaluating in 10 HPFs.

We also attempted to determine if there was a pattern to the distribution of mitoses (such as within the tumor's center or in the periphery); however, we did not see a uniform tendency (unpublished results). Travis et al. counted the number of mitoses in

pulmonary neuroendocrine tumors in three sets of 10 HPF and calculated the mean [6,16]. Their results indicated that one set of 10 HPFs is not enough to evaluate the mitotic activity because of the mitotic heterogeneity in carcinoid tumors. Tiny material, such as biopsy specimens may not be suitable for a final diagnosis of TC or AC, because there may not be enough HPFs. The results of our study are based on surgically resected materials,



**Table 2**

Correlation between necrosis and unfavorable outcomes.

	Recurrence/death		<i>P</i> -value <sup>a</sup>	Lymph node metastasis		<i>P</i> -value <sup>b</sup>
	(–)	(+)		(–)	(+)	
Comedo-like necrosis						
Absent	69	6	<0.0001	60	14	0.0639
Present	1	4		2	3	
Coagulative necrosis						
Absent	62	8	0.3143	55	14	0.4414
Present	8	2		7	3	
Pyknotic change						
Absent	25	1	0.0954	22	3	0.2405
Present	45	9		40	14	
Cholesterol cleft						
Absent	67	9	0.4762	59	16	1.00
Present	3	1		3	1	
Hemorrhage						
Absent	47	4	0.102	41	9	0.3176
Present	23	6		21	8	
Psammomatous body						
Absent	61	6	0.0559	53	13	0.4611
Present	9	4		9	4	

<sup>a</sup> Log-rank test.<sup>b</sup> Fisher's exact test.

and it is unclear whether calculating the overall mean number of mitoses would be applicable for materials acquired from a biopsy.

The presence of necrosis is another criterion for differentiating TC from AC. In the current study, we analyzed the necrosis separating comedo-like and coagulative necrosis. We found that comedo-like necrosis was significantly associated with tumor recurrence and patient death when compared to coagulative necrosis. In fact, we did not see tumor recurrence or patient death in the cases with only coagulative necrosis. This may be because coagulative necrosis is not related to the tumor's malignant behavior but rather it may be related to preoperative biopsy or erosion. Travis et al. also pointed out that the large zone of infarct-like necrosis (corresponding to current coagulative necrosis) was not seen in ACs but was seen in high-grade neuroendocrine carcinomas [16].

It has been reported that hemorrhage, psammoma bodies, and/or cholesterol cleft form after the degeneration and disappear-

ance of tumor cells [18–20]. However, we found that these factors were not associated with the patients' clinical outcomes in our study. We observed pyknotic cells, which can sometimes be confused with incipient necrosis, in 69% of patients with both ACs and TCs. Similar to previous reports, our results demonstrated that the presence of pyknotic cells was not associated with the patients' clinical outcomes [7,8].

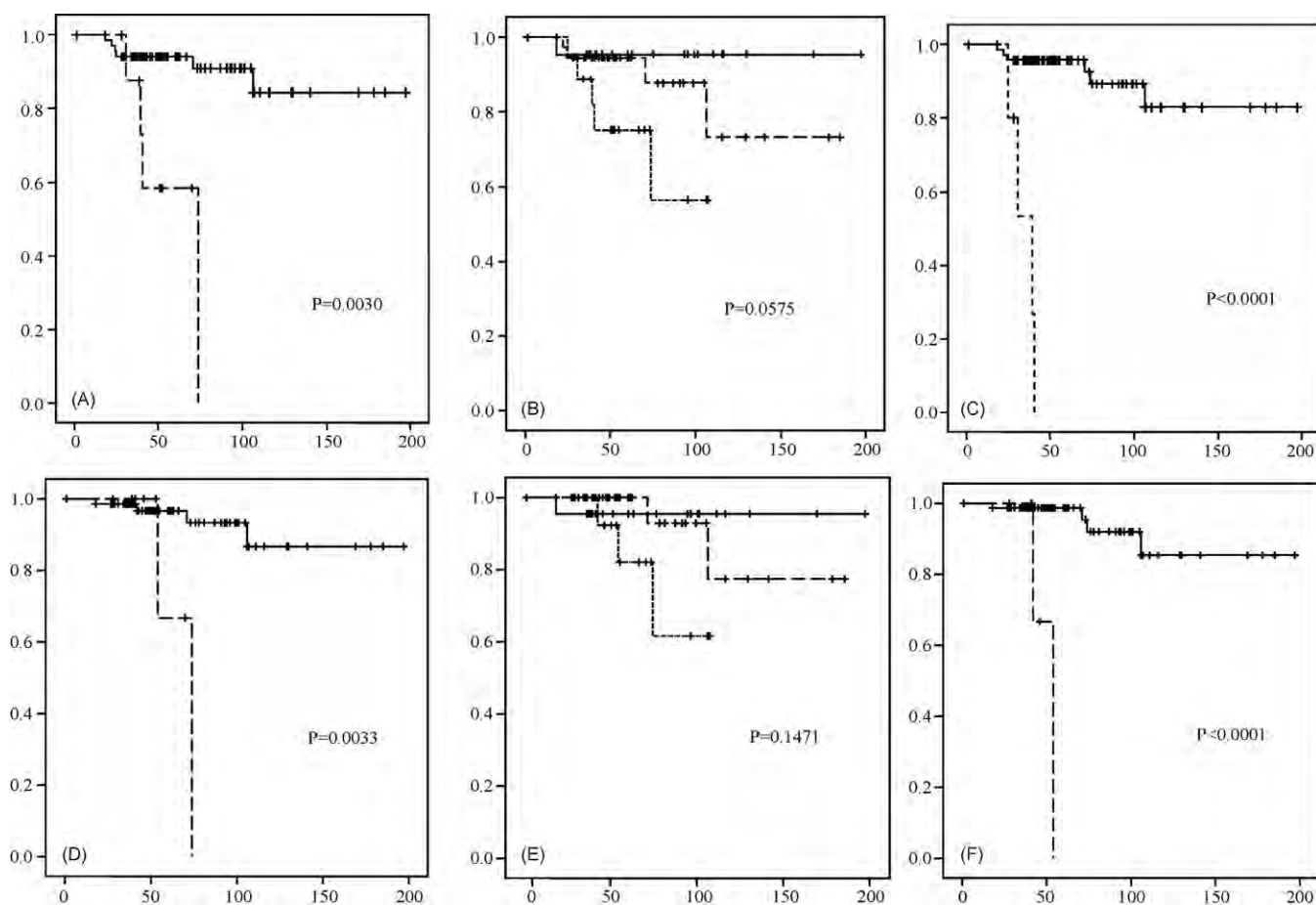
The presence of an active fibroblastic proliferation is one of the known unfavorable clinical outcomes in patients with pulmonary adenocarcinomas [12]. In our study, we observed active fibroblastic proliferation in 48% of the cases, which was significantly associated with tumor recurrence or patient death ( $P=0.0184$ ). All patients who had tumor specimens with active fibroblastic proliferation had undergone a preoperative biopsy and/or cytologic diagnostic procedure. However, these results did not exclude the possibility of the active fibroblastic proliferation induced by preoperative diagnostic procedures. Therefore, it will be necessary to study a larger number of patients who have not undergone

**Table 3**

Correlation between three mitotic count methods and unfavorable outcomes.

	Recurrence/death		<i>P</i> -value <sup>a</sup>	Lymph node metastasis		<i>P</i> -value <sup>b</sup>
	(–)	(+)		(–)	(+)	
Randomly selected 10 HPF						
<2	65	6	0.003	56	14	0.3957
≥2	5	4		6	3	
<2	69	8	0.002	60	16	0.522
≥2	1	2		2	1	
Highest 10 area						
<2	21	1	0.0575	21	1	0.0641
2–10	35	4		28	11	
>11	14	5	0.0238	13	5	0.180
0–3	37	2		28	11	
≥4	33	8		34	6	
Mean mitosis						
<0.2	69	6	<0.0001	60	14	0.0639
≥0.2	1	4		2	3	

<sup>a</sup> Log-rank test.<sup>b</sup> Fisher's exact test.



**Fig. 3.** The recurrence-free survival (RFS) rates for patients with ACs. (A) For cases where the number of mitoses was calculated in randomly selected 10-high-power field (HPF) areas, the 5-year RFS rates for cases with 0–1 mitoses/10 HPF (solid line) and 2–10 mitoses/10 HPF (dashed line) were 94.2% and 58.3%, respectively. (B) For cases where the number of mitoses was calculated in the most mitotically active 10-HPF area, the 5-year RFS rates for cases with 0–1 mitoses/10 HPF (solid line), 2–10 mitoses/10 HPF (dashed line), and  $\geq 11$  mitoses/10 HPF (square-dot line) were 95.5%, 94.6% and 75.2%, respectively. (C) For cases where the average mitotic count was calculated, the 5-year RFS rates for cases with  $<0.2$  mitoses/10 HPF (solid line) and  $\geq 0.2$  mitoses/10 HPF (dashed line) were 95.9% and 0%, respectively. (D) specimens with randomly selected 10-HPF are, the 5-year OS rates with 0–1 mitoses/10 HPF and 2–10 mitoses/10 HPF were 100% and 96% respectively. (E) Specimens with more mitotically active 10 HPF area, 5-year OS rates with 0–1 mitoses/10 HPF, 2–10 mitoses/10 HPF, and  $>11$  mitoses/10 HPF were 100%, 95%, and 82% respectively. (F) Specimens with overall mean of mitoses, the 5-year OS rates with mean  $<0.2$  and a mean mitosis  $>0.2$  were 98.7% and 0% respectively.

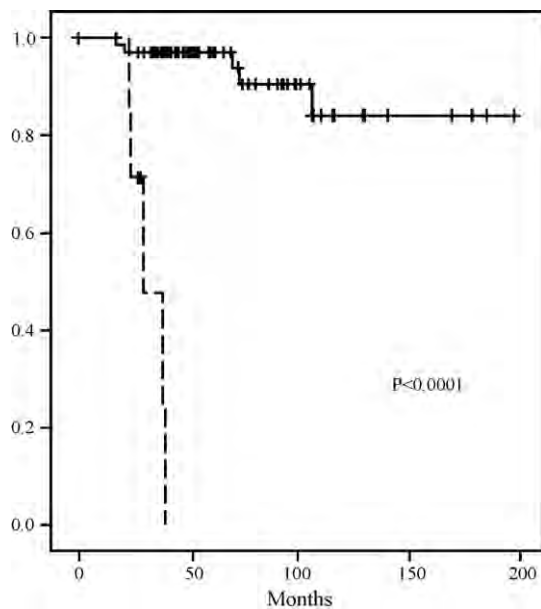
preoperative diagnostic procedures to determine the significance of active fibroblastic proliferation in patients with carcinoid tumors.

Although our cohort was not large enough to analyze each pathologic disease stage, patients with p-stage III or IV disease were more likely to experience a tumor recurrence or death than patients with p-stage I or II disease ( $P=0.00294$ ). Adapting the TNM classification scheme for patients with lung carcinoid tumors is an important factor for predicting survival [21]. However, one of the important factors of TNM classification – lymph node metastasis – was not correlated with tumor recurrence or patient death in our study. Currently, there are conflicting reports about the effect of lymph node metastasis for survival in patients with carcinoid tumors. Some studies have found that in patients with TC, lymph node metastasis did not affect survival [8,22]. However, if some histologic factors can predict the risk of lymph node metastasis, they may be useful for determining the extent of the regional lymph node dissection for surgeons. In our study, the presence of blood-vessel invasion, lymph-vessel invasion, coarse chromatin pattern, nucleolus prominence, and nuclear pleomorphism were correlated with lymph node metastasis, but mitotic activity and/or the presence of necrosis were not. Based on these factors, the presence of a coarse chromatin pattern,

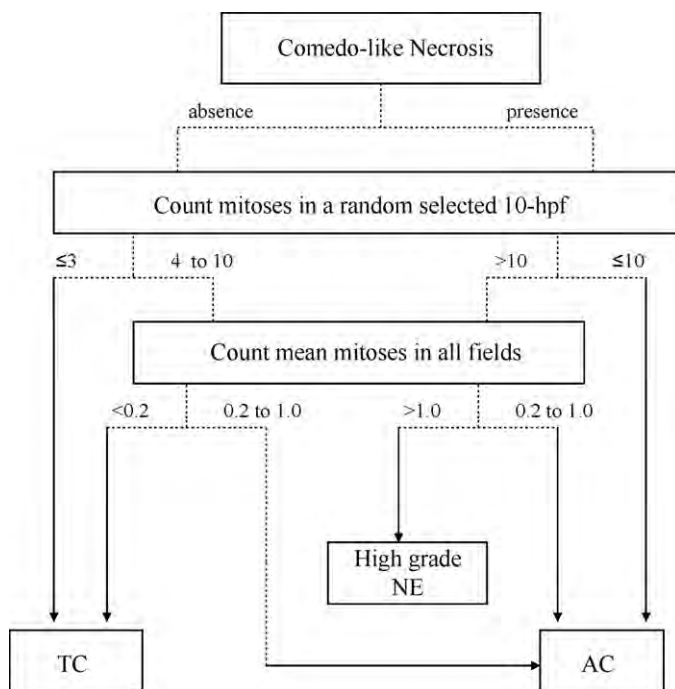
nucleolus prominence, and nuclear pleomorphism can be diagnostic features for lymph node metastasis in preoperative biopsy materials.

We found that counting the overall mean number of mitoses was superior to the other methods for determining the specimens' mitotic counts. However, counting the number of mitoses in all fields in each case at a high magnification may be unsuitable for daily practice because of the substantial time involved. Therefore, based on our results, we made a flow chart (Fig. 5) to aid in the diagnosis of low- and intermediate-grade neuroendocrine carcinomas.

In short, we concluded that the mitotic figures of carcinoid tumors have a heterogeneous distribution. To reduce the selection biases of fields and observer variation, we recommended calculating the overall mean number of mitoses. We also pointed out the potential for overdiagnosing carcinoid tumors using the method for counting mitoses in the most mitotically active 10-HPF. Furthermore, we concluded that comedo-like necrosis was a more important pattern to look for than coagulative necrosis for predicting tumor recurrence or patient death. The combination of calculating the mean number of mitoses and the presence of comedo-like necrosis should be added to the current criteria for diagnosing ACs.



**Fig. 4.** Based on our recommended criteria for atypical carcinoids, the 5-year disease-free survival rates for patients with typical carcinoids (solid line) and atypical carcinoids (comedo-like necrosis and/or an average mitosis  $\geq 0.2$  mitoses/10 HPF; dashed line) were 97.2% and 0%, respectively.



**Fig. 5.** A dichotomous tree for diagnosing neuroendocrine tumors of the lung, according to our results. Abbreviations: TC, typical carcinoid; AC, atypical carcinoid; NE, neuroendocrine tumor; HPF, high-power field.

### Conflict of interest statement

There is no conflict of interest with regard to this manuscript.

### Acknowledgements

We would like to thank Susan Cweren for her skillful technical assistance and Alyson Todd for her skillful English editing.

This work was supported in part by the grant from the US Department of Defense PROSPECT W81XWH-07-1-0306.

### References

- [1] Fink G, Krelbaum T, Yellin A, Bendayan D, Saute M, Glazer M, et al. Pulmonary carcinoid: presentation, diagnosis, and outcome in 142 cases in Israel and review of 640 cases from the literature. *Chest* 2001;119:1647–51.
- [2] Hage R, de la Riviere AB, Seldenrijk CA, van den Bosch JM. Update in pulmonary carcinoid tumors: a review article. *Ann Surg Oncol* 2003;10:697–704.
- [3] Granberg D, Wilander E, Oberg K, Skogseid B. Prognostic markers in patients with typical bronchial carcinoid tumors. *J Clin Endocrinol Metab* 2000;85:3425–30.
- [4] Cooper WA, Thourani VH, Gal AA, Lee RB, Mansour KA, Miller JL. The surgical spectrum of pulmonary neuroendocrine neoplasms. *Chest* 2001;119:14–8.
- [5] Garcia-Yuste M, Matilla JM, Cueto A, Paniagua JM, Ramos G, Cañizares MA. Typical and atypical carcinoid tumours: analysis of the experience of the Spanish Multi-centric Study of Neuroendocrine Tumours of the Lung. *Eur J Cardiothorac Surg* 2007;31:192–7.
- [6] Travis WD, Rush W, Flieder DB, Falk R, Fleming MV, Gal AA. Survival analysis of 200 pulmonary neuroendocrine tumors with clarification of criteria for atypical carcinoid and its separation from typical carcinoid. *Am J Surg Pathol* 1998;22:934–44.
- [7] Beasley MB, Thunnissen FB, Brambilla E, Hasleton P, Steele R, Hammar SP, et al. Pulmonary atypical carcinoid: predictors of survival in 106 cases. *Hum Pathol* 2000;31:1255–65.
- [8] Thomas Jr CF, Tazelaar HD, Jett JR. Typical and atypical pulmonary carcinoids: outcome in patients presenting with regional lymph node involvement. *Chest* 2001;119:1143–50.
- [9] Asamura H, Kameya T, Matsuno Y, Noguchi M, Tada H, Ishikawa Y, et al. Neuroendocrine neoplasms of the lung: a prognostic spectrum. *J Clin Oncol* 2006;24:70–6.
- [10] Beasley MB, Thunnissen FB, Hasleton P, Barbareschi M, Pugatch B. Carcinoid tumour. In: Travis WD, Brambilla E, Muller-Hermelink HK, Harris CC, editors. *Pathology and genetics: tumors of the lung, pleura, thymus and heart*. Lyon, France: IARC; 2004. p. 59–62.
- [11] Arrigoni MG, Woolner LB, Bernatz PE. Atypical carcinoid tumors of the lung. *J Thorac Cardiovasc Surg* 1972;64:413–21.
- [12] Noguchi M, Morikawa A, Kawasaki M, Matsuno Y, Yamada T, Hirohashi S, et al. Small adenocarcinoma of the lung. Histologic characteristics and prognosis. *Cancer* 1995;75:2844–52.
- [13] Kempson RL. Mitosis counting-II (editorial). *Hum Pathol* 1976;7:482–3.
- [14] Baak JPA. Mitosis counting in tumors. *Hum Pathol* 1990;21:683–5.
- [15] van Diest PJ, Baak JP, Matze-Cok P, Wisse-Brekelmans EC, van Galen CM, Kurver PH, et al. Reproducibility of mitosis counting in 2,469 breast cancer specimens: results from the Multicenter Morphometric Mammary Carcinoma Project. *Hum Pathol* 1992;23:603–7.
- [16] Travis WD, Linnoila RI, Tsokos MG, Hitchcock CL, Cutler Jr GB, Nieman L, et al. Neuroendocrine tumors of the lung with proposed criteria for large-cell neuroendocrine carcinoma: an ultrastructural, immunohistochemical, and flow cytometric study of 35 cases. *Am J Surg Pathol* 1991;15:529–53.
- [17] Rugge M, Fassan M, Clemente R, Rizzardi G, Giacomelli L, Pennelli G, et al. Bronchopulmonary carcinoid: phenotype and long-term outcome in a single-institution series of Italian patients. *Clin Cancer Res* 2008;14:149–54.
- [18] Shimosato Y, Suzuki A, Hashimoto T, Nishiwaki Y, Kodama T, Yoneyama T, et al. Prognostic implications of fibrotic focus (scar) in small peripheral lung cancers. *Am J Surg Pathol* 1980;4:365–73.
- [19] McCluggage WG, Lyness RW, Atkinson RJ, Dobbs SP, Harley I, McClelland HR, et al. Morphological effects of chemotherapy on ovarian carcinoma. *J Clin Pathol* 2002;55:27–31.
- [20] Liu-Jarin X, Stoopler MB, Raftopoulos H, Ginsburg M, Gorenstein L, Borczuk AC. Histologic assessment of non-small cell lung carcinoma after neoadjuvant therapy. *Mod Pathol* 2003;160:1102–8.
- [21] Travis WD, Giroux DJ, Chansky K, Crowley J, Asamura H, Brambilla E, et al. The IASLC Lung Cancer Staging Project: proposals for the inclusion of bronchopulmonary carcinoid tumors in the forthcoming (seventh) edition of the TNM Classification for Lung Cancer. *J Thorac Oncol* 2008;3:1213–23.
- [22] Schreurs AJ, Westermann CJ, van den Bosch JM, Vanderschueren RG, Brutel de la Riviere A, Knaepen PJ. A twenty-five-year follow-up of ninety-three resected typical carcinoid tumors of the lung. *Thorac Cardiovasc Surg* 1992;104:1470–5.

# Sox10-positive sustentacular cells in neuroendocrine carcinoma of the lung

Koji Tsuta,<sup>1,2</sup> Maria G Raso,<sup>1</sup> Neda Kalhor,<sup>1</sup> Diane C Liu,<sup>3</sup> Ignacio I Wistuba<sup>1,4</sup> & Cesar A Moran<sup>1</sup>

<sup>1</sup>Department of Pathology, The University of Texas M.D. Anderson Cancer Center, Houston, TX, USA, <sup>2</sup>Division of Clinical Laboratory, National Cancer Center Hospital, Tokyo, Japan, <sup>3</sup>Departments of Biostatistics and <sup>4</sup>Thoracic/Head and Neck Medical Oncology, The University of Texas M.D. Anderson Cancer Center, Houston, TX, USA

Date of submission 1 October 2009  
Accepted for publication 30 March 2010

Tsuta K, Raso M G, Kalhor N, Liu D C, Wistuba I I & Moran C A  
(2011) *Histopathology* 58, 276–285

## Sox10-positive sustentacular cells in neuroendocrine carcinoma of the lung

**Aims:** Sustentacular cells are found in approximately half of pulmonary carcinoid tumours. However, most studies of sustentacular cells have used the less-specific antibody to the S100 protein, and any correlation between the presence of sustentacular cells and other clinicopathological factors is unclear. The aim of this study was to analyse the significance of sustentacular cells in pulmonary neuroendocrine carcinomas (NECs). **Methods and results:** A Sox10 antibody was used to investigate 113 pulmonary NECs. Sustentacular cells were observed in 66.7% of typical carcinoid (TC) and 58.3% of atypical carcinoid (AC) cases, but not in high-grade NECs. Sustentacular-rich tumours had a statistically significant correlation with peripheral locations.

We found no statistical differences in age, gender, smoking history, overall survival, or the occurrence of lymph node metastasis. In all but one case, when sustentacular cells were present in the primary site, they were also present in the metastatic lymph nodes. The presence of sustentacular cells differed in morphological subtypes, with the spindle pattern being the most common subtype.

**Conclusions:** Sox10-positive sustentacular cells were observed in carcinoid tumours but not in high-grade NECs. Sustentacular-rich carcinoid tumours did not show a correlation with the occurrence of lymph node metastasis or survival. The sustentacular cells found differed in morphological subtypes.

**Keywords:** pulmonary neuroendocrine carcinomas, Sox10, sustentacular cell

**Abbreviations:** AC, atypical carcinoid; HPF, high power field; LCNEC, large-cell neuroendocrine carcinomas; NEC, neuroendocrine carcinomas; SCLC, small-cell lung carcinoma; TC, typical carcinoid

## Introduction

Bronchopulmonary neuroendocrine tumours comprise about 20% of all lung tumours and represent a spectrum of tumours arising from neuroendocrine cells. The different types of bronchopulmonary neuroendocrine carcinomas (NECs) share structural, morphological, immunohistochemical and ultrastructural features, and are categorized into four subgroups in

increasing order of biological aggressiveness: low-grade [typical carcinoids (TCs)], intermediate-grade [atypical carcinoids (ACs)] and high-grade [large-cell neuroendocrine carcinomas (LCNECs) or small-cell lung carcinomas (SCLCs)]. The differential diagnostic criteria for the above three grades are based only on the presence of neoplastic necrosis and the number of mitoses.<sup>1</sup>

Sustentacular cells are a well-recognized secondary population in certain normal neuroendocrine tissues, such as the paraganglia and adrenal medulla. Immunohistochemical and ultrastructural analyses have demonstrated the Schwannian nature of sustentacular cells.<sup>2,3</sup> The exact mechanisms of sustentacular cells are unknown, but they probably play a role in maintaining

Address for correspondence: C A Moran, MD, Department of Pathology, Unit 85, The University of Texas M. D. Anderson Cancer Center, 1515 Holcombe Boulevard, Houston, TX 77030, USA.  
e-mail: CesarMoran@mdanderson.org



architectural integrity. However, they are also found in a proportion of some neoplasms such as extra-adrenal paragangliomas,<sup>4–6</sup> pheochromocytomas<sup>7–10</sup> and carcinoid tumours.<sup>2,3,6,11–18</sup>

Most immunohistochemical analyses to identify sustentacular cells have used antibodies to the S100 protein. The S100 protein is used as a marker for a wide variety of lesions, notably malignant melanomas, peripheral nerve sheath tumours, cartilaginous tumours, adipocytic tumours, myoepithelial tumours and histiocytic and dendritic cell lesions. However, because S100 has a low specificity, more specific markers need to be added to an immunohistochemical panel to obtain an accurate diagnosis. In analysing sustentacular cells, some Langerhans cells and dendritic reticulum cells in tumour nests are positive for the S100 protein.<sup>11,13,17</sup> Similarly, in bronchial carcinoid tumours, not only sustentacular cells but occasionally tumour cells are positive for S100 protein.<sup>16</sup>

Sox10 is a transcription factor that participates in the late stage of neural crest cell formation, maintenance of multipotency crest cells as stem cells and specification of derivative cell fates to Schwannian and melanocytic destinations.<sup>19</sup> Recent studies have revealed that Sox10 is a more sensitive and specific marker for the diagnosis of Schwannian and melanocytic tumours than is the S100 protein. Sustentacular cells from some cases of pheochromocytomas, paragangliomas and carcinoid tumours of various organs have tested positive for the presence of Sox10.<sup>18</sup>

In the present study, we evaluated the distribution of sustentacular cells as labelled by Sox10 in pulmonary NECs. We analysed the correlations between various clinicopathological factors and the presence of sustentacular cells. We also evaluated the relationships between certain morphological patterns and the distribution of sustentacular cells. Finally, we studied the correlation between the presence of Sox10 in primary tumour sites and its presence in metastatic lymph nodes.

## Materials and methods

### CASE SELECTION

Tumour specimens were reviewed retrospectively from patients who had been diagnosed with pulmonary NECs between 1990 and 2005 and were deposited in the files of The University of Texas M.D. Anderson Cancer Center (Houston, TX, USA) Lung SPORE Tissue Bank, which is approved by the institutional review board. The pathological records of the specimens and all available haematoxylin and eosin (H&E)-stained

slides were reviewed. The patients' clinical information was collected, including age, gender, smoking history, duration of tumour recurrence and patient survival, tumour location (central, which was defined as proximal to second-order bronchi and peripheral, which was defined as third or further distal bronchi), maximum tumour size (in millimetre), and pathological disease stage (p-stage).

### HISTOLOGICAL EXAMINATION

All available H&E-stained slides for each case were examined by two pathologists (K.T. and C.A.M.); each pathologist was blinded to the clinical details of each patient. Infiltrative growth was defined as a tumour growing with ill-defined margins and showing isolated small clusters of tumour cells in the adjacent normal architecture. For immunohistochemistry staining, 4- $\mu$ m-thick sections were deparaffinized. Heat-induced epitope retrieval with Target Retrieval Solution (Dako, Carpinteria, CA, USA) was performed. After the slides were allowed to cool at room temperature for about 30 min, they were rinsed with deionized water. After that slides were treated with 3% hydrogen peroxide for 20 min to block endogenous peroxidase activity, followed by washing in deionized water for 2–3 min. The slides were then incubated with primary antibodies against Sox10 (1:100, goat polyclonal, N-20; Santa Cruz Biotechnology, Inc., Santa Cruz, CA, USA) and Ki-67 (1:100, MIB1; Dako) for 1 h at room temperature. Immunoreactions were detected using the LSAB-multisystem (Dako) for Sox10 and Envision-plus system (Dako) for Ki-67. The reactions were visualized with 3, 3'-diaminobenzidine, followed by counterstaining with haematoxylin. Appropriate positive and negative controls were used for each antibody.

We evaluated the immunostaining for Sox10 at magnifications of  $\times 40$ ,  $\times 100$  and  $\times 400$  on an Olympus CX31 microscope (Olympus, Tokyo, Japan). This microscope's standard field of view number is 20; therefore, a  $\times 400$  magnification equals 0.2 mm<sup>2</sup>. We recorded the highest number of positive cells per high-power field (HPF) ( $\times 400$ ) and evaluated the extent of the area deficient in Sox10-positive cells.

The Sox10 expression score represented the highest number of Sox10-positive cells per HPF; a score of 0 meant the field tested negative, a score of 1 meant the number of positive cells was 1–19, a score of 2 meant the number of positive cells was 20–49 and a score of 3 meant the number of positive cells was 50 or more.

The size of the Sox10 deficient area was defined thus: a score of 0 meant there was a greater than  $\times 40$  field-sized area without Sox10-positive cells (equal to

an area 0.5 mm in diameter), a score of 1 meant there was a  $\times 40$  to  $\times 100$  field-sized area without Sox10-positive cells (an area of  $<5$  and  $\geq 2$  mm in diameter), a score of 2 meant there was a  $\times 100$  to  $\times 400$  field-sized area without Sox10-positive cells (a Sox10 deficiency area of  $<2$  and  $\geq 0.5$  mm in diameter) and a score of 3 meant there was a less than  $\times 400$  field-sized area without Sox10-positive cells (an area  $<0.5$  mm in diameter).

Finally, the Sox10 index was obtained by multiplying the Sox10 expression score by the deficient area score (range 0–9). We then considered a Sox10 index of  $<1$  to indicate a sustentacular-negative tumour, 1–5 to indicate a sustentacular-sparse tumour and  $>5$  to indicate a sustentacular-rich tumour.

Ki-67 immunoreactivity was evaluated in the positive nuclei of the highest labelling region (so-called 'hot spots') of 1000 tumour nuclei. The Ki-67 index was calculated from all tumour nuclei using the printed paper and was expressed as a percentage of Ki-67-positive nuclei of all tumour nuclei.

Disagreements about the above-mentioned histological and immunohistochemical features were resolved by means of a joint review of the slides using a multiheaded microscope.

#### ADDITIONAL EXAMINATION IN TC AND AC TUMOURS

We performed further analysis which was limited to TC and AC tumours. First, we analysed the highest number of Sox10-positive cells with the following morphological subtypes; organoid/rosette, trabecular/ribbon, pseudogland and/or papillary, solid and spindle. Secondly, we performed immunohistochemical analysis of Sox10 in our cohort of 17 cases involving lymph node metastasis to compare Sox10 expression between the primary and metastatic sites.

#### STATISTICAL ANALYSIS

We performed all statistical analyses using SPSS version 12.0 software for Windows (SPSS, Inc., Chicago, IL, USA). We used the Wilcoxon rank-sum test to analyse continuous variables (age, tumour size, and Ki-67 index) and used the chi-square test or Fisher's exact test when comparing the proportions between two groups. We calculated the overall survival (OS) curves using the Kaplan–Meier method, and compared the curves using the log-rank test. We investigated the highest number of Sox10 per HPF between primary and lymph node metastatic sites using Pearson's correlation coefficient test. We considered  $P \leq 0.05$  to be significant.

## Results

#### CLINICOPATHOLOGICAL FEATURES

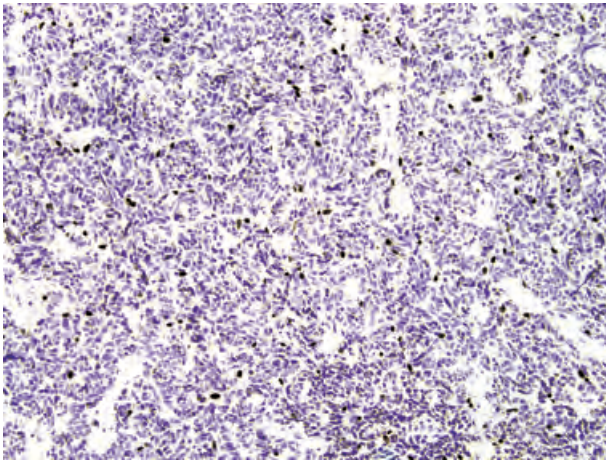
We reviewed tumour specimens from 129 patients with an original diagnosis of pulmonary NEC. We excluded 14 patients who had received therapy preoperatively [13 had received neoadjuvant chemotherapy and one had received yttrium aluminium garnet (YAG) laser ablation]. Another two cases were excluded because the sample sections were peeling during the immunohistochemical procedure. Therefore, our final cohort consisted of 113 patients with pulmonary NEC, including 66 patients with TC, 12 with AC, 20 with LCNEC and 15 with SCLC.

The patient cohort included 61 women and 52 men. The patients' mean age (at the time of diagnosis) was 58.0 years (range 19–81 years). Patients' smoking histories were documented in 101 cases; 31 patients were never smokers, 40 were former smokers and 30 were current smokers. The tumour was located in the central portion of the lung in 53 patients and in the peripheral portion in 60 patients. Tumour size ranged from 10.0 to 130.0 mm (mean, 30.0 mm). Lymph node status was recorded in 109 patients and metastasis was observed in 27. The mean follow-up time for all 113 patients was 61 months (range 1–214 months), with 85 patients still living at the time of this report. Histological analysis revealed that an infiltrative growth was observed in 80 cases. Blood and lymph vessel invasion were observed in 59 and 55 cases, respectively. We found neoplastic necrosis in 40 cases. The mean Ki-67 index was 19.1% (range 0.1–90.5%).

#### SOX10 EXPRESSION

Sox10 expression was observed in the nuclei of sustentacular cells (Figure 1). The highest number of Sox10-positive cells per HPF ranged from 0 to 355, with average and median values of 20.5 and 0, respectively. Subdividing by histological subtype, the mean highest number of Sox10-positive cells per HPF was 31.6 (range 0–355) in TC, 20.0 (range 0–61) in AC and 0 in both LCNEC and SCLC. There were statistical differences between TC and LCNEC ( $P = 0.001$ ) and TC and SCLC ( $P = 0.001$ ).

The Sox10 expression scores assigned to all NECs were 0, 1, 2 and 3 in 62 (54.9%), 22 (19.5%), 14 (12.4%) and 15 (13.3%) cases, respectively. Subdividing by histological subtype, Sox10 expression scores from TC tumours were 0, 1, 2 and 3 in 22 (33.3%), 20 (30.3%), 12 (18.2%) and 12 (18.2%) cases,



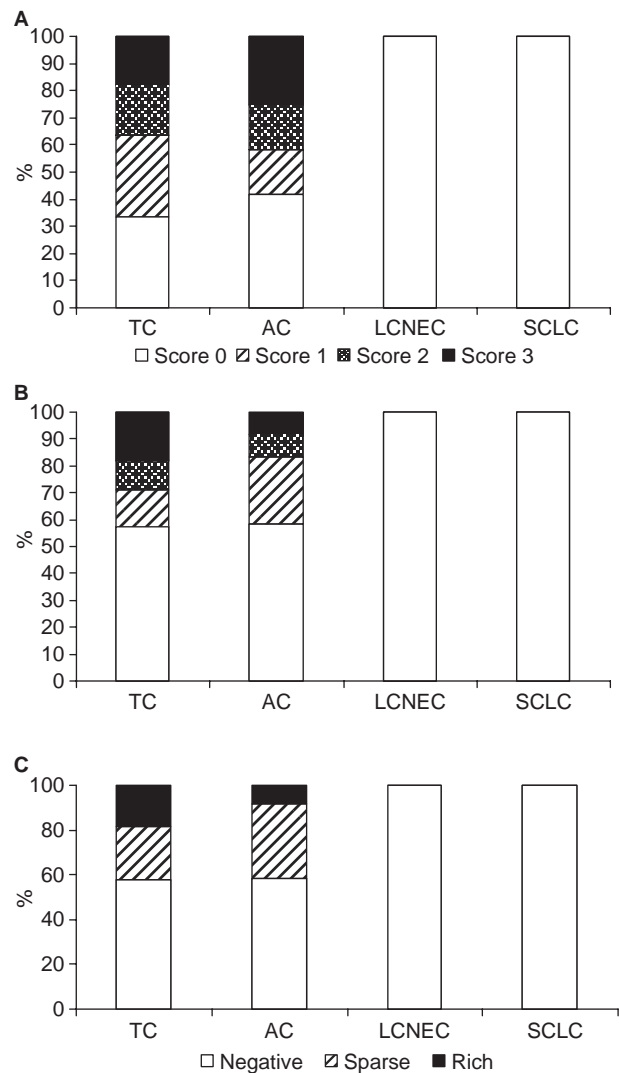
**Figure 1.** Typical carcinoid tumour with Sox10-positive sustentacular cells. The tumour shows organoid structure and many spindle-shaped Sox10-positive nuclei (representing sustentacular cells) surrounding tumour clusters.

respectively (Figure 2A). Sox10 expression scores from AC tumours were 0, 1, 2 and 3 in five (41.7%), two (16.7%), two (16.7%) and three (25.0%) cases, respectively. All LCNEC and SCLC cases were negative for Sox10. The Sox10 deficient areas across all NECs were scored as 0, 1, 2 and 3 in 80 (71.0%), 12 (10.6%), eight (7.1%) and 13 (11.5%) cases, respectively. Subdividing by histological subtype, scores of 0, 1, 2 and 3 were observed in 38 (57.6%), nine (13.6%), seven (10.6%) and 12 (18.2%) TC cases, respectively (Figure 2B) and scores of 0, 1, 2 and 3 were observed in seven (58.3%), three (25.0%), one (8.3%) and one (8.3%) AC cases, respectively.

The Sox10 index was calculated using the above data, yielding 38 (57.6%) sustentacular-negative, 16 (24.2%) sustentacular-sparse and 12 (18.2%) sustentacular-rich TC tumours (Figure 2C). In AC cases, we found seven (58.3%) sustentacular-negative, four (33.3%) sustentacular-sparse and one (8.3%) sustentacular-rich tumour(s).

#### SOX10 EXPRESSION AND CLINICOPATHOLOGICAL FACTORS

Using these results, we classified the Sox10-negative (score <1) and Sox10-sparse tumours (score 1–5) as sustentacular-negative tumours and Sox10-rich tumours (score >5) as sustentacular-positive tumours. This meant that 13 cases (12 TC and one AC) were classified as sustentacular-positive tumours. The clinicopathological correlations with sustentacular-positive tumours were analysed among all NEC, TC and AC tumours (Table 1). Neither patient age, gender



**Figure 2.** Sox10 expression score, Sox10 deficient area and Sox10 index. A, bar graphs depicting the highest number of Sox10-positive cells per high-power field by histological subtype. A score of 1 means the number of positive cells was 1–19, a score of 2 means the number of positive cells was 20–49 and a score of 3 means the number of positive cells was 50 or more. B, bar graphs depicting the deficient areas of Sox10 by histological subtypes. A score of 0 means there was a greater than  $\times 40$  field-sized area without Sox10-positive cells, a score of 1 means there was a  $\times 40$  to  $\times 100$  field-sized area without Sox10-positive cells, a score of 2 means there was a  $\times 100$  to  $\times 400$  field-sized area without Sox10-positive cells and a score of 3 meant there was a less than  $\times 400$  field-sized area without Sox10-positive cells. C, bar graphs depicting the Sox10 index subdivided by the histological subtypes. The Sox10 index was obtained by multiplying the Sox10 expression score by the deficient area score (range 0–9). We defined a Sox10 index of <1 to be a sustentacular-negative tumour, 1–5 to be a sustentacular-sparse tumour and >5 to be a sustentacular-rich tumour.

nor smoking history were correlated statistically to sustentacular-positive or -negative tumours. Sustentacular-positive tumours had a statistically marginal

**Table 1.** Correlation between Sox10 diffuse positive cases and clinicopathological factors

	All neuroendocrine carcinomas			Typical and atypical carcinoid tumours		
	Sox10 index $\leq 5$	Sox10 index $> 5$	<i>P</i>	Sox10 index $\leq 5$	Sox10 index $> 5$	<i>P</i>
Age (years)	58.36 $\pm$ 13.79	58.15 $\pm$ 15.04	0.9570	53.94 $\pm$ 14.11	58.15 $\pm$ 15.04	0.3305
Gender						
Female	53	8	0.7687	41	8	1.000
Male	47	5		24	5	
Smoking						
Never	27	4	0.2114	27	4	0.5298
Former	33	7		24	7	
Present	29	1		11	1	
Location						
Central	50	3	0.0817	44	3	0.0043
Peripheral	50	10		21	10	
Tumour size (cm)	3.15 $\pm$ 2.23	2.03 $\pm$ 1	0.0632	3.1	2.0	0.1069
Lymph node metastasis						
Absent	71	11	0.5124	49	11	0.7210
Present	25	2		15	2	
Infiltrative growth						
Absent	25	8	0.0187	24	8	0.1274
Present	75	5		41	5	
Blood vessel invasion						
Absent	45	9	0.1408	37	9	0.5417
Present	55	4		28	4	
Lymph vessel invasion						
Absent	49	9	0.2400	41	9	0.7607
Present	51	4		24	4	
Neoplastic necrosis						
Absent	60	13	0.0038	60	13	0.5831
Present	40	0		5	0	
Ki-67 index, %	21.28 $\pm$ 26.44	1.9 $\pm$ 2.21	0.0058	3.19 $\pm$ 4.27	1.89 $\pm$ 2.21	0.2580

correlation with peripheral locations in all NEC ( $P = 0.0817$ ) and a significant correlation to peripheral locations in TC and AC tumours ( $P = 0.0043$ ). Sustentacular-positive tumours tended to be smaller than sustentacular-negative tumours ( $P = 0.063$  in all NECs and  $P = 0.1069$  in TCs and ACs). No statistical differences between rates of lymph node metastasis were noted.

Sustentacular-positive tumours showed statistically significant correlation with infiltrative growth in all NECs ( $P = 0.0187$ ) but not in TC or AC tumours ( $P = 0.127$ ). There were no statistical differences in rates of blood and lymph vessel invasion. Neoplastic necrosis was not observed in sustentacular-positive tumours – a statistically significant correlation in all NECs ( $P = 0.0038$ ), but not in TC and AC tumours



( $P = 0.5831$ ). The Ki-67 index in sustentacular-positive tumours was lower (1.89%) than that of sustentacular-negative tumours in all NEC (21.28%) and showed a statistically significant correlation ( $P = 0.0058$ ). However, this correlation was not found in TCs and ACs ( $P = 0.2580$ ).

#### SOX10 EXPRESSION AND OVERALL SURVIVAL

We searched for a correlation between sustentacular-positive tumours and patients' OS. In all NECs, sustentacular-positive tumours were significantly correlated with OS ( $P = 0.05$ ). In addition, the 5-year OS rates for the sustentacular-negative and -positive tumours were 72.3% and 100%, respectively (Figure 3A). However, multivariate analysis revealed that there were no statistical differences in OS between sustentacular-positive tumours versus -negative tumours in all NEC (Table 2).

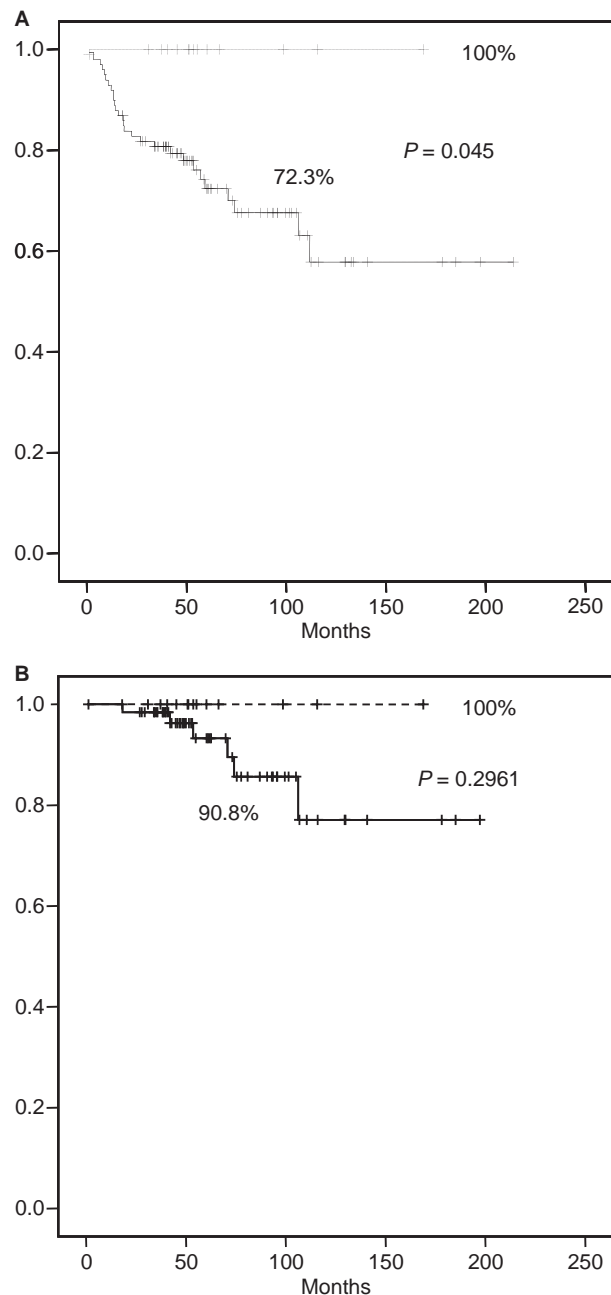
In analysing TC and AC tumours, sustentacular-positive tumours did not correlate with OS ( $P = 0.2961$ ). The 5-year OS rates for sustentacular-negative and -positive tumours were 90.8% and 100%, respectively (Figure 3B).

#### SOX10 EXPRESSION AND MORPHOLOGICAL SUBTYPES OF TC AND AC TUMOURS

We analysed the correlation between Sox10 expression and morphological subtypes. We found the organoid/rosette, trabecular/ribbon, pseudogland and/or papillary, solid and spindle patterns in 33 (42.3%), four (5.1%), 17 (21.8%), 11 (14.1%) and 13 (16.7%) of 78 TC and AC cases (Figure 4). The numbers of Sox10-positive cells per HPF were 16.4, 0.25, 2.8, 31.0 and 106.8 cells/HPF in the organoid/rosette, trabecular/ribbon, pseudogland and/or papillary, solid and spindle patterns, respectively (Figure 5A). Of sustentacular-positive tumours, four (12.1%) were organoid/rosette, 0 were trabecular/ribbon, 0 were pseudogland and/or papillary, one (9.0%) was solid and eight (61.5%) were spindle patterns (Figure 5B).

#### SOX10 EXPRESSION IN LYMPH NODE METASTASIS

We reviewed the lymph node specimens from the 17 patients with lymph node metastasis in both TC and AC tumours. We excluded eight patients because the tumour samples were insufficient (low volume of the tumour blocks or used previously for frozen section diagnosis). In the primary tumour sites, six of nine cases were positive for Sox10 (Figure 6A). Sox10



**Figure 3.** Five-year overall survival analysis. **A**, for cases with a Sox10 index >5 (dashed line) and a Sox10 index ≤5 (solid line), the 5-year overall survival rates were 100% and 72.3%, respectively, in all neuroendocrine carcinomas. **B**, for cases with a Sox10 index >5 (dashed line) and a Sox10 index ≤5 (solid line), the 5-year overall survival rates were 100% and 90.8%, respectively, in typical and atypical carcinoid tumours.

expression scores of 0, 1, 2 and 3 were observed in three (33.3%), two (22.2%), one (11.1%) and three (33.3%) cases, respectively. In the metastatic lymph nodes, five of nine cases were positive for Sox10. In all but one case, when the primary site was positive for

**Table 2.** Results of multivariate analysis of overall survival

	Relative risk	95% CI	P
Typical & atypical carcinoid tumour versus high-grade neuroendocrine carcinoma	9.573	3.846–23.592	<0.0001
Sox10 index >5	0.000	0.000–4.402 + 294	0.973

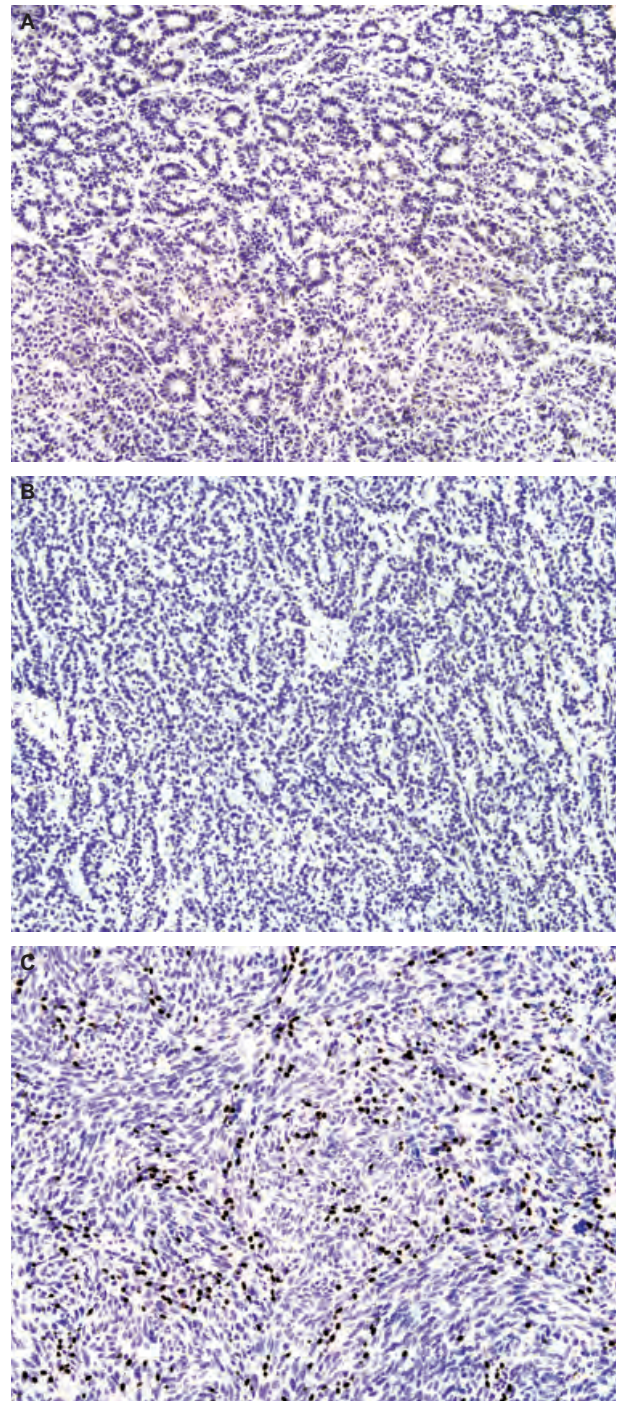
CI, Confidence interval.

Sox10, the metastatic lymph nodes were also positive for Sox10 (Figure 6B). The Sox10 expression scores were 0, 1, 2 and 3 in four (44.4%), two (22.2%), one (11.1%) and two (22.2%) cases, respectively. A statistically significant ( $P = 0.003$ ) strong correlation ( $\gamma = 0.856$ ) was observed between the highest number of Sox10-positive cells per HPF in the primary site and metastatic lymph nodes.

## Discussion

Using Sox10 labelling, we found sustentacular cells in TC (66.7%) and AC (58.3%) tumours but not in LCNEC or SCLC. In previous studies using immunostaining with the less-specific S100 protein, bronchial carcinoid tumours have been found to contain from 18% to 82% sustentacular cells.<sup>3,6,11–17</sup> To our knowledge, there has been only one previous report that used Sox10 labelling to test for the presence of sustentacular cells in AC and TC tumours. That study found 56.8% of TC and 16.7% of AC tumours to contain sustentacular cells.<sup>18</sup> Clearly, our sustentacular prevalence rate in AC tumours is higher than that. This difference could be explained by differences in the sample size; our analysis was based on whole sections of tumour compared with their analysis using tissue microarrays, which were performed on three sets of 0.6-mm-diameter core samples.

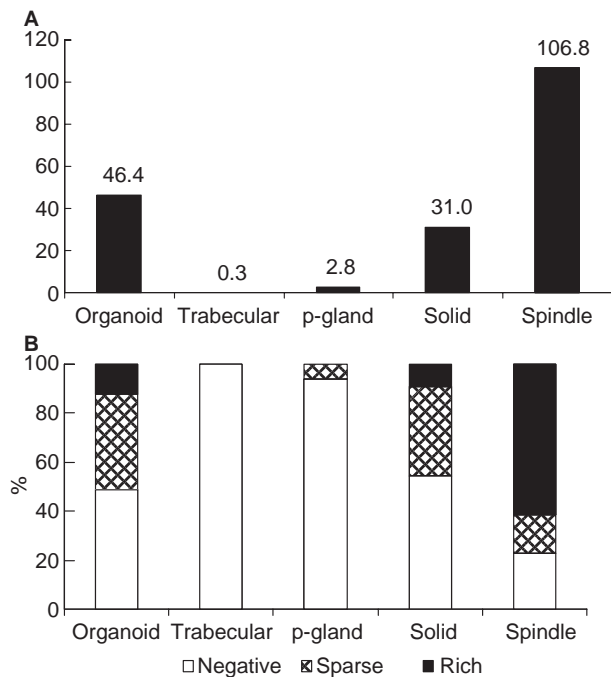
There have been only two additional studies analysing the presence of sustentacular cells in LCNEC of the lung.<sup>17,18</sup> Most of the studies involving sustentacular cells in pulmonary NEC were performed before the application of criteria for diagnosing LCNEC.<sup>20</sup> As in the present study, one study used Sox10 antibody and found no sustentacular cells in LCNEC samples.<sup>18</sup> The other study used S100 protein antibody and reported finding sustentacular cells in 60% of LCNECs, although very few in number.<sup>17</sup> Although they analysed the S100-positive sustentacular cells carefully in order to



**Figure 4.** Different Sox10-positive cell distributions by morphological patterns. A, this tumour shows a trabecular pattern without sustentacular cells. B, this tumour shows a pseudogland pattern without sustentacular cells. C, this tumour shows a spindle pattern with many sustentacular cells.

exclude intratumoural macrophages and Langerhans cells, which can react with S100 proteins, their positivity rate for sustentacular cells in lung carcinoids

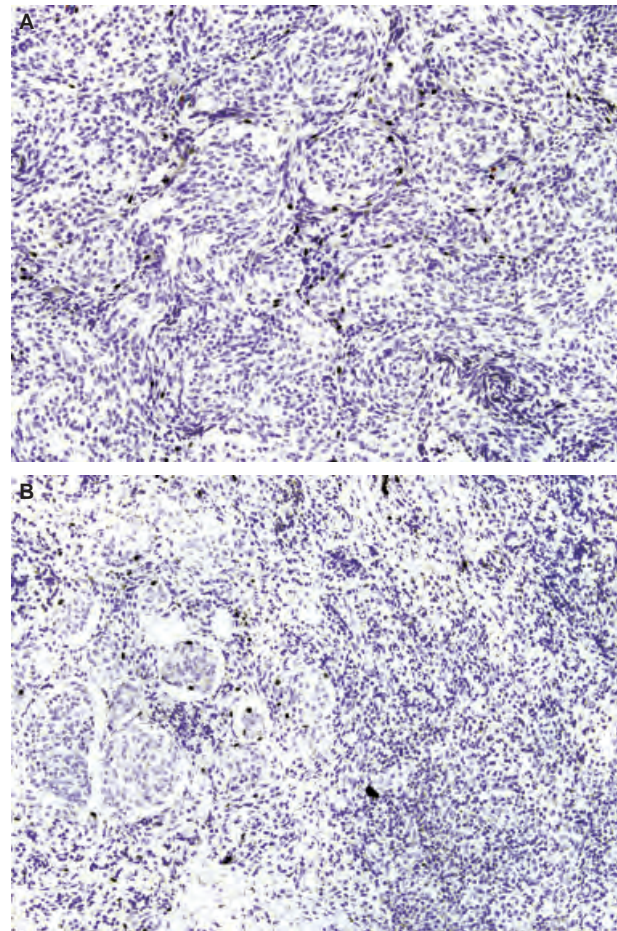




**Figure 5.** Sox10 expression by morphological pattern. **A**, the highest number of Sox10-positive cells subdivided by the morphological pattern. **B**, the Sox10 index subdivided by the morphological patterns.

was higher than in other reports. Furthermore, one study of a series of sporadic cases of SCLC (before the current definition of SCLC was implemented, meaning these cohorts may have included some LCNECs) reported a complete absence of sustentacular cells.<sup>11,13</sup> In other organs, benign counterparts of pheochromocytoma or paraganglioma have shown high prevalence rates of sustentacular cells, whereas the majority of malignant counterparts of malignant pheochromocytoma or paraganglioma have demonstrated an absence or low prevalence of sustentacular cells.<sup>4,5,7,9,10</sup> These results suggest that sustentacular cells are not present or are extremely rare in high-grade pulmonary NECs.

To reveal the significance of the presence of sustentacular cells, we selected sustentacular cell-positive cases showing not only the presence of sustentacular cells, but also their homogeneous distribution. Thus, we used the Sox10 index obtained by multiplying the Sox10 expression score by the deficient area score and then defined a sustentacular cell-positive case as one having a Sox10 index >5. Univariate analysis showed that sustentacular-positive tumours showed a favourable prognosis on analysing all NEC cases. However, multivariate analysis of all NECs did not reveal a statistical correlation between sustentacular-positive tumours and a favourable prognosis. One possible



**Figure 6.** Primary and metastatic sites of Sox10-positive typical carcinoid tumours. **A**, the primary tumour site shows large clusters with spindle cells. Some sustentacular cells are observed peripheral to the tumour clusters. **B**, the tumour at the metastatic lymph node shows the same pattern as does the primary site.

explanation could be that there was no Sox10 expression in high-grade NECs, so tumour differentiation confounded survival. Several studies have described a correlation between the number of sustentacular cells and tumour differentiation and all concluded that the presence of sustentacular cells correlated with favourable clinical outcomes (although they did not use detailed statistical analyses for survival). We agree with the correlation between the presence of sustentacular cells and tumour differentiation. However, sustentacular cells were observed in metastatic lymph nodes, and the presence of sustentacular cells did not correlate with poor prognostic factors in carcinoid tumours with lymph node metastasis<sup>21</sup> and high Ki-67 index.<sup>22</sup> These results indicate that the presence of sustentacular cells is a marker for tumour differentiation, but is not itself a prognostic factor.

We hypothesized that sustentacular-rich tumours might not develop lymph node metastasis because the sustentacular cells could help maintain the tumour structure. Statistical analysis revealed that there was no correlation between sustentacular-positive tumours and the occurrence of lymph node metastasis. All tumours but one, whose primary sites were positive for Sox10, were also positive for Sox10 in the metastatic lymph nodes. We also found that the highest number of Sox10-positive cells in primary sites correlated closely with that in the metastatic lymph nodes. The presence of sustentacular cells in a metastatic site has been reported previously in one case each of bronchial carcinoid tumour<sup>15</sup> and malignant pheochromocytoma.<sup>9</sup> These results indicate that sustentacular cells do not maintain the structure of tumour nests.

Our results suggest that sustentacular cells originate from neoplastic proliferation. There has been considerable debate concerning the nature of sustentacular cells. Some authors have suggested that the presence of sustentacular cells reflects a biphasic tumour with an additional population of neoplastic cells derived from the same lineage as the main tumour component.<sup>3,8,23</sup> Conversely, sustentacular cells could represent a reactive stromal component induced by neoplastic cells.<sup>17</sup> Recently, Douwes Dekker *et al.*<sup>24</sup> have suggested that sustentacular populations are non-neoplastic and may be induced as a tumour-specific stromal component in head and neck paragangliomas using the flow-sorted and restriction digestion analysis of *SDHD* mutations. If the presence of sustentacular cells in pulmonary NEC is reactive, it would not explain their presence in metastatic lymph nodes. Further molecular analysis will be needed to elucidate whether the presence of sustentacular cells in pulmonary NEC is neoplastic or reactive and to find the stem cells responsible.

We have also shown that the prevalence of sustentacular cells differs between morphological patterns in TC and AC tumours. The spindle pattern was the most common subtype, whereas the trabecular pattern was the least common subtype. Some authors have pointed out the correlation between fusiform/spindle morphology and the presence of sustentacular cells.<sup>3,6,12</sup> However, they did not find the exact ratio or explain the significance of the finding. Conventional carcinoid tumours are composed of homogeneous cellular proliferation with an organoid and trabecular pattern. However, our data indicate that the organoid and trabecular patterns might have a different morphological pathogenesis. Furthermore, one of the rare morphological patterns, known as the pseudogland/tubular

pattern, is considered to be close to the trabecular pattern. These morphological patterns are probably influenced by the amount of stromal fibrosis and/or the degree of dilatation of vessels in the trabecular pattern.

Regarding tumour location, the sustentacular-positive TC and AC tumours showed a statistically significant correlation with occurrence in non-central locations (76.9%,  $P = 0.004$ ). Similarly, Barbareschi *et al.*<sup>3</sup> reported that 75% of sustentacular-rich carcinoid tumours occurred in peripheral portions of the lung. One possible explanation is that spindle-cell carcinoid tumours tend to occur peripherally.<sup>25</sup>

In conclusion, Sox10-positive sustentacular cells were observed in TC and AC tumours but not in high-grade NECs. Statistical analysis revealed that sustentacular-positive TC and AC tumours show no correlation with the occurrence of lymph node metastasis or patient OS. We observed sustentacular cells in metastatic lymph nodes, with the highest number of sustentacular cells in metastatic lymph nodes correlating with that found in the primary site. The presence of sustentacular cells differed between morphological subtype, with the spindle pattern being the most prevalent subtype.

## Conflicts of interest

No potential competing interests were disclosed.

## Acknowledgements

This work was supported in part by a grant from the United States Department of Defense PROSPECT W81XWH-07-1-0306. We would like to thank Susan Cweren for her skilful technical assistance and Maude Veech for her skilful English editing.

## References

1. Travis WD, Colby T, Corrin B *et al.* Tumors of the lung. In Kleihues P, Sobin LH eds. *WHO classification of tumor. Pathology and genetics of tumors of the lung, pleura, thymus and heart*. Lyon: IARC Press, 2004; 9–124.
2. Lundqvist M, Wilander E. Subepithelial neuroendocrine cells and carcinoid tumours of the human small intestine and appendix. A comparative immunohistochemical study with regard to serotonin, neuron-specific enolase and S-100 protein reactivity. *J. Pathol.* 1986; **148**: 141–147.
3. Barbareschi M, Frigo B, Mosca L *et al.* Bronchial carcinoids with S-100 positive sustentacular cells. A comparative study with gastrointestinal carcinoids, pheochromocytomas and paragangliomas. *Pathol. Res. Pract.* 1990; **186**: 212–222.
4. Klierer KE, Cochran AJ. A review of the histology, ultrastructure, immunohistology and molecular biology of extra-adrenal



- paragangliomas. *Arch. Pathol. Lab. Med.* 1989; **113**; 1209–1218.
5. Achilles EA, Padberg BC, Hall K *et al*. Immunocytochemistry of paraganglioma – value of staining for S-100 protein and glial fibrillary acidic protein in diagnosis and prognosis. *Histopathology* 1991; **18**; 453–458.
  6. Min KW. Diagnostic usefulness of sustentacular cells in paragangliomas: immunocytochemical and ultrastructural investigation. *Ultrastruct. Pathol.* 1998; **22**; 369–376.
  7. Lloyd RV, Blaivas M, Wilson BS. Distribution of chromogranin and S100 protein in normal and abnormal adrenal medullary tissues. *Arch. Pathol. Lab. Med.* 1985; **109**; 633–635.
  8. Schroder HD, Johannsen L. Demonstration of S-100 protein in sustentacular cells of pheochromocytomas and paragangliomas. *Histopathology* 1986; **10**; 1023–1033.
  9. Unger P, Hoffman K, Pertsemlidis D, Thung S, Wolfe D, Kaneko M. S100 protein-positive sustentacular cells in malignant and locally aggressive adrenal pheochromocytomas. *Arch. Pathol. Lab. Med.* 1991; **115**; 484–487.
  10. Clarke MR, Weyant RJ, Watson CG, Carty SE. Prognostic markers in pheochromocytoma. *Hum. Pathol.* 1998; **29**; 522–526.
  11. Nakajima T, Watanabe S, Sato Y, Kameya T, Hirota T, Shimosato Y. An immunoperoxidase study of S-100 protein distribution in normal and neoplastic tissues. *Am. J. Surg. Pathol.* 1982; **6**; 715–727.
  12. el-Salhy M, Lundqvist M, Wilander E. Bronchial carcinoids and pheochromocytomas. A comparative study with special emphasis on S-100 protein, serotonin and neuron-specific enolase (NSE) immunoreactivity. *Acta Pathol. Microbiol. Immunol. Scand. A* 1986; **94**; 229–235.
  13. Barbareschi M, Mauri MF, Muscara M, Mauri FA, Lo Re V. S-100 protein in human lung neuroendocrine neoplasms. Immunohistochemical study of 14 cases and review of the literature. *Histol. Histopathol.* 1987; **2**; 185–192.
  14. Martin JME, Maung RT. Differential immunohistochemical reactions of carcinoid tumors. *Hum. Pathol.* 1987; **18**; 941–945.
  15. Barbareschi M, Ferrero S, Frigo B, Mariscotti C, Mosca L. Bronchial carcinoid with S-100 positive sustentacular cells. *Tumor* 1988; **74**; 705–711.
  16. Al-Khafaji B, Noffsinger AE, Miller MA *et al*. Immunohistologic analysis of gastrointestinal and pulmonary carcinoid tumors. *Hum. Pathol.* 1998; **29**; 992–999.
  17. Gosney JR, Denley H, Resl M. Sustentacular cells in pulmonary neuroendocrine tumours. *Histopathology* 1999; **34**; 211–215.
  18. Nonaka D, Chiriboga L, Rubin BP. Sox10: a pan-Schwannian and melanocytic marker. *Am. J. Surg. Pathol.* 2008; **32**; 1291–1298.
  19. Kelsh RN. Sorting out Sox10 functions in neural crest development. *Bioessays* 2006; **28**; 788–798.
  20. Travis WD, Colby TV, Corrin B, Shimosato Y, Brambilla E. *World Health Organization International Histological Classification of Tumors. Histological typing of lung and plural tumors*, 3rd edn. Berlin: Springer, 2004.
  21. Travis WD, Giroux DJ, Chansky K *et al*. The IASLC lung cancer staging project: proposals for the inclusion of broncho-pulmonary carcinoid tumors in the forthcoming (seventh) edition of the TNM classification for lung cancer. *J. Thorac. Oncol.* 2008; **3**; 1213–1223.
  22. Costes V, Marty-Ané C, Picot MC *et al*. Typical and atypical bronchopulmonary carcinoid tumors: a clinicopathologic and KI-67-labeling study. *Hum. Pathol.* 1995; **26**; 740–745.
  23. Carlson JA, Dickersin GR. Melanotic paraganglioid carcinoid tumor: a case report and review of the literature. *Ultrastruct. Pathol.* 1993; **17**; 353–372.
  24. Douwes Dekker PB, Corver WE, Hogendoorn PC, van der Mey AG, Cornelisse CJ. Multiparameter DNA flow-sorting demonstrates diploidy and *SDHD* wild-type gene retention in the sustentacular cell compartment of head and neck paragangliomas: chief cells are the only neoplastic component. *J. Pathol.* 2004; **202**; 456–462.
  25. Ranchod M, Levine GD. Spindle-cell carcinoid tumors of the lung: a clinicopathologic study of 35 cases. *Am. J. Surg. Pathol.* 1980; **4**; 315–331.

[Print this Page](#)


## Presentation Abstract

Abstract  
Number: 3196

Presentation  
Title: EZH2 expression is an early event in the pathogenesis of non-small cell lung cancer (NSCLC) and correlates with tumor progression

Presentation  
Time: Tuesday, Apr 05, 2011, 8:00 AM -12:00 PM

Location: Exhibit Hall A4-C, Poster Section 14

Poster  
Section: 14

Poster Board  
Number: 3

Author  
Block: Carmen Behrens<sup>1</sup>, Ping Yuan<sup>2</sup>, Luisa Solis<sup>1</sup>, Pierre Saintigny<sup>1</sup>, Humam Kadara<sup>1</sup>, Junya Fujimoto<sup>1</sup>, Cesar Moran<sup>1</sup>, Stephen G. Swisher<sup>1</sup>, John V. Heymach<sup>1</sup>, Ignacio I. Wistuba<sup>1</sup>. <sup>1</sup>UT M.D. Anderson Cancer Ctr., Houston, TX; <sup>2</sup>Md Anderson, Houston, TX

Abstract  
Body: **Background.** The molecular events associated with NSCLC pathogenesis and tumor progression need to be better elucidated. The enhancer of zeste homolog 2 (EZH2) is a DNA methyl transferase involved in malignant transformation and tumor progression of several human carcinomas, including lung. We investigated EZH2 expression by immunohistochemistry (IHC) in the early pathogenesis of NSCLC and progression in a large series of clinically well-annotated tissue specimens. **Methods.** We examined by IHC nuclear EZH2 expression using formalin-fixed and paraffin-embedded tissue specimens obtained from surgically resected tumors in tissue microarrays (TMAs) including: a) stage I-III NSCLC tumors (SCCs, n=272; adenocarcinomas, n=456); b) paired primary tumors and brain metastases (n=70); and, c) bronchial preneoplastic squamous lesions (n=51) and mildly abnormal/normal bronchial epithelia (n=203). In stage I-III tumors, we correlated EZH2 expression with clinico-pathological features, including patients' recurrence-free survival (RFS), and overall survival (OS), in a subset of these tumors, with IHC expression of 80 proteins and *EGFR* and *KRAS* mutation status. **Results.** EZH2 expression was significantly ( $P<0.0001$ ) higher in SCC (mean score=128.6) compared to adenocarcinoma (mean score=56.8). In adenocarcinoma, higher EZH2 expression significantly correlated with ever-smoking status ( $P<0.0001$ ) and less differentiated histology features (solid histology pattern;  $P<0.0001$ ). In multivariate analysis, for adenocarcinoma patients, higher EZH2 expression, as a continuous variable, associated with significantly worse RFS (HR 1.006 95%CI 1.0-1.011;  $P=0.03$ ) and OS (HR 1.004 95%CI 1.0-1.009;  $P=0.03$ ). In publicly available array datasets of lung adenocarcinoma patients, high *EZH2* mRNA correlated with worse RFS and OS. NSCLC brain metastases showed significantly ( $P=0.0004$ ) higher EZH2 expression than corresponding primary tumors. In bronchial epithelia, normal and hyperplastic cells demonstrated low levels of EZH2 expression; significantly higher expression was associated with increasing severity of squamous dysplastic changes ( $P<0.0001$ ). In NSCLC tumors, EZH2 expression positively correlated ( $P<0.0001$ ) with IHC expression of Ki67, FEN1, and UBE2C. In lung adenocarcinomas, *EGFR*-mutant tumors showed significantly lower EZH2 expression than wild-type tumors. **Conclusions.** Our findings indicate that EZH2 is frequently expressed in NSCLC, particularly in poorly differentiated adenocarcinomas. In adenocarcinomas, EZH2 associates with worse patient outcomes. These data suggest that EZH2 expression represents an early event in NSCLC pathogenesis and associates with tumor progression and metastasis, representing a novel target for chemoprevention and therapeutic strategies. Supported by DoD grants W81XWH-04-1-0142 and DoD W81XWH-07-1-0306.

[American Association for Cancer Research](#)  
615 Chestnut St. 17th Floor  
Philadelphia, PA 19106

[Print this Page](#)


# Presentation Abstract

Abstract Number: 3269

Presentation Title: VEGF inhibitor resistance is associated with stromal EGFR activation and normalized revascularization in an orthotopic model of lung adenocarcinoma

Presentation Time: Tuesday, Apr 05, 2011, 8:00 AM -12:00 PM

Location: Exhibit Hall A4-C, Poster Section 18

Poster Section: 18

Poster Board Number: 4

Author Block: Tina Cascone, Babita Saigal, Donna M. Reynolds, Baruch Erez, Jeorg J. Jacoby, Monique B. Nilsson, Heather Y. Lin, Roy S. Herbst, Robert R. Langley, John V. Heymach. UT M.D. Anderson Cancer Ctr., Houston, TX

Abstract Body: Therapeutic resistance to angiogenesis inhibitors represents a major obstacle in the treatment of non-small cell lung cancer (NSCLC). Previously, we reported that acquired resistance of subcutaneous murine models of NSCLC to the anti-vascular endothelial growth factor (VEGF) antibody bevacizumab (BV) was mediated by upregulation and activation of the epidermal growth factor receptor (EGFR) signaling pathway in stromal cells. Here, we investigated the effects of BV and dual VEGFR/EGFR inhibition, and the mechanisms of therapeutic resistance in H441 NSCLC orthotopic tumors. Short-term BV treatment (2 weeks) resulted in a significant tumor volume reduction compared with vehicle-treated tumors ( $p=0.026$ ). For survival analysis, tumor-bearing mice were randomized to receive vehicle, erlotinib (E), BV, erlotinib + BV (E + B), or the VEGFR/EGFR inhibitor vandetanib (V), until moribund. All therapies significantly prolonged survival compared with vehicle ( $p<0.0001$ ; E vs. vehicle  $p<0.05$ ). Long-term BV administration improved survival compared with E (median survival 77 vs. 58 days,  $p=0.00015$ ); however, both E + BV and V treatments (median survival 101 and 91 days, respectively) prolonged survival compared with E or BV alone ( $p=0.0001$  E + BV vs. E or BV;  $p=0.0004$  V vs. E;  $p=0.022$  V vs. BV). Microvessel density (MVD) was strongly decreased in BV-sensitive tumors compared with 2 week vehicle treatment ( $p=0.0008$ ); however, tumors resistant to BV or dual VEGFR/EGFR inhibition showed revascularization with increased MVD compared with BV-sensitive tumors ( $p=0.045$ ). In erlotinib-resistant group MVD was significantly lower than in BV-resistant tumors ( $p=0.034$ ). Levels of p-EGFR increased in BV-resistant tumors compared with controls ( $p=0.039$ ) and co-localized with the stroma supporting large, normalized vessels. This signaling was suppressed in tumors resistant to VEGFR/EGFR targeting compared with both controls and BV-resistant tumors ( $p=0.0001$  E + BV vs. vehicle;  $p=0.0008$  E + BV vs. BV;  $p=0.011$  V vs. vehicle;  $p=0.009$  V vs. BV), demonstrating persistent EGFR blockade with treatment. Pericyte coverage increased in BV-resistant tumors compared with controls and BV-sensitive tumors ( $p=0.003$  BV vs. vehicle;  $p<0.0001$  BV progression vs. BV 2 weeks). In tumors resistant to erlotinib or VEGFR/EGFR inhibition, pericyte coverage was reduced to levels comparable to controls ( $p=0.001$  E vs. BV;  $p=0.054$  E + BV vs. BV;  $p=0.007$  V vs. BV). These findings demonstrate that in an orthotopic NSCLC model, resistance to BV is associated with tumor revascularization, featuring large, pericyte-covered vessels with increased perivascular EGFR activation. Dual VEGFR/EGFR blockade abrogates the BV-induced increase in pericyte coverage and delays the emergence of resistance. Stromal EGFR may contribute to VEGF inhibitor resistance through activation on perivascular cells.

**[American Association for Cancer Research](#)**  
**615 Chestnut St. 17th Floor**  
**Philadelphia, PA 19106**

[Print this Page](#)



# Presentation Abstract

Abstract Number: 5166

Presentation Title: Identification of prostate stem cell antigen (PSCA) as a potential marker for lung cancer brain metastasis

Presentation Time: Wednesday, Apr 06, 2011, 8:00 AM -12:00 PM

Location: Exhibit Hall A4-C, Poster Section 19

Poster Section: 19

Poster Board Number: 7

Author Block: Hector G. Galindo, Milind Suraokar, Carmen Behrens, Denise M. Woods, Neda Kalhor, Kenneth D. Aldape, Junya Fujimoto, Roy S. Herbst, Heidi S. Erickson, Ignacio I. Wistuba. UT M.D. Anderson Cancer Ctr., Houston, TX

Abstract Body: **Background:** Lung cancer is the leading cause of cancer-related death worldwide. Non-small cell lung cancer (NSCLC) accounts for ~80% of all lung cancers. Brain metastases (BMs) are estimated to occur in up to 40% of patients with NSCLC. DNA copy number changes are common in cancer and lead to altered expression and function of genes residing within the affected region of the genome. The aim of this study was to compare DNA copy number abnormalities between primary tumors (PT) and their corresponding BM in NSCLC to identify genomic regions associated with BM development by using array comparative genomic hybridization (aCGH).

**Material and Method:** From surgically resected NSCLC formalin-fixed and paraffin-embedded (FFPE) tissues, we selected 28 paired PTs and BMs (24 adenocarcinomas, and 4 squamous cell carcinomas, SCCs), and 55 additional BMs (43 adenocarcinomas, 2 SCCs, and 10 NSCLCs) specimens for analysis. Using DNA extracted from FFPE tumor tissues we performed oligo-based aCGH in 10 paired PT and BM adenocarcinomas. Statistical aberration detection algorithms of data were conducted by aCGH with Nexus Copy Number software v5.0. Immunohistochemical (IHC) analysis of two proteins (PSCA and LY6K) coded by genes located in 8q24.3 region was performed in both PT and BM specimens.

**Results:** In the aCGH analysis, multiple chromosomal regions with significant ( $P \leq 0.05$ ) copy number gain and loss were detected. Whereas PT demonstrated 32 regions (harboring 933 genes) of copy number gain and 16 regions (108 genes) of copy number loss, BM showed 31 regions (1274 genes) with gains and 16 regions (90 genes) with losses. BM demonstrated significantly ( $P \leq 0.01$ ) higher frequency of copy number gains in 3 chromosomal regions: 8q24.3 (BM 100% vs. PT 40%), 19q13.33 (BM 90% vs. PT 20%), and 20q13.12 (BM 60% vs. PT 0%). The 8q24.3 region with copy number gain in tumors harbors 7 genes, including Prostate Stem Cell Antigen (*PSCA*) and Lymphocyte Antigen 6 Complex Locus K (*LY6K*). Interestingly, in our IHC analysis, BMs (n=84; mean score 141.8) showed a significantly ( $P=0.008$ ) higher score of expression of PSCA than the corresponding PTs (n=27; mean score 97.8). Similar significant differences were detected when we analyzed only adenocarcinomas samples. No significant differences in the level of IHC expression was detected comparing BMs (n=83; mean score 64) and PTs (n=27; mean score 68.5) for LY6K.

**Conclusions:** By aCGH and subsequent protein expression analysis we have identified that PSCA may play an important role in the development of NSCLC brain metastasis. Similarly to prostate cancer, PSCA represents a novel potential marker for NSCLC metastasis and therapeutic target for advanced lung tumors. Supported by grant US DoD W81XWH-07-1-0306 and Jimmy L Hewlett Foundation.

[American Association for Cancer Research](#)  
615 Chestnut St. 17th Floor  
Philadelphia, PA 19106



[Print this Page](#)



# Presentation Abstract

Abstract  
Number: LB-88

Presentation  
Title: **Gene expression signatures predictive of clinical outcome and tumor mutations in refractory NSCLC patients (pts) in the BATTLE trial (Biomarker-integrated Approaches of Targeted Therapy for Lung Cancer Elimination)**

Presentation  
Time: Sunday, Apr 03, 2011, 3:45 PM - 4:05 PM

Location: Room W415 B/C, (Valencia Ballroom), Orange County Convention Center

Author  
Block: *John V. Heymach, Pierre Saintigny, Edward S. Kim, Lauren A. Byers, J. Jack Lee, Kevin Coombes, Lixia Diao, Jing Wang, Hai Tran, You H. Fan, Anne Tsao, George R. Blumenschein Jr., Vassiliki A. Papadimitrakopoulou, Ximing Tang, Michael Story, Yang Xie, Luc Girard, John Weinstein, Li Mao, John D. Minna, Roy Herbst, Scott M. Lippman, Waun K. Hong, Ignacio I. Wistuba.* UT MD Anderson Cancer Center, Houston, TX, UT Southwestern Medical Center at Dallas, Dallas, TX, University of Maryland Dental School, Baltimore, MD

Abstract  
Body: **Background:** There are currently no established markers to identify pts bearing wild-type EGFR who are likely to benefit from erlotinib (ERLO). The EGFR and Kras pathways, and epithelial to mesenchymal transition (EMT), have been associated with response/resistance to EGFR inhibitors. We developed gene signatures for these pathways and tested whether they were predictive of disease control (DC) and tumor mutations using gene expression profiles from pts in the BATTLE trial, and developed novel markers for ERLO benefit in wt EGFR pts.

**Methods:** Gene expression profiles (Affymetrix HG1.0ST) from pretreatment core needle biopsies (CNBs) were obtained from 101 BATTLE pts. Pathways signatures were developed using independent datasets from resected NSCLC pts and cell lines. A robust EGFR mutation signature was derived by comparing genes differentially expressed in mutated and wt *EGFR* lung adenocarcinoma from 3 independent institutions, and validated in three independent sets, both *in vivo* and *in vitro*. A KRAS signature was similarly derived. An EMT signature was derived by identifying genes with a bimodal distribution and correlated with known EMT genes (E-cadherin, vimentin, N-cadherin, FN-1) using 54 NSCLC cell lines, and validated in an independent panel of HN cell lines and across different platforms. A novel 5-gene signature was derived using erlotinib-treated BATTLE patients with or without 8 week DC, the primary study endpoint.

**Results:** The EGFR and Kras signatures predicted *EGFR* and *Kras* mutations, respectively, in BATTLE patients (AUC 0.72 by ROC analysis,  $p=0.03$  for EGFR; AUC 0.67,  $p=0.001$  for KRas signature). In pts with wt *EGFR* and *Kras*, the EMT and 5-gene, but not the EGFR or KRas signatures, were associated with improved DC in ERLO treated pts (EMT signature: 64% for epithelial vs 10% mesenchymal groups,  $p=0.02$ ; 5-gene: 83% vs 0%,  $p<.001$ ) and progression-free survival (PFS). The EGFR, EMT and 5-gene signatures were also significantly associated with *in vitro* sensitivity to ERLO in NSCLC cell lines. LCN2/NGAL, part of the 5-gene signature, was found to be associated with the epithelial phenotype. Potential therapeutic targets associated with mesenchymal phenotype including Axl were identified by the EMT signature.

**Conclusions:** Gene expression profiling from CNBs is a feasible approach for predicting response and identifying activated oncogenic pathways and potential therapeutic targets in refractory NSCLC pts. EGFR and Kras signatures predicted mutation status but, in wt *EGFR* patients, did not predict efficacy. EMT and a novel 5-gene signature including LCN2/NGAL were predictive of DC in pts with wt EGFR treated in BATTLE and merit further investigation as markers of benefit for EGFR inhibitors.

Webcast: <http://webcast.aacr.org/portal/p/2011annual/9787>

**[American Association for Cancer Research](#)**  
615 Chestnut St. 17th Floor  
Philadelphia, PA 19106

[Print this Page](#)



# Presentation Abstract

Abstract  
Number:

955

Presentation  
Title:

Specific forms of mutant *KRAS* predict patient benefit from targeted therapy in the BATTLE-1 clinical trial in advanced non-small cell lung cancer

Presentation  
Time:

Sunday, Apr 03, 2011, 4:20 PM - 4:35 PM

Location:

Room W311 E-H, Orange County Convention Center

Author  
Block:

Nate T. Ihle<sup>1</sup>, Roy S. Herbst<sup>1</sup>, Edward S. Kim<sup>1</sup>, Ignacio I. Wistuba<sup>1</sup>, J. Jack Lee<sup>1</sup>, George R. Blumenschein, Jr.<sup>1</sup>, Anne S. Tsao<sup>1</sup>, Lu Chen<sup>1</sup>, Shuxing Zhang<sup>1</sup>, Christine M. Alden<sup>1</sup>, Ximing Tang<sup>1</sup>, Suyu Liu<sup>1</sup>, David J. Stewart<sup>1</sup>, Vassiliki Papadimitrakopoulou<sup>1</sup>, John V. Heymach<sup>1</sup>, Hai T. Tran<sup>1</sup>, Marshall E. Hicks<sup>1</sup>, Jeremy J. Erasmus<sup>1</sup>, Sanjay Gupta<sup>1</sup>, John D. Minna<sup>2</sup>, Jill Larsen<sup>2</sup>, Scott M. Lippman<sup>1</sup>, Waun Ki Hong<sup>1</sup>, Garth Powis<sup>1</sup>. <sup>1</sup>The University of Texas MD Anderson Cancer Center, Houston, TX; <sup>2</sup>The University of Texas Southwestern Medical Center, Dallas, TX

Abstract  
Body:

Mutant *KRAS* (mut-*KRAS*) is present in 17-25% of all human cancers, where it plays a critical role in driving cancer cell growth and resistance to therapy. Despite numerous attempts, there is still no effective therapy for mut-*KRAS* tumors. Understanding the signaling mechanisms activated by mut-*KRAS* and finding agents to inhibit mut-*KRAS* signaling are important unmet needs in cancer therapy today. The recently completed BATTLE-1 clinical trial, a prospective, multi-arm, biopsy-mandated, biomarker-driven, clinical trial in advanced refractory non-small cell lung cancer (NSCLC), found that mut-*KRAS* did not accurately predict patient outcome (progression-free survival) to targeted intervention. This finding contradicted published evidence for such a relationship from colon cancer and some previous NSCLC studies. We explored more specifically the nature of the *KRAS* mutations, which are primarily found at codons 12 and 13, where different base substitutions lead to alternate amino acid (aa) substitutions. NSCLC has a much higher proportion of mut-*KRAS* G12C(cysteine) aa substitutions (47%) due to carcinogens in tobacco smoke, and only 15% mut-*KRAS* have G12D(aspartate). These data contrast those in other solid tumors, such as colon or pancreas, which predominantly manifest mut-*KRAS* G12D (50%) and only 9% mut-*KRAS* G12C. In a subset analysis of the BATTLE-1 data, we showed significantly worse progression-free survival in patients with mut-*KRAS* G12C, versus other mut-*KRAS* including G12D ( $p=.041$ ) and who were treated with erlotinib, vandetanib or sorafenib. In a panel of NSCLC cell lines with known mut-*KRAS* aa substitutions to identify pathways activated by the different mut-*KRAS* genotypes, we found that mut-*KRAS* G12D activates both PI-3-K and MEK signaling, while mut-*KRAS* G12C does not and alternatively activates PKC $\zeta$  and RAL signaling. This finding was confirmed in immortalized human bronchial epithelial (HBEC) cells stably transfected with wt-*KRAS* or different forms of mut-*KRAS*. Our molecular modeling studies show that the different conformation imposed by mut-*KRAS* G12C could lead to altered association with downstream signaling transducers, compared to mut-*KRAS* G12D. The significance of the findings for developing mut-*KRAS* therapies is profound, since it suggests that not all mut-*KRAS* may be additive; and that different combinations of inhibitors of downstream signaling may be needed for different mut-*KRAS*.

CME  
Designation:

CME-Designated

[American Association for Cancer Research](#)  
615 Chestnut St. 17th Floor  
Philadelphia, PA 19106

**[1788] High Expression of Folate Receptor Alpha in Lung Cancer Correlates with Adenocarcinoma Histology and *EGFR* Mutation.**

*Maria I Nunez, Carmen Behrens, Denise M Woods, Heather Lin, Milind Suraokar, Humam Kadara, John D Minna, Wayne Hofstetter, Neda Kalhor, Wong K Hong, Jack J Lee, Wilbur Franklin, David Stewart, Ignacio I Wistuba. MD Anderson Cancer Center, Houston, TX; The University of Texas Southwestern Medical Center, Dallas; University of Colorado, Denver*

**Background:** Folate receptor alpha (FRa) and receptor folate carrier-1 (RFC1) regulate cellular uptake of folate molecules inside the cell, and are potential biomarkers of tumor response to antifolate chemotherapy. Information on the protein expression of these receptors in non-small cell lung carcinoma (NSCLC) is limited.

**Design:** Expressions of FRa and RFC1 were examined by IHC in 320 surgically resected NSCLC (202 ADC and 118 SCC) tissue specimens using TMA. The findings were correlated with patient clinicopathologic characteristics. To address FRa expression level with tumor progression, analysis of specimens from advanced tumors and brain metastasis was performed. *FOLR1* mRNA expression was examined using publicly available microarray datasets. FRa expression was correlated with tumors' thymidylate synthase (TS) in NSCLCs, and with *EGFR* and *KRAS* mutations in ADC.

**Results:** NSCLC frequently over expressed both FRa and RFC1 in samples from early and advanced stages of the disease. In a multivariate analysis, lung ADC were more likely to express FRa in the cytoplasm (odds ratio [OR] = 4.39;  $P < 0.0001$ ) and membrane (OR = 5.34;  $P < 0.0001$ ) than SCC. Tumors from never-smokers were significantly more likely to express cytoplasmic (OR = 3.35;  $P < 0.03$ ) and membrane (OR = 3.60;  $P = 0.0005$ ) FRa than those from smokers. FRa and RFC1 expressions did not correlate with NSCLC patients' outcome. In ADC, *EGFR* mutations correlated with higher expression of membrane FRa and *FOLR1* gene expressions. FRa and TS expression inversely and significantly correlated ( $P = 0.03$ ).

**Conclusions:** Membrane transporter FRa and RFC1 proteins are frequently over expressed in NSCLC tissues at all tumor stages. The higher levels of FRa correlate with lung ADC histotype and presence of *EGFR* mutation. This study was supported in part by grants from the DO (W81XWH-07-1-0306 to J.D.M., W.K.H., D.J.S., and I.I.W.), the SPORE (P50CA70907 to J.D.M. and I.I.W.), and the NCI (Cancer Center Support Grant CA-16672).  
Category: Pulmonary

**Tuesday, March 1, 2011 1:00 PM**

**Poster Session IV # 264, Tuesday Afternoon**

[Close Window](#)

[Print this Page](#)


## Presentation Abstract

Abstract  
Number: 4121

Presentation  
Title: Folate pathway in malignant pleural mesothelioma (MPM): Novel therapeutic opportunities due to folate receptor alpha overexpression

Presentation  
Time: Tuesday, Apr 05, 2011, 1:00 PM - 5:00 PM

Location: Exhibit Hall A4-C, Poster Section 13

Poster  
Section: 13

Poster Board  
Number: 13

Author  
Block: Maria Ines Nunez<sup>1</sup>, Milind Suraokar (Equal contribution)<sup>2</sup>, Carmen Behrens<sup>2</sup>, Denise M. Woods<sup>1</sup>, Heather Lin<sup>3</sup>, Jack Lee<sup>3</sup>, Reza J. Mehran<sup>4</sup>, Wilbur Franklin<sup>5</sup>, Anne Tsao<sup>2</sup>, Ignacio Ivan Wistuba<sup>1</sup>. <sup>1</sup>Pathology Research. UT M.D. Anderson Cancer Center, Houston, TX; <sup>2</sup>Thoracic/ Head & Neck Medical Oncology. UT M.D. Anderson Cancer Center, Houston, TX; <sup>3</sup>Biostatistics. UT M.D. Anderson Cancer Center, Houston, TX; <sup>4</sup>Thoracic & Cardiovasc Surgery. UT MD Anderson Cancer Center, Houston, TX; <sup>5</sup>Pathology. UCD-School of Medicine, Anschutz Medical Campus, Aurora, CO

Abstract  
Body: **Background.** The folate pathway is active in several cancers including malignant pleural mesothelioma (MPM). Membrane receptors folate receptor alpha (FR $\alpha$ ), reduced folate carrier 1 (RFC1), proton coupled folate transporter (PCFT) and the enzyme thymidylate synthase (TS) regulate intra-cellular uptake of folate molecules and antifolate drugs. Due to the documented overexpression of folate markers in MPM they arise as potential targets for novel specific therapies with humanized monoclonal anti-FR $\alpha$  antibody and also to antifolate chemotherapy with pemetrexed.

**Material and Methods.** We studied 79 surgically resected MPM (43 epithelioid, 28 biphasic and 13 sarcomatoid histology types). Protein expression of FR $\alpha$ , RFC1, PCFT and TS was examined by immunohistochemistry (IHC) in FFPE tissues placed in tissue microarray platform and results correlated to clinical-pathologic characteristics. Gene expression and DNA copy number changes of the FR $\alpha$  gene (*FOLR1*) were examined in 53 mesothelioma tumors using Affymetrix U133 Plus 2.0 microarray's and Illumina HumanOmni1-Quad v1.0 chips, respectively. The expression microarray data was analyzed in the GeneSpring GX 11 software (Agilent technologies Inc.) while DNA copy number changes were detected using the Nexus 5.0 software (BioDiscovery Inc.).

**Results.** MPM frequently showed protein over-expression of FR $\alpha$ , RFC1 and PCFT. Nuclear TS expression positively correlated ( $P < 0.043$ ) with cytoplasmic TS and membrane RFC1. Patients with T1/T2 tumor had significantly ( $P = 0.038$ ) higher levels of membrane FR $\alpha$ , compared to patients with T3/T4 tumors. Epithelioid MPM had the highest level of cytoplasmic PCFT ( $P = 0.005$ ) among the three histological types, while patients with sarcomatoid histology had the lowest. In the multivariate analysis, with adjustment of gender, N and M stage, Patients who expressed any nuclear TS (score  $> 0$ ) had a lower hazard ratio than those who did not (HR=0.309; 95%CI 0.159, 0.601;  $P = 0.0005$ ). Patients with any level (score  $> 0$ ) of cytoplasmic PCFT had lower hazard ratio than those with absence of the marker (HR=0.539; 95%CI 0.306, 0.952;  $P = 0.0332$ ). Our gene expression data analysis on 53 mesothelioma tumors showed greater than 2-fold increase in the *FOLR1* and 3-fold increase in the TYMS messenger RNA levels compared to paired normal tissue. Additionally, at least 7 of these tumors show increased gene copy number at the *FOLR1* locus (Ch11q 13.4).

**Conclusions.** Folate membrane transporters (FR $\alpha$ , RFC1, PCFT) and the enzyme TS are frequently over expressed in MPM tumor tissues, and PCFT and TS are associated with tumors' clinico-pathological features. The high level of expression of FR $\alpha$  in MPM supports the rational use of potential utilization of humanized monoclonal anti-FR $\alpha$  antibody and also standard antifolate chemotherapy in this disease. Supported by grant US DoD W81XWH-07-1-0306, ASCO CDA.

**American Association for Cancer Research**  
615 Chestnut St. 17th Floor  
Philadelphia, PA 19106



[Print this Page](#)



# Presentation Abstract

Abstract Number: 4031

Presentation Title: CNG *c-myc* in mesothelioma

Presentation Time: Tuesday, Apr 05, 2011, 1:00 PM - 5:00 PM

Location: Exhibit Hall A4-C, Poster Section 9

Poster Section: 9

Poster Board Number: 28

Author Block: Erick M. Riquelme<sup>1</sup>, Milind B. Suraokar<sup>1</sup>, Maria I. Nunez<sup>1</sup>, Adi F. Gazdar<sup>2</sup>, Laurent A. Byers<sup>1</sup>, John V. Heymach<sup>1</sup>, Reza J. Mehran<sup>1</sup>, Anne Tsao<sup>1</sup>, Ignacio I. Wistuba<sup>1</sup>. <sup>1</sup>MD Anderson, UT Texas, Houston, TX; <sup>2</sup>The University of Texas Southwestern Medical Center, Dallas, TX

**Abstract Body:** Background Malignant pleural mesothelioma (MPM) is a deadly disease with poor prognosis, few treatment options, and an increasing incidence worldwide. There is, therefore, a great need to identify new therapeutic targets and develop more effective therapies for patients with MPM. To better characterize the molecular changes occurring in MPM, we determined genetic and proteomic abnormalities in MPM cell lines and correlated them with those found in MPM tumor tissue specimens. Methods We performed SNP/copy number analysis using Affymetrix SNP 6.0 chips, messenger RNA (mRNA) analysis using Affymetrix U133 plus 2.0 chips, and Reverse Protein Phase Array (RPPA) analysis in 4 mesothelioma cell lines (H28, MSTO-211H, H2052 and H2452) along with the control normal cell line HCT-4012, for comparison. DNA copy number microarray data were analyzed using the Nexus 5.0 software (BioDiscovery Inc.), while mRNA expression array data were analyzed using the GeneSpring GX 11 software (Agilent technologies, Inc.). Additionally, we evaluated copy number gain (CNG) of the *c-myc* gene and expression of *c-myc* protein in the mesothelioma cell lines and control cell line by fluorescent in situ hybridization (FISH) and Western blot, respectively. Furthermore, we investigated CGN in MPM tumor tissue specimens by performing FISH using the *c-myc* probe on tissue microarrays (TMAs) containing 80 MPM samples from different histological subtypes (41 epithelioid, 27 biphasic, 12 sarcomatoid). Results DNA copy number analysis using the Affymetrix chip revealed CNG or amplification of the *c-myc* oncogenic locus in 3 out of 4 mesothelioma cell lines compared to the control HCT-4012 cell line. In concordance, the mRNA microarray data also showed increased number of transcripts from this locus; more importantly, the RPPA array data showed increased *c-myc* protein expression in these cell lines compared to control. These results were confirmed by FISH and Western blot analysis, which showed CNG or amplification at this locus and increased levels of the *c-myc* protein in the mesothelioma cell lines. FISH analysis of TMAs also revealed a relatively high frequency (21%) of CNG ( $\geq 4$  copies in  $\geq 70\%$  of cells) for the *c-myc* locus in the MPM tumors. Interestingly, this amplification were seen in either epithelioid (10%) or biphasic (11%) histotype, and none were observed in the sarcomatoid cases. Similarly, within the biphasic cases, we observed that the amplification was present only in the epithelioid component, and not in the sarcomatoid component. Conclusion Our findings suggest that CNG of the *c-myc* locus is characteristic for MPM tumors of the epithelioid histotype or of the epithelioid component of biphasic histotype, and suggest that *c-myc* CNG could have a role in pathogenesis of this disease; however, further studies are needed to clarify the role of *c-myc* in MPM development and progression. Supported by grant US DoD W81XWH-07-1-0306.

**American Association for Cancer Research**  
615 Chestnut St. 17th Floor  
Philadelphia, PA 19106

[Print this Page](#)


# Presentation Abstract

Abstract Number: 3273

Presentation Title: Estrogen contributes to bevacizumab resistance in xenograft models of non-small cell lung cancer (NSCLC)

Presentation Time: Tuesday, Apr 05, 2011, 8:00 AM -12:00 PM

Location: Exhibit Hall A4-C, Poster Section 18

Poster Section: 18

Poster Board Number: 8

Author Block: Babita Saigal, Mathew H Herynk, Tina Cascone, Monique Nilsson, Mehrdad Khajavi, Pierre Saintigny, John V. Heymach. UT M.D. Anderson Cancer Ctr., Houston, TX

**Abstract Body:** Previous studies have established that there are differences in the oncogenic pathways activated in women and men with NSCLC and that women with hormonal replacement therapy have significantly decreased survival. Furthermore, in the ECOG4599 study comparing chemotherapy with or without the VEGF inhibitor bevacizumab (BV), overall survival benefit was seen in men but not women. Together these studies suggest that estrogen (E2) may contribute to cancer progression and response to antiangiogenic therapy. The mechanism(s) by which this may occur is not well understood, although it has been previously reported that E2 increases the secretion of Vascular Endothelial Growth Factor (VEGF) in vitro, that the vast majority of NSCLC express estrogen receptors (ER), and that estrogen stimulates the growth of NSCLC xenografts in nude mice. To evaluate whether E2 promotes the growth of NSCLC and resistance to antiangiogenic therapy, we tested the impact of E2 on response to BV in murine models of NSCLC. Briefly, ovariectomized nude female mice were primed with an extended release pellet of estradiol-17 $\beta$ . Mice were then subcutaneously injected with HCC827 lung cancer cells and randomized when tumor volume reached 200-250mm<sup>3</sup>. Tumor progression was defined when tumor volume reached 1000mm<sup>3</sup> in size. Mice were treated with BV in the presence or absence of E2 and were sacrificed at progression. We observed prolonged survival in the BV alone group compared to the BV+E2 group (median survival more than 200 days for BV vs. 56 days for the BV+E2 group p=0.006). In addition, the combination of BV+E2 group had a significantly improved survival compared with vehicle+E2 (56 days vs. 26 days, p < 0.0001). Furthermore, in absence of E2, a trend towards a decrease in MVD was observed in BV vs Vehicle (11 vs 20, t-Test, p=0.08); in the presence of E2, by contrast, no significant changes in vascular density were observed between BV+E2 vs Vehicle+E2 (24.8 vs 21.75, t-Test, p=0.37). To investigate the contribution of estrogen signaling pathway in response to BV, a similar study was performed with the addition of the ER antagonist, fulvestrant (F). The addition of F to BV+E2 significantly prolonged the median survival compared with BV + E2 (88 days in F+BV+E2 group vs. 47 days in BV+E2, p=0.007). This was accompanied with significant reduction of MVD compared with BV+E2 (BV+F+E2 (12.77) vs BV+E2(22.12), t-Test, p= 0.03). No difference in survival was observed in F+E2 vs. Control+E2 (p=0.159) or F+E2 vs. BV+E2 (p=0.3). **Conclusions:** Our findings indicate that in a preclinical model of NSCLC, estrogen promoted resistance to anti-VEGF therapy and increased tumor microvessel density. The addition of the ER antagonist fulvestrant was able to block the E2-induced BV resistance. These data suggest that estrogen blockade merits further investigation as a potential therapeutic strategy to mitigate resistance to antiVEGF therapy in women with NSCLC.

[American Association for Cancer Research](#)  
615 Chestnut St. 17th Floor  
Philadelphia, PA 19106

[Print this Page](#)


# Presentation Abstract

Abstract  
Number: 4109

Presentation Title: A 5-gene signature (sig) predicts clinical benefit from erlotinib in non-small cell lung cancer (NSCLC) patients (pts) harboring wild-type (wt) EGFR & KRAS

Presentation Time: Tuesday, Apr 05, 2011, 1:00 PM - 5:00 PM

Location: Exhibit Hall A4-C, Poster Section 13

Poster  
Section: 13

Poster  
Board  
Number: 1

Author Block: Pierre Saintigny<sup>1</sup>, Lixia Diao<sup>1</sup>, Jing Wang<sup>1</sup>, Luc Girard<sup>2</sup>, Steven H. Lin<sup>1</sup>, Kevin R. Coombes<sup>1</sup>, Suyu Liu<sup>1</sup>, J. Jack Lee<sup>1</sup>, John N. Weinstein<sup>1</sup>, Yang Xie<sup>2</sup>, You H. Fan<sup>1</sup>, Xi Ming Tang<sup>1</sup>, Edward S. Kim<sup>1</sup>, Roy S. Herbst<sup>1</sup>, Anne Tsao<sup>1</sup>, George R. Blumenschein<sup>1</sup>, Li Mao<sup>3</sup>, Scott M. Lippman<sup>1</sup>, John D. Minna<sup>2</sup>, Waun Ki Hong<sup>1</sup>, Ignacio I. Wistuba<sup>1</sup>, John V. Heymach<sup>1</sup>. <sup>1</sup>UT M.D. Anderson Cancer Ctr., Houston, TX; <sup>2</sup>UT SouthWestern Medical Center, Dallas, TX; <sup>3</sup>University of Maryland, Baltimore, MD

Abstract Body: Background: Despite a low response rate, erlotinib (E) improves survival in a subset of NSCLC pts with wt EGFR but there are no established markers for identifying pts likely to have clinical benefit. We hypothesized that a gene expression sig could be used for this purpose. Material and Methods: We used pretreatment gene expression profiles (Affymetrix HG1.0ST) from 101 chemo-refractory pts in our Biomarkers-Integrated Approaches of Targeted Therapy for Lung Cancer Elimination (BATTLE) treated with E, E+bexarotene (EB), sorafenib (S), or vandetanib (V). 24 cases of wt EGFR & KRAS tumors treated with E or EB were compared to train the signature (two-sided t-test), using the primary end-point of the trial [8-week disease control (8wDC)]. Principal component (PC) analysis and a logistic regression model were used to develop the sig. Gene expression profiles from 108 NSCLC cell lines (Illumina), with available E IC50 (N=94) and DNA methylation profiling (N=66, Illumina), were used for in vitro studies. Results: 113 genes were differentially expressed between pts with or without 8wDC (false discovery rate 30%; P=0.004). Leave-one-out cross validation with various gene list lengths produced a 5-gene sig, including lipocalin 2 (LCN2), with a specificity, sensitivity and accuracy of 80% to predict 8wDC. In pts treated with E or EB, using the median sig score, the 8wDC rate in the sig-positive group was 83% compared with 0% in the sig-negative group; the sig did not predict 8wDC in pts treated with S or V (Mantel-Haenszel chi-squared test P=0.023). The improvement in 8wDC in the sig-positive group translated to an increased progression-free survival (PFS) (hazard ratio=0.12, 95% confidence interval: 0.03-0.46, P=0.001; log-rank P=0.0004; median PFS: 12.5 weeks vs. 7.2 weeks). We tested the sig in an independent set of 47 wt EGFR&KRAS cell lines. It predicted E sensitivity with an area under the curve of 78% (P=0.002). The first PC of the sig and the IC50 for E were correlated (r=-0.47, P=0.0009). In 108 NSCLC cell lines, LCN2 gene expression was bimodal and correlated with the IC50 for E (r=-0.46, P=0.001). Degree of methylation and expression level of LCN2 were inversely in wt EGFR & KRAS NSCLC cells (r=-0.79, P<0.0001, N=33). Cell lines with completely unmethylated LCN2 were more sensitive to E compared to those with LCN2 full methylation (N=36) (P=0.006); the difference remained significant in wt EGFR & KRAS cell lines (P=0.014). Conclusion: We identified a 5-gene sig predictive of PFS benefit in NSCLC pts with wt EGFR & KRAS treated with E, but not S or V. The sig was also predictive of E sensitivity in vitro. LCN2 was the strongest individual marker of sensitivity and may be epigenetically regulated.

[American Association for Cancer Research](#)  
615 Chestnut St. 17th Floor  
Philadelphia, PA 19106

[Print this Page](#)



# Presentation Abstract

Abstract Number: 678

Presentation Title: Study of 2, 9-disecbutyl-1, 10-phenanthroline as a novel anticancer agent

Presentation Time: Sunday, Apr 03, 2011, 1:00 PM - 5:00 PM

Location: Exhibit Hall A4-C, Poster Section 28

Poster Section: 28

Poster Board Number: 22

Author Block: Dongsheng Wang<sup>1</sup>, A.R.M. Ruhul Amin<sup>1</sup>, Shifang Peng<sup>1</sup>, Chinar Sanghvi<sup>1</sup>, Dong M. Shin<sup>1</sup>, Jack F. Eichler<sup>2</sup>. <sup>1</sup>Emory University, Atlanta, GA; <sup>2</sup>University of California Riverside, Riverside, CA

Abstract Body: Development of new, safe, and effective drugs or strategies targeting molecular events and pathways which are responsible for cancer initiation and progression is an urgent need to improve cancer patient care. In this study, we tested the antitumor effect of a novel agent, 2, 9-disecbutyl-1, 10-phenanthroline (dsBPT), a 1, 10-phenanthroline derivative. Both *in vitro* cell line and *in vivo* xenograft models were applied to study the antitumor efficacy and underlying mechanism of this compound. IC<sub>50</sub>s were initially determined using lung cancer cell lines: A549 (0.25  $\mu$ M) and H1703 (0.1  $\mu$ M), head and neck cancer cell lines: TU686 (0.08  $\mu$ M) and TU212 (0.2  $\mu$ M), and normal bronchial epithelial cells: BEAS-2B (2.0  $\mu$ M), indicating that the growth inhibitory effect of dsBPT on cancer cell lines was about 10 times greater than that on normal human epithelial cells. Further studies demonstrated that dsBPT at a concentration of 1-2  $\mu$ M induced autophagy and G1 cell cycle arrest. At higher doses between 4-8  $\mu$ M, the compound further induced apoptosis (40-80%). Combination of dsBPT with the cytotoxic agent cisplatin synergistically inhibited cancer cell growth (combination index = 0.3) and induced apoptosis (80-90%) at a concentration of 1  $\mu$ M for each drug. Two experiments were then performed to test dsBPT *in vivo*. First, xenografted mice implanted with TU212 cells were treated with three drug doses (2mg/kg, 5mg/kg, 10mg/kg). Compound was given by IV injection once per week for 3 weeks. We found that 10 mg/kg treatment significantly reduced tumor growth as compared with the control group ( $p = 0.004$ ). Under the same treatment schedule, further study showed that the combination of dsBPT (2 mg/kg) with cisplatin (2 mg/kg) significantly reduced the tumor volume as compared with the untreated control ( $p = 0.0017$ ), while each of the single drugs at the same concentration showed no significant inhibitory effect on tumor growth ( $p = 0.10$  and  $0.15$  for cisplatin and dsBPT, respectively). Neither significant weight loss nor major organ damage was observed by histology examination in the experimental animals in this study. In summary, our study suggests that dsBPT is a novel, highly potent antitumor drug that warrants further preclinical and clinical development either as a single agent or in combination with known chemotherapy drugs such as cisplatin. (This study is supported by grants from DOD W81XWH-07-1-0306 Project 5, and GCC Distinguished Scholar Award to ZC).

[American Association for Cancer Research](#)  
615 Chestnut St. 17th Floor  
Philadelphia, PA 19106

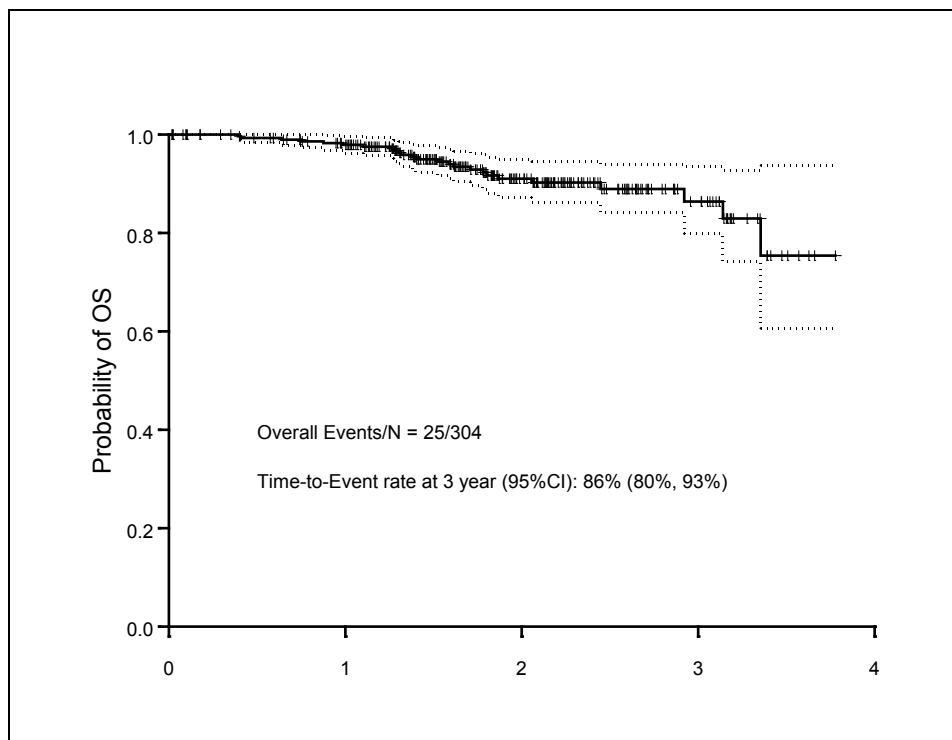
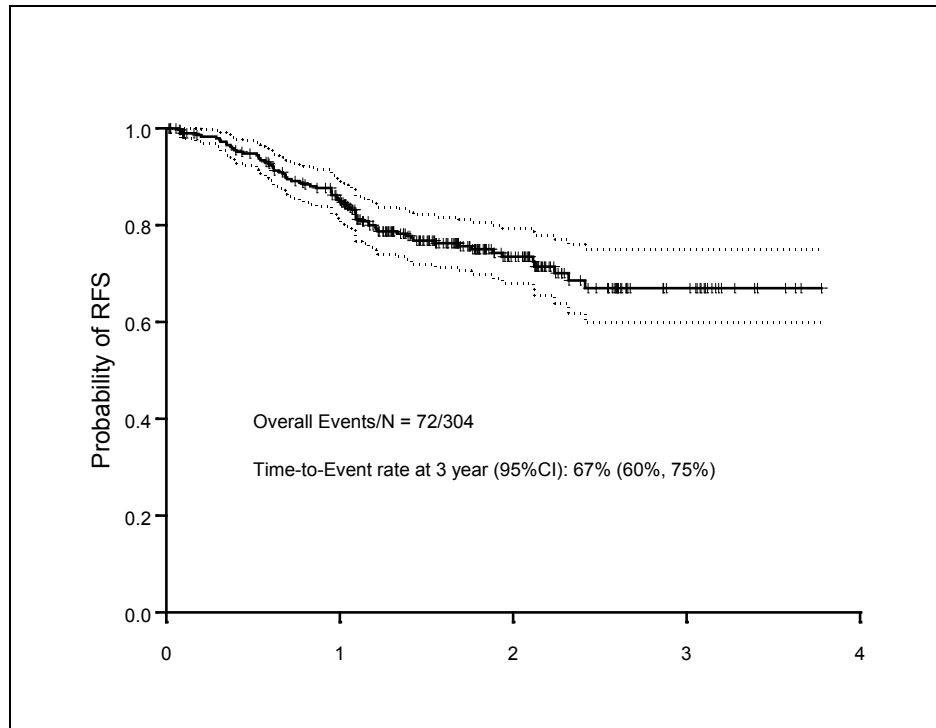


**Appendix B1: Summary of the prospectively collected data in the PROSPECT project.**

<b>Table 1. Patient's demographic and pathological characteristics</b>			
Variable	Category	Frequency Count	Percent of Total Frequency
Gender	F	150	49.34
	M	154	50.66
Race	Black	16	5.26
	Hispanic	11	3.62
	Oriental	11	3.62
	White	266	87.50
Surgical_Path_T	T1	134	44.08
	T2	143	47.04
	T3	13	4.28
	T4	12	3.95
	TX	2	0.66
Surgical_Path_N	N0	220	72.37
	N1	43	14.14
	N2	37	12.17
	NX	4	1.32
Surgical_Path_M	NULL	304	100.00
Dx	NSCLC	304	100.00
NSCLC_Type	Adenocarcinoma	193	63.49
	Adenosquamous carcinoma	4	1.32
	Large cell carcinoma	5	1.64
	NULL	14	4.61
	Squamous cell carcinoma	88	28.95

Analysis Variable : age							
N	Minimum	Lower Quartile	Median	Upper Quartile	Maximum	Mean	Std Dev
304	39.61	59.29	66.40	72.80	86.75	65.89	9.40

Median follow-up time for surviving patients is 1.83 years.



## Appendix B2: PROSPECT Database Screenshots (new development shown on exhibits 12-15.)

### 1) Clinical module: Patient Information, Social History, Medical History

Admin	Projects	Histo-Pathology Lab	Logout
-------	----------	---------------------	--------

MRN	<input type="text"/>		<input type="text"/>	Name		<input type="text"/>
Path#	<input type="text"/>		<input type="text"/>	Protocol	PROSPECT	<input type="checkbox"/> Patient Completed

Status: Editing new patient....

Other Malignancy	Treatment	Staging	Follow up	Pathology	All Clinical TO EXCEL
------------------	-----------	---------	-----------	-----------	-----------------------

**Patient Information**
[EXPORT TO EXCEL](#)

Last	<input type="text" value="Xx"/>	Middle	<input type="text"/>	First	<input type="text" value="Xxx"/>	MDAH	<input type="text" value="110000"/>
Gender	Female	Race	White	DOB	<input type="text" value="1/1/1980"/>		
City	Houston	State	TX	Enter Date	<input type="text" value="6/3/2011"/>		
Zip Code	77010	Country	USA	Age	<input type="text"/>		
Last Visit Date	02/08/2011	Death or Alive	Alive	Chemotherapy	Yes		
Lost To Follow up	No	Recurrence	No				
Radiotherapy	Yes						

**Social History**
[EXPORT TO EXCEL](#)


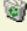
Smoking History	<input type="radio"/> Yes <input checked="" type="radio"/> No	Pack Years	<input type="text" value="74"/>
Are you currently smoking?	<input type="radio"/> Yes <input checked="" type="radio"/> No		
If no, date quit smoking	<input type="text"/>		Age Quit Smoking
Age started smoking regularly	<input type="text" value="0"/>		Overall Smoking Years
Average number of cigarettes smoked per day?	<input type="text" value="0"/>		Actual Smoking Years
If there was a quit-smoking period, total time during the smoking years.	<input type="text" value="0"/> yrs., <input type="text" value="0"/> mos.		Pack Years
Asbestos Exposure	<input type="radio"/> Yes <input checked="" type="radio"/> No		
Alcohol History	<input type="radio"/> Yes <input checked="" type="radio"/> No	No. of Drinks / Month	<input type="text" value="0"/>

**Medical History**
[EXPORT TO EXCEL](#)

Hypertension	<input checked="" type="radio"/> Yes <input type="radio"/> No	Heart Problem	<input checked="" type="radio"/> Yes <input type="radio"/> No	Thyroid	<input type="radio"/> Yes <input checked="" type="radio"/> No
Diabetes	<input type="radio"/> Yes <input checked="" type="radio"/> No	Renal Insufficiency	<input type="radio"/> Yes <input checked="" type="radio"/> No	Asthma	<input checked="" type="radio"/> Yes <input type="radio"/> No
DVT	<input checked="" type="radio"/> Yes <input type="radio"/> No	Pulmonary Embolism	<input checked="" type="radio"/> Yes <input type="radio"/> No	Mild hemoptysis	<input checked="" type="radio"/> Yes <input type="radio"/> No
Radiation Fibrosis	<input type="radio"/> Yes <input checked="" type="radio"/> No	Hepatic Problem	<input type="radio"/> Yes <input checked="" type="radio"/> No	COPD	<input type="radio"/> Yes <input checked="" type="radio"/> No
Other	<input type="text"/>	Date COPD Dx	<input type="text"/>		

2) Clinical module: Other Malignancy

OtherMalignancy: 888888				Status: Ready...	
<a href="#">Click here</a> to add <input type="text" value="1"/> more row(s). <a href="#">Save it</a> <a href="#">Cancel it</a> <a href="#">Open it</a> <a href="#">Save and Close</a> <a href="#">EXPORT TO EXCEL</a>					
Malig. ID	Patient ID	Dx Date	Malig. Detail		Treatment
 288	1434		Period: <input type="text" value="n/a"/> Organ: <input type="text" value="Hematological"/> Histology: <input type="text" value="n/a"/> Comments: <input type="text"/> NED: <input type="checkbox"/> NED Date: <input type="text"/>		Surgery: <input type="checkbox"/> Date: <input type="text" value="5/21/2008"/> Chemo: <input checked="" type="checkbox"/> Date: <input type="text"/> Radio: <input type="checkbox"/> Date: <input type="text"/>
 417	1434		Period: <input type="text" value="n/a"/> Organ: <input type="text" value="Prostate"/> Histology: <input type="text" value="n/a"/> Comments: <input type="text"/> NED: <input type="checkbox"/> NED Date: <input type="text"/>		Surgery: <input checked="" type="checkbox"/> Date: <input type="text" value="5/21/2008"/> Chemo: <input type="checkbox"/> Date: <input type="text"/> Radio: <input checked="" type="checkbox"/> Date: <input type="text"/>



3) Clinical module: Treatment: Surgery, Chemotherapy, Radiotherapy and Other Treatments.

Status: Ready...

Surgery: 888888

[Click here](#) to add 1 more row(s). [Save it](#) [Cancel it](#) [Open it](#) [Save and Close](#) [EXPORT TO EXCEL](#)

Surgery ID	Patient ID	Surgery Date	Is MDA	Surgery Procedure	Comments	Margin Left
312	490	6/15/2004	<input type="checkbox"/>	n/a		<input type="checkbox"/>

**Chemotherapy**

[Click here](#) to add 1 more row(s). [Save it](#) [Cancel it](#) [Open it](#) [Save and Close](#) [EXPORT TO EXCEL](#)

Chemo ID	Chemo Type	Chemo Date	Drug	Tumor Size	Response	Comments
422	Is MDA: <input type="checkbox"/>	Start: 1/1/1900	A: Carboplatin	Before(CT) 0	Clin.: n/a CT: n/a Patho: n/a	(Carbo-Docetaxel)
490	Chemo. Type: Adjuvant	Stop: 1/1/1900	B: Docetaxel	After(CT) 0		
			C: n/a	% Reduction NaN		
			#crs:	Before(Patho) 0		
				After(Patho) 0		
				% Reduction NaN		

**Radiotherapy**

[Click here](#) to add 1 more row(s). [Save it](#) [Cancel it](#) [Open it](#) [Save and Close](#) [EXPORT TO EXCEL](#)

Radio ID	Treatment Option	Radio Date	Tumor Size	Response	Comments
177	Is MDA: <input type="checkbox"/>	Start: 1/1/1900	Before(CT) 0	Clin.: n/a CT: n/a Patho: n/a	
490	Site1: n/a	Stop: 1/1/1900	After(CT) 0		
	Site2: n/a		% Reduction NaN		
	Site3: n/a		Before(Patho) 0		
	Treatment Option: Adjuvant		After(Patho) 0		
			% Reduction NaN		

**Other Treatment**

[Click here](#) to add 1 more row(s). [Save it](#) [Cancel it](#) [Open it](#) [Save and Close](#) [EXPORT TO EXCEL](#)

Treatment ID	Patient ID	Surgery Date	Other Treatment	Comments
--------------	------------	--------------	-----------------	----------

#### 4) Clinical module: Staging

Staging: 888888		Status: Ready...								
<a href="#">Click here</a> to add <input type="text" value="1"/> more row(s). <a href="#">Save it</a> <a href="#">Cancel it</a> <a href="#">Open it</a> <a href="#">Save and Close</a> <a href="#">EXPORT TO EXCEL</a>										
Stage ID	Patient ID	Staging Date	Current Situation	Clin. T	Clin. N	Clin. M	Clin. Stage	Pleu Eff	Malig PI Eff	Comments
1192	1190	3/23/2010	n/a	T1	N0	M0	n/a	<input type="checkbox"/>	<input type="checkbox"/>	
<b>Pathology</b>										
<b>Tumor Specimens</b>										
Surgical Date	Single Wedge	Multiple Wedge	Single Segmentectomy	Multiple Segmentectomy	Lobectomy	Bilobectomy	Pneumonectomy	# Nodules	Tumor ID	Tumor specimen Site type
03/23/2010					True				1338	
<div> <div> <div></div> <div>   </div> <div></div> </div> </div>										
<b>Dx Specimens</b>										
Patient_ID	AccessionNo	Path	Type	Event	Dx Specimen	Date	Specimen	Type	Tumor Site	Specimen Avail
<b>Metastasis Specimens</b>										
Patient_ID	AccessionNo	Path	Type	Event	Met Date	Specimen	Type	Tumor Site	Specimen	Avail

Follow up: 888888				Status: Ready...	
<a href="#">Click here</a> to add <input type="text" value="1"/> more row(s). <a href="#">Save it</a> <a href="#">Cancel it</a> <a href="#">Open it</a> <a href="#">Save and Close</a> <a href="#">EXPORT TO EXCEL</a>					
Person Review <input type="text" value="n/a"/>				Date Updated <input type="text"/>	
Fu ID	Patient ID	Fu Date	Fu Detail		
	1727	1348	12/3/2010	Status <input type="text" value="recurrence"/>	
				If "no change or no recurrence": Form of contact: <input type="text"/>	
				If "recurrence": Form of contact: <input type="text" value="visit to clinic"/> Date of recurr: <input type="text" value="12/3/2010"/>	
				Site of Recur: <input type="text" value="Thoracic Lymph N"/>	
				<input type="radio"/> local recur <input type="text" value="Thoracic Lymph N"/>	
				<input type="radio"/> 2nd primary <input type="text"/>	
				<input checked="" type="radio"/> n/a <input type="text" value="Thoracic Lymph N"/>	
				Recur Biopsy: <input checked="" type="checkbox"/> Image Date: <input type="text" value="11/9/2010"/>	
				If "death": Death Date: <input type="text"/> Cause of Death: <input type="text"/>	
				Info by: <input type="text"/>	
Comments:					
	1728	1348	3/3/2011	Status <input type="text" value="no change"/>	
				If "no change or no recurrence": Form of contact: <input type="text" value="visit to clinic"/>	
				If "recurrence": Form of contact: <input type="text"/> Date of recurr: <input type="text"/>	
				Site of Recur: <input type="text"/>	
				<input type="radio"/> local recur <input type="text"/>	
				<input type="radio"/> 2nd primary <input type="text"/>	
				<input checked="" type="radio"/> n/a <input type="text"/>	
				Recur Biopsy: <input type="checkbox"/> Image Date: <input type="text"/>	
				If "death": Death Date: <input type="text"/> Cause of Death: <input type="text"/>	
				Info by: <input type="text"/>	
Comments:					

## 6) Pathological module: Tissue Pathological Data

- Primary Diagnosis Specimen
- Primary Surgical Specimen
- Metastasis Diagnosis Specimen
- Metastasis Surgical Specimen

Admin
Projects
Histo-Pathology Lab
Logout

MRN
Path#
Name

888888
Status: Ready...

Hist Dx TO EXCEL
All Pathology TO EXCEL
Clinical
Click here to add 1 more row(s).
Save It
Cancel It
Open It
Save and Close
EXPORT TO EXCEL

Accession	Biopsy	Event
1218 S-09-064850	Primary	Surgical Specimen

Dx Specimen
Click here to add 1 more row(s).
Save It
Cancel It
Open It
Save and Close
EXPORT TO EXCEL

Dx Specimen ID	Obtained Date	Accession ID	Accession No	Specimen Type	Tumor Site	Specimen Avail
----------------	---------------	--------------	--------------	---------------	------------	----------------

Surgical Specimen
Click here to add 1 more row(s).
Save It
Cancel It
Open It
Save and Close
EXPORT TO EXCEL

Surg ID	Acc. ID	Accession No	Surgical Date	Single Wedge	Multi Wedge	Single Segmen tectomy	Multi Segmen tectomy	Lobec tomy	Bilo bectomy	Pneumo nectomy	No of Nodules	T	N	M	Path Stage	Comments
1293	1218	S-09-064850	10/2/2009									T2	NC	n/a	n/a	

Met Specimen
Click here to add 1 more row(s).
Save It
Cancel It
Open It
Save and Close
EXPORT TO EXCEL

Met Specimen ID	Met Date	Accession ID	Accession No	Specimen Type	Tumor Site	Specimen Avail
-----------------	----------	--------------	--------------	---------------	------------	----------------

## 7) Pathological module: Histology


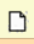
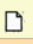


<b>Histology: S-09-888888</b>		<b>Status: Ready</b>	
<div><div>Update</div><div>Delete</div><div>EXPORT TO EXCEL</div></div>			
Hist ID:	616	Dx Specimen ID:	0
		Met Specimen ID:	0
		Tumor ID:	635
Index	0.70	Total Blocks Analyzed	1
Histology Dx:	NSCLC		
NSCLC Type:	Squamous cell carcinoma		
NSCLC Grade:	Moderately		
NSCLC Variant:	n/a		
Other Tumoral Characteristics (Hist Dx)			
Necrosis %	25		
Fibrosis %	20		
Inflammation	Mild		
Comments:			



## 8) Pathological module: Staging and Tumor Information

Tumor: S-09-888888 (8888)		Status: Ready...																																																											
<a href="#">Click here</a> to add <input type="text" value="1"/> more row(s). <a href="#">Save it</a> <a href="#">Cancel it</a> <a href="#">Open it</a> <a href="#">Save and Close</a>																																																													
Tumor ID	Surgical ID	Specimen Type	Tumor Site																																																										
1225	1293	n/a	n/a																																																										
Localization	n/a																																																												
<div> <div> <input type="checkbox"/> Tissue Available           <div> <input type="checkbox"/> Bronchus           <div>             Extrapulmonary             <div> <input type="checkbox"/> Principal             <input type="checkbox"/> Lobar           </div>             Intrapulmonary             <div> <input type="checkbox"/> with Cartilage             <input type="checkbox"/> w/o Cartilage             <input type="checkbox"/> Bronchiole             <input type="checkbox"/> Alveoli           </div> </div> </div> </div> <div> <div> <input type="checkbox"/> Tumor Invasion           <div> <input checked="" type="checkbox"/> LV           <input type="checkbox"/> Pleural           <input type="checkbox"/> Neural           <input type="checkbox"/> Vascular           <input type="checkbox"/> Bronchial           <input type="checkbox"/> Other           <input type="checkbox"/> Margin Positive           <div> <input type="checkbox"/> Bronchial <input type="checkbox"/> Parenchymal <input type="checkbox"/> Soft Tissue <input type="checkbox"/> Other </div> </div> </div> </div> </div> <div> <div> <b>Pathological T</b> <div> <b>Pathological T:</b> <div>n/a</div> <div> <input type="checkbox"/> Tx           T1: &lt;= 3 cm.           T2: &gt; 3 cm or &lt;= 3cm and/or attached to visceral pleura           <input checked="" type="checkbox"/> Pleural Attached           T3:           <div> <input type="checkbox"/> Parietal Pleura <input type="checkbox"/> Mediastinal Pleura <input type="checkbox"/> Chest Wall <input type="checkbox"/> Pericardium <input type="checkbox"/> Phrenic Nerve <input type="checkbox"/> Vagus Nerve <input type="checkbox"/> Sympathetic Chain <input type="checkbox"/> Atelectasis Entire Lung </div>           T4:           <div> <input type="checkbox"/> &gt;1 Nodal <input type="checkbox"/> Invades to Great Vessel <input type="checkbox"/> Invades to Heart <input type="checkbox"/> Invades to Trachea <input type="checkbox"/> Invades to Carina <input type="checkbox"/> Invades to Esophagus <input type="checkbox"/> Invades to Vertebral Bones <input type="checkbox"/> Associated with Malignant Pleural Effusion <input type="checkbox"/> Satellite Tumor Nodule (size) <input type="checkbox"/> Mediastinal </div> </div> </div> </div> </div> <div> <div>Field Study</div> <div> <input type="checkbox"/> Normal Bronchial Epithelium <input type="checkbox"/> Normal Lung Parenchyma <input type="checkbox"/> Hyperplastic Alveoli <input type="checkbox"/> Bronchial Hyperplasia <input type="checkbox"/> Squamous Metaplasia <input type="checkbox"/> Mild Squamous Dysplasia <input type="checkbox"/> Moderately Squamous Dysplasia <input type="checkbox"/> High Squamous Dysplasia <input type="checkbox"/> In Situ Squamous Carcinoma <input type="checkbox"/> Atypical Adenomatous Hyperplasia <input type="checkbox"/> Tumorlet </div> </div> <div> <div>Lymph Node Metastasis</div> <div> <input checked="" type="checkbox"/> Lymph Node Involvement </div> </div> <div> <div>Analysis of Lymph Node Station</div> <table border="1"> <thead> <tr> <th></th> <th>+</th> <th>Total</th> <th></th> <th>+</th> <th>Total</th> <th></th> <th>+</th> <th>Total</th> <th></th> <th>+</th> <th>Total</th> </tr> </thead> <tbody> <tr> <td>S1</td> <td>0</td> <td>0</td> <td>S2</td> <td>0</td> <td>1</td> <td>S3</td> <td>0</td> <td>0</td> <td>S4</td> <td>0</td> <td>1</td> </tr> <tr> <td>S5</td> <td>0</td> <td>0</td> <td>S6</td> <td>0</td> <td>0</td> <td>S7</td> <td>0</td> <td>1</td> <td>S8</td> <td>0</td> <td>0</td> </tr> <tr> <td>S9</td> <td>0</td> <td>1</td> <td>S10</td> <td>0</td> <td>0</td> <td>S11</td> <td>0</td> <td>1</td> <td>S12</td> <td>0</td> <td>1</td> </tr> <tr> <td>S13</td> <td>0</td> <td>0</td> <td>S14</td> <td>0</td> <td>0</td> <td>NS</td> <td>0</td> <td>0</td> <td>Total</td> <td>0</td> <td>0</td> </tr> </tbody> </table> <div> <input type="checkbox"/> Positive Contralateral LN mtt           Path N: n/a         </div> <div> <div>Type of LN metastasis</div> <div> <input type="checkbox"/> Intranodal           <input type="checkbox"/> Capsular           <input type="checkbox"/> Subcapsular           <input type="checkbox"/> Perinodal         </div> </div> <div> <div>Size of Metastasis</div> <div>           Min. Size: <input type="text" value="0"/>           Max. Size: <input type="text" value="0"/> </div> </div> </div> <div> <div>Comments :</div> <div>Pt Does Not Have Tumor In Other Location-Pathology</div> </div>			+	Total		+	Total		+	Total		+	Total	S1	0	0	S2	0	1	S3	0	0	S4	0	1	S5	0	0	S6	0	0	S7	0	1	S8	0	0	S9	0	1	S10	0	0	S11	0	1	S12	0	1	S13	0	0	S14	0	0	NS	0	0	Total	0	0
	+	Total		+	Total		+	Total		+	Total																																																		
S1	0	0	S2	0	1	S3	0	0	S4	0	1																																																		
S5	0	0	S6	0	0	S7	0	1	S8	0	0																																																		
S9	0	1	S10	0	0	S11	0	1	S12	0	1																																																		
S13	0	0	S14	0	0	NS	0	0	Total	0	0																																																		

## 9) Pathological module: Tissue Bank (Frozen and Paraffin)

Tissue Bank: S-09-888888				Status: Ready...			
<a href="#">Click here</a> to add <input type="text" value="1"/> more row(s). <a href="#">Save it</a> <a href="#">Cancel it</a> <a href="#">Open it</a> <a href="#">Save and Close</a> <a href="#">EXPORT TO EXCEL</a>							
		Frozen	FFPE	TBID	Collection Date	Frozen Avail	FFPE Avail
				<input type="text" value="1038"/>	<input type="text"/>	<input checked="" type="checkbox"/>	
<b>Frozen</b>							
<a href="#">Click here</a> to add <input type="text" value="1"/> more row(s). <a href="#">Save it</a> <a href="#">Cancel it</a> <a href="#">Open it</a> <a href="#">Save and Close</a> <a href="#">EXPORT TO EXCEL</a>							
		ID		Tissue	Blood	Pleural	
		Frozen ID: <input type="text" value="867"/> TB ID: <input type="text" value="1038"/> SPORE No: <input type="text" value="2605"/> TID No: <input type="text"/>	Normal Lung <input checked="" type="checkbox"/>	DNA Conc <input type="text"/>	DNA Conc <input type="text"/>	DNA Conc <input type="text"/>	
			Tumor <input checked="" type="checkbox"/>	DNA Vol <input type="text"/>	DNA Vol <input type="text"/>	DNA Vol <input type="text"/>	
			Bronchus <input type="checkbox"/>	DNA Quality <input type="text" value="n/a"/>	DNA Quality <input type="text" value="n/a"/>	DNA Quality <input type="text" value="n/a"/>	
			LN <input type="checkbox"/>	RNA Conc <input type="text"/>	RNA Conc <input type="text"/>	RNA Conc <input type="text"/>	
			Serum <input checked="" type="checkbox"/>	RNA Vol <input type="text"/>	RNA Vol <input type="text"/>	RNA Vol <input type="text"/>	
			Lymphocyte <input type="checkbox"/>	RNA Quality <input type="text" value="n/a"/>	RNA Quality <input type="text" value="n/a"/>	RNA Quality <input type="text" value="n/a"/>	
			Pleural <input type="checkbox"/>	Prot Conc <input type="text"/>	Prot Conc <input type="text"/>	Prot Conc <input type="text"/>	
				Prot Vol <input type="text"/>	Prot Vol <input type="text"/>	Prot Vol <input type="text"/>	
				Prot Quality <input type="text" value="n/a"/>	Prot Quality <input type="text" value="n/a"/>	Prot Quality <input type="text" value="n/a"/>	
<b>FFPE</b>							
<a href="#">Click here</a> to add <input type="text" value="1"/> more row(s). <a href="#">Save it</a> <a href="#">Cancel it</a> <a href="#">Open it</a> <a href="#">Save and Close</a> <a href="#">EXPORT TO EXCEL</a>							
		FFPE ID	TB ID	Cabinet	Tray	Block	Slide

## 10) Dictionary module

Admin
Projects
Histo-Pathology Lab
Logout

**Dictionaries**

Country
Update

Page 1 [2] [3] [4] [5] [...]

	Dictionaries	Set Order
+		
	Afghanistan	1
	Albania	2
	Algeria	3
	American Samoa	4
	Andorra	5
	Angola	6
	Anguilla	7
	Antarctica	8
	Antigua and Barbuda	9
	Arctic Ocean	10
	Argentina	11
	Armenia	12
	Aruba	13
	Ashmore and Cartier Islands	14
	Atlantic Ocean	15
	Australia	16
	Austria	17
	Azerbaijan	18
	Bahamas	19

Page 1 [2] [3] [4] [5] [...]

Page 1 of 14

## 11) Dictionary module

Admin
Projects
Histo-Pathology Lab
Logout

### Dictionaries

Country
Update

Page 1 [2] [3] [4] [5] [...]

	Dictionaries	Set Order
+		
	Afghanistan	1
	Albania	2
	Algeria	3
	American Samoa	4
	Andorra	5
	Angola	6
	Anguilla	7
	Antarctica	8
	Antigua and Barbuda	9
	Arctic Ocean	10
	Argentina	11
	Armenia	12
	Aruba	13
	Ashmore and Cartier Islands	14
	Atlantic Ocean	15
	Australia	16
	Austria	17
	Azerbaijan	18
	Bahamas	19

Page 1 [2] [3] [4] [5] [...]

Page 1 of 14

12) Query Tool.



## Query Generator

### Query Template Management

select query:   enter query name:  ☐ private

Status: Ready

Query Criteria [Reset](#) [Create a new query](#)

	Field ID	Field Name	Operator	Field Value	And/Or
+	0	Select...	Select...		and

Field Selection [Reset](#)

Selected Fields [Unselect](#) [Clear](#)    Ordering Fields [Unselect](#) [Clear](#)    Sorting Fields [Unselect](#) [Clear](#)

The screenshot shows a Jupyter Notebook with three empty code cells. The bottom cell has a toolbar with 'asc' and 'desc' buttons. The interface is in a light theme.

[Clear](#)
[Reset](#)
[Select All](#)

☒ All
 ☐ Accession
 ☐ Chemotherapy
 ☐ FFPE
 ☐ Frozen Bank
 ☐ General Info
 ☐ Histological Dx
 ☐ Other Malignancy
 ☐ Other Treatment
 ☐ Patient
 ☐ Radiology
 ☐ Staging
 ☐ Surgery
 ☐ Tissue Bank
 ☐ Tumor

Acet No	Date COVID Dx	Invasion Heart	Middle Name	Protocol ID	Site
Accession No	Date Other Tx	Invasion Intracra	Mild Hemoptysis	Race	Side
AccessionID	Date Quit Smoke	Invasion Vertebral Bones	Mild Squamous Dysplasia	Reduction Fibrosis	Smoked -> 100
Acname	Date Screening	Invasion Vessel	Mild Squamous Dysplasia	Radio Clin Response	Soft Tissue Margins
Address1	Date Staging	Is Chemo	More Than 1 Nodal	Radio Comments	Solid
Address2	Date Surgery	Is NED	Multiple Segmentectomy	Radio CT Response	Specimen Avail
Age Start Smoke	Diabetes	Is Radio	Multiple Wedge	Radio MDA	Specimen Type
Alcohol	DOB	Is Surgery	N Clin	Radio Patho Response	SPORE_Na
Asbestos	Dx	Last Name	Necrosis	Radio Site	Squamous Metaplasia
Asthma	Dx Date	LN	NED Date	Radio Start Date	Stage
Atelectic Lung	Dx Specimen Date	LN Involve	No Drinks a Mo	Radio Stop Date	Study ID
Atypical Adeno Hyper	Dx Variant	LN Max Size	No of Nodules	Radio Treatment Options	Sub Type
Avg Cig a Day	Dxp Acname	LN Met	No Smoke Mo	Radio Tumor Size After CT	Surgery
BAC	Dxlp BAC	LN Met Capsular	No Smoke Years	Radio Tumor Size After Patho	Surgery Comments
Biochemistry	Dxlp Carcinoma Met Site	LN Met Intracodal	Normal Benign Epi	Radio Tumor Size Before Patho	Surgery Procedure
Block	Dxlp Dx	LN Met Pericodal	Normal Lung Parenchyma	Radiotherapy	Surgical Date
Blood DNA Conc	Dxlp Dx Variant	LN Met Subcapsular	Normal Lung	Radio Tumor Size Before CT	Sypex Chain
Blood DNA Quality	Dxlp Fibrosis	LN Min Size	NS +	Remal Ineffct	T Clin
Blood DNA Volume	Dxlp Grade	Lobectomy	NS Analyzed	S1	TID
Blood Protein Conc	Dxlp Inflammation	Lymphocyte	NSCLC Type	S1 +	Thyroid
Blood Protein Quality	Dxlp Met Dx	M Clin	On Study	S10	TID_No
Blood Protein Volume	Dxlp Microcapillary	Ndxg Pl Eff	Other Margins	S10 +	Time Line
Blood RNA Conc	Dxlp Necrosis	Malignant Pleural Eff	Other MDA Rx	S11	Tissue RNA Conc
Blood RNA Quality	Dxlp NSCLC Type	Margen +	Other Med History	S11 +	Tissue RNA Quality
Blood RNA Volume	Dxlp Papillary	Margen Residual	Other Treatment Comments	S12	Tissue RNA Volume
Breast Hyperplasia	Dxlp Sarcoma Met Site	MDA	Papillary	S12 +	Tissue Protein Conc
Breast L Margin	Dxlp Solid	MDAH	Paraneural Margen	S13	Tissue Protein Quality
Breast Lobe	Dxlp Sub Type	Mediastinal Pleura	Parietal Pleura	S13 +	Tissue Protein Volume
Breast Lx	Dxlpp Dx	Mediastinal Fat	Path M	S14	Tissue RNA Conc
Breast Lx Sample	Endobion	Met Date	Path N	S14 +	Tissue RNA Quality
Cabinet	Event	Met Dx	Path T	S2	Tissue RNA Volume
Carcinoma Met Site	Ever Consumed Alcohol	Met Specimen Avail	Path Type	S2 +	Total +
Cardio	Expiratory Inhaler	Met Specimen Type	Patho N	S3	Total Analyzed
Cardio DVT	Expiratory Principal	Met Tumor Site	Patho T	S3 +	Try
Cell Phone	FFPE	Metp Acname	Patient Comments	S4	Tumor
Chemo Drug A	Fibrosis	Metp BAC	Patient ID	S4 +	Tumor Invasion
Chemo Drug B	First Name	Metp Carcinoma Met Site	Percutaneous	S5	Tumor Invasion Neural
Chemo Drug C	Frozen	Metp Dx	Phrenic Nerve	S5 +	Tumor Invasion Other
Chemo MDA	Gender	Metp Dx Variant	Pneud	S6	Tumor Invasion Pleural
Chemo Start Date	Grade	Metp Fibrosis	Neural Attached	S6 +	Tumor Invasion Vascu

### 13) The query results page

Query Name: Adenocarcinoma																										
Record Count: 13																										
Accession No	Dx Bilobectomy	Specimen Date	Event	Lobectomy	Met Date	Met Specimen Avail	Met Specimen Type	Met Specimen Site	Multiple Segmentectomy	Multiple Wedge	No of Nodes	Path M	Path N	Path I	Path Type	Pneumonectomy	Single Segmentectomy	Single Wedge	Specimen Avail	Specimen Type	Surgical Date	Tumor Site	Acinar BAC	Carcinoma Met Site	Dx	
S.03-000993	False		Surgical Specimen	False					False	False	1	M0	N0	T2	Primary	False	False	True			1/8/2003 12:00:00 AM	35	5	n/a	NSCLC	
S.03-015760	False		Surgical Specimen	False					False	False	1	M0	N0	T1	Primary	False	False	True			4/2/2003 12:00:00 AM	80	0	n/a	NSCLC	
S.03-018420	False		Surgical Specimen	True					False	False	1	M0	N2	T1	Primary	False	False	False			4/16/2003 12:00:00 AM	0	0	n/a	NSCLC	
S.03-020423	False		Surgical Specimen	False					False	False	1	M0	N2	T2	Primary	False	False	True			4/29/2003 12:00:00 AM	60	0	n/a	NSCLC	
S.03-024985	False		Surgical Specimen	True					False	False	1	M0	N0	T1	Primary	False	False	False			5/23/2003 12:00:00 AM	20	80	n/a	NSCLC	
S.03-052181	False		Surgical Specimen	True					False	False	3	M0	N2	T4	Primary	False	False	False			10/23/2003 12:00:00 AM	0	0	n/a	NSCLC	
S.04-051605	False		Surgical Specimen	True					False	False	1	M0	N0	T2	Primary	False	False	False			10/6/2004 12:00:00 AM	25	75	n/a	NSCLC	
S.04-056678	False		Surgical Specimen	True					False	False	2	M1	N0	T2	Primary	False	False	True			11/2/2004 12:00:00 AM	35	50	n/a	NSCLC	
S.05-020799	False		Surgical Specimen	True					False	False	1	M0	N0	T2	Primary	False	False	False			4/19/2005 12:00:00 AM	0	0	n/a	NSCLC	
S.05-029775	False		Surgical Specimen	True					False	False	1	M0	N1	T3	Primary	False	False	False			6/6/2005 12:00:00 AM	0	0	n/a	NSCLC	
S.05-050475	False		Surgical Specimen	True					False	False	1	M0	N2	T2	Primary	False	False	False			9/19/2005 12:00:00 AM	0	0	n/a	NSCLC	
S.05-065030	False		Surgical Specimen	False					False	False	1	M0	N0	T2	Primary	False	False	True			12/7/2005 12:00:00 AM	0	0	n/a	NSCLC	
S.05-068150	False		Surgical Specimen	True					False	False	1	M0	N1	T2	Primary	False	False	False			12/27/2005 12:00:00 AM	0	0	n/a	NSCLC	

14) The example of the Excel reports.

	K	L	M	N	O	P	Q
1	Specimen Avail	Surgical Date	Single Wedge	Multiple Wedge	Single Segmentectomy	Multiple Segmentectomy	Lobectomy
2							
3							
4			+				
5		5/11/2005 0:00	FALSE	FALSE	FALSE	FALSE	TRUE
6		5/11/2005 0:00	FALSE	FALSE	FALSE	FALSE	TRUE
7		5/11/2005 0:00	FALSE	FALSE	FALSE	FALSE	TRUE
8		5/11/2005 0:00	FALSE	FALSE	FALSE	FALSE	TRUE
9							
10							
11							
12							
13		1/1/1900 0:00	FALSE	TRUE	TRUE	FALSE	FALSE
14		1/1/1900 0:00	FALSE	TRUE	TRUE	FALSE	FALSE
15	FALSE						
16	TRUE						
17							
18							
19		1/1/1900 0:00	FALSE	FALSE	FALSE	FALSE	FALSE
20							
21							
22							
23							
24							
25							
26		1/1/1900 0:00	FALSE	FALSE	FALSE	FALSE	FALSE
27							
28							
29							
30							
31							
32							
33							
34							
35							

## 15). Patient Summary Report

